



Universidad de Oviedo

Programa de Doctorado en Materiales

SÍNTESIS Y SINTERIZACIÓN DE MATERIALES
CERÁMICOS AVANZADOS

SYNTHESIS AND SINTERING OF ADVANCED CERAMIC
MATERIALS

TESIS DOCTORAL

Cristian Gómez Rodríguez

Junio 2024



Universidad de Oviedo

Programa de Doctorado en Materiales

SÍNTESIS Y SINTERIZACIÓN DE MATERIALES
CERÁMICOS AVANZADOS

SYNTHESIS AND SINTERING OF ADVANCED CERAMIC
MATERIALS

TESIS DOCTORAL

Directores de tesis

Dr. D. Daniel Fernández González

Dr. D. Luis Felipe Verdeja González



RESUMEN DEL CONTENIDO DE TESIS DOCTORAL

1.- Título de la Tesis	
Español: Síntesis y sinterización de materiales cerámicos avanzados	Inglés: Synthesis and sintering of advanced ceramic materials
2.- Autor	
Nombre: Cristian Gómez Rodríguez	
Programa de Doctorado: Materiales	
Órgano responsable: Centro Internacional de Postgrado	

RESUMEN (en español)

Desde hace un tiempo las sociedades avanzadas vienen reclamando un mayor cuidado del planeta, ya sea en los productos que consumen como en los procesos que se emplean para su obtención. Esta cuestión sumada al hecho de la inestabilidad creciente en el mercado de la energía ya sea del gas natural, los derivados del petróleo o los combustibles nucleares han hecho que los gobiernos y empresas privadas hayan apostado de modo decidido por una transición hacia fuentes de energía renovables. Pese a la fuerte apuesta que se está haciendo por la energía solar para la generación de calor y electricidad, todavía hay margen para la extensión de su uso hacia la síntesis de materiales. De esta manera, la primera parte de la tesis doctoral se centra en la investigación de procesos de síntesis de materiales cerámicos mediante el empleo de la energía solar concentrada como fuente de calor para el proceso. En este sentido, por una parte, se estudió la descomposición de las arenas de silicato de zirconio empleando la energía del sol para generar óxido de zirconio (IV), que es un material cerámico fundamental. Por otra parte, se sintetizó aluminato de magnesio ($MgAl_2O_4$) a partir de MgO y un residuo de la metalurgia del aluminio, como son los finos de electrofiltro del proceso Bayer, utilizando como fuente de calor la energía solar concentrada.

La síntesis de materiales cerámicos es un aspecto fundamental, pero también lo es la sinterización de estos materiales para obtener cuerpos densos que se puedan emplear en diferentes campos, desde el de los refractarios hasta el de las cerámicas funcionales. En la segunda parte de la tesis doctoral se abordó la sinterización de materiales cerámicos (cerámico-cerámico y cerámico-metal) empleando diferentes tecnologías, incluyendo la sinterización en horno convencional de alta temperatura, la sinterización por *spark plasma sintering* o el empleo de la tecnología de láser de CO_2 . Los sistemas de materiales compuestos cerámicos densos estudiados pivotaron entorno a los materiales oxidicos de uso común, como el MgO y el Al_2O_3 , a los que se incorporan diferentes tipos de refuerzos en forma de nanopartículas cerámicas (ZrO_2 , Fe_2O_3 , Al_2O_3 o TiO_2) o metálicas (molibdeno) con el objeto de mejorar su densificación y su comportamiento ya sea frente a la corrosión por escorias o sus propiedades mecánicas.

RESUMEN (en inglés)

For some time now, advanced societies have been demanding greater care for the planet, both in the products they consume, and the processes used to obtain them. This issue, added to the fact of growing instability in the energy market, whether for natural gas, petroleum derivatives, or nuclear fuels, has caused governments and private companies to have decidedly opted for a transition towards renewable energy sources. Despite the strong commitment that is being made to solar energy for the generation of heat and electricity, there is still room for the extension of its use towards the synthesis of materials. In this way, the first part of the doctoral thesis focuses on the investigation of synthesis processes of ceramic materials using concentrated solar energy as a heat source for the process. In this sense, on the one hand, the analysis of zirconium silicate



Universidad de Oviedo

sands using the sun's energy to generate zirconium (IV) oxide, which is a fundamental ceramic material, was studied. On the other hand, magnesium aluminate ($MgAl_2O_4$) was synthesized from MgO and waste from aluminum metallurgy, such as electrofilter fines from the Bayer process, using concentrated solar energy as a heat source.

The synthesis of ceramic materials is a fundamental aspect, but so is the sintering of these materials to obtain dense bodies that can be used in different fields, from refractories to functional ceramics. In the second part of the doctoral thesis, the sintering of ceramic materials (ceramic-ceramic and ceramic-metal) was addressed using different technologies, including sintering in a conventional high-temperature furnace, sintering by spark plasma sintering, or the use of the technology laser of CO_2 . The dense ceramic composite material systems studied in this doctoral thesis pivoted around commonly used oxidized materials, such as MgO and Al_2O_3 , to which different types of reinforcements are incorporated in the form of ceramic (ZrO_2 , Fe_2O_3 , Al_2O_3 , or TiO_2) or metallic nanoparticles (molybdenum) to improve its densification and its behavior either against corrosion by slag or its mechanical properties.

**SR. PRESIDENTE DE LA COMISIÓN ACADÉMICA DEL PROGRAMA DE DOCTORADO
EN MATERIALES**

AGRADECIMIENTOS

Esta tesis es un trabajo en conjunto de personas que tenemos en común el gusto por la investigación, y que aportaron de manera directa e indirecta un granito de arena para la culminación de este trabajo, es por ello por lo que quiero expresarles mi agradecimiento.

Durante nuestro caminar uno encuentra a personas que marcan una diferencia en nuestras vidas ya que son un “parte aguas” en el rumbo de vida, ideas, metas y gustos, y que, aunque sean de lugares distantes o lejanos el bien común en lo humano, académico e investigación se caracteriza, ya que son lazos que nos unen y que nos dan fuerzas en el día a día, Gracias: Dr. Daniel Fernández González y Dr. Luis Felipe Verdeja.

Agradecimientos también al Dr. Ignacio Verdeja González y al Geólogo Lucio García-Pertierra Luiña cuyos aportes fueron significativos en aspectos científicos, técnicos, consejos y experiencias de vida para los diferentes artículos publicados.

También agradecer al Dr. Adolfo Fernández Valdés por su apoyo científico y permitirme realizar una estancia dentro de las instalaciones del CINN-CSIC (Asturias, España).

Agradecer al Dr. Guadalupe Alan Castillo Rodríguez por permitirme realizar una estancia de investigación en la FIME-UANL-México.

Agradecer a la Universidad Veracruzana (Vicerrectoría y Dirección General de Investigación) por permitirme realizar estancias de investigación, en las instituciones antes mencionadas.

Agradecer a la Asociación Universitaria Iberoamericana de Posgrado (AUIP) con Programa de Becas de Movilidad entre Instituciones asociadas a la AUIP 2023. Y también a la

Universidad Veracruzana, México por la beca "Habilitación del Perfil Internacional: HAPI" – UV, convocatoria 2023, ya que ambas instituciones me permitieron realizar movilidad académica.

Así mismo al laboratorio PROMES-CNRs (Procédés, Matériaux et Energie Solaire-Centre National de la Recherche Scientifique) por permitirnos utilizar infraestructura (horno solar y equipos) en el marco del proyecto de la Unión Europea para el acceso a la infraestructura de investigación SFERA II, por financiar viaje y estancia por 1 semana (en 2023) de experimentación en Odeillo (Francia).

Así mismo, en especial agradecer a mi esposa Dra. Linda Viviana García Quiñonez una vez más por apoyarme y tenerme paciencia en momentos difíciles, una meta que se logró juntos.

Y a mi hija Ximena Lizbeth Gómez García le dedico este trabajo de investigación.

Oviedo/Uviéu, Asturias, España, Junio 2024

Resumen

Desde hace un tiempo las sociedades avanzadas vienen reclamando un mayor cuidado del planeta, ya sea en los productos que consumen como en los procesos que se emplean para su obtención. Esta cuestión sumada al hecho de la inestabilidad creciente en el mercado de la energía ya sea del gas natural, los derivados del petróleo o los combustibles nucleares han hecho que los gobiernos y empresas privadas hayan apostado de modo decidido por una transición hacia fuentes de energía renovables. Pese a la fuerte apuesta que se está haciendo por la energía solar para la generación de calor y electricidad, todavía hay margen para la extensión de su uso hacia la síntesis de materiales. De esta manera, la primera parte de la tesis doctoral se centra en la investigación de procesos de síntesis de materiales cerámicos mediante el empleo de la energía solar concentrada como fuente de calor para el proceso. En este sentido, por una parte, se estudió la descomposición de las arenas de silicato de zirconio empleando la energía del sol para generar óxido de zirconio (IV), que es un material cerámico fundamental. Por otra parte, se sintetizó aluminato de magnesio ($MgAl_2O_4$) a partir de MgO y un residuo de la metalurgia del aluminio, como son los finos de electrofiltro del proceso Bayer, utilizando como fuente de calor la energía solar concentrada.

La síntesis de materiales cerámicos es un aspecto fundamental, pero también lo es la sinterización de estos materiales para obtener cuerpos densos que se puedan emplear en diferentes campos, desde el de los refractarios hasta el de las cerámicas funcionales. En la segunda parte de la tesis doctoral se abordó la sinterización de materiales cerámicos (cerámico-cerámico y cerámico-metal) empleando diferentes tecnologías, incluyendo la sinterización en horno convencional de alta temperatura, la sinterización por *spark plasma sintering* o el empleo de la tecnología de láser de CO_2 . Los sistemas de materiales compuestos

cerámicos densos estudiados pivotaron entorno a los materiales oxídicos de uso común, como el MgO y el Al₂O₃, a los que se incorporan diferentes tipos de refuerzos en forma de nanopartículas cerámicas (ZrO₂, Fe₂O₃, Al₂O₃ o TiO₂) o metálicas (molibdeno) con el objeto de mejorar su densificación y su comportamiento ya sea frente a la corrosión por escorias o sus propiedades mecánicas.

Summary

For some time now, advanced societies have been demanding greater care for the planet, both in the products they consume, and the processes used to obtain them. This issue, added to the fact of growing instability in the energy market, whether for natural gas, petroleum derivatives, or nuclear fuels, has caused governments and private companies to have decidedly opted for a transition towards renewable energy sources. Despite the strong commitment that is being made to solar energy for the generation of heat and electricity, there is still room for the extension of its use towards the synthesis of materials. In this way, the first part of the doctoral thesis focuses on the investigation of synthesis processes of ceramic materials using concentrated solar energy as a heat source for the process. In this sense, on the one hand, the analysis of zirconium silicate sands using the sun's energy to generate zirconium (IV) oxide, which is a fundamental ceramic material, was studied. On the other hand, magnesium aluminate (MgAl_2O_4) was synthesized from MgO and waste from aluminum metallurgy, such as electrofilter fines from the Bayer process, using concentrated solar energy as a heat source.

The synthesis of ceramic materials is a fundamental aspect, but so is the sintering of these materials to obtain dense bodies that can be used in different fields, from refractories to functional ceramics. In the second part of the doctoral thesis, the sintering of ceramic materials (ceramic-ceramic and ceramic-metal) was addressed using different technologies, including sintering in a conventional high-temperature furnace, sintering by *spark plasma sintering*, or the use of the technology laser of CO_2 . The dense ceramic composite material systems studied in this doctoral thesis pivoted around commonly used oxidized materials, such as MgO and Al_2O_3 , to which different types of reinforcements are incorporated in the

form of ceramic (ZrO_2 , Fe_2O_3 , Al_2O_3 , or TiO_2) or metallic nanoparticles (molybdenum) to improve its densification and its behavior either against corrosion by slag or its mechanical properties.

Contenido

Resumen	7
Summary.....	9
1. Introducción.....	13
2. Objetivos.....	19
3. Síntesis de materiales cerámicos empleando energía solar concentrada: Motivación de la investigación, novedad y discusión de los principales avances en el área.	23
3.1. La energía solar en el campo de los materiales.....	24
3.2. Síntesis de materiales cerámicos.....	29
3.3. Síntesis del óxido de zirconio: Novedad y discusión	30
3.4. Síntesis de aluminato de magnesio: Novedad y discusión	32
4. Sinterización de materiales cerámicos de matriz MgO o Al ₂ O ₃ con nanopartículas de óxidos cerámicos o metálicas empleando técnicas convencionales o avanzadas (láser de CO ₂ y <i>spark plasma sintering</i>): Motivación de la investigación, novedad y discusión de los principales avances en el área.....	35
4.1. Fabricación de materiales cerámicos	36
4.2. Sinterización de materiales cerámicos	38
4.2.1. Técnicas de sinterizado	40
4.3. Sinterización convencional de refractarios de matriz MgO.....	47
4.4. Sinterización no convencional de refractarios de matriz Al ₂ O ₃	54
5. Bibliografía.....	57
6. Artículos publicados	67
Artículo 1: Solar dissociation of zirconium silicate sand: A clean alternative to obtain zirconium dioxide.	73
Artículo 2: Solar assisted production of MgAl ₂ O ₄ from Bayer process electrofilter fines as source of Al ₂ O ₃	89

Artículo 3: MgO–ZrO ₂ ceramic composites for silicomanganese production.	105
Artículo 4: Selective laser sintering of alumina-molybdenum nanocomposites.	125
Artículo 5: Alumina/molybdenum nanocomposites obtained by colloidal synthesis and spark plasma sintering.	133
Trabajo complementario 1: Morphological study of refractory composite materials based on magnesia (MgO) with additions of hercinite (Fe ₂ Al ₂ O ₄).	145
Trabajo complementario 2: Nano-Oxide (SiO ₂ and Fe ₂ O ₃) effect on magnesium oxide compound (MgO).	151
Trabajo complementario 3: Synthesis and characterization of dense MgO–TiO ₂ nanocomposites obtained by two novel processing routes.	167
Trabajo complementario 4: Desarrollo de un refractario de MgO dopado con η-Al ₂ O ₃	179
7. Conclusiones.....	197
8. Conclusions	203

1. Introducción

La palabra “cerámica” proviene del término griego “keramos”, que significa “material calcinado” o “material horneado” (Pero-Sanz Elorz et al., 2019; Verdeja, 2008a, 2008b).

Los materiales cerámicos se suelen clasificar de varias formas (origen, aplicación, estructura cristalina, tipo de enlace, procesamiento, entre otros), pero la más común y sencilla puede ser: cerámica tradicional y cerámica avanzada (Rahaman, 2003; Schacht, 2004). Desde luego, pese a la importancia de las cerámicas tradicionales por su aplicación ornamental o alimentaria, las cerámicas avanzadas abarcan un campo más amplio motivado por su uso estructural y funcional a nivel industrial, entre otros. Es por ello por lo que la investigación se centra con mayor diligencia hacia el campo de las cerámicas avanzadas en general, y los materiales refractarios en particular, los cuales se caracterizan por sus extraordinarias propiedades físicas, químicas, mecánicas y refractarias, ya que están diseñados para que sus prestaciones no se deterioren con las elevadas temperaturas, incluso bajo la influencia de materiales fundidos. Debido a esto, los materiales refractarios son indispensables en toda actividad industrial, en específico en la industria de los metales o metalurgia, siendo utilizados principalmente como revestimientos de paredes, pisos y bóvedas de diferentes hornos.

Los materiales refractarios se pueden dividir en tres grupos dependiendo del grado de acidez: básicos, neutros y ácidos (Schacht, 2004; Verdeja, 2008b). Su uso y aplicación para la cual fueron diseñados depende del tipo de horno, entre los que podemos mencionar:

- i) ladrillo de sílice, en el cual se le añaden de un 3 a 3.5 % de CaO para promover la sinterización en fase líquida,
- ii) ladrillo de semi-sílice, el cual contiene de un 18 a 25% de Al_2O_3 ,

- iii) ladrillo de arcilla refractaria, que está hecho de caolinita ($\text{Al}_2\text{O}_3 \cdot \text{SiO}_2 \cdot 2\text{H}_2\text{O}$) entre un 25 a 45 % de Al_2O_3 ,
- iv) ladrillo con alto contenido en alúmina de un 45 a 100 % de alúmina,
- v) ladrillo de dolomita, el cual está hecho de ($\text{CaCO}_3 \cdot \text{MgCO}_3$),
- vi) el ladrillo de magnesia, que contiene principalmente MgO (>90% MgO),
- vii) ladrillos de cromita, pueden contener entre un 34% de Al_2O_3 y un 30% de Cr_2O_3 , a menudo se producen ladrillos de magnesia-cromita,
- viii) ladrillos refractarios de zircón ($\text{ZrO}_2 \cdot \text{SiO}_2$), los cuales pueden contener un 4% de CaO (**Carter, 2013**).

Como se puede constatar, las grandes familias de refractarios de naturaleza oxidica se basan en CaO , MgO , Al_2O_3 , Cr_2O_3 , SiO_2 o ZrO_2 , aunque hay otro tipo de materiales de tipo carburo o nitruro que también se emplean con finalidad de refractarios. Estos ladrillos refractarios son fabricados de diferentes materias primas, como las anteriores, se prensan, para obtener compactos en verde, y, posteriormente, se tratan térmicamente a elevadas temperaturas (sinterización).

La industria cerámica se enfrenta a toda una serie de problemas relacionados con la lucha contra el cambio climático. Este aspecto afecta tanto a la obtención de las materias primas como a la obtención de los productos sinterizados porque ambos procesos requieren de elevadas temperaturas y, por ende, implican elevados consumos de energía que, en la actualidad, son satisfechos por combustibles fósiles o electricidad. Estos consumos de energía tienen un impacto en las emisiones de gases de efecto invernadero (y otros contaminantes), inclusive la electricidad que, por ejemplo, en el caso de España tiene un factor de emisión del entorno de los 250 g CO_2 eq/kWh consumido. Asimismo, las

condiciones cambiantes en lo que a la geopolítica respecta tienen un impacto relevante en la política de precios de los combustibles fósiles, que también se traslada a la electricidad como producto final. Así, por ejemplo, en los meses posteriores al intento de conquista de Kiev (mayo-julio de 2022) durante la invasión rusa de Ucrania (2014-actualidad) los precios del gas alcanzaron máximos que, en el caso de Europa, dieron lugar a estratosféricos precios de la electricidad porque era el coste de la generación de electricidad con gas natural el que fijaba los precios mínimos de la electricidad.

Por otra parte, los consumidores de productos cerámicos y refractarios vienen demandando materiales con mejores prestaciones, e incluso con formas semiacabadas, o acortar los tiempos de sinterización. Algunas de estas cuestiones pueden ser respondidas mediante el empleo de técnicas de sinterización no convencionales, como la sinterización por descarga de plasma (más conocida por su denominación en inglés *Spark Plasma Sintering* o SPS) o la sinterización mediante el empleo de láseres. En el caso de la tecnología *Spark Plasma Sintering* es posible lograr materiales con unas propiedades mejoradas en ciclos cortos de sinterización debido a una combinación de calentamiento, presión y condiciones de vacío simultáneas. Permite, igualmente, lograr temperaturas de sinterización muy superiores a las que permiten los hornos convencionales (es posible alcanzar temperaturas de sinterización superiores a los 2500 °C) (**Guardia-Valenzuela et al., 2018**), a excepción, si cabe de los hornos de grafito. Estas altas temperaturas permiten, junto con los efectos de las condiciones de vacío y la presión, lograr que fenómenos de sinterización que empleando métodos convencionales ocurren a una temperatura muy elevada ocurran a temperaturas mucho más bajas empleando la tecnología SPS. Todo ello sumado a que es posible lograr un efecto sobre el tamaño de grano del material a sinterizar (**Suárez et al., 2013**). Otras técnicas, como la

sinterización por láser o *selective laser sintering*, están emergiendo como una interesante alternativa en el campo de la fabricación aditiva, aunque se trata de un campo todavía muy incipiente (Yan et al., 2020).

Volviendo nuevamente a la síntesis de materiales cerámicos, la obtención de estos se enfrenta, como se decía, a una problemática de emisiones de gases de efecto invernadero. Aunque todavía no existen muchas alternativas sostenibles, una de las más prometedoras es el empleo de la energía solar concentrada. Mediante esta tecnología, aunque todavía a escala de laboratorio (o piloto) se ha logrado llevar a cabo procesos de la síntesis de materiales (obtención de metales y cerámicos refractarios duros), el procesado de materiales (tratamientos superficiales, soldadura o sinterización) o reciclado de materiales (descontaminación de suelos, reciclado de aluminio o reciclado de otros residuos industriales). La aplicación de la energía solar al campo de los materiales cerámicos podría, por lo tanto, contribuir a eliminar las emisiones de gases de efecto invernadero y a una reducción de los costes energéticos (Fernández-González, 2023; Fernández-González et al., 2018).

De esta manera, esta tesis doctoral va a centrarse en dos aspectos fundamentales de la industria cerámica, por una parte, en la síntesis mediante el empleo de energía solar de materiales cerámicos, y, por otra parte, en la sinterización de materiales cerámicos avanzados empleando diferentes técnicas de sinterización (horno convencional, sinterización por láser de CO₂ y *spark plasma sintering*). Por lo que respecta a las familias de materiales a estudiar se incluye, en la síntesis de materiales, la obtención de zirconia por descomposición térmica del silicato de zirconio y la obtención de aluminato de magnesio a partir de MgO y un residuo de la metalurgia del aluminio de alto contenido en Al₂O₃, y en la sinterización de materiales,

la obtención de cuerpos densos de composites Al_2O_3 -molibdeno y MgO con nanopartículas de óxidos metálicos (ZrO_2 , TiO_2 , Al_2O_3 , Fe_2O_3 , SiO_2).

2. Objetivos

La investigación recogida en esta tesis doctoral se centra en el campo de los materiales cerámicos avanzados, enfocándose en dos grandes líneas de trabajo como son la síntesis de materiales cerámicos y la sinterización de materiales compuestos de matriz cerámica empleando técnicas convencionales de sinterización. Los objetivos generales de la investigación son, para cada una de las líneas de trabajo propuestas, los que siguen:

Línea de la síntesis de materiales cerámicos:

- Emplear la energía solar concentrada como una fuente de calor para procesos industriales de interés tecnológico, como la fabricación de materiales cerámicos, como una alternativa para contribuir a la reducción de las emisiones de gases de efecto invernadero.

Línea de la sinterización de materiales compuestos de matriz cerámica:

- Utilizar rutas de sinterización convencionales (hornos de alta temperatura) y no convencionales (sinterización con láser de CO₂ y por *spark plasma sintering*) para obtener cuerpos densos que pudieran ser empleados en aplicaciones de interés tecnológico.

A continuación, se profundizará en los objetivos particulares de cada una de las líneas de investigación anteriormente expuestas. Comenzando con la síntesis de materiales cerámicos:

- Estudiar la descomposición térmica empleando energía solar concentrada de las arenas de silicato de zirconio para obtener óxido de zirconio (ZrO₂) y recuperación del mismo por lixiviación con sosa a baja temperatura (200 °C).

- Analizar el empleo de aditivos para mejorar-facilitar la extracción del óxido de zirconio, incluyendo la descomposición sin aditivos, empleando un 10 % en peso de carbonato de sodio o utilizando diferentes contenidos de óxido de calcio (II) (10, 25 y 50% en peso).
- Investigar la síntesis de la espinela $MgAl_2O_4$ empleando energía solar concentrada como una alternativa de síntesis sencilla empleando una energía renovable a partir de magnesia industrial y residuos de la industria metalúrgica (finos de electrofiltro del proceso Bayer).
- Evaluar la influencia del empleo de residuos de tres plantas de fabricación de alúmina metalúrgica, analizar sus parámetros microestructurales y considerar la factibilidad tecno económica del proceso.

Por lo que respecta a la línea de la sinterización de materiales cerámicos los objetivos que se proponen son los que a continuación se detallan para el refuerzo de cerámicas de matriz magnesia y aditivos en forma de nanopartículas, empleando para ello la metodología de sinterización convencional:

- Estudiar la incorporación de nanopartículas de ZrO_2 , TiO_2 , SiO_2 , Al_2O_3 , Fe_2O_3 y $Fe_2Al_2O_4$ en diferentes contenidos a un cerámico de matriz MgO y evaluar la influencia en la microestructura y propiedades del material compuesto obtenido.
- En el caso del material compuesto $MgO-TiO_2$, estudiar el empleo de nanopartículas de TiO_2 , en diferentes contenidos 1, 3 y 5 % en peso, y variando el precursor del MgO , que podía ser MgO caustico o brucita ($Mg(OH)_2$). Evaluar la microestructura, y propiedades físicas y mecánicas del composite obtenido.

- En el caso de los materiales compuestos MgO-SiO₂ y MgO- Fe₂O₃, estudiar el empleo de diferentes contenidos 1, 3 y 5 % en peso en la densificación y microestructura del material denso obtenido.
- En el caso del material compuesto MgO- Al₂O₃, estudiar diferentes contenidos de Al₂O₃ en peso: 1, 2 y 5, en la microestructura y las propiedades físicas y mecánicas del composite obtenido. También, evaluar la influencia de la temperatura de sinterización: 1300, 1500 y 1600 °C.
- En el caso del material compuesto MgO-ZrO₂, analizar diferentes contenidos en ZrO₂ en peso: 1, 3 y 5, en la microestructura y las propiedades físicas y mecánicas del composite obtenido. También, evaluar la influencia de la temperatura de sinterización: 1550 y 1650 °C, y el modo de prensado: presión en frío uniaxial, prensado isostático, o ambas. Asimismo, el objetivo es estudiar el comportamiento de refractario frente al empleo de escoria de silicomanganeso con el fin de buscar un potencial uso industrial para el composite.
- En el caso del material compuesto MgO- Fe₂Al₂O₄, analizar diferentes contenidos en Fe₂Al₂O₄ en peso: 1, 2.5, 5, 10 y 20, en la microestructura y las propiedades físicas y mecánicas del composite obtenido.

Finalmente, dentro de la línea de la sinterización de materiales cerámicos, se propone estudiar el empleo de novedosas tecnologías de sinterización y procesamiento de polvos en la obtención de cuerpos densos de un cerámico común como el de Al₂O₃:

- Obtener nanocomposites de alúmina y molibdeno mediante la ruta coloidal empleando cloruro de molibdeno como precursor del molibdeno. Estudiar la influencia de diferentes contenidos en peso (1, 5 y 10 %) en las propiedades físicas

(densificación) y mecánicas del composite (dureza, resistencia a flexión y tenacidad), y como el molibdeno afecta a la microestructura en términos de crecimiento de grano. Evaluar el papel que desempeña el empleo de la tecnología de sinterización *spark plasma sintering* en estas cuestiones.

- Emplear la tecnología de sinterización de láser de CO₂ para obtener cuerpos densos de Al₂O₃-Mo, variando el contenido en molibdeno (1, 2.5, 5, 10 y 20 % en peso), y evaluar cómo influye en la densificación y la microestructura el empleo de esta tecnología.

3. Síntesis de materiales cerámicos empleando energía solar concentrada: Motivación de la investigación, novedad y discusión de los principales avances en el área.

Las sociedades modernas avanzadas demandan cada vez más que la producción de los diferentes elementos de consumo se realice de la forma más sostenible desde el punto de vista medioambiental posible. A esto se suma la cada vez más creciente inestabilidad geopolítica que, junto con el hecho de que los combustibles de uso común se encuentren en manos de pocas corporaciones o países, conduce a una crisis energética poco más que perpetua, en parte motivada por una falta de soberanía energética. Así hemos visto que durante los meses posteriores a la invasión a gran escala de Ucrania los precios del gas natural se dispararon a niveles nunca vistos lo que generó una crisis de grandes dimensiones en Europa por una parte en el sector eléctrico como el industrial con subidas de precios que alcanzaron las dos cifras porcentuales. Esta situación viene siendo recurrente desde las grandes crisis del petróleo que tienen lugar casi cada década. En estos periodos de incertidumbre la política es la de buscar fuentes alternativas que vengán a paliar estos problemas, y al albur de los cuales el desarrollo de las energías renovables ha adquirido una dimensión tal que actualmente prácticamente el 50% de la eléctrica en España es generada mediante estas fuentes de energía (**Figura 1**).

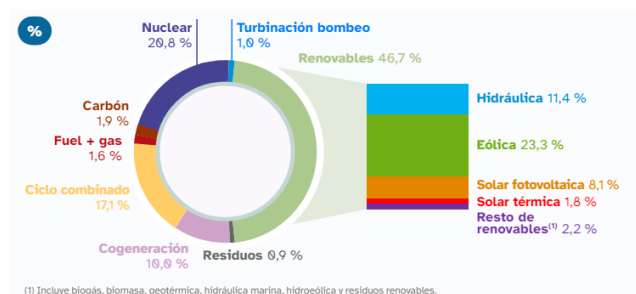


Figura 1. Mix energético para España en el año 2021 (*El sistema eléctrico español, 2021*).

Pese a la implantación de las energías renovables en la generación de electricidad o calor, todavía son pocas las investigaciones llevadas a cabo para buscar un uso directo de las energías renovables en la producción de materiales metálicos o cerámicos. En este campo, la energía solar puede jugar un papel fundamental pues, cuando se encuentra adecuadamente concentrada permite alcanzar temperaturas que pueden llegar a superar los 2000 °C, que son los suficientes para llevar a cabo la mayoría de los procesos de la industria de los materiales.

3.1. La energía solar en el campo de los materiales

La utilización de la energía solar en el campo de los materiales viene de lejos. Cuenta la leyenda que Arquímedes hundió la flota romana durante el Sitio de Siracusa durante la Segunda Guerra Púnica allá por el siglo III antes de Cristo (**Figura 2**). Más allá de este hecho, la aplicación tradicional de la energía solar en el campo de los materiales es el secado de los ladrillos de adobe al sol.



Figura 2. Fotograma de la película *Indiana Jones y el dial del destino* donde se recrea el empleo por parte de Arquímedes de espejos durante el Sitio de Siracusa para hundir la flota romana.

Particularmente en la síntesis de materiales avanzados, la investigación comienza en el siglo XVII cuando un matemático alemán llamado Ehrenfried Walter Von Tschirnhaus diseñó, construyó y trabajó con lentes y espejos con el objetivo de concentrar la energía del sol y así

fue capaz de fundir hierro y obtener porcelana. Posteriormente, durante el periodo Moderno, Cassini diseñó una lente de 1 metro de diámetro y fundió hierro y plata, mientras que Lavoisier demostró que era posible el tratamiento de metales empleando atmósferas especiales como nitrógeno (**Flamant & Balat-Pichelin, 2009**). Fue, sin embargo, tras la Segunda Guerra Mundial cuando Felix Trombé logró la fusión de cerámicos refractarios de alto punto de fusión (alúmina, óxido de cromo, zirconia, óxido de hafnio y óxido de torio), y junto con sus colaboradores Marc Foex and Charlotte Henry La Blanchetais montaron el horno solar de Meudon, el horno solar de Mont Louis y el famoso horno solar de Font Romeu-Odeillo-Via (este último a finales de los años 60) (**Figura 3**).

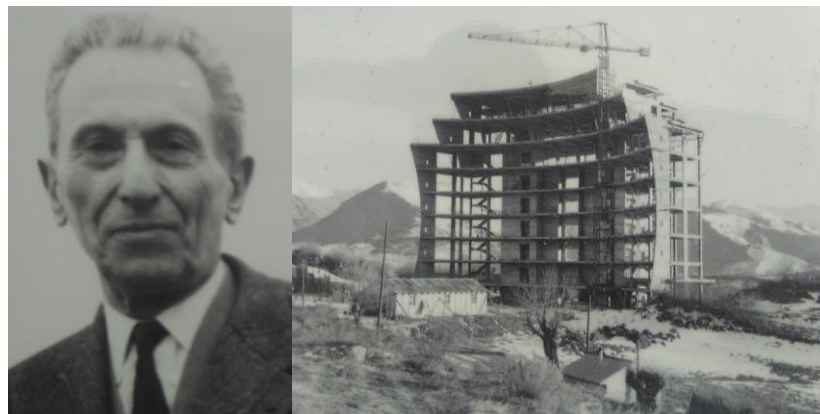


Figura 3. Felix Trombé, Horno Solar de Odeillo en construcción y horno solar en la actualidad.

Para alguien no acostumbrado a la investigación en el campo de la energía solar puede resultar llamativo el hecho de que se puedan lograr temperaturas superiores a los 3000 °C con el simple empleo de espejos y lentes. Ciertamente es lo común es que se pueda operar a temperaturas entre 1500 y 2000 °C en un volumen de material razonable debido a cuestiones relacionadas con la meteorología (humedad, contaminación o nubosidad), aunque es temperatura suficiente para la mayoría de los procesos empleados en metalurgia.

Existen varios tipos de hornos solares, que se definen como sistemas ópticos que permiten concentrar la radiación solar en pequeñas superficies. Se describen de modo breve a continuación los distintos tipos de concentradores que existen:

- Horno solar de tipo directo y una sola lente, mejor conocido como lente Fresnel (haciendo un símil, como una lupa), **Figura 4**.



Figura 4. Horno solar de tipo lente de Fresnel.

- Los reflectores parabólicos, también de tipo directo, porque la radiación solamente se desvía en una ocasión, **Figura 5**.



Figura 5. Reflector parabólico.

- Concentradores parabólicos de eje horizontal, de tipo indirecto, porque la radiación ya sufre dos desviaciones antes de alcanzar la muestra, **Figura 6.**

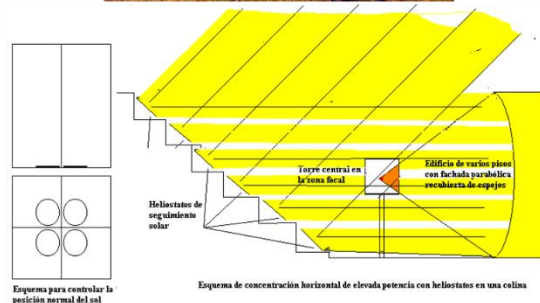
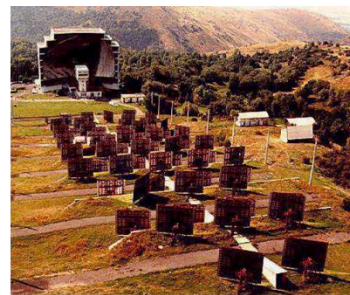
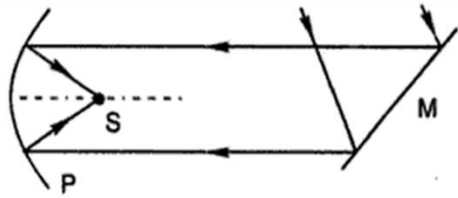


Figura 6. Concentrador parabólico de eje horizontal.

- Concentrador parabólico de eje vertical, análogo al anterior, pero el concentrador parabólico se encuentra en la vertical con relación a la superficie de la Tierra. El esquema se muestra en la **Figura 7.**

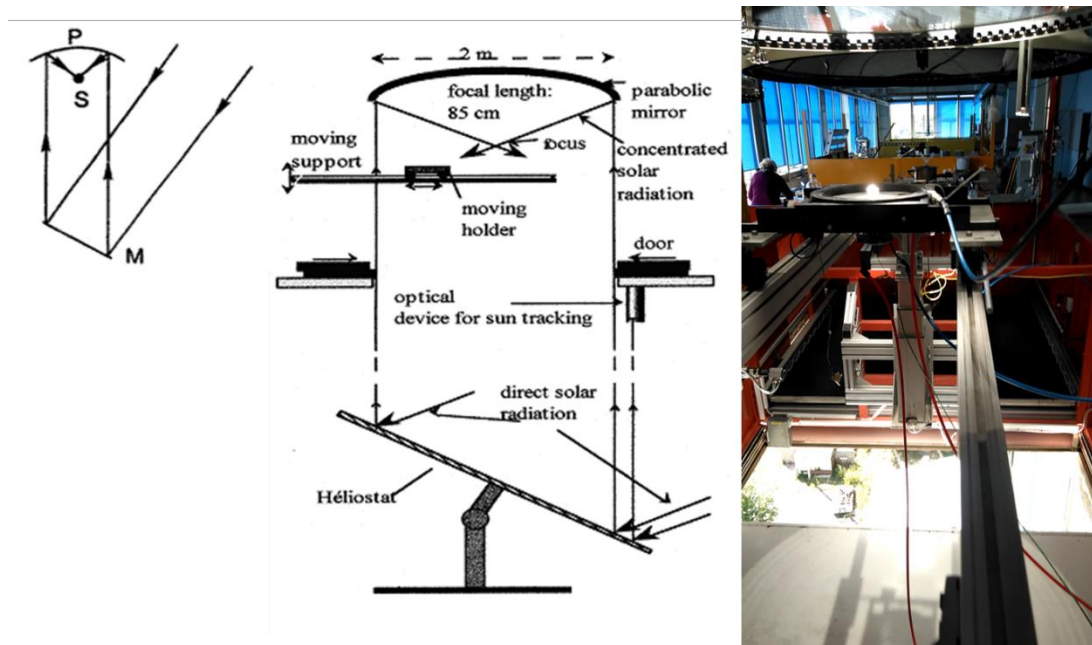


Figura 7. Concentrador parabólico de eje vertical.

En el caso del equipamiento empleado en esta tesis doctoral, se utilizó el horno solar (*Medium Size Solar Furnace*) de eje vertical de 0.9 kW localizado en Font Roméu-Odeillo-Via (Francia) perteneciente al PROMES-CNRS (PROCédés Matériaux et Energie Solaire-Centre National de la Recherche Scientifique). Consiste en un concentrador parabólico de 1.5 metros de diámetro, donde se logra concentrar la radiación 15000 veces en el punto focal de 1 centímetro de diámetro. Se muestra un esquema completo del equipo en la **Figura 8**.

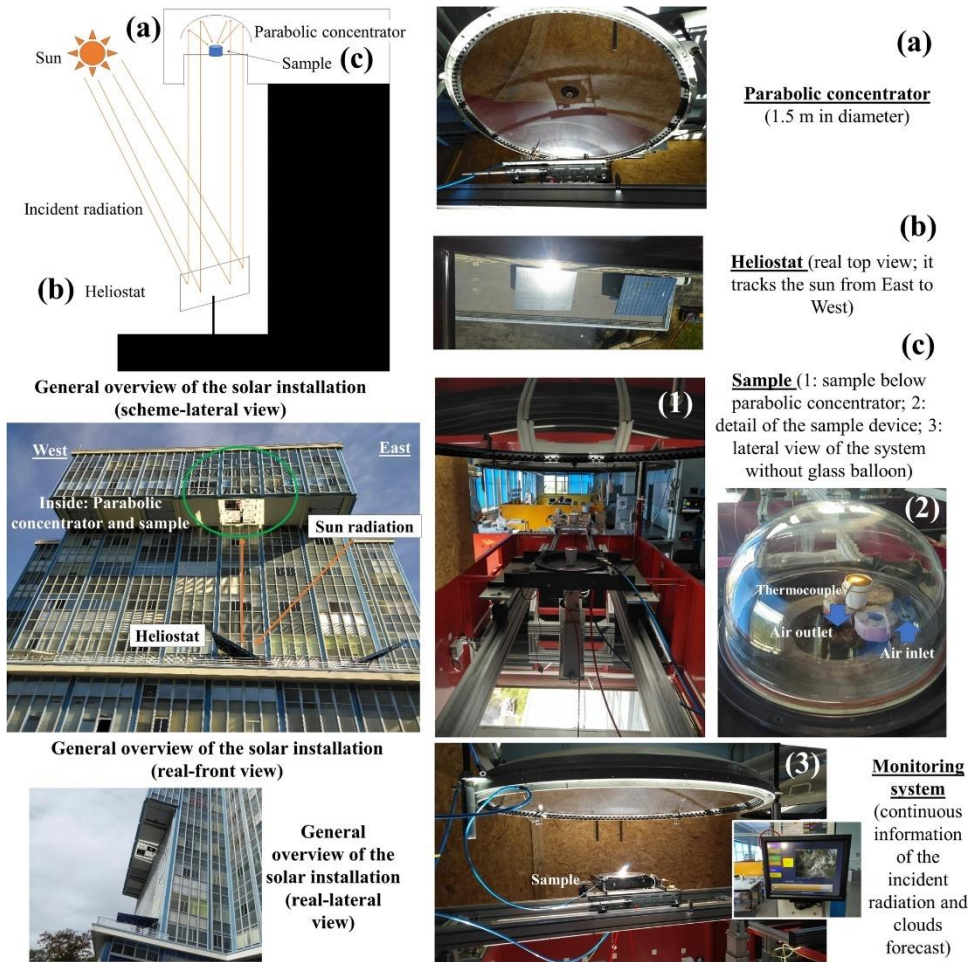


Figura 8. Imágenes reales y esquemáticas de la instalación y equipos empleados (Fernández-González et al., 2024).

3.2. Síntesis de materiales cerámicos

La energía solar ha sido ampliamente utilizada en la síntesis de materiales cerámicos, entre los que se incluyen la obtención de cordierita a partir de las constituyentes temperaturas de 1300 °C (Oliveira et al., 2009). Sin embargo, el campo más prolífico en la síntesis de materiales empleando energía solar concentrado fue el de los materiales cerámicos refractarios duros pues se han obtenido desde carburos, nitruros u óxidos como son (Fernández-González, 2023):

- Nitruros y carburos de silicio.

- Carburos y nitruros de tungsteno.
- Carburos y nitruros de titanio.
- Nitruros y carburos de molibdeno.
- Carburos de calcio.
- Nitruros de zirconio.
- Carburos y nitruros de aluminio.
- Alúmina.
- Nitruros y carburos de cromo.
- Carburos y nitruros de tántalo.
- Carburos y nitruros de vanadio.
- Nitruros y carburos de niobio.

Otros trabajos en esta línea tuvieron lugar en la síntesis de ferritas, como el $\text{Mg}(\text{Cr}, \text{Fe})_2\text{O}_4$, (Michalsky et al., 2014) a 1200 °C en tiempos cortos. Otros investigadores abordaron la sinterización del titanatos de magnesio empleando energía solar (Apostol et al., 2018).

3.3. Síntesis del óxido de zirconio: Novedad y discusión

El óxido de zirconio se puede encontrar en la naturaleza en la forma de baddeleyita, aunque se obtiene por vía térmica o termoquímica a partir de las arenas de silicato de zirconio con separación posterior de los productos fundamentalmente por diferencia de solubilidad. De esta manera, la manera de producir zirconia consiste en la calcinación/disociación por fusión directamente, o empleando diferentes aditivos como la sosa, el carbonato de sodio, el óxido de calcio o magnesio, fluorosilicato de potasio o carbonatos de calcio. En este sentido, debido al gran potencial que ofrece la energía solar, dado que permite alcanzar temperaturas que superan las necesarias para lograr la descomposición del silicato de zirconio, se propuso en

este primer artículo la obtención del óxido de zirconio por descomposición térmica de las arenas de silicato de zirconio. La referencia del artículo 1 es:

Daniel Fernández-González, Juan Piñuela-Noval, Íñigo Ruiz-Bustanza, Carmen González-Gasca, **Cristian Gómez-Rodríguez**, Linda Viviana García Quiñonez, Adolfo Fernández, Luis Felipe Verdeja, 2023: Solar dissociation of zirconium silicate sand: A clean alternative to obtain zirconium dioxide, *Journal of Cleaner Production*, 420, 138371. <https://doi.org/10.1016/j.jclepro.2023.138371>

En este trabajo lo que se propuso fue la síntesis de la zirconia mediante un proceso de dos etapas, pirometalurgia e hidrometalurgia, en las que la primera se llevó a cabo empleando energía solar concentrada. La segunda consistió en una lixiviación en medio acuoso con sosa cáustica a 200 °C durante 6 horas en un reactor a presión, seguido de una filtración con agua. De esta manera, en la primera etapa se llevó a cabo el calentamiento de la arena de silicato de zirconio sin aditivos, con un 10% en peso de carbonato de sodio y con diferentes contenidos de óxido de calcio (10, 25, y 50% en peso) (**Figura 9**). Llegados a este punto ya se observa la formación de fases complejas de zirconio con los aditivos, con lo que la ruta más prometedora resultó ser la que consistía en la simple descomposición del silicato de zirconio.

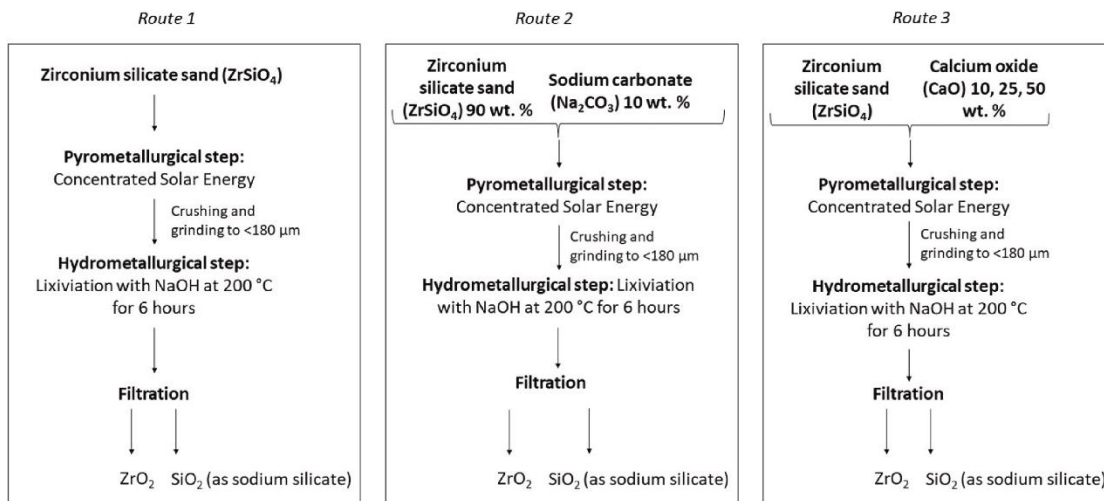


Figura 9. Rutas de síntesis empleadas para obtener el óxido de zirconio empleando energía solar concentrada.

Para la segunda fase (ruta hidrometalúrgica), hay que tener en cuenta que el dióxido de zirconio es insoluble en agua y, además, se considera químicamente no reactivo. Por otra parte, la sílice reacciona con la sosa (hidróxido de sodio) para dar lugar a silicatos solubles de sodio. Por ello se lleva a cabo un filtrado final con agua que permitió obtener un producto con casi un 95% de ZrO_2 . De esta manera, empleando la energía solar concentrada se podría obtener un cerámico de uso común sin generar contaminantes gaseosos de efecto invernadero.

3.4. Síntesis de aluminato de magnesio: Novedad y discusión

La metalurgia del aluminio genera durante la fabricación de la alúmina en el proceso Bayer un subproducto recogido en los electrofiltros que se genera en volúmenes próximos a las 80000-100000 toneladas en una planta de 1.2 Mt de alúmina (Sancho et al., 2009). Este subproducto contiene una mezcla de alúminas e hidróxidos de aluminio de pequeño tamaño (finos) y se han propuesto numerosas posible aplicaciones como la eliminación de contaminantes metálicos en aguas (Jose Sancho-Gorostiaga et al., 2021), recuperación de

elementos de valor como el aluminio o el galio (**Okudan et al., 2015**) o la fabricación de refractarios (**Sancho-Gorostiaga et al., 2021**). En cualquier caso, lo que no se había propuesto hasta este trabajo había sido la utilización de este subproducto como materia prima para la síntesis de aluminato de magnesio. Se trata de una espinela con interés debido a sus excelentes propiedades químicas, térmicas, dieléctricas, mecánicas u ópticas (**Ganesh 2013**). Asimismo, se trata de un excelente material refractario de gran importancia como material estructural cerámico debido a sus propiedades físicas, químicas y térmicas a temperatura ambiente y altas temperaturas (**Ping et al., 2001**). Aunque existen numerosas rutas de síntesis, nunca se había empleado la energía solar concentrada para su síntesis que es, junto con la síntesis del aluminato de magnesio a partir de los finos de electrofiltro del proceso Bayer, la principal novedad de este trabajo. La referencia del artículo 2 es:

Daniel Fernández-González, Juan Piñuela-Noval, Íñigo Ruiz-Bustanza, Carmen González-Gasca, **Cristian Gómez-Rodríguez**, Linda Viviana García-Quiñonez, Adolfo López-Liévano, Adolfo Fernández, Luis Felipe Verdeja, 2024: Solar assisted production of $MgAl_2O_4$ from Bayer process electrofilter fines as source of Al_2O_3 , *Journal of Sustainable Metallurgy*, 10, 296-310. <https://doi.org/10.1007/s40831-024-00805-6>

En este trabajo se trabajó con finos de electrofiltro del proceso Bayer generados en tres factorías localizadas en Canadá, Irlanda y España, compuestos mayoritariamente por alúmina α , alúmina γ y gibbsita, y granulometría muy fina. Por otra parte, se empleó MgO de calidad industrial. El mezclado se realizó en seco en una relación molar 1:1 para obtener el $MgAl_2O_4$, a partir del MgO y la cantidad correspondiente de finos teniendo en cuenta el contenido en gibbsita presente en cada subproducto. Se realizaron simulaciones empleando el ANSYS para comprobar que las temperaturas de trabajo eran lo suficientemente elevadas para la síntesis

del material empleando como referencia para los cálculos la medida de un termopar colocado en la cara exterior del crisol donde se realizaron los experimentos. Con una duración máxima de 15 minutos se logra un producto cristalino en el caso de los tres tipos de residuos sin generar emisiones de gases contaminantes. El esquema global del proceso se recoge en la

Figura 10.

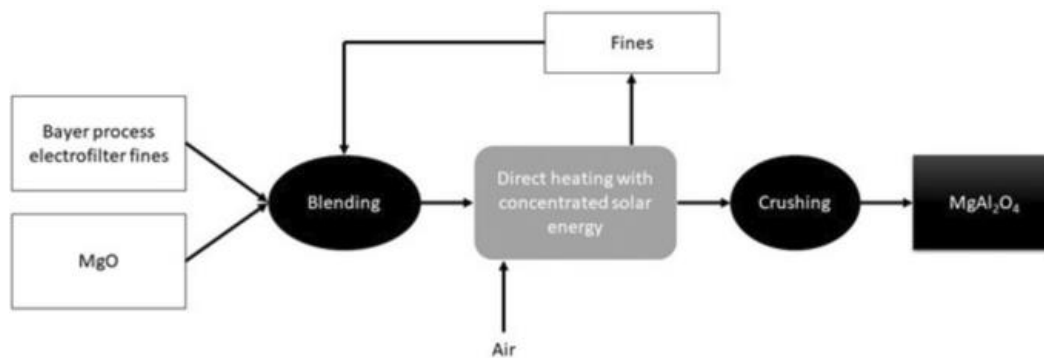


Figura 10. Diagrama de flujo del proceso basado en energía solar para obtener la espinela $MgAl_2O_4$.

Como se ha podido comprobar, esta primera parte de la tesis doctoral se ha centrado en la síntesis de materiales de uso típico en el campo de los materiales cerámicos refractarios. Por un lado, tenemos la síntesis del dióxido de zirconio, que es uno de los óxidos que se emplearon como refuerzo en los refractarios sinterizados en la segunda parte de la tesis doctoral, aunque hay que señalar que no fueron los polvos que se obtuvieron en esta primera parte los que se emplearon (aunque se hubiera podido) como refuerzo de los refractarios de magnesita. Por otro lado, tenemos la síntesis de $MgAl_2O_4$ empleando los dos óxidos que se emplearon como constituyente matriz para los refractarios sinterizados en la segunda parte de la tesis doctoral: el MgO y el Al_2O_3 , aunque en este caso se hayan mezclado en una proporción molar 1:1 para obtener un material refractario.

4. Sinterización de materiales cerámicos de matriz MgO o Al₂O₃ con nanopartículas de óxidos cerámicos o metálicas empleando técnicas convencionales o avanzadas (láser de CO₂ y *spark plasma sintering*): Motivación de la investigación, novedad y discusión de los principales avances en el área.

El progreso de las sociedades viene demandando cada vez más requisitos cada vez más exigentes en lo que a los materiales se refiere. En este sentido, es habitual prestar una mayor atención a los materiales o producto final, pero también es necesario pensar en los equipos e instalaciones que se emplean para fabricar los diferentes materiales, los cuales se enfrentan a cada vez más restrictivas condiciones medioambientales y de productividad. Así pues, si bien la primera parte de la tesis se centraba en la síntesis de materiales empleando energía solar concentrada, la segunda parte de la tesis doctoral se centra en el desarrollo de materiales compuestos de matriz MgO o Al₂O₃ mejorados con nanopartículas de óxidos metálicos y metales para su empleo en los refractarios de hornos y equipos industriales. Los trabajos se dividieron en dos grandes bloques, que son:

- Materiales cerámicos de matriz MgO y reforzados con nanopartículas de óxidos metálicos sinterizados en diferentes condiciones por la ruta convencional de horno de alta temperatura.
- Materiales cerámicos de matriz Al₂O₃ y reforzados con nanopartículas de molibdeno metal sinterizados por dos rutas novedosas como son el láser de CO₂ y la tecnología *spark plasma sintering*.

4.1. Fabricación de materiales cerámicos

La fabricación de los materiales cerámicos es un campo muy amplio de estudio que abarca desde la obtención de materias primas o el mezclado de las materias primas para obtener compuestos, la preparación del compacto verde o el proceso de sinterización. En este sentido, hemos visto en la primera parte de la tesis dos casos prácticos de lo que sería la síntesis de materias primas fundamentales para la industria cerámico-refractaria, como el ZrO_2 o el $MgAl_2O_4$. En este segundo caso, los polvos obtenidos se podrían emplear como materia prima para obtener cuerpos densos por alguna de las técnicas existentes en la actualidad, i.e. prensado en frío y sinterización en horno convencional de alta temperatura. La síntesis de este material se realizó por reacción en estado sólido empleando energía solar concentrada, aunque, como se comenta en la introducción de ese trabajo existen numerosas técnicas de síntesis. Entre ellos destacan los basados en precursores químicos porque permiten obtener materiales muy homogéneos. A modo de ilustración, el proceso sol-gel atrae la atención, ya que actualmente existen varios estudios donde desde sales reactivas sintetizan nanoestructuras cerámicas obtenidas a baja temperatura (**Ahmed & Abdel-Messih, 2011; Jayasankar et al., 2008; Zhang et al., 2004**). Un limitante es que su uso en la producción de cerámicas avanzadas puede implicar graves dificultades como microestructuras no deseadas (**Rahaman, 2003**). Así mismo otros métodos como el spray pirolisis o la deposición química de vapor son utilizados mayoritariamente para la obtención de materiales semiconductores de películas delgadas con grosores del orden de nanómetros (**Boughalmi et al., 2014; Messina et al., 2007**), limitando su uso a capas con grosores muy pequeños. En general cada procesamiento tiene sus ventajas e inconvenientes y como cada metodología tiene su interés ya sea por la posibilidad de síntesis de materiales a bajas temperaturas, la

obtención de películas cerámicas delgadas o la mejora en la distribución de la segunda fase sobre el constituyente matriz, entre muchas otras cuestiones que son objeto de estudio individualizado.

Pasando ya la obtención de cuerpos densos cerámicos, la sinterización de polvos se erige como la opción más razonable por su bajo coste y buenos resultados en la producción de materiales cerámicos policristalinos densos (**Rahaman, 2003**). La combinación con alguna de las metodologías existentes para la preparación de los polvos, como es la ruta basada en el dopaje coloidal, permite lograr cuerpos densos con mejores propiedades que las de los obtenidos por el simple mezclado con bolas y sinterización a elevada temperatura (**Piñuela-
Noval et al., 2023**). El método de sinterización se puede, pues, dividir en dos partes: procesos antes y después de la sinterización. Antes de la sinterización se pueden incluir:

1.- Síntesis del polvo partiendo de materias primas comerciales o empleando alguna de las rutas químicas que existen, como es el dopaje coloidal, que son técnicas que se emplean en algunos de los trabajos que forman esta tesis doctoral.

2. Consolidación del polvo para producir un cuerpo conformado en verde, generalmente se han obtenido con alguna de las siguientes técnicas, al igual que se hace en alguno de los trabajos que acompañan a esta tesis doctoral:

- i) prensado en polvo (seco o semisecco) en un dado metálico,
- ii) mezcla de polvo con agua o polímero orgánico para producir masa plástica a la que se le da forma mediante presión,
- iii) fundición a partir de una suspensión concentrada (fundición en barbotina).

3.- Proceso de sinterización, en la que el cuerpo conformado en verde es calentado para producir una microestructura deseada (German, 1996; Rahaman, 2003). En este sentido, el proceso de sinterización se puede llevar a cabo empleando ya sean hornos convencionales de alta temperatura o novedosas técnicas de sinterización, como el láser de CO₂ o la sinterización por *spark plasma sintering*.

Esta segunda parte de la tesis, aunque se estudian diferentes métodos de preparación de los polvos y varias tecnologías de preparación de los compactos en verde, lo que da unidad temática es el empleo de diferentes metodologías de sinterización como son los hornos de sinterización de alta temperatura el láser de CO₂ o la sinterización por *spark plasma sintering*. Se hará, pues, en las siguientes líneas una introducción al tema de la sinterización y las diferentes técnicas de sinterización que existen disponibles en la actualidad.

4.2. Sinterización de materiales cerámicos

La sinterización es un proceso térmico que se utiliza en diferentes materiales para la obtención de cuerpos densos, ya sean metálicos, cerámicos o compuestos. La sinterización es una de las tecnologías humanas más antiguas y se originó en la era prehistórica con la cocción de la cerámica (Kang, 2005a). En cerámicos se emplea para ofrecer resistencia y una estructura más sólida a un determinado cuerpo en verde que fue compactado o prensado previamente. Generalmente la sinterización ocurre en hornos especiales con diversas zonas de temperatura.

Cuando se lleva a cabo la sinterización los poros son eliminados y la pieza llega a ser más densa y con mayor resistencia mecánica. La sinterización de las partículas se puede llevar a

cabo en estado sólido y en estado líquido (**German et al., 2009; Kang, 2005d**). En estado sólido, ocurren cuatro etapas importantes, las cuales son (**German, 1996; Kang, 2005b**):

a) adhesión; es cuando las partículas se acomodan debido a las vibraciones ocasionadas por la energía que existe en la alta temperatura,

b) inicial; ocurren diferentes mecanismos de difusión (superficial, en volumen, por límite de grano, vapor-condensación, flujo viscoso o plástico), los cuales crean formación y crecimiento de cuellos entre las partículas, estos cuellos crecen hasta formar una sola partícula o grano,

c) intermedia; existe un alargamiento y redondeo de los poros, es decir se elimina la porosidad y crece el grano de la matriz refractaria y,

d) final, que es cuando ocurre la contracción o densificación del material

Desde un punto de vista termodinámico, la sinterización está impulsada por la reducción de energía superficial. Las partículas pequeñas tienen más energía superficial y se sinterizan más rápido que las partículas grandes, por esta razón varios artículos han estudiado el efecto que tienen nanopartículas (Fe_2O_3 , Al_2O_3 , ZrSiO_4 , MgAl_2O_4 , Cr_2O_3 , TiO_2 , ZrO_2 , $\eta\text{-C}$) sobre matrices refractarias básicas (**Dehsheikh & Ghasemi-Kahrizangi, 2017; Dehsheikh et al., 2018; Salman Ghasemi-Kahrizangi et al., 2016; Ghasemi-Kahrizangi, Dehsheikh, & Boroujerdnia, 2017; Ghasemi-Kahrizangi et al., 2017; Ghasemi-Kahrizangi et al., 2016; Ghasemi-Kahrizangi et al., 2018; Gómez Rodríguez et al., 2015**). Dado que el movimiento atómico aumenta con la temperatura, las altas temperaturas aceleran la sinterización, la gran mayoría de los tratamientos térmicos por sinterizado ocurren de 1000 °C a 2000 °C (**Siegel, 1993**). Estas temperaturas de sinterizado se establecen de acuerdo con

la regla “dos tercios con respecto a la temperatura de fusión de cada material a sinterizar”. Algunas industrias cuando realizan el sinterizado, presentan desventajas ya que significan altos consumos de energía y un alto costo en la producción de los productos a sinterizar. Además, cuando ocurre el sinterizado a elevada temperatura, generalmente se presenta un crecimiento excesivo del tamaño de grano (**Kang, 2005c**). Esto puede repercutir en propiedades mecánicas, por lo que se busca en ocasiones disminuir la temperatura de sinterizado, así como controlar y obtener tamaño de granos pequeños homogéneos (el cual se recomienda para evitar la propagación de grietas).

4.2.1. Técnicas de sinterizado

Actualmente existen diferentes técnicas de sinterizado, entre las cuales se pueden mencionar: horno convencional, *spark plasma sintering*, sinterización por microondas y sinterización selectiva por láser, cuyo desarrollo ha permitido dar solución a algunos de los problemas que se mencionaban anteriormente, como las elevadas temperaturas de sinterización o el excesivo crecimiento de grano en el caso de largas estancias a alta temperatura o velocidades de calentamiento lentas. Otras técnicas de sinterización vienen a erigirse como las más adecuadas para piezas bajo demanda. En cualquier caso, ninguna tecnología parece que se vaya a sobreponer a las otras, si no que unas complementarán a otras en la búsqueda de los materiales densos con las mejores prestaciones.

4.2.1.1. Horno convencional

Los hornos eléctricos convencionales son los más utilizados cuando se sinterizan materiales refractarios fundamentalmente debido a una cuestión de productividad. Estos pueden ser utilizados utilizando atmosfera ambiente, aunque también es posible efectuar la sinterización en atmósfera controlada. El empleo de diferentes tipos de atmósferas permite controlar o

promover cierto tipo de reacciones químicas, dando lugar, en el segundo caso lugar a una forma diferente de sinterización reactiva.

. Así mismo también pueden trabajar con cámaras al vacío o cámaras especiales de atmósfera controlada, con gases inertes que sirven para controlar reacciones químicas en las que se debe evitar la presencia de un gas reactivo (por ejemplo, el oxígeno) con probetas que se sinterizan. Con estos hornos se puede llevar a cabo la sinterización en un amplio rango de temperaturas, que pueden llegar por encima de los 2000 °C. Esta ruta ha sido ampliamente utilizada en la sinterización de materiales cerámicos y refractarios, incluyendo uno de los que es objeto de estudio en esta tesis doctoral: el óxido de magnesio (MgO), que es un material refractario de interés y que es utilizado como revestimientos en hornos de metalurgia secundaria. La obtención de cuerpos cerámicos densos con incorporación de nanopartículas de óxidos metálicos (ZrO₂, Al₂O₃, Fe₂O₃, TiO₂) para la mejora de propiedades físicas, químicas y mecánicas se ha realizado empleando hornos convencionales variando diferentes condiciones como se recoge en la literatura (**Gómez Rodríguez et al., 2015; Gómez-Rodríguez et al., 2020; Gómez-Rodríguez et al., 2019; Hernández-Reséndiz et al., 2023**).

4.2.1.2. Spark plasma sintering

El *spark plasma sintering* (SPS) es una técnica de sinterización que se basa en la aplicación simultánea de una presión uniaxial y una corriente eléctrica pulsada bajo una atmósfera controlada (habitualmente en vacío, aunque se puede operar en atmósfera de argón, nitrógeno o hidrógeno según se requiera) (**Omori, 2000; Ragulya, 2010**). El SPS puede ser considerado como una variante del prensado en caliente, donde el horno se reemplaza por el molde que contiene la muestra, que se calienta por efecto Joule mediante el paso de una corriente eléctrica a través de la muestra donde las juntas de grano y el propio material, dependiendo

de su naturaleza, actúan como resistencias eléctricas, produciéndose el calentamiento (Omori, 2000). El SPS, ha estado recibiendo una atención creciente en las últimas dos décadas debido a su alta eficacia, permitiendo obtener una rápida sinterización y densificación, particularmente con materiales que son considerados difíciles de sinterizar, como materiales refractarios o fases metaestables (Fang & Wang, 2010). Uno de los principales intereses de este proceso, radica en la extrema rapidez del tratamiento térmico, reduciéndose el tiempo, de horas, en el caso del sinterizado convencional, a pocos minutos para el proceso SPS. La temperatura de consolidación disminuye en comparación con el sinterizado convencional debido a un efecto simultáneo de presión, temperatura y condiciones de vacío. Asimismo, otro de los aspectos que interesa del SPS es la posibilidad de un control en el crecimiento de grano motivado precisamente por las elevadas velocidades de calentamiento.

Dado que la aplicación de altas temperaturas y tiempos de permanencia dentro del horno durante el proceso de sinterizado favorece el crecimiento de grano, con el SPS, las altas presiones y cortos tiempos estancia de sinterizado permiten mantener granos pequeños (nanoestructuras en la matriz cerámica) (Díaz Campbell-Smith, 2014). A través de esta técnica diferentes materiales se han sinterizado como: alúmina (Shen et al., 2002), cerámicos a base de NASICON (Lee et al., 2004), Niquel (Borkar & Banerjee, 2014), carburo de silicio (Hayun et al., 2012), nanocristales de zirconia (ZrO_2) (Li & Gao, 2000), nanocomposites de titanio reforzados con nanotubos (Okoro et al., 2019), nanocomposites de Al_2O_3/Ni y TiN/Si_3N_4 (Isobe et al., 2008; Lee et al., 2010), ZrO_2/Al_2O_3 (Xu et al., 2020), $BaTiO_3/Al_2O_3$ (Zhan et al., 2003), entre otros y se ha comprobado mejoras en cuanto a las

propiedades microestructurales y por ende en propiedades físicas, químicas y mecánicas de los materiales sinterizados por SPS.

4.2.1.3. Sinterizado por energía solar

La energía solar es una fuente de energía renovable, prácticamente ilimitada, la cual podría ser considerada como un potencial sustituto para los combustibles fósiles (**Patidar et al., 2015**). Hasta ahora los costes dependen de los gastos de instalación de los grandes hornos, los cuales se utilizan para concentrar la energía solar puntualmente, alcanzando temperaturas superiores a los 2000 °C (**Fernández-González, 2023**). Las altas temperaturas se pueden alcanzar sin la necesidad de emisión de contaminantes y también permiten utilizar atmosferas controladas. Por otro lado, con el uso de la energía solar se han estudiado diferentes materiales, principalmente se ha visto favorecida la metalurgia, principalmente en lo que se conoce como combustibles metálicos, por su potencial en el almacenamiento de energía, aunque también la fabricación de cemento, la síntesis de materiales cerámicos, el procesamiento de materiales o el reciclado de estos, una vez concluida su vida útil (**Fernández-González, 2023**).

De las investigaciones en el campo de los cerámicos ya se habló con anterioridad en esta tesis doctoral cuando se dio cuenta de aquellos que se habían sintetizado empleando energía solar, aunque se puede recordar aquí un cerámico de interés en la industria refractaria como es el aluminato de calcio. Fernández-González y col. estudiaron la síntesis de cementos de aluminato de calcio por energía solar concentrada, haciendo una comparación con la ruta convencional y observándose una potencial reducción de costes que podría llegar hasta el 40% (**Fernández-González et al., 2018**). Así mismo, se han sintetizado cerámicos refractarios duros, como se había indicado. Sirvan a modo de ejemplo los nitruros de hierro

(500 y 600°C) y nitruros de molibdeno (800 y 900°C) con energía solar concentrada en horno solar de 40 kW, utilizando una atmosfera de amoníaco con tiempo de 30 y 60 min (**Shohoji et al., 2013**). También, se han sintetizado diferentes tipos de carburos (Ti, V, Nb y Ta) con energía solar. Es importante mencionar que el tipo de atmosfera juega un papel importante en la sinterización de materiales utilizando energía solar, ya que se ha obtenido carburo de tantalito utilizando presión atmosférica ambiente a 1600 °C por 30 min y atmosfera de argón a 1200 °C por 30 min, es decir la temperatura bajó 400 °C con el uso de argón (**Carvajal-Campos et al., 2019; Cruz Fernandes et al., 2006**).

Pero, más allá de la síntesis de materiales cerámicos, la sinterización que emplea energía solar no es un campo muy explorado, más allá de la sinterización de aceros, donde hay un cierto bagaje investigador (**Fernández-González, 2023**). Podemos remarcar en este punto la sinterización de discos cerámicos de alúmina utilizando diferentes atmosferas (aire, Ar and 95N₂:5H₂). En este caso, se observó que los granos crecieron (no así en el caso de la sinterización de aceros especiales donde las elevadas velocidades de calentamiento y enfriamiento promovieron un grano fino y la formación de carburos metaestables observados incluso a temperatura ambiente) y la densidad se incrementó después del sinterizado con energía solar por arriba de 1780°C con una atmosfera de N₂:H₂, en comparación con sinterización de horno convencional (**Román et al., 2008**).

4.2.1.4. Sinterización por microondas

Se trata de una técnica no-convencional donde los materiales absorben las ondas electromagnéticas y las transforman en calor. La energía de microondas tiene un rango de frecuencia de 300 MHz a 300 GHz. El calentamiento por microondas es un proceso en el que los materiales se acoplan con las microondas, absorben la energía electromagnética

volumétricamente y la transforman en calor. Esto es diferente de los métodos convencionales en los que el calor se transfiere entre objetos mediante mecanismos de conducción, radiación y convección. En el calentamiento convencional, la superficie del material es primero calentada y luego el calor se mueve hacia adentro de la pieza. Esto significa que hay un gradiente de temperatura desde la superficie hacia el interior. Sin embargo, el calentamiento por microondas, primero genera el calor dentro del material y luego calienta todo el volumen de la pieza que se sinteriza (**Oghbaei & Mirzaee, 2010**).

Esta técnica puede ser aplicada tanto para sinterizar o procesar materiales óxidos y no óxidos en polvo ("**Advances in Induction and Microwave Heating of Mineral and Organic Materials**," 2011). Mediante esta técnica se permite una distribución rápida y uniforme de calor en el núcleo cerámico debido a la excitación de cada unidad constituyente de la red cristalina.

Los beneficios de la sinterización por energía de microondas, en comparación con la convencional, es que este método realiza un calentamiento rápido y volumétrico de la muestra, así como existe una mejora de la densificación y control del grano (**Riedel & Svoboda, 2006; Upadhyaya et al., 2001**). La sinterización por microondas puede reducir el tiempo total de sinterizado, por ejemplo, una sinterización convencional de 5 horas 46 minutos la reduce a 1 hora y 45 minutos, (excluyendo el proceso de enfriamiento), es decir se ha comprobado una disminución del 70% del tiempo de sinterización (**Barchetta et al., 2017**). La irradiación por microondas puede producir un calentamiento interno eficiente, ya que la energía se suministra directamente y penetra en el material a través de la interacción molecular con el campo electromagnético.

Los procesos por microondas pueden mejorar la eficiencia de la densificación y reducir considerablemente el tiempo de ciclo de procesamiento para calentar rápida y uniformemente la muestra, especialmente materiales cerámicos gruesos, lo que resulta en ahorros sustanciales de energía y costos. Por tanto, existe suficiente motivación para promover el uso de microondas en la sinterización de diversas cerámicas, así como vitrocerámicas, nanocerámicas y biocerámicas. Actualmente, se promueve la investigación para estudiar el efecto de las condiciones (parámetros) de sinterización por microondas en la microestructura, formación de nuevas fases, composición y propiedades de los materiales producidos en comparación con los sinterizados convencionales. Por lo que diferentes materiales cerámicos se han estudiado con esta novedosa técnica (**Agrawal, 2006; Breval et al., 2005; Chen et al., 2009; Kähäri et al., 2016; Oghbaei & Mirzaee, 2010**).

4.2.1.5. Sinterización selectiva por láser

La sinterización selectiva por láser (SLS) es un proceso de creación de prototipos capaz de fabricar piezas de objetos totalmente funcionales, principalmente con formas pequeñas, contornos de piezas de alta precisión y acabados superficiales específicos, que difícilmente se obtienen con otros procesos (**Gross et al., 2014; Kumar, 2003**). Este método se ha empleado recientemente debido a su idoneidad para procesar casi cualquier material: polímeros, metales y cerámicas, utilizando tiempos de procesamiento cortos durante la sinterización y conformación de materiales, y puede implementarse a presión ambiente, y temperatura ambiente (**Gross et al., 2014; Kumar, 2003**). En SLS, generalmente, se utiliza un láser de CO₂ o Nd:YAG para formar un componente completo a partir de materiales en polvo, donde en algunos casos se utilizan aglutinantes intermedios (**Bertrand et al., 2007; Chen & Zhang, 2007**). En ambos tipos de láseres, parámetros como la potencia, la velocidad

de escaneo y el tiempo de exposición juegan un papel importante durante la sinterización de un material. La potencia del láser controla la energía disponible para el proceso, mientras que la velocidad de escaneo dosifica la transferencia de energía al lecho de polvo por unidad de área; juntos, regulan la longitud, anchura y espesor de la zona irradiada (Li et al., 2017). En algunos materiales, como la cerámica, el elevado punto de fusión, así como la formación de grietas debido a la diferencia en los coeficientes de expansión térmica de las fases generadas in situ, y la baja o nula plasticidad, hacen que el SLS sea un desafío. (Shahzad et al., 2012), ya que se debe controlar la energía utilizada para unir los polvos cerámicos para lograr una pieza sinterizada con buenas propiedades térmicas, mecánicas, químicas y físicas. Además, la sinterización de piezas que contienen polvos de óxidos refractarios se consigue, en general, por difusión en estado sólido, si no existe alguna fase ligante; además, se requiere un tiempo de exposición suficiente para lograr las densidades deseadas (Chen et al., 2019).

4.3. Sinterización convencional de refractarios de matriz MgO

En esta parte de la tesis doctoral en lo que se profundiza es en los materiales compuestos de matriz cerámica reforzados con nanopartículas de óxidos metálicos y sinterización en diferentes condiciones de temperatura, prensado o contenido en segunda fase. Se denominan *artículos complementarios* aquellos trabajos que se publicaron en revistas no indexadas, o se trata de capítulos de libros.

Cristian Gómez-Rodríguez, Linda Viviana García-Quiñonez, Josué Amilcar Aguilar-Martínez, Guadalupe Alan Castillo-Rodríguez, Edén Amaral Rodríguez-Castellanos, Jesús Fernando López-Perales, María Isabel Mendivil-Palma, Luis Felipe Verdeja, Daniel Fernández-González, 2022: MgO–ZrO₂ ceramic composites for silicomanganese production, *Materials*, 15, 2421. <https://doi.org/10.3390/ma15072421>

En este artículo de la tesis doctoral se estudió la corrosión de composites de MgO-ZrO₂, en presencia de escoria de silicomanganeso (**Gómez-Rodríguez et al., 2019**). La idea fue reforzar a la matriz de MgO con diferentes concentraciones de nanopartículas de ZrO₂ (0, 1, 3 y 5% en peso), sinterizadas en horno convencional durante 4 horas, variando tanto la temperatura (1550°C y 1650°C) y presión de conformado (100 MPa y 200 MPa con presión uniaxial y presión isostática, respectivamente). En este sentido, aunque se obtuvieron probetas densificadas con 1650°C y 200 MPa, las propiedades físicas de densidad no variaron relativamente y, realmente no se obtuvo un cambio significativo al utilizar dos variables en presión y temperatura. Así mismo, en la prueba de corrosión estática se obtuvo que la corrosión es controlada por el cambio de la viscosidad de la escoria debido a la reacción de nuevas fases formadas in situ (durante el sinterizado) como CaZrO₃, y la escoria fundida. En general las nanopartículas de ZrO₂ ayudaron a la formación in situ de la fase de CaZrO₃, ya que el ZrO₂ entró en solución sólida con el CaO (el cual se encontraba libre en la materia prima utilizada). Además, el ZrO₂ fue localizado en los puntos triples y dentro del grano de MgO con la nueva fase formada (CaZrO₃), ambas actuaron como barrera evitando el avance de escoria dentro del refractario. Este tipo de refractarios representa una opción potencial para uso como revestimiento en horno para producción de aleaciones de SiMn desde el punto de vista medioambiental y económico.

Artículo complementario: **Cristian Gómez Rodríguez**, Beatriz Escobedo-Trujillo, Luis Felipe Verdeja, Daniel Fernández-González, Adolfo Fernández, Linda-Viviana García-Quiñónez, Guadalupe Alan Castillo Rodríguez, 2023: Morphological study of refractory composite materials based on magnesia (MgO) with additions of hercinite (Fe₂Al₂O₄),

Esta investigación trató acerca del estudio morfológico y mecánico de materiales refractarios basados en magnesia (MgO) con adiciones de 0, 1, 2.5, 5, 10, y 20 % en peso de hercinita ($\text{Fe}_2\text{Al}_2\text{O}_4$), sinterizados a 1600 °C durante 4 horas en un horno eléctrico convencional (Gomez Rodriguez). En esta investigación se proporciona conocimiento en cuanto al desarrollo microestructural de un material refractario base MgO con adiciones de hercinita. De acuerdo con las micrografías presentadas en el artículo, se pudo observar que el mejor resultado en términos microestructurales, es decir, con menor porosidad, formación de límites de granos y piezas mejor densificadas, correspondieron a las probetas de 20 % en peso de $\text{Fe}_2\text{Al}_2\text{O}_4$. Con esta concentración se observaron puntos triples con ángulos diédricos (ángulos de 120 °). Esto fue indicativo que ocurrió una buena sinterización entre los granos de MgO (Schacht, 2004). Además, con aumento de hercinita, durante el proceso de sinterizado, la porosidad fue gradualmente disminuyendo lo que permitió que los granos también fueran creciendo y las probetas fueran densificando. Con 10 y 20 % en peso de hercinita, se detectó sobre los límites de grano la presencia de elementos como Ca y Fe, mientras que en los puntos triples se detectaron elementos como Si, Ca y Fe. Con mayor concentración de hercinita, dentro de los granos de MgO se evidenció la formación de magnesioferrita ($\text{MgFe}_2\text{O}_4 = 4.51 \text{ g/cm}^3$), la cual ayudó a aumentar la densidad de las probetas de MgO (3.58 g/cm^3). La probeta de 20% en peso de hercinita presentó un mejor valor de dureza (339.44 HV) en comparación a los otros porcentajes en peso de hercinita. La idea fue proponer este tipo de refractarios como ladrillos con características morfológicas y

mecánicas en zonas específicas (para uso en zonas de quemado) en hornos rotatorios de cemento Clinker.

Capítulo de libro: **Cristian Gómez-Rodríguez**, Luis Felipe Verdeja, Guadalupe Alan Castillo-Rodríguez, Eden Amaral Rodríguez-Castellanos, Daniel Fernández-González, Adolfo Collado-Hernández, Linda Viviana García-Quiñonez, 2022: Nano-Oxide (SiO_2 and Fe_2O_3) effect on magnesium oxide compound (MgO), Capítulo 3, En: Izabela Gabryelewicz, Maciej Wedrychowicz, Patryk Krupa, Daniel Fernández González (Eds.), Production of engineering materials (pp. 48-61). Zielona Góra, Polonia: University of Zielona Góra.

En este trabajo se estudió el efecto de la adición de nanopartículas de Fe_2O_3 y SiO_2 en una matriz de MgO (**Gómez-Rodríguez et al., 2022**). Los composites fueron sinterizados en un horno eléctrico convencional a $1600\text{ }^\circ\text{C}$ por 4 horas, las concentraciones de nanopartículas utilizadas fueron 0, 1, 3 y 5 % en peso de Fe_2O_3 y SiO_2 al MgO. Esto permitió que se alcanzara una mayor densificación de probetas cuando las nano- Fe_2O_3 fueron agregadas en 5% peso al MgO. Debido a la alta solubilidad del óxido de hierro (Fe_2O_3) en la magnesia existió la formación de vacancias catiónicas en la magnesia resultando una alta movilidad atómica, fomentando la precipitación de enlaces de espinel de magnesioferrita (MgFe_2O_4), permitiendo un transporte de masa mayor entre granos de MgO (densificando la pieza) en comparación con composites MgO- SiO_2 . La mejor concentración correspondió a un 5 % peso de Fe_2O_3 en la magnesia (MgO), ya que se obtuvo una densidad de 3.37 g/cm^3 y una porosidad del 1.8%. Con probetas de MgO- SiO_2 se obtuvo formaciones de silicatos de magnesio, los cuales son fases de bajo punto de fusión que afectan el rendimiento de las piezas en elevada temperatura.

Artículo complementario: Marina Hernández-Reséndiz, **Cristian Gómez-Rodríguez**, Daniel Fernández-González, Guadalupe Alan Castillo-Rodríguez, 2023: Synthesis and characterization of dense MgO–TiO₂ nanocomposites obtained by two novel processing routes, *Ceramics International*, 49, 12604-12614. <https://doi.org/10.1016/j.ceramint.2022.12.123>

Este trabajo consistió en la obtención de refractarios de magnesia densos reforzados con nanopartículas de TiO₂, que se añadieron en diferentes proporciones: 1, 3 y 5% en peso. La principal novedad del trabajo fue el empleo de brucita (Mg(OH)₂) o magnesia cáustica (MgO) como fuentes del MgO en el composite. En este sentido, se establecieron dos rutas (se sintetizó MgO como referencia) y se varió el punto en el que se añadieron las nanopartículas de TiO₂: en la ruta 1 se añadieron las nanopartículas a la brucita y se calcinó el material a 960 °C durante 2 horas ya con las nanopartículas de TiO₂; en la ruta 2 se calcinó la brucita a 960 °C durante 2 horas y se añadieron en este punto las nanopartículas de TiO₂. En los dos casos, el proceso continuó con un prensado uniaxial en verde a 150 °C y una sinterización del compacto en verde a 1600 °C durante 4 horas. El empleo de la ruta denominada 1 condujo a una mayor densificación (la densidad resultó ser al menos un 3.29% mayor) mientras que la resistencia a la compresión en frío fue al menos un 20% mejor que en la ruta en la que las nanopartículas de TiO₂ se añaden sobre el MgO cáustico.

Artículo complementario: **Cristian Gómez-Rodríguez**, Linda Viviana García-Quiñonez, Josué Amilcar Aguilar-Martínez, Francisco Javier Vázquez-Rodríguez, Daniel Fernández-González, Luis Felipe Verdeja, José Fernando López-Perales, Guadalupe Alan Castillo-Rodríguez, Edén Rodríguez, 2023: Desarrollo de un refractario de MgO dopado con η-Al₂O₃, *EYA ACADEMY*, 1 (1), 46-61. <http://doi.org/10.59335/nvyu9288>

En línea con lo indicado con relación al refuerzo de los refractarios de MgO con nanopartículas de óxidos metálicos, en este trabajo se emplean nanopartículas de η -Al₂O₃ también en diferentes proporciones (además de la referencia sin aditivos) que fueron el 1, 3 y 5% en peso, para respetar unas condiciones comparables de sinterización en los diferentes tipos de nanopartículas. Así, se hizo un prensado en verde a 100 MPa para posteriormente realizar la sinterización a tres temperaturas: 1300 °C, 1500 °C y 1600 °C. Se observó una mejora en la densificación con la temperatura de sinterización, mientras que un incremento en el contenido en nanopartículas producía un efecto negativo en la microdureza. Por otra parte, la resistencia a la compresión en frío medida sobre muestras sinterizadas a diferentes temperaturas y con diferentes contenidos en nanopartículas dio lugar a que los mayores valores de esta propiedad fueran medidos para muestras sinterizadas a 1500 °C y con un contenido en η -Al₂O₃ del 5% en peso.

En esta línea de la tesis se profundizó en la síntesis de refractarios de MgO con nanopartículas de diferentes óxidos metálicos. En todos los casos se apreció una mejora de la densificación y una mejora de las propiedades mecánicas, en particular de la resistencia a la compresión en frío, con la adición de las nanopartículas, al menos en los que esta propiedad se midió (se constata también una mejora de la dureza con el contenido de esta segunda fase). Se recoge en la **Tabla 1** un cuadro resumen de la *resistencia a la compresión en frío* para ilustrar la mejora, en aquellos casos en los que se dispone de esa información, que se produce con relación al valor del MgO sin emplear nanopartículas, aunque se debe acudir a los diferentes artículos para profundizar en los detalles microestructurales, de densificación y de proceso. Sirva, pues, esta **Tabla 1** para ilustrar la evidente mejora que la adición de las nanopartículas produce en una propiedad relevante de los ladrillos refractarios de magnesia.

Tabla 1. Valores de la resistencia a la compresión en frío para los sistemas estudiados.

Mejor composición del sistema	Resistencia a la compresión en frío (MPa)	Condiciones de fabricación
Artículo: MgO–ZrO₂ ceramic composites for silicomanganese production		
MgO	120	Prensado uniaxial + prensado isostático (ambos en frío y 100 MPa) y sinterización a 1650 °C durante 4 horas
MgO–(5% en peso) ZrO ₂	323.78	Prensado uniaxial + prensado isostático (ambos en frío y 100 MPa) y sinterización a 1650 °C durante 4 horas
Artículo: Synthesis and characterization of dense MgO–TiO₂ nanocomposites obtained by two novel processing routes		
MgO	150	Prensado uniaxial en frío a 150 MPa + sinterización a 1600 °C durante 4 horas
MgO (cáustico)-(5% en peso) TiO ₂	203	Mezclado del MgO con nanopartículas de TiO ₂ + Prensado uniaxial en frío a 150 MPa + sinterización a 1600 °C durante 4 horas
MgO (brucita)-(5% en peso)TiO ₂	236	Mezclado del Mg(OH) ₂ con nanopartículas de TiO ₂ + calcinación a 960 °C durante 2 horas + Prensado uniaxial en frío a 150 MPa + sinterización a 1600 °C durante 4 horas
Artículo: Desarrollo de un refractario de MgO dopado con η-Al₂O₃		
MgO	64	100 MPa en frío + 1500 °C durante 4 horas sinterización
MgO-(5% en peso) η-Al ₂ O ₃	156	100 MPa en frío + 1500 °C durante 4 horas sinterización

4.4. Sinterización no convencional de refractarios de matriz Al_2O_3

El último bloque de la tesis lo constituyen las publicaciones relacionadas con la técnicas de sinterización no convencionales aplicadas al refuerzo de materiales cerámicos de matriz Al_2O_3 : sinterización por láser de CO_2 y sinterización por *spark plasma sintering*. En este sentido, el refuerzo con molibdeno de una matriz de alúmina es novedoso, habiéndose aplicado por vez primera en los trabajos que en esta memoria se recogen.

Cristian Gómez-Rodríguez, Linda Viviana García-Quiñonez, Luis Felipe Verdeja, Guadalupe Alan Castillo-Rodríguez, Josué Amilcar Aguilar-Martínez, Aldo E Mariño-Gómez, Daniel Fernández-González, 2022: Selective laser sintering of alumina-molybdenum nanocomposites, *Ceramics International*, 48(19), 29540-29545.

<https://doi.org/10.1016/j.ceramint.2022.08.058>

En este trabajo se investigó la sinterización utilizando un láser de CO_2 de composites de Al_2O_3 -Mo (**Gómez-Rodríguez et al., 2022**). La alta concentración de energía puntual permitió la sinterización del compuesto refractario Al_2O_3 -Mo. El láser fue utilizado como medio de calentamiento, además con la adición de Mo se pudo controlar los tamaños de granos de la alúmina. En este artículo principalmente se estudió la microestructura en función a la concentración de Mo, la cual impacta de manera directa en las propiedades mecánicas, en particular en la tenacidad a la fractura. Por lo que, polvos de alúmina en grado reactivo con diferentes concentraciones de molibdeno (0, 1, 2.5, 5, 10 y 20 % en peso) fueron mezclados y posteriormente prensados. Los compactos en verde posteriormente fueron irradiados con un movimiento traslacional sobre el área superior de la muestra con un láser de dióxido de carbono (CO_2). Los parámetros utilizados del láser fue $\lambda = 10.64 \mu m$, diámetro del rayo del láser 3 mm, densidad de potencia $70.29 W/cm^2$, con una velocidad de traslación

de 1.25 mm/s. Se sabe que el principal problema es que el molibdeno fácilmente se oxida y que requiere de atmosfera reductoras (Ar, H₂) o inclusive en vacío, para evitar su oxidación. Aun así, con el uso de esta técnica de sinterización rápida como es la tecnología láser se pudo a temperatura ambiente minimizar la perdida de molibdeno (evitando la transformación de MoO₃ o molibdeno (VI)).

En los resultados morfológicos, se observaron diferentes tamaños de granos los cuales fueron reduciéndose en función al porcentaje de Mo. Así mismo, el Mo actuó como un efecto de fijación, en los puntos triples como en los límites de grano. El Mo permitió que los límites de grano no se desplazaran y que el grano creciera. Con concentraciones de 1, 2.5 y 5% en peso se observaron granos mayores de 5 µm. Además, se pudo observar que las mejores propiedades morfológicas se obtuvieron con un 10 % en peso, ya que se obtuvieron granos pequeños homogéneos con tamaños menores a 5 µm. Con la muestra de 20% en peso, existió una sobresaturación de Mo, dentro de los granos como en los límites de grano. Así mismo, con mayor presencia de Mo (20% en peso) el molibdeno se oxidó presentándose la fase MoO₃.

Daniel Fernández-González, Marta Suárez, Juan Piñuela-Noval, Luis Antonio Díaz, **Cristian Gómez-Rodríguez**, Linda Vivian García Quiñonez, Amparo Borrell, Adolfo Fernández, 2023: Alumina/molybdenum nanocomposites obtained by colloidal synthesis and spark plasma sintering, *Ceramics International*, 49(6), 9432-9441. <https://doi.org/10.1016/j.ceramint.2022.11.108>

Este trabajo trata del estudio de nanocomposites de alúmina-molibdeno obtenidos por síntesis coloidal y posteriormente sinterizados por *spark plasma sintering* (SPS) (**Fernández-González et al., 2022**). El empleo de la técnica de SPS no se había reportado para el sistema

Al₂O₃-Mo. La idea de incorporar como segunda fase al Mo en la alumina (Al₂O₃) por SPS, fue que este metal es atractivo por tener propiedades refractarias y puede mejorar las propiedades mecánicas al Al₂O₃, particularmente la tenacidad a la fractura a elevada temperatura. En esta investigación los nanocomposites se prepararon por síntesis coloidal desde polvos de alumina y cloruro de molibdeno (V) usando etanol como medio dispersante. Los composites que se estudiaron tenían concentraciones de 0, 1, 5 y 10 % en peso de Mo. Posteriormente fueron sinterizados en SPS durante 3 minutos a 1400 °C, con velocidades de calentamiento muy rápidas (decenas de grados centígrados por minuto). Se obtuvieron estructuras de grano muy fino, y resultados importantes en cuanto a valores de dureza y a tenacidad. En el caso de la muestra de 1% en peso de Mo, la dureza es 28% mayor, y la tenacidad es 50% mayor con respecto a la muestra de Al₂O₃ monolítica. Asimismo, en este estudio se obtuvo que los tamaños de granos de Al₂O₃ de los composites de Al₂O₃-Mo, fueron de < 1.6 μm, mientras para el caso de Al₂O₃ monolítica, > 70% de los granos de alumina tuvieron un tamaño de 2 μm.

Así pues, estos dos trabajos reflejan que es posible lograr una mejora de las prestaciones mecánicas cuando se incorpora molibdeno a la matriz de Al₂O₃ dado que el carácter metálico dota de mayor plasticidad a la muestra mientras que su naturaleza nanométrica impide el crecimiento del grano, lo que se traslada a una mejora de la tenacidad. Igualmente, el empleo incipiente de técnicas como el láser de CO₂ permite ir aproximándose al campo de la fabricación aditiva de piezas bajo demanda en cerámicos reforzados como el propuesto. Por otra parte, el empleo de la tecnología *spark plasma sintering* permite obtener cuerpos densos con propiedades mejoradas en tiempos de sinterización inferiores a los 20 minutos, lo cual permite actuar sobre las propiedades microestructurales de este tipo de materiales.

5. Bibliografía

- Agrawal, D. (2006). Microwave Sintering of Ceramics, Composites and Metallic Materials, and Melting of Glasses. *Transactions of the Indian Ceramic Society*, 65(3), 129-144. <https://doi.org/10.1080/0371750X.2006.11012292>
- Ahmed, M. A., Abdel-Messih, M. F. (2011). Structural and nano-composite features of TiO₂-Al₂O₃ powders prepared by sol-gel method. *Journal of Alloys and Compounds*, 509(5), 2154-2159. <https://doi.org/10.1016/j.jallcom.2010.10.172>
- Apostol, I., Rodríguez, J., Cañadas, I., Galindo, J., Mendez, S. L., de Abreu Martins, P. L., Cunha, L., Saravanan, K. V. (2018). Concentrated solar energy used for sintering magnesium titanates for electronic applications. *Applied Surface Science*, 438, 59-65. <https://doi.org/10.1016/j.apsusc.2017.09.224>
- Barchetta, N., Nanni, L., Miranda, J., Lazar, D., Assui, V., Saavedra, G. (2017). Surface roughness and volumetric contraction of a Y-TZP ceramic sintered by microwave energy and by resistive heating. *Brazilian Dental Science*, 20, 124-129. <https://doi.org/10.14295/bds.2017.v20i4.1481>
- Bertrand, P., Bayle, F., Combe, C., Goeuriot, P., Smurov, I. (2007). Ceramic components manufacturing by selective laser sintering. *Applied Surface Science*, 254(4), 989-992. <https://doi.org/10.1016/j.apsusc.2007.08.085>
- Borkar, T., Banerjee, R. (2014). Influence of spark plasma sintering (SPS) processing parameters on microstructure and mechanical properties of nickel. *Materials Science and Engineering: A*, 618, 176-181. <https://doi.org/https://doi.org/10.1016/j.msea.2014.08.070>
- Boughalmi, R., Boukhachem, A., Kahlaoui, M., Maghraoui, H., Amlouk, M. (2014). Physical investigations on Sb₂S₃ sprayed thin film for optoelectronic applications. *Materials Science in Semiconductor Processing*, 26, 593-602. <https://doi.org/10.1016/j.mssp.2014.05.059>
- Breval, E., Cheng, J. P., Agrawal, D. K., Gigl, P., Dennis, M., Roy, R., Papworth, A. J. (2005). Comparison between microwave and conventional sintering of WC/Co composites. *Materials Science and Engineering: A*, 391(1), 285-295. <https://doi.org/10.1016/j.msea.2004.08.085>

- Campbell-Smith, P. (2014). *Sinterización por Spark Plasma Sintering (SPS) de materiales compuestos para herramientas de corte* Universidad de Oviedo]. Oviedo, España. <http://hdl.handle.net/10651/28434>
- Carter, M. G. N. (2013). *Ceramic Materials: Science and Engineering*. Springer New York, NY. <https://doi.org/10.1007/978-1-4614-3523-5>
- Carvajal-Campos, Y., Ceballos-Mendivil, L., Baldenebro-López, F., Pérez-Rábago, C., Estrada, C. A. (2019). Synthesis and characterization of tantalum carbide nanoparticles using concentrated solar energy. *Advanced Powder Technology*, 30(11), 2574-2579. <https://doi.org/10.1016/j.appt.2019.08.004>
- Chen, T., Zhang, Y. (2007). Thermal modeling of laser sintering of two-component metal powder on top of sintered layers via multi-line scanning. *Applied Physics A*, 86(2), 213-220. <https://doi.org/10.1007/s00339-006-3739-1>
- Chen, Y.-C., Tsao, S.-M., Lin, C.-S., Wang, S.-C., Chien, Y.-H. (2009). Microwave dielectric properties of $0.95\text{MgTiO}_3\text{-}0.05\text{CaTiO}_3$ for application in dielectric resonator antenna. *Journal of Alloys and Compounds*, 471(1), 347-351. <https://doi.org/10.1016/j.jallcom.2008.03.118>
- Chen, Z., Li, Z., Li, J., Liu, C., Lao, C., Fu, Y., Liu, C., Li, Y., Wang, P., He, Y. (2019). 3D printing of ceramics: A review. *Journal of the European Ceramic Society*, 39(4), 661-687. <https://doi.org/10.1016/j.jeurceramsoc.2018.11.013>
- Cruz Fernandes, J., Almeida Costa Oliveira, F., Granier, B., Badie, J.-M., Rosa, L. G., Shohoji, N. (2006). Kinetic aspects of reaction between tantalum and carbon material (active carbon or graphite) under solar radiation heating. *Solar Energy*, 80(12), 1553-1560. <https://doi.org/10.1016/j.solener.2006.01.001>
- Dehsheikh, H. G., Ghasemi-Kahrizsangi, S. (2017). Performance improvement of MgO-C refractory bricks by the addition of Nano-ZrSiO₄. *Materials Chemistry and Physics*, 202, 369-376. <https://doi.org/10.1016/j.matchemphys.2017.09.055>
- Dehsheikh, H. G., Ghasemi-Kahrizsangi, S., Karamian, E. (2018). Addition impact of nano-carbon black on the performance of MgO.CaO compounds. *Ceramics International*, 44(5), 5524-5527. <https://doi.org/10.1016/j.ceramint.2017.12.195>

- El sistema eléctrico español.* (2021). https://www.sistemaelectrico-ree.es/sites/default/files/2022-06/InformeEnergiaRenovable2021_Resumen.pdf (accedido el 25 de mayo de 2024).
- Fang, Z. Z., Wang, H. (2010). 17 - Sintering of ultrafine and nanosized particles. In Z. Z. Fang (Ed.), *Sintering of Advanced Materials* (pp. 434-473). Woodhead Publishing. <https://doi.org/10.1533/9781845699949.3.434>
- Fernández-González, D. (2023). A State-Of-The-Art Review on Materials Production and Processing Using Solar Energy. *Mineral Processing and Extractive Metallurgy Review*, 1-43. <https://doi.org/10.1080/08827508.2023.2243008>
- Fernández-González, D., Prazuch, J., Ruiz-Bustanza, I., González-Gasca, C., Piñuela-Noval, J., Verdeja, L. F. (2018). Solar synthesis of calcium aluminates. *Solar Energy*, 171, 658-666. <https://doi.org/10.1016/j.solener.2018.07.012>
- Fernández-González, D., Ruiz-Bustanza, I., González-Gasca, C., Noval, J. P., Mochón-Castaños, J., Sancho-Gorostiaga, J., Verdeja, L. F. (2018). Concentrated solar energy applications in materials science and metallurgy. *Solar Energy*, 170, 520-540. <https://doi.org/10.1016/j.solener.2018.05.065>
- Fernández-González, D., Suárez, M., Piñuela-Noval, J., Díaz, L. A., Gómez-Rodríguez, C., García Quiñonez, L. V., Fernández, A. (2022). Alumina/molybdenum nanocomposites obtained by colloidal synthesis and spark plasma sintering. *Ceramics International*, 49(6), 9432-9441. <https://doi.org/10.1016/j.ceramint.2022.11.108>
- Fernández-González, D., Piñuela-Noval, J., Ruiz-Bustanza, Í., González-Gasca, C., Gómez-Rodríguez, C., García-Quíñonez, L. V., López-Lievano, A., Fernández, A., Verdeja, L. F. (2024). Solar Assisted Production of MgAl₂O₄ from Bayer Process Electrofilter Fines as Source of Al₂O₃. *Journal of Sustainable Metallurgy*, 10(1), 296-310. <https://doi.org/10.1007/s40831-024-00805-6>
- Flamant, G., Balat-Pichelin, M. (2009). Elaboration and testing of materials using concentrated solar energy. *Solar Energy Conversion And Photoenergy System-Volume I*, 8, 306.
- Ganesh, I. (2013). A review on magnesium aluminate (MgAl₂O₄) spinel: synthesis, processing and applications. *International Materials Reviews*, 58(2), 63-112. <https://doi.org/10.1179/1743280412Y.0000000001>

- German, R. M. (1996). *Sintering theory and practice*. Londres: Wiley and Sons.
- German, R. M., Suri, P., Park, S. J. (2009). Review: liquid phase sintering. *Journal of Materials Science*, 44(1), 1-39. <https://doi.org/10.1007/s10853-008-3008-0>
- Ghasemi-Kahrizsangi, S., Barati Sedeh, M., Gheisari Dehsheikh, H., Shahraki, A., Farooghi, M. (2016). Densification and properties of ZrO₂ nanoparticles added magnesia–dolomite refractories. *Ceramics International*, 42(14), 15658-15663. <https://doi.org/10.1016/j.ceramint.2016.07.021>
- Ghasemi-Kahrizsangi, S., Dehsheikh, H. G., Boroujerdnia, M. (2017). MgO-CaO-Cr₂O₃ composition as a novel refractory brick: Use of Cr₂O₃ nanoparticles. *Boletín de la Sociedad Española de Cerámica y Vidrio*, 56(2), 83-89. <https://doi.org/10.1016/j.bsecv.2016.11.002>
- Ghasemi-Kahrizsangi, S., Dehsheikh, H. G., Karamian, E., Boroujerdnia, M., Payandeh, K. (2017). Effect of MgAl₂O₄ nanoparticles addition on the densification and properties of MgO-CaO refractories. *Ceramics International*, 43(6), 5014-5019. <https://doi.org/10.1016/j.ceramint.2017.01.011>
- Ghasemi-Kahrizsangi, S., Nemati, A., Shahraki, A., Farooghi, M. (2016). Densification and Properties of Fe₂O₃ Nanoparticles added CaO Refractories. *Ceramics International*, 42(10), 12270-12275. <https://doi.org/10.1016/j.ceramint.2016.04.173>
- Ghasemi-Kahrizsangi, S., Shahraki, A., Farooghi, M. (2018). Effect of Nano-TiO₂ Additions on the Densification and Properties of Magnesite-Dolomite Ceramic Composites. *Iranian Journal of Science and Technology Transaction a-Science*, 42(A2), 567-575. <https://doi.org/10.1007/s40995-016-0143-3>
- Gomez Rodriguez, C., Verdeja, L.F., Fernández-González, D., Fernández, A., García-Quiñónez, L. (2023). Morphological study of refractory composite materials based on magnesia (MgO) with additions of hercynite (FeAl₂O₄). *Materiales Compuestos I*.
- Gross, B. C., Erkal, J. L., Lockwood, S. Y., Chen, C., Spence, D. M. (2014). Evaluation of 3D Printing and Its Potential Impact on Biotechnology and the Chemical Sciences. *Analytical Chemistry*, 86(7), 3240-3253. <https://doi.org/10.1021/ac403397r>
- Grundas, S. (2011). *Advances in Induction and Microwave Heating of Mineral and Organic Materials*. Rijeka: IntechOpen.

- Guardia-Valenzuela, J., Bertarelli, A., Carra, F., Mariani, N., Bizzaro, S., Arenal, R. (2018). Development and properties of high thermal conductivity molybdenum carbide-graphite composites. *Carbon*, 135, 72-84. <https://doi.org/10.1016/j.carbon.2018.04.010>
- Gómez Rodríguez, C., Das Roy, T. K., Shaji, S., Castillo Rodríguez, G. A., García Quiñonez, L., Rodríguez, E., González, J.O., Aguilar-Martínez, J. A. (2015). Effect of addition of Al₂O₃ and Fe₂O₃ nanoparticles on the microstructural and physico-chemical evolution of dense magnesia composite. *Ceramics International*, 41(6), 7751-7758. <https://doi.org/10.1016/j.ceramint.2015.02.107>
- Gómez-Rodríguez, C., Castillo-Rodríguez, G. A., Rodríguez-Castellanos, E. A., Vázquez-Rodríguez, F. J., López-Perales, J. F., Aguilar-Martínez, J. A., Fernández-González, D., García-Quiñonez, L.V., Verdeja, L. F. (2020). Development of an Ultra-Low Carbon MgO Refractory Doped with α -Al₂O₃ Nanoparticles for the Steelmaking Industry: A Microstructural and Thermo-Mechanical Study. *Materials*, 13(3), 715. <https://doi.org/10.3390/ma13030715>
- Gómez-Rodríguez, C., Fernández-González, D., García-Quiñonez, L. V., Castillo-Rodríguez, G. A., Aguilar-Martínez, J. A., Verdeja, L. F. (2019). MgO Refractory Doped with ZrO₂ Nanoparticles: Influence of Cold Isostatic and Uniaxial Pressing and Sintering Temperature in the Physical and Chemical Properties. *Metals*, 9(12). <https://doi.org/10.3390/met9121297>
- Gómez-Rodríguez, C., García-Quiñonez, L. V., Verdeja, L. F., Castillo-Rodríguez, G. A., Aguilar-Martínez, J. A., Mariño-Gámez, A. E., Fernández-González, D. (2022). Selective laser sintering of alumina-molybdenum nanocomposites. *Ceramics International*, 48(19, Part B), 29540-29545. <https://doi.org/10.1016/j.ceramint.2022.08.058>
- Gómez-Rodríguez, C., Verdeja, L. F., Castillo-Rodríguez, G. A., Rodríguez-Castellanos, E. A., Fernández-González, D., Collado-Hernández, A., García-Quiñonez, L. V. (2022). Nano-oxide (SiO₂ and Fe₂O₃) effect on magnesium oxide compound (MgO). En: *Production of Engineering Materials* (editado por Izabela Gabryelewicz, Maciej Widrychowicz, Patryk Krupa, Daniel Fernández González) (pp. 48-61). Zielona Góra, Polonia: University of Zielona Góra.

- Hayun, S., Paris, V., Mitrani, R., Kalabukhov, S., Dariel, M. P., Zaretsky, E., Frage, N. (2012). Microstructure and mechanical properties of silicon carbide processed by Spark Plasma Sintering (SPS). *Ceramics International*, 38(8), 6335-6340. <https://doi.org/10.1016/j.ceramint.2012.05.003>
- Hernández-Reséndiz, M., Gómez-Rodríguez, C., Fernández-González, D., Castillo-Rodríguez, G. A. (2023). Synthesis and characterization of dense MgO–TiO₂ nanocomposites obtained by two novel processing routes. *Ceramics International*, 49(8), 12604-12614. <https://doi.org/10.1016/j.ceramint.2022.12.123>
- Isobe, T., Daimon, K., Sato, T., Matsubara, T., Hikichi, Y., Ota, T. (2008). Spark plasma sintering technique for reaction sintering of Al₂O₃/Ni nanocomposite and its mechanical properties. *Ceramics International*, 34(1), 213-217. <https://doi.org/10.1016/j.ceramint.2006.08.017>
- Jayasankar, M., Ananthakumar, S., Mukundan, P., Wunderlich, W., Warriar, K. G. K. (2008). Al₂O₃ @ TiO₂—A simple sol–gel strategy to the synthesis of low temperature sintered alumina–aluminium titanate composites through a core–shell approach. *Journal of Solid State Chemistry*, 181(10), 2748-2754. <https://doi.org/10.1016/j.jssc.2008.06.057>
- Kang, S.-J. L. (2005a). 1 - Sintering Processes. En S.-J. L. Kang (Ed.), *Sintering* (pp. 3-8). Butterworth-Heinemann. <https://doi.org/10.1016/B978-075066385-4/50001-7>
- Kang, S.-J. L. (2005b). 4 - Initial Stage Sintering. En S.-J. L. Kang (Ed.), *Sintering* (pp. 39-55). Butterworth-Heinemann. <https://doi.org/10.1016/B978-075066385-4/50004-2>
- Kang, S.-J. L. (2005c). 6 - Normal Grain Growth And Second-Phase Particles. En S.-J. L. Kang (Ed.), *Sintering* (pp. 91-96). Butterworth-Heinemann. <https://doi.org/10.1016/B978-075066385-4/50006-6>
- Kang, S.-J. L. (2005d). 14 - Basis Of Liquid Phase Sintering. En S.-J. L. Kang (Ed.), *Sintering* (pp. 199-203). Butterworth-Heinemann. <https://doi.org/10.1016/B978-075066385-4/50014-5>
- Kumar, S. (2003). Selective laser sintering: A qualitative and objective approach. *JOM*, 55(10), 43-47. <https://doi.org/10.1007/s11837-003-0175-y>

- Kähäri, H., Teirikangas, M., Juuti, J., Jantunen, H. (2016). Room-temperature fabrication of microwave dielectric $\text{Li}_2\text{MoO}_4\text{-TiO}_2$ composite ceramics. *Ceramics International*, 42(9), 11442-11446. <https://doi.org/10.1016/j.ceramint.2016.04.081>
- Lee, C.-H., Lu, H.-H., Wang, C.-A., Nayak, P. K., Huang, J.-L. (2010). Microstructure and mechanical properties of $\text{TiN/Si}_3\text{N}_4$ nanocomposites by spark plasma sintering (SPS). *Journal of Alloys and Compounds*, 508(2), 540-545. <https://doi.org/10.1016/j.jallcom.2010.08.116>
- Lee, J.-S., Chang, C.-M., Lee, Y. I. L., Lee, J.-H., Hong, S.-H. (2004). Spark Plasma Sintering (SPS) of NASICON Ceramics. *Journal of the American Ceramic Society*, 87(2), 305-307. <https://doi.org/10.1111/j.1551-2916.2004.00305.x>
- Li, W., Gao, L. (2000). Rapid sintering of nanocrystalline $\text{ZrO}_2(3\text{Y})$ by spark plasma sintering. *Journal of the European Ceramic Society*, 20(14), 2441-2445. [https://doi.org/10.1016/S0955-2219\(00\)00152-7](https://doi.org/10.1016/S0955-2219(00)00152-7)
- Li, Y., Hu, Y., Cong, W., Zhi, L., Guo, Z. (2017). Additive manufacturing of alumina using laser engineered net shaping: Effects of deposition variables. *Ceramics International*, 43(10), 7768-7775. <https://doi.org/10.1016/j.ceramint.2017.03.085>
- Messina, S., Nair, M. T. S., Nair, P. K. (2007). Antimony sulfide thin films in chemically deposited thin film photovoltaic cells. *Thin Solid Films*, 515(15), 5777-5782. <https://doi.org/10.1016/j.tsf.2006.12.155>
- Michalsky, R., Peterson, B. A., Pfromm, P. H. (2014). Rapid synthesis of nanocrystalline magnesium chromite and ferrite ceramics with concentrated sunlight. *Thermochimica acta*, 582, 10-16. <https://doi.org/10.1016/j.tca.2014.02.018>
- Oghbaei, M., Mirzaee, O. (2010). Microwave versus conventional sintering: A review of fundamentals, advantages and applications. *Journal of Alloys and Compounds*, 494(1), 175-189. <https://doi.org/10.1016/j.jallcom.2010.01.068>
- Okoro, A. M., Lephuthing, S. S., Oke, S. R., Falodun, O. E., Awotunde, M. A., Olubambi, P. A. (2019). A review of spark plasma sintering of carbon nanotubes reinforced titanium-based nanocomposites: Fabrication, densification, and mechanical properties. *JOM*, 71(2), 567-584. <https://doi.org/10.1007/s11837-018-3277-2>
- Okudan, M. D., Akcil, A., Tuncuk, A., Deveci, H. (2015). Recovery of gallium and aluminum from electrofilter dust of alumina calcination plant in Bayer process. *Separation*

- Science and Technology*, 50(16), 2596-2605.
<https://doi.org/10.1080/01496395.2015.1062027>
- Oliveira, F. A. C., Rosa, L. G., Fernandes, J. C., Rodríguez, J., Canadas, I., Martínez, D., Shohoji, N. (2009). Mechanical properties of dense cordierite discs sintered by solar radiation heating. *Materials transactions*, 50(9), 2221-2228.
<https://doi.org/10.2320/matertrans.MRA2008369>
- Omori, M. (2000). Sintering, consolidation, reaction and crystal growth by the spark plasma system (SPS). *Materials Science and Engineering: A*, 287(2), 183-188.
[https://doi.org/10.1016/S0921-5093\(00\)00773-5](https://doi.org/10.1016/S0921-5093(00)00773-5)
- Patidar, D., Tiwari, S., Sharma, P., Pardeshi, R., Chandra, L., Shekhar, R. (2015). Solar convective furnace for metals processing. *JOM*, 67(11), 2696-2704.
<https://doi.org/10.1007/s11837-015-1633-z>
- Pero-Sanz Elorz, J. A., Fernández González, D., Verdeja, L. F. (2019). Structural Materials: Ceramics. En J. A. Pero-Sanz Elorz, D. Fernández González, & L. F. Verdeja (Eds.), *Structural Materials: Properties and Selection* (pp. 77-132). Springer International Publishing. https://doi.org/10.1007/978-3-030-26161-0_4
- Ping, L. R., Azad, A.-M., Dung, T. W. (2001). Magnesium aluminate (MgAl₂O₄) spinel produced via self-heat-sustained (SHS) technique. *Materials research bulletin*, 36(7-8), 1417-1430. [https://doi.org/10.1016/S0025-5408\(01\)00622-5](https://doi.org/10.1016/S0025-5408(01)00622-5)
- Piñuela-Noval, J., Fernández-González, D., Suárez, M., Gómez-Rodríguez, C., Fernández, A. (2023). Spark plasma sintering of graphite-chromium carbide composites: Influence of the sintering temperature and powder synthesis method. *Ceramics International*, 49(21), 33891-33900.
<http://dx.doi.org/10.1016/j.ceramint.2023.08.083>
- Ragulya, A. V. (2010). Fundamentals of Spark Plasma Sintering. En K. H. J. Buschow, R. W. Cahn, M. C. Flemings, B. Ilshner, E. J. Kramer, S. Mahajan, & P. Veyssi re (Eds.), *Encyclopedia of Materials: Science and Technology* (pp. 1-5). Elsevier.
<https://doi.org/10.1016/B978-008043152-9.02249-1>
- Rahaman, M. N. (2003). *Ceramic Processing and Sintering*. Londres: Taylor and Francis.
<https://doi.org/10.1201/9781315274126>

- Riedel, H., Svoboda, J. (2006). *Simulation of Microwave Sintering with Advanced Sintering Models. Advances in Microwave and Radio Frequency Processing*, Berlin, Heidelberg.
- Román, R., Cañadas, I., Rodríguez, J., Hernández, M. T., González, M. (2008). Solar sintering of alumina ceramics: Microstructural development. *Solar Energy*, 82(10), 893-902. <https://doi.org/10.1016/j.solener.2008.04.002>
- Sancho, J., Fernández Pérez, B., Ayala, J. N., García, P., Verdeja, L. (2009). The recycling of bayer electrofilter fines for diverse applications. 1st Spanish National Conference on Advances in Materials Recycling and Eco – Energy, Madrid, 12-13 November 2009.
- Sancho-Gorostiaga, J., Bernardo-Sanchez, A., Sancho-Martínez, J. P., Fernandez-Gonzalez, D., Verdeja, L. F. (2021). Study of copper fixation mechanisms on Bayer Process Electrostatic precipitator Microparticles (BPEM) using ¹H and ²⁷Al NMR spectroscopy. *Journal of Water Process Engineering*, 39, 101872. <https://doi.org/10.1016/j.jwpe.2020.101872>
- Sancho-Gorostiaga, J., Bernardo-Sánchez, A., Sancho-Martínez, J. P., Fernández-González, D., Verdeja, L. F. (2021). Manufacture of a High Temperature Structural Insulator (HTSI) using electrofilter powders generated in the Bayer process. *Transactions of the Indian Ceramic Society*, 80(3), 163-173. <https://doi.org/10.1080/0371750X.2021.1915872>
- Schacht, C. (2004). *Refractories Handbook*. Londres: CRC Press.
- Shahzad, K., Deckers, J., Boury, S., Neirinck, B., Kruth, J.-P., Vleugels, J. (2012). Preparation and indirect selective laser sintering of alumina/PA microspheres. *Ceramics International*, 38(2), 1241-1247. <https://doi.org/10.1016/j.ceramint.2011.08.055>
- Shen, Z., Johnsson, M., Zhao, Z., Nygren, M. (2002). Spark Plasma Sintering of alumina. *Journal of the American Ceramic Society*, 85(8), 1921-1927. <https://doi.org/10.1111/j.1151-2916.2002.tb00381.x>
- Shohoji, N., Almeida Costa Oliveira, F., Cruz Fernandes, J., Guerra Rosa, L., Rodríguez Garcia, J., Canadas Martínez, I., Ramos Miñarro, C., Magalhaes, T., Cestari, F. (2013). Synthesizing higher nitride of molybdenum (Mo) and iron (Fe) in ammonia

- (NH₃) gas stream under irradiation of concentrated solar beam in a solar furnace. *Materialwissenschaft und Werkstofftechnik*, 44(12), 959-971. <https://doi.org/10.1002/mawe.201300163>
- Siegel, R. W. (1993). Synthesis and properties of nanophase materials. *Materials Science and Engineering: A*, 168(2), 189-197. [https://doi.org/10.1016/0921-5093\(93\)90726-U](https://doi.org/10.1016/0921-5093(93)90726-U)
- Suárez, M., Fernández, A., Menéndez, J., Torrecillas, R., Kessel, H., Hennicke, J., Kessel, T. (2013). Challenges and opportunities for spark plasma sintering: a key technology for a new generation of materials. En: B. Ertug (ed.), *Sintering applications*, 13, 319-342. <https://doi.org/10.5772/53706>
- Upadhyaya, D. D., Ghosh, A., Dey, G. K., Prasad, R., Suri, A. K. (2001). Microwave sintering of zirconia ceramics. *Journal of Materials Science*, 36(19), 4707-4710. <https://doi.org/10.1023/A:1017966703650>
- Verdeja, L. F., Sancho, J., Ballester, A. (2008a). *Materiales refractarios y ceramicos*, Madrid: Ed. Sintesis.
- Verdeja, L. F., Sancho, J., Ballester, A., González, R. (2014). *Refractory and ceramic materials*, Madrid: Ed. Sintesis.
- Xu, X., Tao, T., Zhang, X., Cao, Z., Huang, D., Liang, H., Hu, Y. (2020). Spark plasma sintering of ZrO₂-Al₂O₃ nanocomposites at low temperatures aided by amorphous powders. *Ceramics International*, 46(4), 4365-4370. <https://doi.org/10.1016/j.ceramint.2019.10.160>
- Yan, C., Shi, Y., Zhaoqing, L., Wen, S., Wei, Q. (2020). *Selective laser sintering additive manufacturing technology*. Londres: Academic Press.
- Zhan, G.-D., Kuntz, J., Wan, J., Garay, J., Mukherjee, A. K. (2003). Spark-plasma-sintered BaTiO₃/Al₂O₃ nanocomposites. *Materials Science and Engineering: A*, 356(1), 443-446. [https://doi.org/10.1016/S0921-5093\(02\)00812-2](https://doi.org/10.1016/S0921-5093(02)00812-2)
- Zhang, H., Xiaolin, J., Zhanjie, L., Zhenzhen, L. (2004). The Low Temperature Preparation of Nanocrystalline MgAl₂O₄ Spinel by Citrate Sol-Gel Process. *Materials Letters*, 58, 1625-1628. <https://doi.org/10.1016/j.matlet.2003.09.051>

6. Artículos publicados

A raíz de esta tesis doctoral se han publicado un total de 5 artículos indexados en el *Journal of Citations Reports*. Los artículos se referencian a continuación en los que los dos primeros forman parte del bloque de la síntesis de materiales cerámicos empleando energía solar concentrada, y los tres siguientes se corresponden con el bloque de la sinterización de materiales compuestos de matriz cerámica y disperso de óxido metálico y metal.

1. Daniel Fernández-González, Juan Piñuela-Noval, Íñigo Ruiz-Bustanza, Carmen González-Gasca, **Cristian Gómez-Rodríguez**, Linda Viviana García Quiñonez, Adolfo Fernández, Luis Felipe Verdeja, 2023: Solar dissociation of zirconium silicate sand: A clean alternative to obtain zirconium dioxide, *Journal of Cleaner Production*, 420, 138371. <https://doi.org/10.1016/j.jclepro.2023.138371>
2. Daniel Fernández-González, Juan Piñuela-Noval, Íñigo Ruiz-Bustanza, Carmen González-Gasca, **Cristian Gómez-Rodríguez**, Linda Viviana García-Quíñonez, Adolfo López-Liévano, Adolfo Fernández, Luis Felipe Verdeja, 2024: Solar assisted production of $MgAl_2O_4$ from Bayer process electrofilter fines as source of Al_2O_3 , *Journal of Sustainable Metallurgy*, 10, 296-310. <https://doi.org/10.1007/s40831-024-00805-6>
3. **Cristian Gómez-Rodríguez**, Linda Viviana García-Quíñonez, Josué Amilcar Aguilar-Martínez, Guadalupe Alan Castillo-Rodríguez, Edén Amaral Rodríguez-Castellanos, Jesús Fernando López-Perales, María Isabel Mendivil-Palma, Luis Felipe Verdeja, Daniel Fernández-González, 2022: MgO–ZrO₂ ceramic composites for silicomanganese production, *Materials*, 15, 2421. <https://doi.org/10.3390/ma15072421>

4. **Cristian Gómez-Rodríguez**, Linda Viviana García-Quiñonez, Luis Felipe Verdeja, Guadalupe Alan Castillo-Rodríguez, Josué Amilcar Aguilar-Martínez, Aldo E Mariño-Gámez, Daniel Fernández-González, 2022: Selective laser sintering of alumina-molybdenum nanocomposites, *Ceramics International*, 48(19), 29540-29545. <https://doi.org/10.1016/j.ceramint.2022.08.058>
5. Daniel Fernández-González, Marta Suárez, Juan Piñuela-Noval, Luis Antonio Díaz, **Cristian Gómez-Rodríguez**, Linda Vivian García Quiñonez, Amparo Borrell, Adolfo Fernández, 2023: Alumina/molybdenum nanocomposites obtained by colloidal synthesis and spark plasma sintering, *Ceramics International*, 49(6), 9432-9441. <https://doi.org/10.1016/j.ceramint.2022.11.108>

Por lo que respecta a los índices de calidad de las revistas en los que se han publicado los artículos, estos se recogen en la **Tabla 2** con los últimos datos disponibles (2022).

Tabla 2. Métricas de las revistas en las que se publicaron los trabajos que sustentan esta tesis doctoral.

Nombre de la revista	Categoría	Factor de impacto	Cuartil	Ranking
Journal of Cleaner Production	ENGINEERING, ENVIRONMENTAL ENVIRONMENTAL SCIENCES GREEN & SUSTAINABLE	11.1	Q1	8/55
			Q1	22/275
			Q1	8/46

	SCIENCE & TECHNOLOGY			
Journal of Sustainable Metallurgy	GREEN & SUSTAINABLE SCIENCE & TECHNOLOGY	2.4	Q4	43/46
	METALLURGY & METALLURGICAL ENGINEERING		Q2	29/79
	CHEMISTRY, PHYSICAL MATERIALS		Q3	84/161
Materials	SCIENCE, MULTIDISCIPLINARY METALLURGY & METALLURGICAL ENGINEERING	3.4	Q3	174/344
	PHYSICS, APPLIED PHYSICS, CONDENSED MATTER		Q2	57/160
Ceramics International	MATERIALS SCIENCE, CERAMICS	5.2	Q1	3/29

Se incluyen igualmente varios artículos en revistas no indexadas, y otros trabajos publicados como capítulos de libro.

1. **Cristian Gómez Rodríguez**, Beatriz Escobedo-Trujillo, Luis Felipe Verdeja, Daniel Fernández-González, Adolfo Fernández, Linda-Viviana García-Quiñónez, Guadalupe Alan Castillo Rodríguez, 2023: Morphological study of refractory composite materials based on magnesia (MgO) with additions of hercinite ($\text{Fe}_2\text{Al}_2\text{O}_4$), *Revista de Materiales Compuestos*, https://www.scipedia.com/public/Gomez_Rodriguez_et_al_2023a
2. **Cristian Gómez-Rodríguez**, Luis Felipe Verdeja, Guadalupe Alan Castillo-Rodríguez, Eden Amaral Rodríguez-Castellanos, Daniel Fernández-González, Adolfo Collado-Hernández, Linda Viviana García-Quiñónez, 2022: Nano-Oxide (SiO_2 and Fe_2O_3) effect on magnesium oxide compound (MgO), Capítulo 3, En: Izabela Gabryelewicz, Maciej Wedrychowicz, Patryk Krupa, Daniel Fernández González (Eds.), *Production of engineering materials* (pp. 48-61). Zielona Góra, Polonia: University of Zielona Góra.
3. Marina Hernández-Reséndiz, **Cristian Gómez-Rodríguez**, Daniel Fernández-González, Guadalupe Alan Castillo-Rodríguez, 2023: Synthesis and characterization of dense MgO–TiO₂ nanocomposites obtained by two novel processing routes, *Ceramics International*, 49, 12604-12614. <https://doi.org/10.1016/j.ceramint.2022.12.123>
4. **Cristian Gómez-Rodríguez**, Linda Viviana García-Quiñónez, Josué Amilcar Aguilar-Martínez, Francisco Javier Vázquez-Rodríguez, Daniel Fernández-González, Luis Felipe Verdeja, José Fernando López-Perales, Guadalupe Alan

Castillo-Rodríguez, Edén Rodríguez, 2023: Desarrollo de un refractario de MgO dopado con η -Al₂O₃, *EYA ACADEMY*, 1 (1), 46-61.

<http://doi.org/10.59335/nvyu9288>

Artículo 1: Solar dissociation of zirconium silicate sand: A clean alternative to obtain zirconium dioxide.



Solar dissociation of zirconium silicate sand: A clean alternative to obtain zirconium dioxide

Daniel Fernández-González^{a,*}, Juan Piñuela-Noval^a, Íñigo Ruiz-Bustinsa^b,
Carmen González-Gasca^c, Cristian Gómez-Rodríguez^d, Linda Viviana García Quiñonez^e,
Adolfo Fernández^a, Luis Felipe Verdeja^f

^a *Nanomaterials and Nanotechnology Research Center (CINN-CSIC), Universidad de Oviedo (UO), Principado de Asturias (PA), Avda. de la Vega, 4-6, 33940, El Entrego, Asturias, Spain*

^b *Departamento de Ingeniería Geológica y Minera, Escuela Técnica Superior de Ingenieros de Minas y Energía, Universidad Politécnica de Madrid, 28003, Madrid, Spain*

^c *Universidad Internacional de Valencia - VIU, 46002, Valencia, Spain*

^d *Departamento de Mecánica, Facultad de Ingeniería, Campus Coatzacoalcos, Universidad Veracruzana, Av. Universidad Km 7.5 Col. Santa Isabel, Coatzacoalcos, 96535, Veracruz, Mexico*

^e *Centro de Investigación en Recursos Energéticos y Sustentables (CIRES), Universidad Veracruzana, Av. Universidad Veracruzana km 7.5, Col. Santa Isabel I, 96538, Coatzacoalcos, Veracruz, Mexico*

^f *Department of Materials Science and Metallurgical Engineering, School of Mines, Energy and Materials, Universidad de Oviedo, 33004, Oviedo/Uvieu, Asturias, Spain*

ARTICLE INFO

Handling Editor: Panos Seferlis

Keywords:

Zirconia
Solar energy
Sustainability
Renewable energy
Concentrated solar energy
Ceramics

ABSTRACT

Application of concentrated solar energy (CSE) in the industry of materials is a promising alternative that is developing in recent years to reduce the environmental impact while accomplishing the objective of producing high-quality products. It is important to enlarge the processes being studied with the competition of CSE to find the most attractive for the scalation up to the industrial level and thus contributing to the energy transition in the field of materials. Systematic laboratory research has been conducted within the thermal decomposition of metal carbonates, sulphates, hydroxides, and metal oxides with promising results using CSE, which has the competing advantage of heat production without releasing pollutants and the construction of the installation as principal cost. Nevertheless, the thermal decomposition of zirconium silicate ($ZrSiO_4$), despite of the importance of zirconium dioxide in the field of ceramics and the high energy consumption in the process, has never been reported in the literature using CSE. The process proposed in this manuscript consists of two stages, the pyrometallurgical one, based on the direct application of CSE to $ZrSiO_4$ to dissociate it into ZrO_2 and SiO_2 , and the hydrometallurgical one, based on the aqueous extraction of the zirconium dioxide with NaOH at 200 °C for 6 h in pressure reactor. The double-stage process based on CSE leads to the synthesis of close to 95% purity monoclinic ZrO_2 . The energy for the pyrometallurgical route is supplied by a renewable energy source (CSE), thus contributing to reduce carbon dioxide emissions in the synthesis of ZrO_2 .

1. Introduction

Zirconium dioxide is one of the most important ceramic materials, which has been widely researched and used due to the high toughness and strength, compared with that of the common ceramic materials, combined with some other relevant properties as the high thermal and corrosion resistances, chemical inertness, low thermal conductivity, or insulating characteristics (Verdeja et al., 2014). These interesting properties have made zirconium dioxide to be used in a wide range of different applications as abrasive products (Park et al., 2008),

refractories (Zanelli et al., 2010; Weinberg et al., 2021; Xuekun et al., 2023; Kusiorowski, 2020; Chen et al., 2020), dental and biomedical applications (Seo et al., 2020; Hu et al., 2019; Chen et al., 2021; Hanawa, 2020; Lorusso et al., 2020; Schünemann et al., 2019; Grech and Antunes, 2019), additive in paints and lacquers (Author, 1978), fuel cell membranes (Vinodh et al., 2011; Rambabu et al., 2020; Nawn et al., 2015), among others.

Zirconium dioxide can be found in the nature as baddeleyite, although this oxide is usually produced by thermal or thermochemical methods from zirconium silicate sand, with separation of the products

* Corresponding author.

E-mail address: d.fernandez@cinn.es (D. Fernández-González).

<https://doi.org/10.1016/j.jclepro.2023.138371>

Received 21 April 2023; Received in revised form 31 July 2023; Accepted 6 August 2023

Available online 8 August 2023

0959-6526/© 2023 Elsevier Ltd. All rights reserved.

by solubility or phase state of matter differentiation. The methods commercially used to produce zirconia include the thermal dissociation/calcination or the decomposition by fusion with different materials as sodium hydroxide, sodium carbonate, calcium oxide and magnesium oxide, potassium fluorosilicate or calcium carbonate. The temperatures required for the process are high, which makes the process energy intensive, where the source of energy is habitually the electricity. Considering that the greenhouse gas emission intensity of electricity generation in Europe is 275 g CO₂/kWh (European Environment Agency), every kWh of electric power consumed in the production of ZrO₂ will generate this amount of carbon dioxide. Therefore, the utilization of any method that might avoid the utilization of electricity will become the process zero-CO₂. However, the synthesis of zirconia habitually involves the presence of coke, apart from the electricity, to promote the thermal decomposition of the ZrSiO₄ into ZrO₂ (s) and SiO (g), which makes the process a contributor to the greenhouse gas emissions. This route would avoid the subsequent processes of products' separation, as zirconia is obtained as solid product and silicon is separated as silicon monoxide gas, although the temperatures required for the process well exceed the melting point of the zircon. In any case, the dissociation of the ZrSiO₄ starts at temperatures below the melting point of the ZrO₂-SiO₂ binary diagram (2430 °C) since the zircon has an incongruent melting point, which makes possible to obtain zirconia with processes that employ lower temperatures and use thermochemical separation.

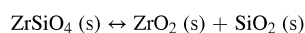
The European Green Deal, approved in 2020, as initiative of the European Commission aims to reach climate neutrality in the European Union in 2050. This objective involves all the sectors but particularly the industry, where the decarbonization and modernization of energy-intensive industries is a key point. The greatest efforts are being made on the cement and steel industries because they account for >10% of the anthropogenic CO₂ emissions. Nevertheless, the other industries should also play an important role in the energy transition. Otherwise, the objective of climate neutrality will be difficultly reached by 2050. Within these other industries, it is possible to include the production of zirconia, whose contribution to the anthropogenic CO₂ emissions is significantly lower than that of other energy intensive industries since the production of zircon is around 1.1 Mt/year (Selby, 2007), which is partially used in the production of zirconia, but relevant to accomplish the above-reported goal.

Significant research is being carried out to extract energy from the sun in an efficient manner (Ahmadinejad et al., 2022a, 2022b; Ahmadinejad and Moosavi, 2022). This will make solar energy very attractive for other industries apart from the energy generation. Within this context, solar energy will play an important role in metallurgical processes as it is possible to use it to produce electricity, heat, or steam for the traditional processes, but it might be directly applied in new processes especially conceived considering the particular characteristics of the concentrated solar energy (CSE) technologies. In this line, solar energy has been considered as a suitable alternative to produce metals as it is reported in Fernández-González et al. (2018), and more recently in the extended state-of-the-art review of Fernández-González (2023). Research focused on the beginning in the obtaining of the commodities (Murray, 1999) but soon the investigation oriented towards the obtaining of metals for the field of metal fuels. Chuayboon and Abanades, as part of the PROMES-CNRS (PROcédés Matériaux et Energie Solaire- Centre National de la Recherche Scientifique) laboratory, reported flexibility, reliability, and robustness of the solar based metallurgical process for the co-production of metals as zinc or magnesium (to be used as metal fuels) and product gases as CO or syngas (Chuayboon and Abanades, 2022). Metal fuels are the most promising line that has arisen from the thermal decomposition (sometimes supported by the presence of carbon-based reductants) of metal oxides with CSE for the process. Apart from the zinc oxide-zinc pair, which is the most developed line reaching even pilot plant scale research (Wieckert et al., 2006), CSE has been used to produce metal fuels by thermal decomposition of other metal oxides, as for instance the aluminum obtained from

alumina (Vishnevetsky et al., 2013) or commodities, as the iron from hematite (Fernández-González et al., 2018b). Moreover, solar energy has been also used in the production of silicon, although problems of purity reduced the interest of this line (Murray et al., 2006). Other researchers focused on the utilization of CSE in the production of Si-Ca and Si-Mn alloys, considering the silicothermic reduction process of calcium and manganese oxides (Fernández-González et al., 2019a, 2019b). Researchers have not only centered on the integration of solar energy in the production of metals by thermal decomposition or reduction of oxides but have investigated about: the production of calcium aluminate cements (Fernández-González et al., 2018d) or Portland clinker cement (Costa-Oliveira et al., 2019); the synthesis of hard ceramic materials taking advantage of the possibility of conducting experiments in special or controlled atmospheres (Costa-Oliveira et al., 2015; Cruz-Fernandes et al., 1998; Shohoji et al., 2012, 2021); or the valorization of industrial wastes as the recycling of Waelz oxide to recover zinc (Tzouganatos et al., 2013), the recovery of iron or copper from metal slags (Fernández-González et al., 2019c, 2021), the obtaining of glasses using secondary materials (Padilla et al., 2021) or the decontamination of mercury soils (Navarro et al., 2012).

As reported, CSE has been widely employed in the decomposition of metal oxides to obtain the metal. Nevertheless, research about the application of solar energy in the decomposition of different phases has been widely researched, particularly to obtain materials for the cement industry. This way, it is possible to find the decomposition of phosphogypsum (Palla et al., 2022), gypsum (Salman and Khraishi, 1988), and, especially, calcium carbonate (Flamant et al., 1980; Meier et al., 2004; Abanades and André, 2018; Tescari et al., 2018). The thermal decomposition of the above-reported compounds requires from temperatures that can be easily attained with the participation of the concentrated solar energy: gypsum, >900 °C; and, calcium carbonate, >750 °C. Research does not limit to only these raw materials for the cement industry but extended to decomposition of aluminum hydroxide (Davis et al., 2017; Kakosimos et al., 2022), which is a fundamental energy intensive step of the Bayer process to obtain the alumina, or the decomposition of copper sulphides into copper and sulphur gas, as a process that generates neither carbon dioxide nor sulphur dioxide and allows obtaining copper and sulphur as separated phases (Winkel et al., 2008). In all these processes, CSE is used to provide both the activation energy and the energy for the chemical reaction (decomposition) without generating any pollutants.

Zirconia is obtained, as reported above, by thermal decomposition/dissociation of zirconium silicate sand at high temperatures. **Reaction 1** indicates the process followed by the thermal decomposition of the zirconium silicate into zirconia and silica.



Reaction 1

Zircon decomposes by a solid-state reaction with dissociation temperatures varying between 1285 and 1700 °C (Kraiser et al., 2008). Despite the importance of this reaction in the obtaining of a fundamental raw material for the ceramics industry and the possibilities that CSE offers in this line, the process has never been studied using solar energy as a route that has a zero contribution to greenhouse gas emissions. **Reaction 1** gives as a result insoluble zirconium dioxide and silica. SiO₂ can be removed by leaching the products of decomposition with sodium hydroxide solution at low temperatures (200 °C). This way, the ZrO₂ is obtained as product of the filtration process and the silica, in the form of soluble sodium silicate, is separated from the zirconia in the liquid of filtration.

This manuscript proposes a novel route to produce ZrO₂ consisting of two stages: pyrometallurgical (to dissociate the zircon sand into zirconia and silica) and hydrometallurgical (to separate zirconia and silica), where solar energy plays an important role. CSE is used in this manuscript to provide the energy required for the thermal dissociation of the zircon sand, which is nowadays supplied by electric power in electric arc

furnaces using coke-carbon to support the process. The utilization of solar energy contributes to the reduction of greenhouse gas emissions, associated to both the generation of the electricity for the process and the carbon material employed to promote the process. Therefore, the novelty of the process proposed in this manuscript is the utilization of a renewable energy source, as concentrated solar energy, to heat the sample up to the temperature required for the dissociation, thus contributing to reduce carbon dioxide emissions in the production of zirconia. The second stage consists of the hydrometallurgical route to obtain ZrO_2 and SiO_2 separated as independent products using a basic lixiviation process.

2. Materials and methods

Zirconium silicate sand was employed as raw material. Zirconium silicate sand consists of industrial grade quality with the chemical composition showed in Table 1.

X-ray diffraction analysis (XRD) was carried out in the samples to explore their crystalline structure and phase identification. XRD analysis in Fig. 1 shows the structural characterization of the zircon ($ZrSiO_4$) sample before irradiation with solar energy. For this system, the planes (101), (200), (211), (112), (220), (202), (301), (103), (321), (312), (400), (411), (303), (420), (402), (332), (204) and (323) correspond to the zircon silicate ($ZrSiO_4$) phase, tetragonal crystal system, which are indexed with PDF No. 96-900-2558.

Fig. 2 shows images of the starting powders. The size of the particles is important to avoid the losses of materials or the deterioration of the parabolic concentrator. This issue is relevant in the case of very fine particles that can fly. The starting zircon sand particle size was analyzed using ImageJ software. 55.42% of the zircon sand has a size between 1 and 2.5 μm , 24.01% a size between 2.5 and 5 μm , while the rest has a greater size. With this particle size, its flight inside of the glass hood was not appreciated during the experiments.

Sodium hydroxide (NaOH) was used as leaching agent to separate ZrO_2 from SiO_2 in the second step of the process (hydrometallurgical step). This reagent has also laboratory quality: Panreac, >98%. Traces of silica, 0.001%; sodium carbonate, 1%; and potassium, 0.02%.

Experimental work was conducted in a vertical axis parabolic concentrator belonging to the PROMES-CNRS and located in Font Roméu-Odeillo-Via (France). The parabolic concentrator had 1.5 m in diameter, as reported Fig. 3a, while the maximum concentration ratio was 15000 in a focal point of 1 cm in diameter, with a maximum angle of incidence of 56° and a distance to the focal point of 65 cm. The maximum concentrated power that could be reached with this equipment is 900 W for a 1000 W/m^2 DNI (Direct Normal Irradiation). Samples in this manuscript were subjected to values of DNI within 850 and 975 W/m^2 in all the experiments and these were covered with a protective glass as shown in Fig. 3b to avoid the deterioration of the parabolic concentrator. Tests lasted 5 min without including the operations of preparation of the sample and cooling. A thermocouple was placed close to wall of the crucible to control the progress of the process in such a way that when the thermocouple was burned, the temperature was above 1400 °C. The appearance of the sample after its removal from the solar beam can be observed in Fig. 3c.

Samples obtained in the solar furnace were milled to <180 μm after removing the “unreacted material” and the “partially reacted material”. The powders were treated in Parr Instruments Company reactor of 15 ml of capacity, with Teflon recipient for 6 h at 200 °C in presence of sodium hydroxide and water. The objective was to concentrate the ZrO_2 phase by removal of the silica as soluble sodium silicate. The product extracted

from the reactor was filtered with water once removed from the furnace, and both products were later dried in stove at 100 °C for further analyses.

Three routes were explored according to Fig. 4: Route 1, employed only $ZrSiO_4$ as starting material; Route 2, used $ZrSiO_4$ and 10 wt % Na_2CO_3 ; and Route 3, consisting of $ZrSiO_4$ and 10, 25 or 50 wt % of CaO.

The characterization of the starting materials as well as of the final products was carried out using the following equipment:

- X-ray diffraction, carried out with the Empyrean PANalytical diffractometer using $K\alpha_1$ and $K\alpha_2$ radiation from Cu anode. All measurements were performed with Bragg-Brentano setup at room temperature with the 0.006° step size at 5–90° 2 θ scanning range and the 145 s of measurement time for each step. Data analysis and the peak profile fitting procedure were carried out using X'Pert High-score Plus (Database PDF2 (70–0.94)).
- Chemical composition was determined with S8 Tiger-Bruker X-ray fluorescence spectrometer.
- Scanning Electron Microscope was used to take micrographs at different magnification with a Hitachi T3000 with a voltage of 5 kV, with Energy Dispersive X-ray Spectrometer Quantax70.

3. Results and discussions

3.1. Macroscopic analysis

The treatment of the samples with concentrated solar energy affected only a region of the entire volume of material treated in the solar furnace (Fig. 5a and b). This is schematically indicated in Fig. 5c, where it is possible to see the zones in the sample that can be found in Fig. 5a and b. This is an important issue because when extracting and further processing the sample, it is necessary to first remove the weakly adhered material by conventional methods as air or brushing and then, the partially reacted material by harder methods, as sandpaper. Therefore, the material subjected to further processing and analysis is all from the zone of completely reacted material.

Mass losses during the process were around 2–3%, associated to the presence of moisture due to the storing conditions of the industrial material, and minor projections of material produced during the process. Minor losses of material might be also associated to the formation of silicon monoxide during the process.

3.2. Results from the treatment in the solar furnace

X-ray diffraction analysis (XRD) was carried out for $ZrSiO_4$ samples irradiated with solar energy to explore their crystalline structure and new phase identification (Fig. 6). In this Fig. 6, the zircon phase ($ZrSiO_4$) is clearly identified, some characteristic peaks and planes of this phase were present, which were indexed with the same crystallographic reference (PDF No. 96-900-2558) shown in Fig. 2. These peaks found corresponded to small undissociated peaks of $ZrSiO_4$. As observed in Fig. 6, highest intensity peaks correspond to the phases of ZrO_2 and SiO_2 due to the dissociation of $ZrSiO_4$. From this Fig. 6, it is possible to see the diffraction peaks of ZrO_2 (baddeleyite, corresponding to monoclinic crystal system) at $2\theta = 17.449, 24.070, 24.465, 28.197, 31.490, 34.181, 35.320, 38.580, 40.748, 44.856, 45.540, 49.293, 50.144, 51.224, 54.126, 57.193, 59.830, 62.87, 64.332$ and 65.737° , which were indexed respectively with the crystalline planes (100), (011), (110), (-111), (111), (002), (200), (021), (-211), (112), (-202), (022), (220), (-122), (202), (-311), (131), (311), (-123), (222) of the reference card PDF 96-900-7846. The SiO_2 peaks (quartz, corresponding to hexagonal crystal system) were detected at 2θ values: 22.328, 28.22, 39.188, 41.455, 43.014, 58.362, 61.628 and 64.450° with their respective crystalline planes (100), (10 -1), (110), (102), (111), (202), (210), (211), which were indexed with the reference code, PDF 96-901-2605.

Table 1

Specifications of zirconium silicate sand (wt. %).

ZrO ₂	HfO ₂	SiO ₂	Fe ₂ O ₃	MgO	K ₂ O	Na ₂ O	TiO ₂	CaO
62.60	1.52	32.70	0.50	0.11	0.15	0.47	0.16	0.50

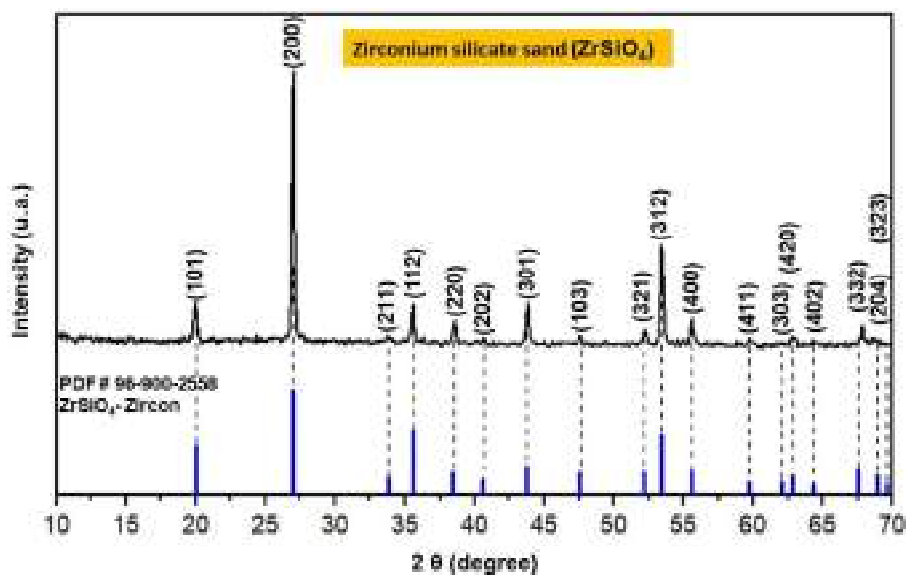


Fig. 1. X-ray diffraction pattern of the zirconium silicate sand.

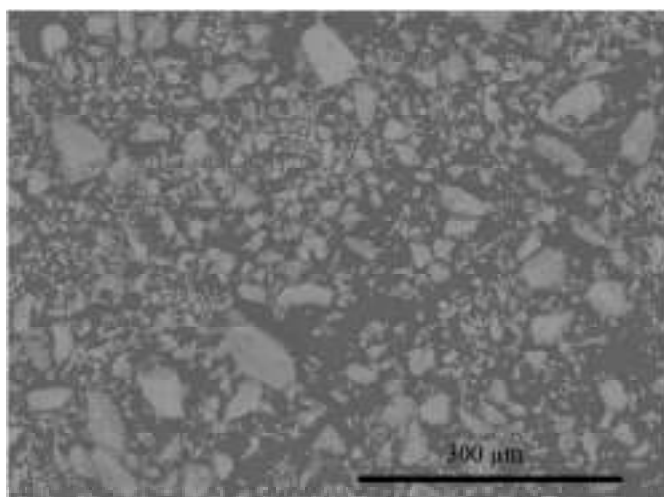
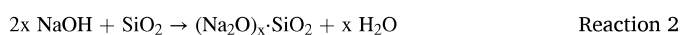


Fig. 2. Images of the starting powders of zirconium silicate sand.

3.3. Removal of soluble phases

X-ray diffraction results already anticipated the success of the subsequent step of removal of soluble phases, which indicates that *route 1* (Fig. 4) is the most suitable to obtain the zirconia. Zirconium silicate decomposed into zirconia and silica according to the **reaction 1**, where zirconium dioxide is chemically considered unreactive. However, silica, formed because of the **reaction 1**, reacts with caustic soda to form highly soluble sodium silicates as represented by the **reaction 2**.



The solubility in water of the sodium silicate changes with the temperature: 22.2 g/100 ml at 25 °C and 160 g/100 ml at 80 °C. The samples, solar obtained material, once milled, were treated in reactor with NaOH at 200 °C for 6 h and once removed the reactor from the stove, filtration is immediately made in hot water.

It is possible to see in Table 2 that the product of filtration consists only of ZrO₂ (95%) with minor quantities of either SiO₂ or non-transformed ZrSiO₄. The initial product contained 67.89% ZrO₂ and 30.48% SiO₂ in the form of ZrSiO₄, which indicates a clear concentration

of the zirconium in the product of filtration. On the other hand, determined the zirconium content in the soluble product, it is possible to observe 558 ppm of zirconium, which indicates that most of the zirconium dioxide is recovered in the product of filtration.

3.4. SEM-EDX analysis

Scanning electron microscope was used to characterize the microstructure of the product obtained after the treatment of zirconium silicate sand with concentrated solar energy. The micrographs correspond to the *route 1*, the simple dissociation of the ZrSiO₄ with CSE. Fig. 7 is an example of the microstructure of the bulk material obtained by the direct application of solar radiation, without being crushed for subsequent operations. Fig. 7a corresponds to the bulk material, where it is possible to appreciate pores and holes that might be associated with the formation of silicon monoxide, which oxidized later due to the oxidizing environment where the experiments were conducted. Even when this phase was not detected in the XRD analyses and, therefore, the dissociation of the zircon through this intermediate step cannot be demonstrated, this mechanism is the habitual in the industrial route used to obtain zirconia from the zirconium silicate sand. Fig. 7b corresponds to an image of the bulk material taken at further magnification. There, it is possible to clearly identify to phases: one white as disperse constituent and the other grey that corresponds to the matrix constituent. EDX line analysis in Fig. 7c allows to indicate that white phase is zirconia (ZrO₂) and grey constituent correspond to silica (SiO₂). This is confirmed by EDX mapping in Fig. 7d.

The cooling in the process described in this manuscript is conducted in air and it is, for that reason, very fast. The sample cools from the dissociation temperature to ambient temperature in minutes. This resulted in the appearance of dendritic structure in the treated sample, as reported in Fig. 8.

As it is possible to see in Fig. 9, the grains of zirconia have rounded morphology and a size <5 μm. The short duration of the treatment and the fast-cooling rates impeded the development of grains of greater size.

The microstructure of the product of filtration appears in Fig. 10. The microstructure, as deduced from the EDX mapping, corroborates the XRD results as it comprises only sodium, silicon, and oxygen in the elemental analysis. The characteristic morphology of the zirconia cannot be observed in the microstructure.

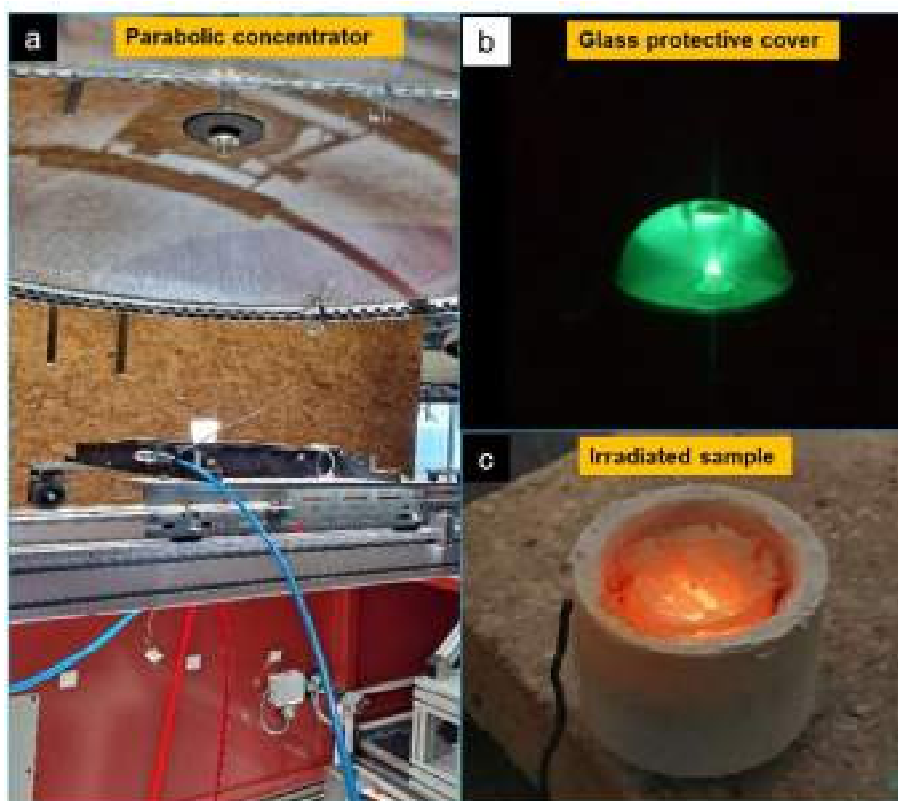


Fig. 3. (a) Image of the 1.5 m in diameter parabolic concentrator located in Font Roméu-Odeillo-Via and belonging to the PROMES-CNRS; (b) Irradiated sample with glass protective cover (seen through a security lens); (c) Sample in the focal point after irradiation next to thermocouple.

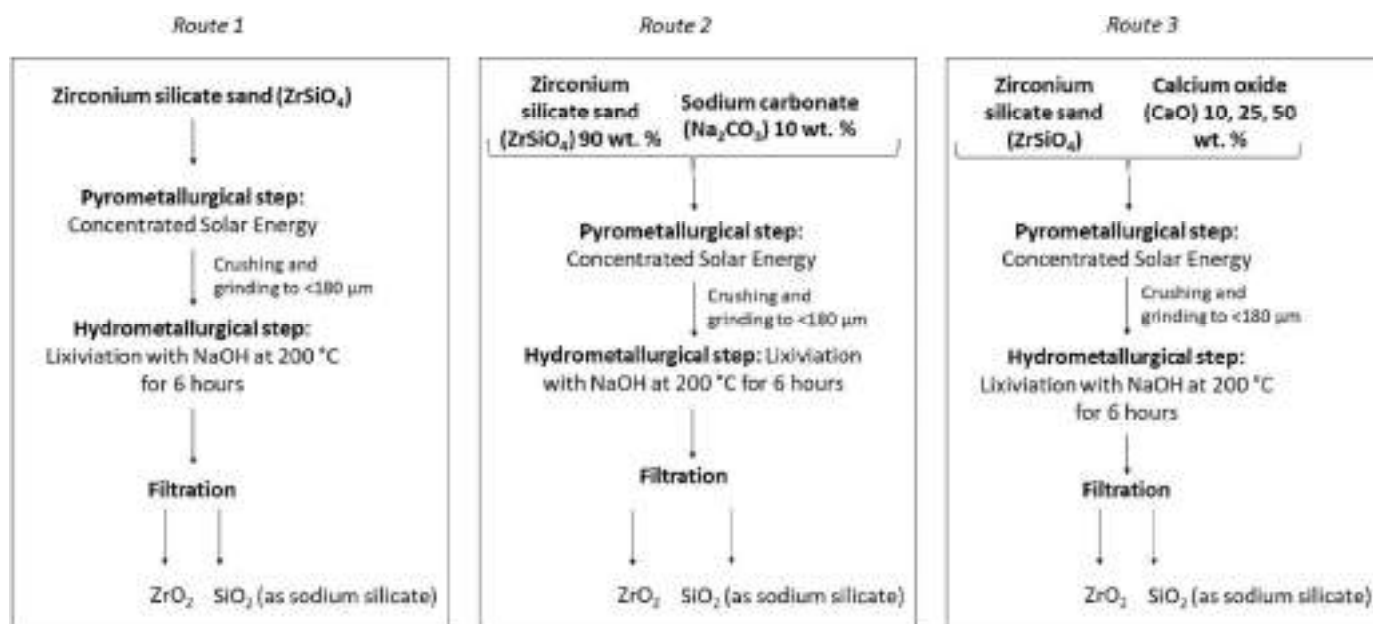


Fig. 4. Schematic diagram of three different routes considered to obtain the zirconia using solar energy, considering the expected results.

4. Discussion

Solar energy might be a suitable manner of achieving the decomposition of several compounds (carbonates (Flamant et al., 1980; Meier et al., 2004; Abanades and André, 2018; Tescari et al., 2018), sulphides (Winkel et al., 2008), oxides (Murray, 1999; Vishnevsky et al., 2013),

or hydroxides (Davis et al., 2017; Kakosimos et al., 2022)), which is a typical route followed by this technology in the obtaining of metals (i.e., zinc) or metal oxides (i.e., calcium oxide). However, the decomposition of silicates is a field yet to be explored and, therefore, this manuscript has proposed for the first time the thermal dissociation of zirconium silicate, to produce zirconium dioxide, which is an oxide with a wide

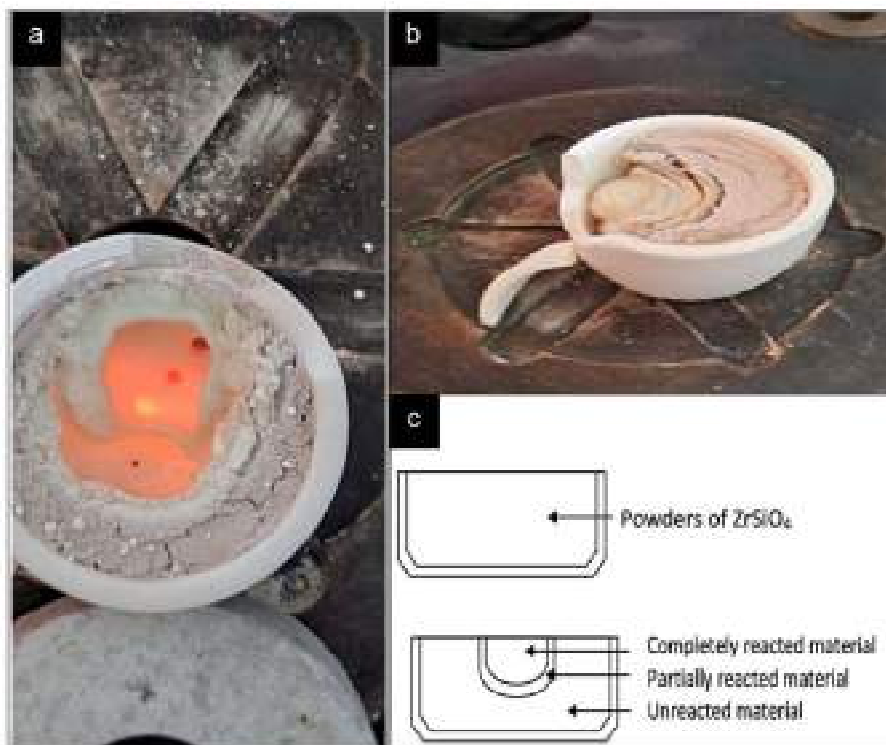


Fig. 5. (a) Sample just after the removal of the sample from below the solar beam; (b) Sample once cold; (c) Schematic representation of unirradiated and irradiated powders.

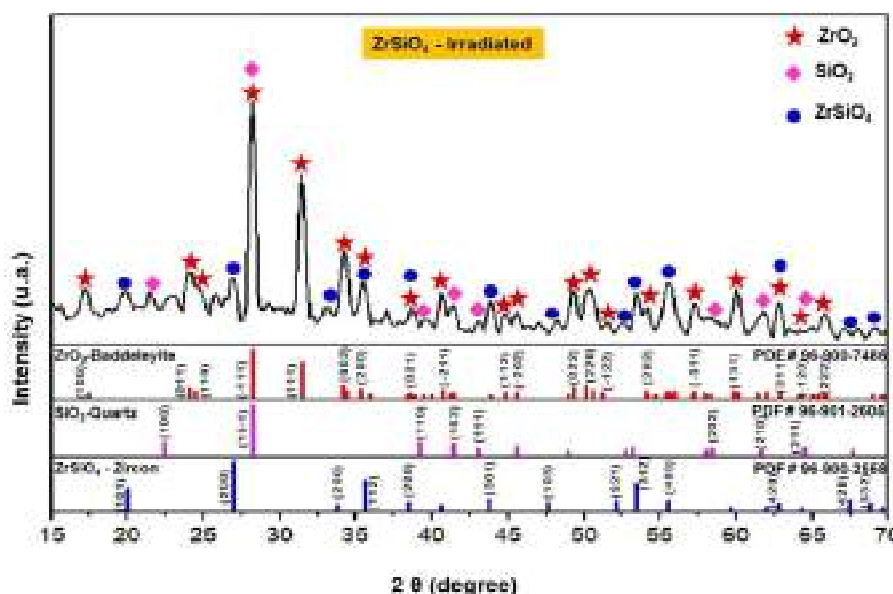


Fig. 6. Sample once treated under solar beam: Route 1.

range of applications in different fields, particularly in that of ceramics and bio-ceramics.

The production of the zirconia, or zirconium dioxide (ZrO₂), is usually carried from zirconium silicate sand, or zircon (ZrSiO₄), due to the abundance and distribution on earth crust. There are other alternative less available minerals, as baddeleyite (ZrO₂), which would be the most attractive due to the composition, or catapleite ((Na₂Ca)ZrSiO₃O₉·2H₂O), zirkelite ((Ca,Fe)(Zr,Ti)₂O₅), wholerite (NaCa₂(Zr,Nb)Si₂O₈(O,OH,F)), among others, which have less zirconium oxide content in their formulation (30.5–31.5, 51.7–59.9 and 15.6–17.6 wt % ZrO₂,

respectively). The ZrO₂ content in the zircon approaches 65 wt %, which becomes it in one of the minerals with the greatest zirconium dioxide contents, as it is possible to check in the composition of the zircon sand used in this manuscript and, it is, for that reason, the ore for ZrO₂ production.

As it was reported in the introduction of the manuscript, there are different methods to obtain the ZrO₂ from the ZrSiO₄. The thermal decomposition of the silicate seems, at first sight, the best option. Nevertheless, the temperature for the thermal dissociation of ZrSiO₄ was assessed at 1673 ± 10 °C, where a eutectic point can be found in the

Table 2
X-ray fluorescence results for solar dissociation of zircon.

%	Solar decomposition	Product of filtration
ZrO ₂	67.89	94.73
HfO ₂	0.89	1.27
SiO ₂	30.48	2.25
Fe ₂ O ₃	0.27	0.15
Na ₂ O	<0.01	<0.01
TiO ₂	0.14	0.13
CaO	0.36	0.42

ZrO₂–SiO₂ binary diagram in Fig. 11. The decomposition of the zircon occurs by solid-state reaction releasing SiO₂ in the form of intermediate phases with superstoichiometric Si-content, as reported by Kaiser (Kaiser et al., 2008). These high temperatures were a challenge for the industry since the energy consumption represents an important part of the production costs. This has led to search about the utilization of reagents to reduce the temperatures required for the thermal dissociation of the zircon. Apart from that, carbon materials are usually employed to reach temperatures even higher than those collected in Table 3 and achieve the formation of silicon monoxide (gas) and directly separate silicon-phase from the zirconia.

Table 3 collects different research works about the dissociation of the ZrSiO₄ into the ZrO₂ and SiO₂. The thermal dissociation of ZrSiO₄ is clearly influenced by the impurities in the raw material, and also that there is a significant dissociation at temperatures well below the melting point of ZrSiO₄ (established in 2277 °C (Nakamori et al., 2017) or 2430 °C (Abdel-Rehim, 2005), depending on the authors, which is related with the incongruent melting point of the zircon). Reaching such temperatures in conventional furnaces is difficult and energy consuming (expensive), as it was already indicated. This way, unconventional high energy methods, as plasma process, have been used to conduct the dissociation of zircon at high temperatures with high energy density and high quenching-cooling rates (avoiding risks of recombination) (Ananthapadmanabhan et al., 1993). This method allowed the high temperatures required for the dissociation of the zircon without additives (that report problems of undesired phases) but with a significant consumption of energy, which does not overcome the problem of the cost (and

contribution to carbon dioxide emissions). These first research of Ananthapadmanabhan reported a complete dissociation for a power input of 12 kW, while in the research presented in the manuscript maximum power of the parabolic concentrator was 0.9 kW for a maximum of 5 min of treatment. Research has been conducted in this line since the 70s (Evans and Williamson, 1977), which even reached the pilot-plant scale (Wilks et al., 1974) and continues nowadays with the purpose of achieving the in-situ removal of the silica as SiO gas (Yugeswaran et al., 2015; Manikandan et al., 2021a). Plasma technology is considered as a competing alternative to concentrated solar power (CSP) regarding the characteristics of the process (power, flux density, surface area, and temperature). Already in 1999, Flamant and colleagues made a comparison between the different high flux emerging technologies, which can be observed in Table 4 (Flamant et al., 1999). Nevertheless, the source of energy is directly renewable in the case of solar energy, and, in the case of plasma, it might be still considered as

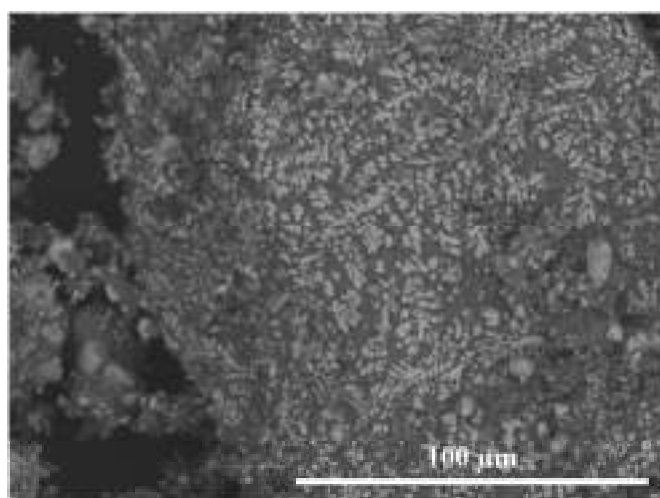


Fig. 8. Dendritic structure in the samples treated with concentrated solar energy, which is the result of the fast-cooling rates.

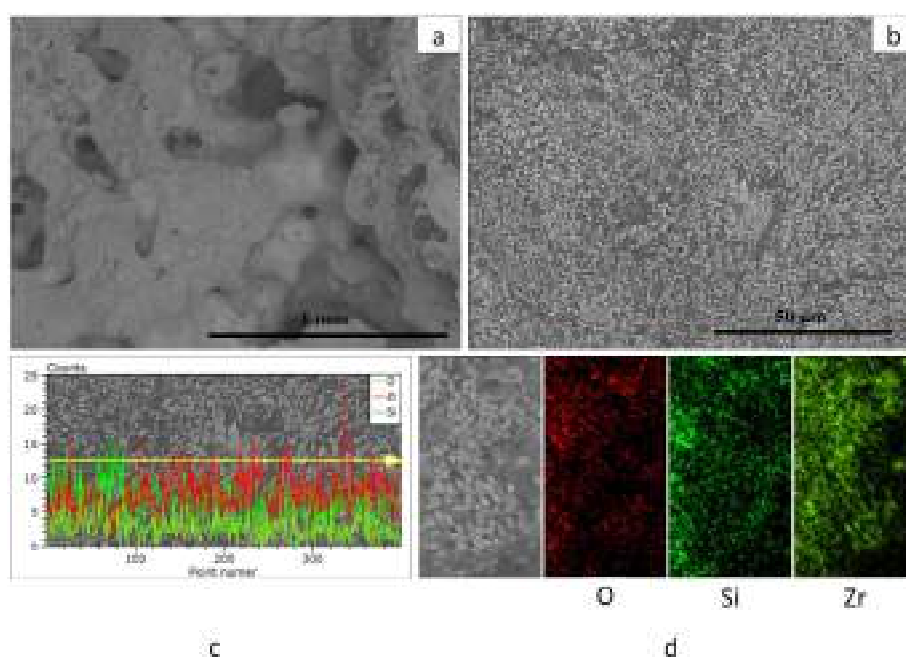


Fig. 7. (a) Image of the bulk material after the treatment with concentrated solar energy; (b) Image in detail of the sample treated with CSE: white, zirconia; grey, silica; (c) EDX line scan.

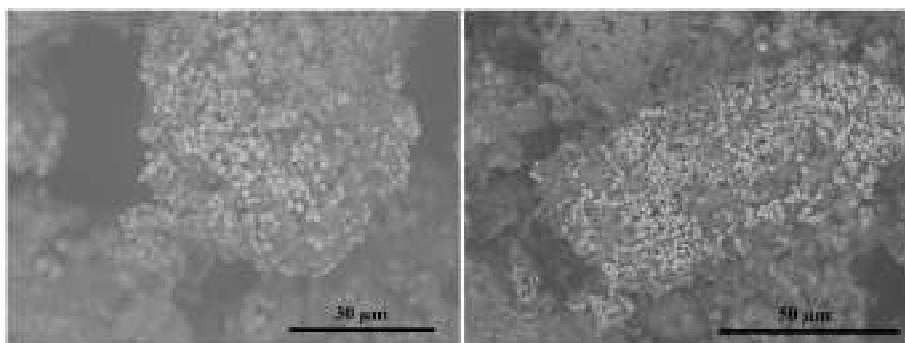


Fig. 9. Microstructure of the zirconia grains in white with rounded microstructure and small size.

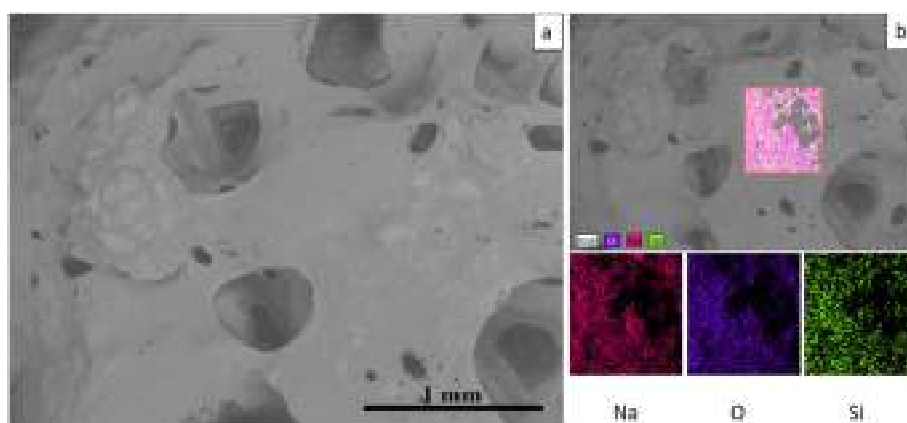


Fig. 10. (a) SEM micrograph of the residue of filtration; (b) Mapping: oxygen, purple; sodium, pink; silicon, light green. (For interpretation of the references to colour in this figure legend, the reader is referred to the Web version of this article.)

contributing to climate change (electricity). This way, electricity generation is still a contributor to carbon dioxide emissions. The CO₂ emission intensity (g CO₂/kWh), calculated as the ratio of CO₂ emissions from public electricity production (as a share of CO₂ emissions from public electricity and heat production related to electricity production), and gross electricity production, was in 2022 of 275 g CO₂/kWh. Therefore, the utilization of CSE in zircon dissociation is the best alternative to accomplish the goal of the European Union of being climate-neutral by 2050 with net-zero greenhouse gas emissions, and reducing emissions by at least 55% by 2030 compared with levels of 1990, Regulation (EU) 2021/1119 of the European Parliament and of the Council of June 30, 2021 establishing the framework for achieving climate neutrality and amending Regulations (EC) No 401/2009 and (EU) 2018/1999 ('European Climate Law').

Solar energy, when concentrated with the suitable methods allows reaching temperatures >3000 °C (Table 4), which are sufficient for most of the processes used to produce materials. There are nowadays different issues that hinder the deployment of this technology in a larger scale:

- the limited research in this field,
- and, the cost of the concentrating systems (mirrors),

among others. Therefore, temperature in the case of concentrated solar energy is not a problem for the process of zircon dissociation, although knowing the exact temperature just below the solar beam is not possible-easy in this type of processes, the same as it is difficult to control the radiation that is applied to the sample in processes based on the direct application of the solar radiation to the sample. However, the burning of the thermocouple located close to the crucible walls (>1400 °C), at 2–3 mm from the solar beam, confirmed that temperatures reached in the zone affected by the beam were sufficient for the

thermal dissociation of the ZrSiO₄. A better control of the temperature and flux density is important in the case of samples that require from a strict control of the temperature, but not in this case.

Different reagents are used for the industrial processing of zircon to extract zirconium dioxide at temperatures well below the temperatures required for the solid-state dissociation of the zircon (Abdel-Rehim, 2005). This is important in the cases where high temperatures involve more expensive equipment and greater consumption of energy. This way, methods traditionally employed to reduce the temperatures required for the decomposition of the zircon are to use sodium carbonate (900–1200 °C), sodium hydroxide (650–750 °C) (Menon et al., 1980; Manhique et al., 2003; Mukhachev et al., 2023), or combinations CaO–NaOH or KOH–NaOH (Abdelkader et al., 2008). The decomposition without supporting reagents, as seen in Table 3, requires from further temperatures >1750 °C (Farnworth et al., 1981). Alternatively, potassium hexafluorosilicate allows decomposing zircon into zirconia and silica at temperatures above 700 °C (Nielsen et al., 2000). ZrSiO₄ can be also decomposed with alkaline earth metal oxides as CaO or MgO–CaO (El-Tawil et al., 1999). Within this line, some experimental work was conducted in this project with Na₂CO₃ and CaO, using concentrated solar energy.

Hence, the effect of adding sodium carbonate on zircon treated under solar beam was studied by XRD analysis, and the sample of 90 wt% ZrSiO₄ + 10 wt% Na₂CO₃ was considered. From Fig. 12, we can observe the ZrSiO₄ phase, and the dissociation of phases found and discussed in Fig. 6 (ZrO₂ and SiO₂). Also, in this sample peaks were observed at 2θ = 19.498, 22.774, 27.576, 31.028, 33.774, 42.265, 44.409, 46.516, 46.860, 51.132, 52.683, 64.128, 66.673 and 67.659° which can be assigned respectively to the (104), (113), (20–4), (116), (300), (1010), (21–8), (226), (2,0–10), (2110), (410), (42–4), (21–14), (514) planar reflections of the hexagonal Na₄Zr₂Si₃O₁₂ phase (formation of a complex

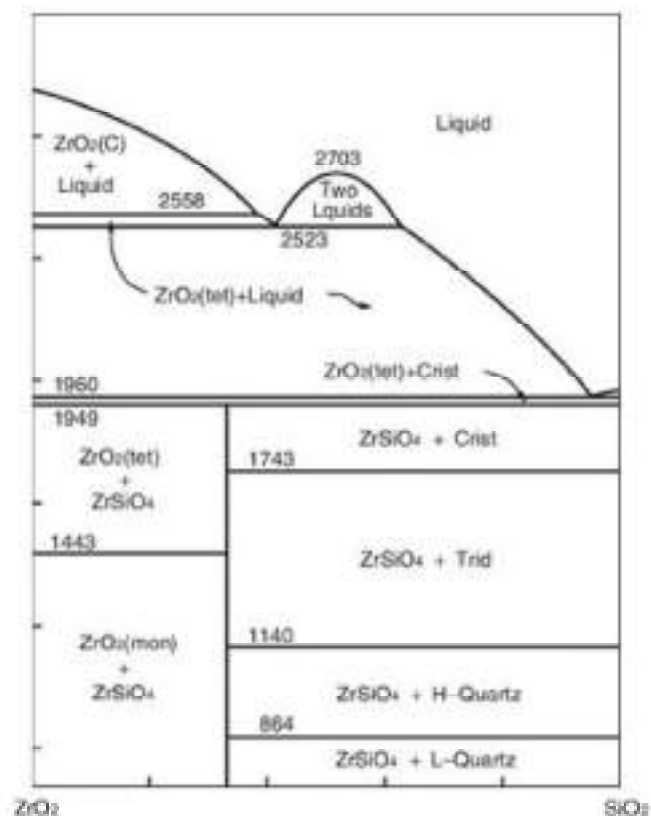


Fig. 11. ZrO_2 - SiO_2 binary diagram (Suzuki et al., 2005).

Table 3

Dissociation temperatures and melting point of the zircon according to different authors (Kaiser et al., 2008; Ayala, 1989).

Researchers	Year	Temperature (°C)	Remarks
Washburn and Libman	1920	2550	Congruent melting
Matignon	1923	2000	Dissociation
Barlett	1931	1450	Dissociation
Heindl	1933	1800	Dissociation
Zhirnowa	1934	2430	Congruent melting
Bauer	1939	1650	Dissociation
Geller and Lang	1945	1775	Incongruent melting
Stott and Hilliard	1946	1500–1750	Dissociation depending on purity
Geller and Lang	1945	1775	Incongruent melting
Curtis and Sowman	1953	1540	Solid-state dissociation
Toropov and Galakhov	1956	1540	Solid-state dissociation
Cocco and Schromek	1958	1720	Incongruent melting
Butterman and Foster	1967	1676	Solid-state dissociation
Anseau, Biloque, Fierens	1976	>1525–1634	Solid-state dissociation
Klute and Woermann	1982	1681 ± 5	Solid-state dissociation
Kanno	1989	1650–1700	Solid-state dissociation
Kocyan and Meulenber	1997	>1550	Solid-state dissociation
Levin	2001	1550	Solid-state dissociation
Pavlik and Holland	2001	1285	Solid-state dissociation
O'Neill	2003	1667	Solid-state dissociation

zirconium and sodium silicates, reported by Manhique and collaborators (Manhique et al., 2003), these planes were identified and indexed comparing with PDF 96-152-7313.

On the other hand, the samples of 90 wt % $ZrSiO_4$ + 10 wt % CaO; 75 wt % $ZrSiO_4$ + 25 wt % CaO and 50 wt % $ZrSiO_4$ + 50 wt % of CaO were

studied microstructurally through XRD analyses (see Fig. 13). This figure shows that with 10 and 25 wt% of CaO, characteristic peaks of phases of ZrO_2 and SiO_2 were also detected as in previous samples studied (in Figs. 6 and 12). However, it is worth nothing that from 25 wt % CaO, the formation of a new phase was evident at $2\theta = 30.137$ and 50.243° assigned to the cubic structure $Ca_{0.16}Zr_{0.86}O_{1.86}$ (non-stoichiometric calcium zirconate) with reflections at (111) and (022).

With higher amounts of CaO (50 wt% $ZrSiO_4$ + 50 wt% CaO), it was evident that the zirconia (ZrO_2) and silica (SiO_2) were consumed to form other phases and their respective peaks were present in less intensity or were not evident. Obviously, the silica went into solid solution with the calcium (forming $Ca_2(SiO_4)$) and the zirconia formed with the calcium, $CaZrO_3$ and $Ca_{0.16}Zr_{0.86}O_{1.86}$. Zircon ($ZrSiO_4$) peaks and only one SiO_2 peak, were also detected.

The $CaZrO_3$ peaks were detected at $2\theta = 22.094$, 31.446 , 45.068 , 50.741 and 65.636° with their respective planar reflections at (010), (011), (020), (021) and (022). These peaks match the standard pattern for the mineral calcium zirconate (PDF 96-154-2030, cubic crystal system). Likewise, peaks of calcium silicate $Ca_2(SiO_4)$, were detected at $2\theta = 18.348$, 24.886 , 31.095 , 32.060 , 37.188 and 45.267° with their crystallographic plans in (100), (002), (102), (110), (200) and (202). The diffraction pattern of $Ca_2(SiO_4)$ matches the standard (PDF 96-153-5812, hexagonal crystal system).

These compounds found ($CaZrO_3$, $Ca_2(SiO_4)$, $Ca_{0.16}Zr_{0.86}O_{1.86}$ and $Na_4Zr_2Si_3O_{12}$) are detrimental for the recovery of ZrO_2 from the zircon sand in terms related to the solubility in water. The formation of these compounds is a problem habitually observed by other authors attempting the decomposition of zircon by alkali fusion process in conventional furnace. This way, Liu and colleagues (Liu et al., 2016) and Manhique and collaborators (Manhique et al., 2003) observed the formation of water insoluble Na_2ZrSiO_5 and $Na_4Zr_2Si_3O_{12}$ compounds, particularly at high temperatures, which has a clear influence on the extraction of zirconium dioxide from the zircon sand. The formation of calcium zirconate ($CaZrO_3$) is detrimental for the extraction of ZrO_2 from zircon sand, although it is a material used in high temperature applications due to its melting point of $2368^\circ C$ and chemical inertness (Schafföner et al., 2013). The formation of this compound during the treatment of samples $ZrSiO_4$ + CaO, particularly in the sample with 50 wt % CaO, suggests that solar energy might be used in the synthesis of the $CaZrO_3$, although the process is yet to be studied.

The problem emerged from the routes 2 and 3 is that the lack of a strict control of the temperature in the sample together with the addition of phases that exhibit a basic character (sodium carbonate or calcium oxide) while zirconium oxide is amphoteric (more acid nature than the additives) leads to the reaction of these phases to form metastable compounds at high temperature that remain even at room temperature after a fast cooling. This is detrimental to the process and makes route 1 the most adequate to obtain zirconia using concentrated solar energy.

Therefore, after the preliminary experiments that resulted in undesired phases. The route of the thermal dissociation of the zircon was the only considered promising to extract ZrO_2 from zircon sand using solar energy. The product after the treatment with concentrated solar energy consists of a bulk piece with the geometry like that of a hemisphere of approximately 10 mm in diameter, with unreacted and partially reacted material adhered. The product comprised, according to X-ray diffraction results, ZrO_2 (monoclinic, baddeleyite) and SiO_2 (quartz), which are the stable phases at low temperature according to the ZrO_2 - SiO_2 binary diagram in Fig. 11. The thermal dissociation of the $ZrSiO_4$ to give these products is thermodynamically favorable based on the calculations made with the software HSC5.1 collected in Table 5. The value of the free energy is negative for all the studied temperatures and becomes even more negative as the temperature increases, which indicates that the process is thermodynamically favorable. These values validate the experimental results. This Table 5 also provides the enthalpy of reaction, which is the minimum required for the dissociation process, although CSE provides significantly greater quantities of energy due to the

Table 4

Comparison of plasma, and solar energy in terms of power, flux density, temperatures, efficiency, and cost.

Technology	Typical power (kW)	Flux density (W/cm ²)	Surface area (cm ²)	Temperature (K)	Overall efficiency (%)	Capital cost (kECU/kW)
Plasma	10–2000	10 ⁴	≈100	>5000	25	0.8–1.5 (50–1000 kW)
Solar	≤1000	10 ³	≈1000	≤3500	60	1.2–1.8 (50–1000 kW)

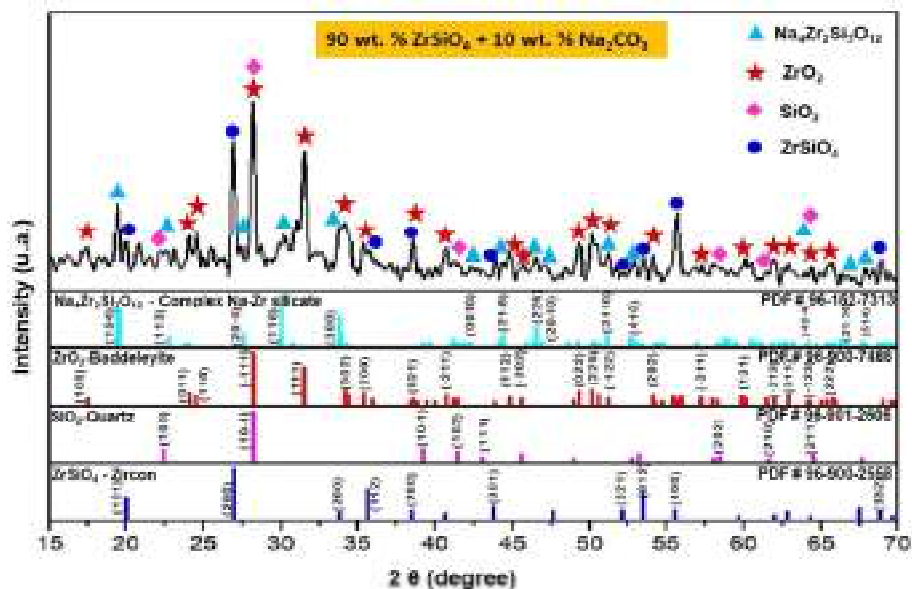


Fig. 12. Sample once treated under solar beam consisting of 90 wt % ZrSiO₄ + 10 wt % Na₂CO₃; Route 2.

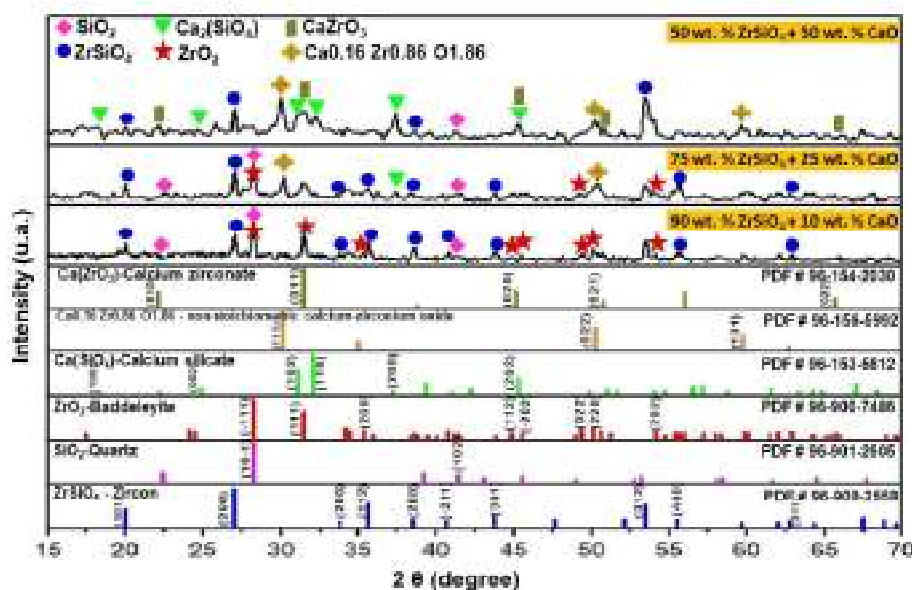


Fig. 13. Sample once treated under solar beam consisting of 90 wt % ZrSiO₄ + 10 wt % CaO; 75 wt % ZrSiO₄ + 25 wt % CaO; 50 wt % ZrSiO₄ + 50 wt % CaO; Route 3.

impossibility of controlling (in the proposed experiments) the values of applied radiation.

Therefore, it was checked that the thermal dissociation of zircon sand using concentrated solar energy is possible. It was also verified that the subsequent extraction of the silica resulted from the decomposition is also possible after a treatment of 6 h at 200 °C in conventional furnace using pressurized reactor. This silica appears as a sodium silicate in agreement with the reaction 2, where the zirconium content is in the

order of magnitude of ppm. This minor zirconium losses are associated to the experimental work. Most of the impurities in the initial raw material are present on the treated product. The practice habitually conducted to improve the purity of the zirconia, consists of an additional acid lixiviation. The second process was carried out in electric furnace although it could be conducted in a furnace heated with solar energy since the required temperatures are easily attainable using this renewable energy source. Fig. 14 collects a scheme of the proposed process to

Table 5
Thermodynamic values for the solid-state solar dissociation of the $ZrSiO_4$.

T (°C)	ΔH (kJ)	ΔS (J/K)	ΔG (kJ)	K	Log(K)
1400	24.875	18.237	-5.638	1.50E+00	0.176
1450	24.924	18.266	-6.551	1.58E+00	0.199
1500	24.981	18.298	-7.465	1.66E+00	0.22
1550	25.045	18.334	-8.381	1.74E+00	0.24
1600	25.116	18.373	-9.298	1.82E+00	0.259
1650	25.194	18.414	-10.218	1.90E+00	0.278
1700	25.278	18.457	-11.14	1.97E+00	0.295

obtain zirconium dioxide using solar energy.

The energy transition is an important issue in advanced economies and, particularly, in the European Union. The EU aims to be climate-neutral by 2050 with net-zero greenhouse gas emissions and reducing emissions by at least 55% by 2030 compared with levels of 1990, Regulation (EU) 2021/1119 of the European Parliament and of the Council of June 30, 2021 establishing the framework for achieving climate neutrality and amending Regulations (EC) No 401/2009 and (EU) 2018/1999 ('European Climate Law'). This objective obliges industries to search alternatives to the current technologies used in the production of materials, which involve the utilization of fossil fuels or electricity (having a CO_2 emission intensity, as reported). The emission of CO_2 is taxed as a method used to oblige industries to reduce carbon dioxide emissions by improving processes or adapting installations to best available techniques, whether the budget dedicated to this purpose wants to be reduced. This tax has an important economic impact in high CO_2 release industries, particularly those whose processes employ carbon or carbon products. The value of this tax, as an average value from January to March 2023, is 87.06 €/ton CO_2 . Its value has sharply increased in the last years, from the 24.75 €/ton CO_2 in 2020 to 80.87 €/ton CO_2 in 2022. This has a repercussion in the cost of the electricity, translated later to the customers and, in the considered case, to the industry of the zirconia production.

Solar energy is virtually free. This is in fact not totally truth because the installation costs would have a significant impact on the cost of the produced material. Purohit and Brooks (2021a) pointed out that one of the challenges is still the capital cost associated to the mirror system and general concentrated solar energy infrastructure. The heliostat field contributes to 40–50% of the capital cost of the solar thermal metallurgical system (Purohit and Brooks, 2021). The improvement in the

thermal efficiency of the reactors together with the reduction in the cost of the heliostats will contribute to reduce the capital cost (Purohit and Brooks, 2021). Additionally, the spread of the solar thermal technologies will also lead to a reduction in cost. For instance, the photovoltaic modules varied the price from 105.7 \$ per watt in 1975 to 0.2 \$ per watt in 2020 according to the *International Energy Agency* when the technology widely spread, and equipment started to be produced in series.

The economic impact and the avoided carbon dioxide emissions are calculated considering the parameters collected in Table 6. The calculations are made considering the generation of the electricity for the process, which has a CO_2 emission intensity, thus representing an environmental impact. The energy supplied in the process by solar energy (E_{solar}) in the experiments conducted in this project is calculated as indicated in equation (1) considering an average incident radiation of 915 W/m^2 (DNI) with an efficiency of 60% (μ , Table 4), a factor of concentration of 15000 (f_c), a treatment duration of 5 min (t) and an area of beam impact of 10 mm in diameter of 0.00007854 m^2 (a_{beam}).

$$E_{solar} = DNI \cdot f_c \cdot a_{beam} \cdot \mu \cdot t = 915 \frac{W}{m^2} \cdot 15000 \cdot 0.00007854 m^2 \cdot 0.6 \cdot 5 \text{ min} \cdot \frac{1 \text{ hour}}{60 \text{ min}}$$

$$= 646.8 \text{ Wh} = 0.65 \text{ kWh}$$

Equation 1

The quantity of material treated in each cycle (W_{ZrO_2}) is calculated as in equation (2) considering a density of zircon silicate sand of 4.56 g/cm^3 (ρ_{ZrSiO_4}) and a volume of material treated in each cycle of 262 mm^3 (hemisphere of 5 mm in radius, $V_{treated}$).

Table 6
Parameters of the solar production process.

Parameter	Value		
Energy per kilogram (kWh/kg ZrO_2)	92		
Electricity price for industrial costumers (€/kWh)	0.10		
Plant size (ton/hour) (Meier et al., 2005)	0.5 (1 MW_{th})	2.5 (5 MW_{th})	12.7 (25 MW_{th})
Operating time (hours/year)	2400		
CO_2 emission intensity (g CO_2/kWh)	275		

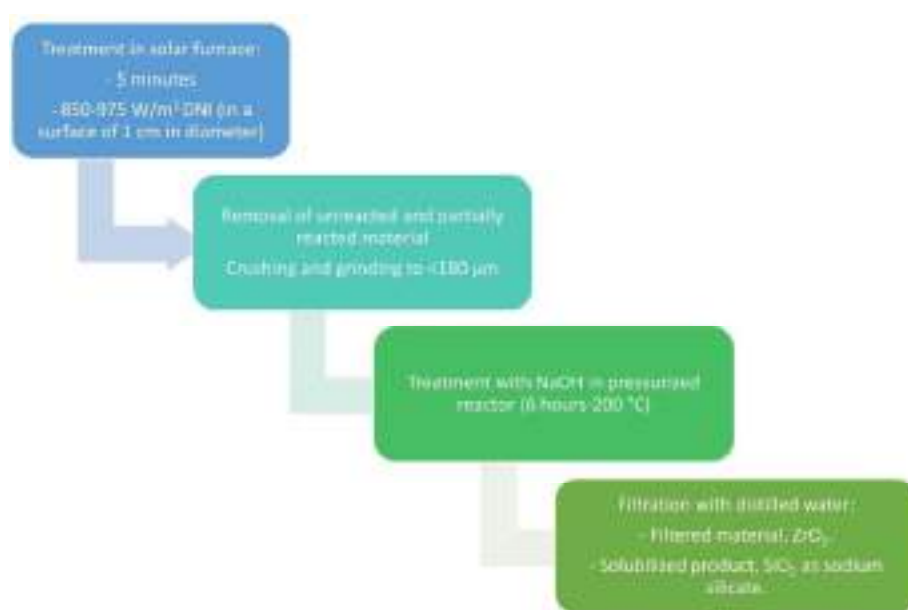


Fig. 14. Scheme of the solar assisted process to obtain zirconia.

$$W_{\text{ZrO}_2} = \rho_{\text{ZrSiO}_4} \cdot V_{\text{treated}} = 4.56 \frac{\text{g ZrSiO}_4}{\text{cm}^3} \cdot 262 \text{mm}^3 \cdot \frac{1 \text{ mol ZrSiO}_4}{183.3 \text{ g ZrSiO}_4} \cdot \frac{1 \text{ mol ZrO}_2}{1 \text{ mol ZrSiO}_4} \cdot \frac{123.2 \text{ g ZrO}_2}{1 \text{ mol ZrO}_2} = 0.812 \text{ g ZrO}_2 \quad \text{Equation 2}$$

This involves an energy supplied of 812 kWh/kg ZrO₂. This energy is significantly greater than that required by the **reaction 1** according to the data in **Table 5**: 0.056 kWh/kg ZrO₂, which assuming an efficiency of 60% would increase up to around 0.1 kWh/kg ZrO₂. It is necessary to consider that radiation during the process carried out with the solar furnace in the experiments of this manuscript was no longer controlled with shutter. If the process is conducted with the competition of electricity, the relative carbon dioxide emissions (rel_{CO₂}) would be, considering the real energy requirements for zircon decomposition, calculated in agreement to **equation (3)**:

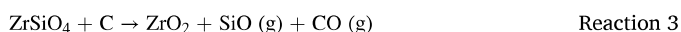
$$\text{rel}_{\text{CO}_2} = 0.1 \frac{\text{kWh}}{\text{kg ZrO}_2} \cdot 275 \frac{\text{g CO}_2}{\text{kWh}} = 27.5 \frac{\text{g CO}_2}{\text{kg ZrO}_2} = 0.0275 \frac{\text{kg CO}_2}{\text{kg ZrO}_2} \quad \text{Equation 3}$$

which for a small plant producing a total of 1200 tons/year would represent a CO₂ emissions avoidance (e_{elec}) of around 33 tons. The energy consumed in the production of the zirconia (E_{con}) in a year is calculated as indicated by **equation (4)**:

$$E_{\text{con}} = 0.1 \frac{\text{kWh}}{\text{kg ZrO}_2} \cdot 1200000 \text{ kg ZrO}_2 = 120000 \text{ kWh} \quad \text{Equation 4}$$

which represent a cost (cos_{elec}), whether the energy would have used in the form of electricity, of 12000 €.

It is necessary to consider that one of the common routes used to produce zirconia involves the utilization of carbon to promote the formation of silicon monoxide gas and directly obtain the zirconia as a separated phase. For instance, studies conducted with thermal plasma process employed 1.5–2 mol of carbon (Manikandan et al., 2021b), thus representing additional carbon dioxide emissions. The emissions associated with the formation of silicon monoxide can be calculated from the **reaction 3**:



where the CO is oxidized to CO₂ before the release to the atmosphere due to health issues. Excesses of carbon indicated in (Meier et al., 2005) of 1.5–2 mol C per mol of ZrO₂ (0.15–0.2 kg C per kg of ZrO₂) lead to carbon dioxide emissions associated with the process of 0.55–0.75 kg CO₂ per kg of ZrO₂. This way, the carbon dioxide emissions avoidance in terms of coke consumption (e_{coke}) would be obtained with **equation (5)**:

$$e_{\text{coke}} = 0.55 (0.75) \frac{\text{kg CO}_2}{\text{kg ZrO}_2} \cdot 1200000 \text{ kg ZrO}_2 \cdot \frac{1 \text{ ton CO}_2}{1000 \text{ kg CO}_2} = 660 - 900 \text{ tons CO}_2 \quad \text{Equation 5}$$

which represent a cost (cos_{tax}, corresponding to the taxes due to the carbon dioxide emission in the EU of 87.06 €/ton CO₂) of 57500–78500 €. The carbon (coke) requirements (C_{coke}) would be determined with **equation (6)**:

$$C_{\text{coke}} = 0.15 (0.2) \frac{\text{kg C}}{\text{kg ZrO}_2} \cdot 1200000 \text{ kg ZrO}_2 \cdot \frac{1 \text{ ton C}}{1000 \text{ kg C}} = 180 - 240 \text{ tons C} \quad \text{Equation 6}$$

which for a coke price of 2500 €/ton coke, would represent a cost (cos_{coke}) of 450000–600000 €.

Three scenarios are considered in **Table 7**, corresponding to different plant sizes. It is possible to infer from the results presented in **Table 7** that the greatest carbon dioxide emissions avoidance would be achieved in the term of coke, which is used to promote the formation of silicon

monoxide. This aspect also represents a significant economic impact in the production of zirconia from the zircon. Therefore, solar thermal dissociation followed by leaching with NaOH seems to be a better alternative to the route of thermal dissociation with carbon-coke to produce silicon monoxide in the case of using the traditional route. Even when both routes consume chemical reagents, the route of the NaOH does not produce carbon dioxide emissions and the price of this material is much lower than that of the metallurgical coke (NaOH: 500–1000 €/ton; coke: 2500–3000 €/ton). This route also avoids the taxes corresponding to carbon dioxide emissions. The term corresponding to electricity is much lower both in carbon dioxide emissions and cost. Therefore, the carbon dioxide emissions avoidance ranges from around 700–950 tons CO₂ in the small plant to around 17600–23700 tons CO₂ in the big plant, which would have an economic impact ranging from around 0.05–0.08 M€ to 1.5–2 M€. On the other hand, the potential economic savings would range from around 0.5 M€ to 17.5 M€.

Nevertheless, despite the importance of the potential economic (and environmental) savings, it is necessary to consider other important issues as the cost of development and installation, as well as the transportation costs from the places with suitable irradiation conditions, to clearly analyze the interest of the process from the economics point of view. This way, detailed manuscript of Meier and colleagues about the lime calcination process (Meier et al., 2005) includes some of these aspects to estimate the price of solar produced lime. They obtained a difference between the solar produced lime and the commercial lime of 2–3 times. Therefore, the development and installation costs still play an important role in the deployment of solar-based processes for the synthesis of materials. As a reference, Flamant and colleagues (Flamant et al., 1999) estimated in 1999 the capital cost (kECU/kW) for solar technology in 1.2–1.8 for plants of 50–1000 kW, which updated with the inflation (around 65% from 1999) would be around 2–3 kECU/kW nowadays. Considering this value, the capital costs for the plant of small size would greatly exceed the 3M€ determined with this data, since it is necessary to conduct different studies about the success of the process at different levels of TRL (Technology Readiness Level) before reaching the commercial scale, including the design of the appropriate reactors. Other issue still important in the implementation of solar assisted technologies in the production of materials is the lack of data of pilot plants operating in real conditions for extended periods. This would allow researchers and industrials to know the real useful number of hours and available power in a year to produce the corresponding material. All these operations would consume economic resources and time. Anyway, these studies exceed the purpose of this investigation, which was to demonstrate the feasibility of using concentrated solar energy in the thermal dissociation of zirconium silicate sand and provide a preliminary information about the importance of this process in the

Table 7
Environmental and economic impact of the utilization of solar based process.

Plant size (ton/hour)	0.5 (1 MW _{th})	2.5 (5 MW _{th})	12.7 (25 MW _{th})
e _{elec} (tons CO ₂)	33	165	838.2
e _{coke} (tons CO ₂)	660–900	3300–4500	16764–22860
E _{con} (kWh)	120000	600000	3048000
C _{coke} (tons coke)	120–240	900–1200	4572–6096
cos _{elec} (€)	12000	60000	304800
cos _{coke} (€)	450000–600000	2250000–3000000	11430000–15240000
cos _{tax} (€)	57500–78500	287300–391800	1459500–1990200

mitigation of carbon dioxide emissions in the industry of ceramics.

5. Conclusions

Concentrated solar energy is a suitable alternative to provide the energy-heat necessary for different processes of the industry of materials, including the field of synthesis of materials by thermal dissociation. The great advantage in this line of CSE is the possibility of supplying heat without releasing pollutants and as main cost the installations required for the concentration of the solar energy. Several examples of application of CSE in the thermal dissociation of materials can be found in the literature, including metal oxides to produce metals (for commodities or metal fuels), carbonates as limestone to obtain calcium oxide (for cement industry), hydroxides as bayerite to obtain alumina (for the aluminum industry) or sulphides as those sulphur and zinc to obtain copper and zinc (as environmentally friendly alternative without releasing pollutants).

Nevertheless, the thermal dissociation of silicates was not explored in the literature. Therefore, this manuscript has proposed for the first time the synthesis of zirconia (ZrO_2) by thermal dissociation of zirconium silicate sand ($ZrSiO_4$), where CSE was used to supply the activation energy and the heat required for the dissociation without releasing pollutants. Three routes were studied by thermal dissociation:

- 100 wt % $ZrSiO_4$.
- 90 wt % $ZrSiO_4$ + 10 wt % Na_2CO_3 .
- $ZrSiO_4$ + 10, 25 or 50 wt % CaO.

The proposed process was divided into two steps:

- Pyrometallurgical, where CSE was directly used to provide the energy required for the process.
- Hydrometallurgical: crushed and grinded material to $<180 \mu m$ was treated with NaOH in pressurized reactor for 6 h at $200^\circ C$.

The best alternative was the thermal dissociation of the zirconium silicate sand, without additives, since the utilization of CaO or Na_2CO_3 involved reaction of these phases with the ZrO_2 to form complex phases that hinder the separation or extraction of the zirconia. The two stages process treating 100 wt % $ZrSiO_4$ gave as a result separated products: monoclinic zirconia with 95% purity and sodium silicate.

As future perspectives of research in this line, the objective should be to take advantage of the high temperatures that it is possible to reach with the competition of concentrated solar energy to achieve the formation of silicon monoxide gas and directly obtain the zirconia and silicon (monoxide) separated in a single step. It would be also interesting to study the possibility of treating powders of $ZrSiO_4$ in reactors especially conceived for this purpose.

Different economic-environmental scenarios about the potential application of CSE in the production of zirconia from zirconium silicate sand suggest that the solar-based process is a potential alternative for the climate change mitigation and increase of the sustainability in the industry of ceramic materials synthesis.

CRedit authorship contribution statement

Daniel Fernández-González: Conceptualization, Methodology, Validation, Formal analysis, Resources, Data curation, Writing – original draft, Supervision, Project administration, Funding acquisition. **Juan Piñuela-Naval:** Writing – review & editing, Funding acquisition. **Íñigo Ruiz-Bustinza:** Investigation, Funding acquisition. **Carmen González-Gasca:** Investigation, Funding acquisition. **Cristian Gómez-Rodríguez:** Data curation, Visualization. **Linda Viviana García Quiñonez:** Data curation, Visualization. **Adolfo Fernández:** Writing – review & editing. **Luis Felipe Verdeja:** Conceptualization, Methodology, Resources, Writing – review & editing, Supervision, Funding acquisition, All

authors have read and agreed to the published version of the manuscript.

Declaration of competing interest

The authors declare that they have no known competing financial interests or personal relationships that could have appeared to influence the work reported in this paper.

Data availability

No data was used for the research described in the article.

Acknowledgement

Daniel Fernández-González acknowledges the grant (Juan de la Cierva-Formación program) FJC2019-041139-I funded by MCIN/AEI/10.13039/501100011033 (Ministerio de Ciencia e Innovación, Agencia Estatal de Investigación).

Juan Piñuela Naval acknowledges the Programa “Severo Ochoa” of Grants for Research and Teaching of the Principality of Asturias for the funds received for the elaboration of the Ph. D. Thesis (Ref: BP20 041).

We thank the PROMES-CNRS (PROcédés Matériaux et Energie Solaire- Centre National de la Recherche Scientifique) for providing access to its installations, the support of its scientific and technical staff, and the financial support of the SFERA-III project (Grant Agreement No 823802).

References

- Abanades, S., André, L., 2018. Design and demonstration of a high temperature solar-heated rotary tube reactor for continuous particles calcination. *Appl. Energy* 212, 1310–1320. <https://doi.org/10.1016/j.apenergy.2018.01.019>.
- Abdel-Rehim, A.M., 2005. A new technique for extracting zirconium form Egyptian zircon concentrate. *Int. J. Miner. Process.* 76 (4), 234–243. <https://doi.org/10.1016/j.minpro.2005.02.004>.
- Abdelkader, A.M., Daher, A., El-Kashef, E., 2008. Novel decomposition method for zircon. *J. Alloys Compd.* 460 (1–2), 577–580. <https://doi.org/10.1016/j.jallcom.2007.06.032>.
- Ahmadinejad, M., Moosavi, R., 2022. Energy and exergy evaluation of a baffled-nanofluid-based photovoltaic thermal system (PVT). *Int. J. Heat Mass Tran.* 203, 123775 <https://doi.org/10.1016/j.ijheatmasstransfer.2022.123775>.
- Ahmadinejad, M., Soleimani, A., Gerami, A., 2022a. Performance enhancement of a photovoltaic thermal (PVT) system with sinusoidal fins: a quasi-transient energy-exergy analysis. *Int. J. Green Energy* 20 (9), 978–996. <https://doi.org/10.1080/15435075.2022.2131434>.
- Ahmadinejad, M., Soleimani, A., Gerami, A., 2022b. The effects of a novel baffle-based collector on the performance of a photovoltaic/thermal system using SWCNT/Water nanofluid. *Therm. Sci. Eng. Prog.* 34, 101443 <https://doi.org/10.1016/j.tsep.2022.101443>.
- Ananthapadmanabhan, P.V., Sreekumar, K.P., Iyer, K.V., Venkatramani, N., 1993. Plasma thermal dissociation of Indian zircon. *J. Alloys Compd.* 196, 251–254.
- Author, N., 1978. Zirconium compounds in paint. *Pigment Resin Technol.* 7 (9), 15–17. <https://doi.org/10.1108/eb041421>.
- Ayala, J.M., 1989. Obtención y caracterización de los óxidos de zirconio sintetizados mediante disgregación básica del silicato de zirconio. Ph.D. Thesis. University of Oviedo.
- Chen, J., Xiao, J., Zhang, Y., Wei, Y., Han, B., Li, Y., Zhang, A., Li, N., 2020. Corrosion mechanism of $Cr_2O_3-Al_2O_3-ZrO_2$ refractories in a coal-water slurry gasifier: a post-mortem analysis. *Corrosion Sci.* 163, 108250 <https://doi.org/10.1016/j.corsci.2019.108250>.
- Chen, F., Wu, Y.-R., Wu, J.-M., Zhu, H., Chen, S., Hua, S.-B., He, Z.-X., Liu, C.-Y., Xiao, J., Shi, Y.-S., 2021. Preparation and characterization of $ZrO_2-Al_2O_3$ bioceramics by stereolithography technology for dental restorations. *Addit. Manuf.* 44, 102055 <https://doi.org/10.1016/j.addma.2021.102055>.
- Chuayboon, S., Abanades, S., 2022. Solar carbo-thermal and methano-thermal reduction of MgO and ZnO for metallic powder and syngas production by green extractive metallurgy. *Processes* 10 (1), 154. <https://doi.org/10.3390/pr10010154>.
- Costa-Oliveira, F.A., Rosa, L.G., Fernandes, J.C., Rodríguez, J., Cañadas, I., Magalhaes, T., Shohji, N., 2015. Nitriding VI-group metals (Cr, Mo and W) in stream of NH_3 gas under concentrated solar irradiation in a solar furnace at PSA (Plataforma Solar de Almería). *Sol. Energy* 114, 51–60. <https://doi.org/10.1016/j.solener.2015.01.028>.
- Costa-Oliveira, F.A., Fernandes, J.C., Galindo, J., Rodríguez, J., Cañadas, I., Vermelhudo, V., Nunes, A., Rosa, L.G., 2019. Portland Cement Clinker Production Using Concentrated Solar Energy – A Proof-Of-Concept Approach, vol. 183, pp. 677–688. <https://doi.org/10.1016/j.solener.2019.03.064>.

- Cruz-Fernandes, J., Guerra, L., Martínez, D., Rodríguez, J., Shohoji, N., 1998. Influence of gas environment on synthesis of silicon carbide through reaction between silicon and amorphous carbon in a solar furnace at PSA (Plataforma Solar de Almería). *J. Ceram. Soc. Jpn.* 106, 839–841. <https://doi.org/10.2109/jcersj.106.839>.
- Davis, D., Müller, F., Saw, W.L., Steinfeld, A., Nathan, G.J., 2017. Solar-driven alumina calcination for CO₂ mitigation and improved product quality. *Green Chem.* 19 (13), 2992–3005. <https://doi.org/10.1039/C7GC00585G>.
- El-Tawil, S.Z., El-Barawy, K.A., Francis, A.A., 1999. Cubic zirconia from zircon sand by firing with CaO/MgO mixture. *J. Ceram. Soc. Jpn.* 107 (3), 193–198. <https://doi.org/10.2109/jcersj.107.193>.
- Evans, A.M., Williamson, J.P.H., 1977. Composition and microstructure of dissociated zircon produced in a plasma furnace. *J. Mater. Sci.* 12 (4), 779–790. <https://doi.org/10.1007/BF00548171>.
- Farnworth, F., Jones, S., McAlpine, I., 1981. *The production, properties and uses of zirconium chemicals*. In: Thompson, R. (Ed.), *Speciality Inorganic Chemicals Special Publication*, vol. 40. Royal Society of Chemistry, London, pp. 247–283, 1981.
- Fernández-González, D., 2023. A State-Of-The-Art Review on Materials Production and Processing Using Solar Energy. *Mineral Processing and Extractive Metallurgy Review*. <https://doi.org/10.1080/08827508.2023.2243008> (in press).
- Fernández-González, D., Ruiz-Bustintza, I., González-Gasca, C., Piñuela-Naval, J., Mochón-Castaños, J., Sancho-Gorostiza, J., Verdeja, L.F., 2018. Concentrated solar energy applications in materials science and metallurgy. *Sol. Energy* 170, 520–540. <https://doi.org/10.1016/j.solener.2018.05.065>.
- Fernández-González, D., Prazuch, J., Ruiz-Bustintza, I., González-Gasca, C., Piñuela-Naval, J., Verdeja, L.F., 2018b. Iron metallurgy via concentrated solar energy. *Metals* 8 (11), 873. <https://doi.org/10.3390/met8110873>.
- Fernández-González, D., Prazuch, J., Ruiz-Bustintza, I., González-Gasca, C., Piñuela-Naval, J., Verdeja, L.F., 2018d. Solar synthesis of calcium aluminates. *Sol. Energy* 171, 658–666. <https://doi.org/10.1016/j.solener.2018.07.012>.
- Fernández-González, D., Prazuch, J., Ruiz-Bustintza, I., González-Gasca, C., Piñuela-Naval, J., Verdeja, L.F., 2019a. Transformations in the Mn-O-Si system using concentrated solar energy. *Sol. Energy* 184, 148–152. <https://doi.org/10.1016/j.solener.2019.04.004>.
- Fernández-González, D., Prazuch, J., Ruiz-Bustintza, I., González-Gasca, C., Piñuela-Naval, J., Verdeja, L.F., 2019b. Transformations in the Si-O-Ca system: silicon-calcium via solar energy. *Sol. Energy* 181, 414–423. <https://doi.org/10.1016/j.solener.2019.02.026>.
- Fernández-González, D., Prazuch, J., Ruiz-Bustintza, I., González-Gasca, C., Piñuela-Naval, J., Verdeja, L.F., 2019c. The treatment of Basic Oxygen Furnace (BOF) slag with concentrated solar energy. *Sol. Energy* 180, 372–382. <https://doi.org/10.1016/j.solener.2019.01.055>.
- Fernández-González, D., Prazuch, J., Ruiz-Bustintza, I., González-Gasca, C., Gómez-Rodríguez, C., Verdeja, L.F., 2021. Recovery of copper and magnetite from copper slag using concentrated solar power (CSP). *Metals* 11 (7), 1032. <https://doi.org/10.3390/met11071032>.
- Flamant, G., Hernandez, D., Bonet, C., Traverse, J.-P., 1980. Experimental aspects of the thermochemical conversion of solar energy. Decarbonation of CaCO₃. *Sol. Energy* 24 (4), 385–395. [https://doi.org/10.1016/0038-092X\(80\)90301-1](https://doi.org/10.1016/0038-092X(80)90301-1).
- Flamant, G., Ferriere, A., Laplace, D., Monty, D., 1999. Solar processing of materials: opportunities and new frontiers. *Sol. Energy* 66 (2), 117–132. [https://doi.org/10.1016/S0038-092X\(98\)00112-1](https://doi.org/10.1016/S0038-092X(98)00112-1).
- Grech, J., Antunes, E., 2019. Zirconia in dental prosthetics: a literature review. *J. Mater. Res. Technol.* 8 (5), 4956–4964. <https://doi.org/10.1016/j.jmrt.2019.06.043>.
- Hanawa, T., 2020. Zirconia versus titanium in dentistry: a review. *Dent. Mater. J.* 39 (1), 24–36. <https://doi.org/10.4012/dmj.2019-172>.
- Hu, C., Sun, J., Long, C., Wu, L., Zhou, C., Zhang, X., 2019. Synthesis of nano zirconium oxide and its application in dentistry. *Nanotechnol. Rev.* 8 (1), 396–404. <https://doi.org/10.1515/ntrev-2019-0035>.
- Kaiser, A., Lobert, M., Telle, R., 2008. Thermal stability of zircon (ZrSiO₄). *J. Eur. Ceram. Soc.* 28 (11), 2199–2211. <https://doi.org/10.1016/j.jeurceramsoc.2007.12.040>.
- Kakosimos, K.E., Fhatima, N., Al-Rawashdeh, M., 2022. Conversion of boehmite to higher alumina phases by direct irradiation with concentrated light: numerical modelling and experimental verification. *AIP Conf. Proc.* 2445, 130005. <https://doi.org/10.1063/5.0085732>.
- Kraiser, A., Lobert, M., Telle, R., 2008. Thermal stability of zircon (ZrSiO₄). *J. Eur. Ceram. Soc.* 28 (11), 2199–2211. <https://doi.org/10.1016/j.jeurceramsoc.2007.12.040>.
- Kusiorowski, R., 2020. MgO-ZrO₂ refractory ceramics based on recycled magnesia-carbon bricks. *Construct. Build. Mater.* 231, 117084. <https://doi.org/10.1016/j.conbuildmat.2019.117084>.
- Liu, J., Song, J., Qi, T., Zhang, C., Qu, J., 2016. Controlling the formation of Na₂ZrSiO₅ in alkali fusion process for zirconium oxychloride production. *Adv. Powder Technol.* 27 (1), 1–8. <https://doi.org/10.1016/j.apt.2015.08.005>.
- Lorusso, F., Noubissi, S., Francesco, I., Rapone, B., Khater, A.G.A., Scarano, A., 2020. *Materials* 13 (23), 5534. <https://doi.org/10.3390/ma13235534>.
- Manhique, A., Kwela, Z., Focke, W.W., 2003. De Wet process for the beneficiation of zircon: optimization of the alkali fusion step. *Ind. Eng. Chem. Res.* 42, 777–783.
- Manikandan, S., Kuberan, A., Yugeswaran, S., Ananthapadmanabhan, P.V., Pandiyaraj, K.N., Shajan, X.S., Balraju, P., 2021a. Silica-free zirconia from zircon mineral by thermal plasma processing. *Mater. Manuf. Process.* 36 (2), 188–199. <https://doi.org/10.1080/10426914.2020.1832681>.
- Manikandan, S., Kuberan, A., Yugeswaran, S., Ananthapadmanabhan, P.V., Pandiyaraj, K.N., Shajan, X.S., Balraju, P., 2021b. Silica-free zirconia from zircon mineral by thermal plasma processing. *Mater. Manuf. Process.* 36 (2), 188–199. <https://doi.org/10.1080/10426914.2020.1832681>.
- Meier, A., Bonaldi, E., Cella, G.M., Lipinski, W., WUILLEMIN, D., Palumbo, R., 2004. Design and experimental investigation of a horizontal rotary reactor for the solar thermal production of lime. *Energy* 29 (5–6), 811–821. [https://doi.org/10.1016/S0360-5442\(03\)00187-7](https://doi.org/10.1016/S0360-5442(03)00187-7).
- Meier, A., Gremaud, N., Steinfeld, A., 2005. Economic evaluation of the industrial solar production of lime. *Energy Convers. Manag.* 46 (6), 905–926. <https://doi.org/10.1016/j.enconman.2004.06.005>.
- Menon, P., Juneja, J., Krishnan, T., 1980. Decomposition of zircon by soda ash sintering process. *Am. Ceram. Soc. Bull.* 59, 635–639.
- Mukhachev, A., Shevchenko, V., Yelatontsev, D., 2023. Zircon processing in sodium carbonate melt. *IOP Conf. Ser. Earth Environ. Sci.* 1156, 012019. <https://doi.org/10.1088/1755-1315/1156/1/012019>.
- Murray, J.P., 1999. Aluminum production using high-temperature solar process heat. *Sol. Energy* 66 (2), 133–142. [https://doi.org/10.1016/S0038-092X\(99\)00011-0](https://doi.org/10.1016/S0038-092X(99)00011-0).
- Murray, J.P., Flamant, G., Roos, C.J., 2006. Silicon and solar-grade silicon production by solar dissociation of Si₃N₄. *Sol. Energy* 80, 1349–1354. <https://doi.org/10.1016/j.solener.2005.11.009>.
- Nakamori, F., Ohishi, Y., Muta, H., Kurosaki, K., Fukumoto, K.-I., Yamanaka, S., 2017. Mechanical and thermal properties of ZrSiO₄. *J. Nucl. Sci. Technol.* 54 (11), 1267–1273. <https://doi.org/10.1080/00223131.2017.1359117>.
- Navarro, A., Cañadas, I., Rodríguez, J., Martínez, D., 2012. Leaching characteristics of mercury mine wastes before and after solar thermal desorption. *Environ. Eng. Sci.* 29 (10), 915–928. <https://doi.org/10.1089/ees.2010.0017>.
- Nawn, G., Pace, G., Lavina, S., Vezzù, K., Negro, E., Bertasi, F., Polizzi, S., Di Noto, V., 2015. Nanocomposite membranes based on polybenzimidazole and ZrO₂ for high-temperature proton exchange membrane fuel cells. *ChemSusChem* 8 (8), 1381–1393. <https://doi.org/10.1002/cssc.201403049>.
- Nielsen, R.H., Schlewitz, J.H., Nielsen, H., 2000. Zirconium and zirconium compounds. In: Kirk-Othmer Encyclopedia of Chemical Technology. <https://doi.org/10.1002/0471238961.26091803.a01.pub3>.
- Padilla, I., Romero, M., Robla, J.I., López-Delgado, A., 2021. Waste and solar energy: an eco-friendly way for glass melting. *ChemEngineering* 5 (2), 16. <https://doi.org/10.3390/chemengineering5020016>.
- Palla, S., Sharma, P., Rao, M.V.R., Ramakrishna, S., Vanguri, S., Mohapatra, B.N., 2022. Solar thermal treatment of phosphogypsum and its impact on the mineralogical modification for effective utilization in cement production. *J. Build. Eng.* 51, 104218. <https://doi.org/10.1016/j.jobbe.2022.104218>.
- Park, S.-W., Seo, Y.-J., Lee, W.-S., 2008. A study on the chemical mechanical polishing of oxide film using a zirconia (ZrO₂)-mixed abrasive slurry (MAS). *Microelectron. Eng.* 85 (4), 682–688. <https://doi.org/10.1016/j.mee.2007.12.049>.
- Purohit, S., Brooks, G.A., 2021. Chapter Five - application of solar thermal energy to metallurgical processes. *Adv. Chem. Eng.* 58, 197–246. <https://doi.org/10.1016/bs.ache.2021.10.007>.
- Rambabu, K., Bharath, G., Arangadi, A.F., Velu, S., Banat, F., Show, P.L., 2020. ZrO₂ incorporated polysulfone anion exchange membranes for fuel cell applications. *Int. J. Hydrogen Energy* 45 (54), 29668–29680. <https://doi.org/10.1016/j.ijhydene.2020.08.175>.
- Salman, O.A., Khraishi, N., 1988. Thermal decomposition of limestone and gypsum by solar energy. *Sol. Energy* 41 (4), 305–308. [https://doi.org/10.1016/0038-092X\(88\)90025-4](https://doi.org/10.1016/0038-092X(88)90025-4).
- Schaffner, S., Aneziris, C.G., Berek, H., Hubáľková, J., Priese, A., 2013. Fused calcium zirconate for refractory applications. *J. Eur. Ceram. Soc.* 33 (15–16), 3411–3418. <https://doi.org/10.1016/j.jeurceramsoc.2013.07.008>.
- Schünemann, F.H., Galárraga-Vinueza, M.E., Magini, R., Fredel, M., Silva, F., Souza, J.C.M., Zhang, Y., Henriques, B., 2019. Zirconia surface modifications for implant dentistry. *Mater. Sci. Eng. C* 98, 1294–1305. <https://doi.org/10.1016/j.msec.2019.01.062>.
- Selby, J.H., 2007. *The Industrial Uses of Zircon and Zirconia, and the Radiological Consequences of These Uses*. INTERNATIONAL ATOMIC ENERGY AGENCY, Radiation Protection and NORM Residue Management in the Zircon and Zirconia Industries, 2007. IAEA, Vienna. Safety Reports Series No. 51.
- Seo, J.-Y., Oh, D., Kim, D.-J., Kim, K.-M., Kwon, J.-S., 2020. Enhanced mechanical properties of ZrO₂-Al₂O₃ dental ceramic composites by altering Al₂O₃ form. *Dent. Mater.* 36 (4), e117–e125. <https://doi.org/10.1016/j.dental.2020.01.014>.
- Shohoji, N., Costa-Oliveira, F.A., Guerra-Rosa, L., Cruz-Fernandes, J., Magalhaes, T., Caldeira-Coelho, M., Rodríguez, J., Cañadas, I., Ramos, C., Martínez, D., 2012. Synthesising carbo-nitrides of some d-group transition metals using a solar furnace at PSA. *Mater. Sci. Forum* 730–732, 153–158. <https://doi.org/10.4028/www.scientific.net/MSF.730-732.153>.
- Shohoji, N., Costa-Oliveira, F.A., Galindo, J., Rodríguez, J., Cañadas, I., Cruz-Fernandes, J., Guerra-Rosa, L., 2021. Synthesis of non-cubic nitride phases of v-group metals (V, Nb, and Ta) from metal powders in stream of NH₃ gas under concentrated solar radiation. *ChemEngineering* 5 (2), 19. <https://doi.org/10.3390/chemengineering5020019>.
- Suzuki, M., Sodeoka, S., Inoue, T., 2005. Structure control of plasma sprayed zircon coating by substrate preheating and post heat treatment. *Mater. Trans.* 46 (3), 669–674. <https://doi.org/10.2320/matertrans.46.669>.
- Tescari, S., Moumin, G., Bulfin, B., de Oliveira, L., Schaefer, S., Overbeck, N., Willsch, C., Spence, C., Thelen, M., Roeb, M., Sattler, C., 2018. Experimental and numerical analysis of a solar rotary kiln for continuous treatment of particle material. *AIP Conf. Proc.* 2033, 130014. <https://doi.org/10.1063/1.5067148>.
- Tzouganatos, N., Matter, R., Wieckert, C., Antrekwitsch, J., Gamroth, M., Steinfeld, A., 2013. Thermal recycling of waelz oxide using concentrated solar energy. *JOM (J. Occup. Med.)* 65, 1733–1743. <https://doi.org/10.1007/s11837-013-0778-x>.
- Verdeja, L.F., Sancho, J.P., Ballester, A., González, R., 2014. *Refractory and Ceramic Materials, first ed.* Síntesis, Madrid, Spain.

- Vinodh, R., Purushothaman, M., Sangeetha, D., 2011. Novel quaternized polysulfone/ ZrO_2 composite membranes for solid alkaline fuel cell applications. *Int. J. Hydrogen Energy* 36 (12), 7291–7302. <https://doi.org/10.1016/j.ijhydene.2011.03.056>.
- Vishnevetsky, I., Ben-Zvi, R., Epstein, M., Barak, S., Rubin, R., 2013. Solar carboreduction of alumina under vacuum. *JOM (J. Occup. Med.)* 65, 1721–1732. <https://doi.org/10.1007/s11837-013-0777-y>.
- Weinberg, A.V., Goeuriot, D., Poirier, J., Varona, C., Chaucherie, X., 2021. Mullite–zirconia composite for the bonding phase of refractory bricks in hazardous waste incineration rotary kiln. *J. Eur. Ceram. Soc.* 41 (1), 995–1002. <https://doi.org/10.1016/j.jeurceramsoc.2020.08.014>.
- Wieckert, C., Olalde, G., Kräupl, S., Guillot, E., Santén, S., Osinga, T., Epstein, M., Frommherz, U., Steinfeld, A., 2006. A 300 kW solar chemical pilot plant for the carbothermic production of zinc, International Solar Energy Conference. 2006 International Solar Energy Conference 7–13. <https://doi.org/10.1115/ISEC2006-99027>. ISEC2006, 8-13 July 2006.
- Wilks, P.H., Ravinder, P., Grant, C.L., Pelton, P.A., Downer, R.J., Talbot, M.L., 1974. Commercial production of submicron ZrO_2 via plasma. *Chem. Eng. World* 9 (3), 59–65.
- Winkel, L., Wochele, J., Ludwig, C., Alkneit, I., Sturzenegger, M., 2008. Decomposition of copper concentrates at high-temperatures: an efficient method to remove volatile impurities. *Miner. Eng.* 21 (10), 731–742. <https://doi.org/10.1016/j.mineng.2008.02.003>.
- Xuekun, T., Chaojie, Z., Lei, Z., Fei, Z., Quanli, J., Xinhong, L., Xiangchong, Z., 2023. Preparation of ZrB_2 - ZrO_2 -SiC composite powder by carbothermal reduction from zircon. *China's Refract.* 32 (1), 25–29. <https://doi.org/10.19691/j.cnki.1004-4493.2023.01.005>.
- Yugeswaran, S., Ananthapadmanabhan, P.V., Thiagarajan, T.K., Ramachandran, K., 2015. Plasma dissociation of zircon with concurrent in-flight removal of silica. *Ceram. Int.* 41 (8), 9585–9592. <https://doi.org/10.1016/j.ceramint.2015.04.020>.
- Zanelli, C., Dondi, M., Raimondo, M., Guarini, G., 2010. Phase composition of alumina–mullite–zirconia refractory materials. *J. Eur. Ceram. Soc.* 30 (1), 29–35. <https://doi.org/10.1016/j.jeurceramsoc.2009.07.016>.

Artículo 2: Solar assisted production of MgAl_2O_4 from Bayer process electrofilter fines as source of Al_2O_3 .



Solar Assisted Production of MgAl_2O_4 from Bayer Process Electrofilter Fines as Source of Al_2O_3

Daniel Fernández-González¹ · Juan Piñuela-Noval¹ · Íñigo Ruiz-Bustanza² · Carmen González-Gasca³ · Cristian Gómez-Rodríguez⁴ · Linda Viviana García-Quiñonez⁵ · Adolfo López-Liévano⁴ · Adolfo Fernández¹ · Luis Felipe Verdeja⁶

Received: 27 June 2023 / Accepted: 11 February 2024 / Published online: 21 February 2024
© The Minerals, Metals & Materials Society 2024

Abstract

Compared with conventional high-temperature methods based on electricity and fossil fuels, concentrated solar energy route offers distinct advantages in terms of mitigating emissions of contaminants and shortening processing times. Nevertheless, solar-based route also encounters challenges in producing significant quantities of materials, although the deployment of this technology is still conditioned by the limited investigation in the field. This study presents a novel high-temperature process based on solar energy to produce MgAl_2O_4 spinel, which employs as source of Al_2O_3 a waste from the aluminum industry: waste alumina fines from the Bayer process. First, mixtures were prepared by mechanical mixing in a molar ratio 1:1 in agreement with the $\text{MgO}-\text{Al}_2\text{O}_3$ binary phase diagram. Then, synthesis of the MgAl_2O_4 spinel was conducted by static experiments (5 min) with direct application of concentrated solar energy (1150 W/cm^2) at temperatures greatly exceeding $1800 \text{ }^\circ\text{C}$ as reported by ANSYS software. Wastes from three Bayer process factories were studied, which exhibited after the synthesis process a good crystallinity. The carbon dioxide emissions avoidance would range from the 200 to 500 tons of CO_2 /year in the case of a small plant producing 1000 tons/year to 5000 to 12,000 tons of CO_2 /year in the case of a commercial plant producing 25,000 tons/year, thus contributing to mitigate climate change. The proposed process might lead to smaller

The contributing editor for this article was M. Akbar Rhamdhani.

✉ Daniel Fernández-González
d.fernandez@cinn.es

¹ Nanomaterials and Nanotechnology Research Center (CINN-CSIC), Universidad de Oviedo (UO), Principado de Asturias (PA), Avda. de la Vega, 4-6, 33940 El Entrego, Asturias, Spain

² Departamento de Ingeniería Geológica y Minera, Escuela Técnica Superior de Ingenieros de Minas y Energía, Universidad Politécnica de Madrid, 28003 Madrid, Spain

³ Universidad UNIE, Calle Arapiles, 14, 28015 Madrid, Spain

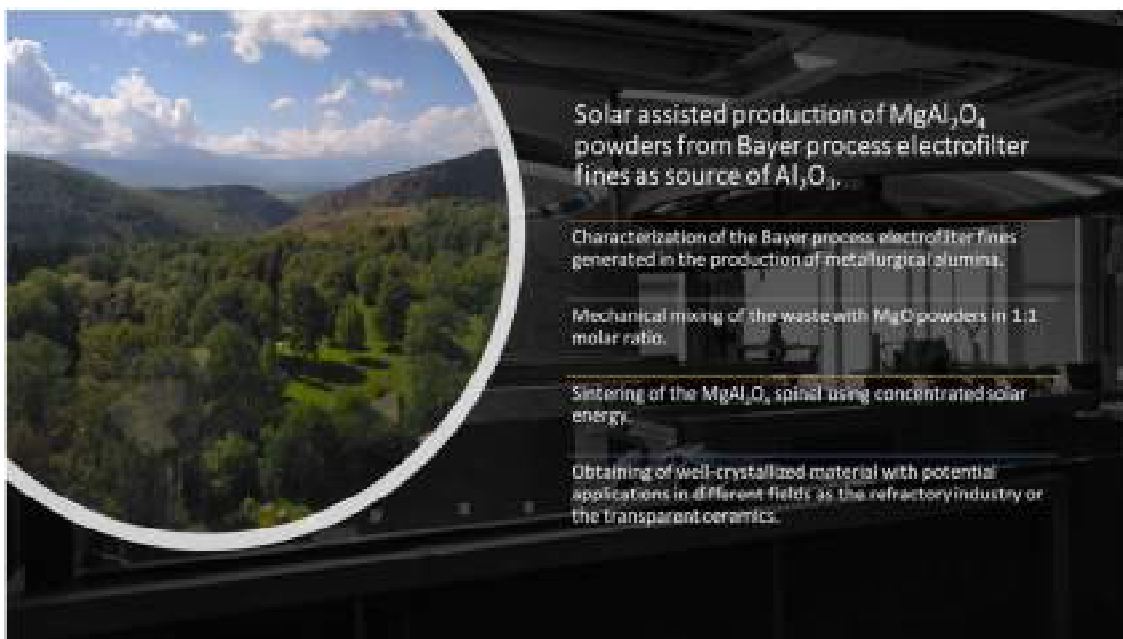
⁴ Departamento de Mecánica, Facultad de Ingeniería, Universidad Veracruzana, Campus Coatzacoalcos, Av. Universidad Km 7.5 Col. Santa Isabel, 96538 Coatzacoalcos, Veracruz, Mexico

⁵ Centro de Investigación en Recursos Energéticos y Sustentables (CIRES), Universidad Veracruzana, Av. Universidad Veracruzana km 7.5, Col. Santa Isabel I, 96538 Coatzacoalcos, Veracruz, Mexico

⁶ Department of Materials Science and Metallurgical Engineering, School of Mines, Energy and Materials, Universidad de Oviedo, 33004 Oviedo, Uviéu, Asturias, Spain

volume of wastes in the aluminum industry, while the MgAl_2O_4 may be used as raw material in the numerous fields based on the chemical, thermal, dielectric, mechanical and optical properties.

Graphical Abstract



Keywords MgAl_2O_4 spinel · Concentrated solar energy · Metallurgy · Circular economy · Sustainability

Introduction

Aluminum industry, accounting for a smelter production of 68 Mt in 2021 according to the *United States Geological Survey*, is one of the most produced materials [1]. The production of aluminum is carried out by means of a process that involves two main stages, one, called Bayer process, which has as objective to produce alumina from bauxite (consisting of mainly aluminum hydroxides with variable quantities of iron oxides, aluminum clays, kaolinite, and minor amounts of other oxides [2]) and the other, called Hall-Héroult process, which aims at producing aluminum by electrolysis in a molten electrolyte of cryolite. Focusing on the Bayer process, it involves several stages that include the pressure leaching of bauxite ore with aqueous soda solution, precipitation of aluminum hydrate (bayerite) from clean solution and calcination of the hydrate to produce alumina, which is later employed as raw material in the Hall-Héroult process.

Electrofilter fines are a residue generated in this process in quantities of around 5–8% of the final alumina product (approximately 80,000–100,000 tons for a 1.2 Mt alumina plants [3]). It consists of a mixture of different aluminas and alumina hydrates with small particle size that are collected

as a residue in the electrofilter equipment. Different studies were conducted to find an application or extract valuable components from the electrofilter powders generated in the Bayer process, although there is still not any process with a massive implementation in the industry. This way, Bayer process electrofilter fines have been used in the production of ceramic materials as Tutic and collaborators, which obtained mullite ceramics from Bayer electrofilter fines and low kaolinite clay [4], and Sancho-Gorostiaga and others [5], which proposed the utilization of this waste in the manufacture of high temperature structural insulators. Other researchers tried to collect components from the residue as Okudan and collaborators, which attempted to recover gallium and aluminum [6]. For their part, Ayala and Pérez [7] investigated the removal of Se(VI) from aqueous solution using Bayer process electrofilter fines. Finally, other research in this line was conducted by Sancho et al. [8] and Ayala et al. [9], which recycled electrofilter fines as aluminum sulphate for water coagulant uses, Sancho and co-authors [3], which suggested that fines could be recycled as industrial quality aluminum sulphate, alums, and abrasives, and Sancho-Gorostiaga and colleagues [10], which investigated about the removal of copper from aqueous solutions using Bayer process electrofilter fines.

Solar energy, when it is adequately concentrated, offers enormous possibilities in metallurgy and materials science [11]. A recent state-of-the-art review of Fernández-González [12] makes a deep literature survey of the applications of solar energy in the field of materials. Our research group has made intensive work in the application of concentrated solar energy in the synthesis of materials: silicon-calcium [13], where the synthesis of this energy-intensive alloy used in deoxidizing of steels was attempted from mixtures of CaO and Si to avoid carbon dioxide emissions and energy costs, although it was produced in minor quantities associated to the atmosphere of the process; silicon-manganese [14], where the synthesis of this alloy typically used in the production of steels was achieved from mixtures of manganese (IV) oxide and silicon; calcium aluminate cements [15], where the most relevant result was the synthesis of main components of the high alumina (> 75%) calcium aluminate cements using limestone as source of CaO for the process; operations in the field of iron and steels [16], where metallic iron was obtained from iron ore sinter fines reduced by coke with the heat support of solar energy; and, zirconia [17], which was obtained by solar thermal decomposition of zirconium silicate sand and subsequent separation of the ZrO_2 by pressure leaching with NaOH of the silica. Focusing on the aluminum field, solar energy has been applied to reduce the environmental impact by using a zero- CO_2 energy. First investigations in this line can be attributed to J. P. Murray [18], who proposed the direct reduction of Al_2O_3 to aluminum or aluminum–silicon alloy or reduction to AlN or Al_2S_3 that could be more easily electrolyzed with non-consumable electrodes. Several studies were conducted from that moment in line with the production of aluminum by carbothermal reduction with more or less success in the obtaining of metallic aluminum [19–24]. Alternatively, Lytvynenko [25] proposed the utilization of solar energy in the obtaining of aluminum by electrolysis through the Hall-Herault's process using the current of a solar battery and employing solar radiation to heat the cell. In the same line, other researchers proposed the calcination of the aluminum hydroxide to obtain alumina to feed the cell for the electrolysis of aluminum using solar energy [26, 27].

Nevertheless, apart from the potential application of solar energy in the synthesis of materials, there is a growing interest in its application to recycle or recover valuable components from industrial wastes, for instance in the extraction of copper and iron from copper slags [28] or iron from basic oxygen furnace slags [29], due to the possibility of heating without releasing pollutant. The research in this field focuses not only on the recovery of metals from slags but in the immobilization of contaminants, as filter dusts [30, 31] or soil and mine waste samples containing mercury [32–35]. Anyway, the application of solar energy in recycling or recovering metals is the most important line due to the lower temperatures required

in the case of operating with them whether compared with ceramics. Therefore, other researchers aimed at recovering metals (Zn, Fe, Pb and Cu) from electric arc furnace dust (EAFD) and automobile shredder residue (ASR) [36, 37], extracting zinc from Waelz oxide produced during the recycling of galvanized steels [38] or used solar energy to melt aluminum scrap [39–42]. Nevertheless, as a consequence of the high temperatures that can be reached with the competition of solar energy (above 2500 °C [11, 12]) researchers have also attempted to recycle aluminum oxides. This way, studies guided by Padilla and collaborators [43] in the field of aluminum waste were conducted to obtain alumina from boehmite prepared by sol–gel process from an aluminum waste that proceeded from the fine suction system used in the aluminum slag milling operation. The same authors, Padilla and researchers [44], attempted the production glasses also from aluminum wastes, which consisted in a powdered solid trapped in filter sleeves during the slag milling process of the aluminum tertiary industry. Apart from the aluminum residue, these researchers employed other wastes as eggshells and mussel shells as sources of calcium for the glass.

Magnesium aluminate compound is a spinel that is gaining interest in different applications due to the excellent chemical, thermal, dielectric, mechanical and optical properties [45]. Nevertheless, magnesium aluminate spinel is an excellent refractory oxide of great importance as structural ceramic due to the physical, chemical, and thermal properties at normal and elevated temperatures [46]. Different methods can be used to obtain the $MgAl_2O_4$ spinel. These methods include sol–gel reaction [47], gelatin method [48], metal-chitosan complexation [49], thermal decomposition [50], hydrothermal [51], high-energy ball mill [52], microwave assisted combustion [53], organic precursor combustion [54], sonochemical [55], spray pyrolysis [56], spray drying [57], among other processes [47]. Anyway, the most habitual technique to synthesize this spinel is the solid-state reaction from powders of MgO and Al_2O_3 , although the process has several disadvantages including long processing times, need for repetition of several calcination stages, requirement of high temperatures for sintering [46]. Some of these issues might be solved with the application of concentrated solar energy. For that reason, this manuscript proposes a novel method to synthesize $MgAl_2O_4$ from Bayer process electrofilter fines at laboratory scale using concentrated solar energy as potential route to reduce carbon dioxide emissions.

Materials and Methods

Raw Materials

Three different Bayer Process Electrofilter Fines (BPEFs) were used as source of Al_2O_3 in the obtaining of the

MgAl₂O₄ spinel, while the MgO was provided by an industrial supplier. The BPEFs were generated in Bayer process plants located in three different countries: Canada, Ireland, and Spain. The chemical composition was determined by inductively coupled plasma mass spectrometry, while carbon and sulphur contents were obtained by combustion with the equipment CS800 Eltra. Results for the BPEFs are collected in Table 1. The structure of the BPEFs was analyzed by X-ray diffraction, which reported different types of alumina (mainly α - and γ -alumina, whose content was determined by means of the area below the X-ray diffraction pattern) with certain amounts of gibbsite (Al(OH)₃). The carbon content gives a characteristic grey color to the sample. Mean particle size (d_{50}) was determined by photo-sedimentometer Lumosed equipment. The water content in the samples is represented by the Moisture on Ignition (MOI, mass losses when heating the sample up to 550 °C for 2 h) and Lost on Ignition (LOI, mass losses when heating the sample up to 900 °C for 2 h). Additionally, the content in aluminum trihydrate (gibbsite) was determined by thermal analysis technique (Mettler-Toledo DSC822e), under a nitrogen atmosphere (50 ml/min) and at a heating rate of 5 °C/min to determine the endothermic peak corresponding to the hydrate water loss, where patterns with variable contents in gibbsite (from 0.5 to 50%) were employed to obtain the calibration line. This parameter is important because gibbsite is also a source of Al₂O₃ for the spinel although before the reaction with the MgO, the aluminum trihydrate decomposes into Al₂O₃ and H₂O, which leads to problems of decrepitation. Numerical values of the characteristics of the BPEFs are collected in Table 2.

Magnesia was provided by Grupo Peñoles (Mexico). The chemical composition of the magnesia was determined by

X-ray fluorescence spectrometry. Results are collected in Table 3.

Methods

Experiments were carried out in a vertical axis solar furnace located in Font Roméu-Odeillo-Via (France), which belongs to the PROMES-CNRS (PROcédés Matériaux et Energie Solaire-Centre National de la Recherche Scientifique). It consisted in a 1.5 m in diameter parabolic concentrator that is illuminated with flat heliostat, which has a sun tracking system. This way, a maximum concentration ratio of 15,000 in a focal point of ≤ 1.5 cm is achieved. This means that the maximum concentrated power would be 900 W for a 1000 W/m² DNI (Direct Normal Irradiation), achieved with clean skies and parabolic concentrator. Experiments were conducted under a glass hood to avoid the deterioration of the parabolic concentrator with the powders that could leave the sample. Besides, air suction was applied to avoid the deposition of the powders in the glass hood, which would have been detrimental to the process. A scheme of the process appears represented in the Fig. 1.

The route chosen to manufacture the MgAl₂O₄ spinel was the solid-state reaction. Mixtures were prepared in a 1:1 molar ration according to the following chemical reaction:



which according to the binary phase diagram MgO-Al₂O₃ is in the stoichiometric spinel zone. Sintering zone, according to Sarkar and Banerjee [58], occurs in the temperature range 1550–1650 °C, although the formation of the spinel occurs also at greater temperatures as it appears in the phase diagram.

Table 1 Composition of the BPEFs of the three Bayer process factories

(%)	Al ₂ O ₃	Na ₂ O	SiO ₂	Fe ₂ O ₃	CaO	K ₂ O	TiO ₂	MgO	Ga ₂ O ₃	C	S
Canada	87	0.70	<0.04	<0.04	0.03	<0.04	<0.01	<0.01	0.008	0.08	0.02
Ireland	92	0.46	<0.04	<0.04	0.02	<0.04	<0.01	<0.01	0.012	0.14	0.02
Spain	91	0.67	<0.04	<0.04	0.01	<0.04	<0.01	<0.01	0.012	0.14	0.02

Table 2 Characteristics of the BPEFs of the three Bayer process factories

	MOI (%)	LOI (%)	α -Alumina	γ -Alumina	Gibbsite (%)	d_{50} (μm)
Canada	10.0	2.30	19.0	49.0	29.0	7.8
Ireland	5.3	1.60	17.0	65.5	14.5	5.3
Spain	6.6	0.7	33.0	32.2	18.0	8.7

Table 3 Characteristics of the MgO

MgO (%)	CaO (%)	SiO ₂ (%)	Al ₂ O ₃ (%)	Fe ₂ O ₃ (%)	B ₂ O ₃ (%)	d_{50} (μm)
98.5	1	0.2	0.15	0.13	0.01	<45

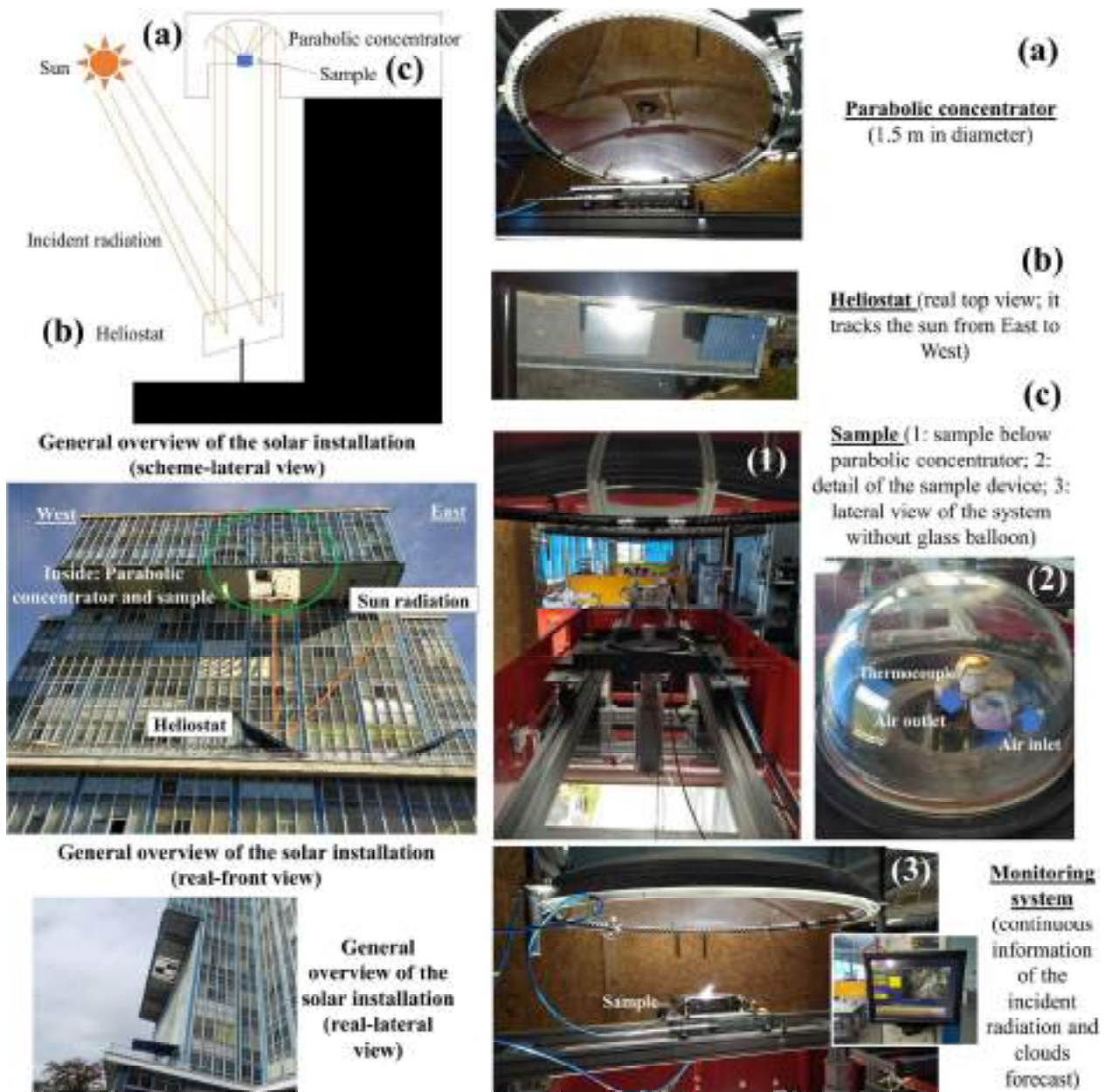


Fig. 1 Scheme and real images of the installation and devices used in the experimental work

The temperature of the spot generated by the concentrated solar energy was determined by finite element method-based software ANSYS. The dimensions of the crucible were 19.55 mm in inner diameter, thickness of 3.28 mm and height of 25.4 mm, manufactured in alumina. The crucible was filled with a mixture of powders of Al_2O_3 and MgO in the proportion 1:1 molar. The following properties were considered for the thermal simulation: density, thermal conductivity, and specific heat of the different materials in agreement with the proportions. It is possible to see in Fig. 2a the scheme of the process with the dimensions used in the calculations. The analysis was carried out in a transient thermal module using

the ANSYS Workbench application. To ensure the reliability of simulation results, a finite element mesh convergence analysis was conducted. This entailed progressively refining the finite element mesh from a coarse (Fig. 2b (1) coarse mesh) to a finer resolution (Fig. 2b (2) refine mesh), resulting in an increased number of elements/nodes. Throughout this iterative process, temperature variations were monitored until reaching a point where the variations became negligible. Additionally, a finer mesh refinement was implemented specifically in the central region of the specimen, where the energy beam impacts. On another note, Fig. 2c and d show the simulations conducted with the software ANSYS for

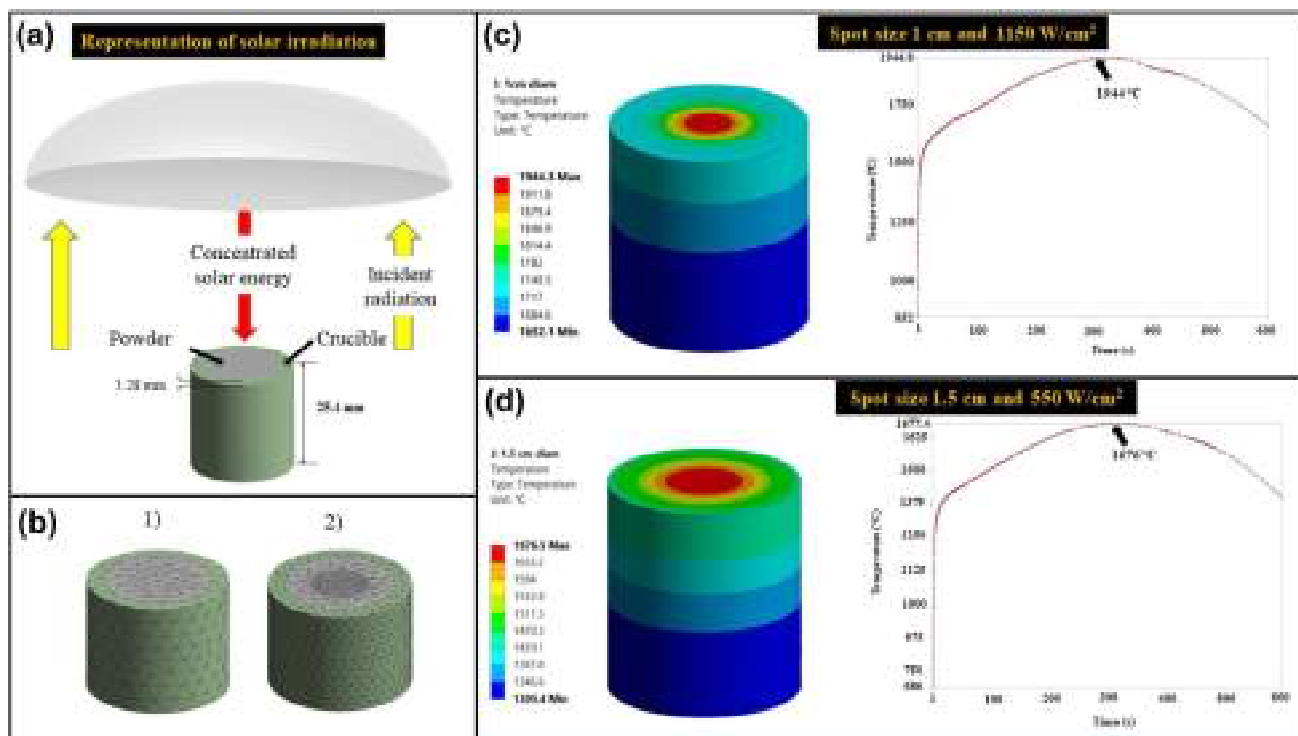


Fig. 2 **a** representation of solar irradiation, **b** meshing of the crucible and charge **c** simulation carried out with a spot size of 1 cm and 1150 W/cm² and **d** simulation carried out with a spot size of 1.5 cm and 550 W/cm²

different spot size and, therefore, energy density. The dwell time was in both situations 5 min, with 5 min of cooling. Figure 2c shows the simulation done with a beam of 10 mm in diameter, which involves 1150 W/cm² of energy density. This situation reported a maximum temperature of 1944 °C. On the other hand, Fig. 2d represents the simulation done with a beam of 15 mm in diameter, which involves 550 W/cm² of energy density. This scenario gave a maximum temperature of 1676 °C.

Mathematical simulations carried out are useful to know the approximate temperature of the spot, but they are not adequate to understand the complete process. This way, mathematical simulations report that the temperature in the spot is sufficiently high to synthesize the MgAl₂O₄ spinel. The simulations did not consider the consumption of the material as the process advances, it is necessary to consider that the final volume is 1/3 of the initial (the reasons are: powders manually compacted and sinter during the process, decrepitation, water losses, and flying of fines due to the air currents inside of the glass chamber). It is necessary to introduce in this point the thermocouple control. The thermocouple can be used to control the advance of the process as when the temperature starts to fall in the point where it is located (Fig. 1b), it is possible to assume that radiation is not producing any effect on the sample. Figure 3 serves as an example of the thermocouple measurements. The utilization

of thermocouples inside of the sample is not a suitable strategy because they move and melt during the process.

There is not a control of the radiation applied to the sample (in other solar furnaces it is possible to employ a shutter to control the percentage of incident radiation that is applied to the sample). Within this line incident radiation during the experiments presented in this manuscript exceeded 950 W/m², which indicates that a power of around 0.9 kW was applied on a surface < 1.5 cm in diameter.

The duration of the treatment was considered a crucial factor in the manufacture of the MgAl₂O₄ spinel. Within this context, each experiment lasted 5 min. If the operations of charging the crucible and cooling are included, the process

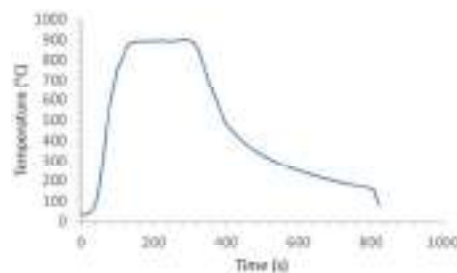


Fig. 3 Thermocouple measurement, located in the point indicated in the Fig. 1B

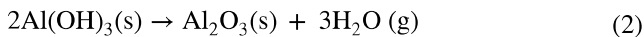
would last approximately 20 min in total. It is necessary to consider that the process presented in this manuscript is based on the direct application of the solar radiation to the sample. Nevertheless, there are technologies to directly process powders in solar furnaces [12]. This might be following step that should be studied in the scalation of this technology up to industrial scale, as the direct processing of powders would significantly increase the productivity of the process.

Results and Discussion

Mass Differences

Table 4 collects the weight losses produced during the experiments, which are consequence of several reasons discussed in the following lines.

Water: this is the main reason of the mass differences resulted from the treatment of the samples with concentrated solar energy. Aluminum industry residue (BPEF) was not subjected to any previous treatment, and it contains certain quantity of physical water resulted from the storage outdoors. This involves that moisture depending on the γ -alumina content was: 0.9% in Canada BPEFs, 2.6% in Ireland BPEFs and 0.4% in Spain BPEFs. Additionally, there is certain quantity of chemical water since the residue contains aluminum hydroxide that decomposes at temperatures of around 550 °C according to the reaction 2.



It is necessary to consider MOI measurements for Canada BPEFs were as high as 10%, while those corresponding to the BPEFs of Ireland and Spain were 5.3% and 6.6%, in agreement with the greater or lower gibbsite content. Average mass losses were 38% in the case of Canada BPEFs, 22.4% in the case of Ireland BPEFs and 26.5% in the case of

Spanish BPEFs. Therefore, losses are directly related to the gibbsite content in the residue, which is reasonable considering the water content in the hydroxide.

Volatile matter: the residue contains alkali metals, mainly Na_2O , which according to the literature can evaporate at temperatures in the range 1500–1560 °C [59]. These authors indicate that the presence of Al_2O_3 promote the evaporation ratio (MgO also plays the same role, but it only slightly enhances the evaporation ratio). Carbon, which is in minor contents but gives the characteristic grey color to the mixture, is also susceptible of being burned at the temperatures of the treatment.

Flying powders and decrepitation: The presence of an air current inside of the glass balloon leads to powder flying at the beginning of the treatment of the sample with concentrated solar energy. This problem is also observed in the case of operating without glass hood. Nevertheless, one of the reasons of the mass losses is the decrepitation produced due to the fast-heating rate and the presence of water and hydrated compounds in the sample. It is necessary to consider that powders are very fine, $d_{50} < 45 \mu\text{m}$, which suggests that green compacts could be a suitable option to process these materials or employ a reactor like those proposed by other authors in the case limestone calcination [60] or ZnO-Zn loop [61].

Quantitatively, mass losses associated with water (moisture + LOI + MOI, included the dehydration of the gibbsite) account for 28.50%, with chemical reactions (volatile compounds + carbon combustion) are < 2% and with projections, decrepitation and flying powders are 69.5%. The presence of impurities might play the role of fluxes, for instance sodium oxide is a common flux, but considering the excesses of energy employed in the proposed process the influence of the impurities in the reduction of the temperature is not relevant.

Microstructural Characteristics

The product at the end of the treatment consisted in bulk material as it is showed in Fig. 4. This sample may be grounded and milled to the desired grain size for further applications. Likewise, other alternative may be the obtaining of sintered discs of MgAl_2O_4 spinel, or the direct processing of powders as it was already anticipated. Despite the final product is obtained as a bulk material, it is crystalline as it is later reported in the X-ray diffraction analyses. In fact, if the Fig. 4 is observed, it is possible to check that crystals of MgAl_2O_4 spinel are obtained at macroscopic scale. Figure 5a and b show images of the MgAl_2O_4 spinel crystals at greater magnification.

Specimens were characterized by X-ray diffraction technique. This technique illustrates that the product obtained after the treatment is really MgAl_2O_4 spinel with the suitable crystallinity. X-ray diffraction patterns are collected in Fig. 6

Table 4 Weight losses produced during the treatment with concentrated solar energy

	Initial weight (g)	Final weight (g)	Mass losses (%)
Canada 1	4.8	2.8	41.7
Canada 2	3.3	2	39.4
Canada 3	3	2	33.0
Ireland 1	3.2	2.4	25.0
Ireland 2	2.8	2.2	21.4
Ireland 3	2.9	2.3	20.7
Spain 1	3	2	33.0
Spain 2	3.8	2.7	29.0
Spain 3	3.4	2.8	17.6

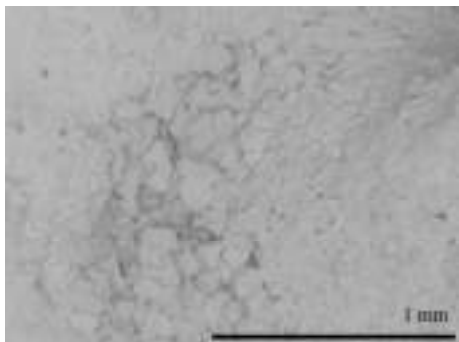


Fig. 4 Bulk MgAl_2O_4 spinel sample obtained after the treatment with concentrated solar energy

for the three MgAl_2O_4 spinel prepared with the three BPEFs: Fig. 6a, MgAl_2O_4 spinel with Canadian BPEFs; Fig. 6b, MgAl_2O_4 spinel with Irish BPEFs; and Fig. 6c, MgAl_2O_4 spinel with Spanish BPEFs.

X-ray diffraction patterns report well crystallized specimens with no traces of the starting raw materials, which indicates that the treatment with concentrated solar energy allowed to obtain the MgAl_2O_4 spinel, as it was expected from the phase diagram. Amorphous content in samples is: Canadian $5.4\% \pm 2.0$, Irish $5.0\% \pm 1.9$, and Spanish $5.6\% \pm 2.0$, determined with the X Powder Software.

Figure 7 collects the X-ray diffraction patterns of various MgAl_2O_4 spinels, either found in the nature as minerals or synthesized in laboratories. The form of the diffractograms analogous in the form to that obtained with the competition of concentrated solar energy.

The X-ray diffraction parameters 2θ and d-spacing for the hkl planes are compared with those of the reference work of Paterson and researchers [62], and some other MgAl_2O_4 spinels found in the nature and synthesized in laboratory. This allows checking the quality of the obtained MgAl_2O_4 spinel. Results are collected in Table 5 for the positions of

the peaks and Table 6 for the d-spacing of the hkl planes. There is significant approximation of the values of the solar synthesized MgAl_2O_4 spinel to those obtained by Paterson and co-authors [58], as well as to those found in the nature and, particularly to that synthesized in the laboratory, which is evidence of the well crystallization of the spinel obtained by means of concentrated solar energy using Bayer process electrofilter fines as source of alumina.

Energy Efficiency and Technical Feasibility

Solar energy is a powerful source of heat that can be used in the obtaining of energy intensive products without carbon dioxide release in short times derived from the fast heating and cooling rates, as it is possible to see in Figs. 2 and 3. The synthesis of MgAl_2O_4 spinel is an energy intensive process, which is usually carried out at temperatures within 1550 and 1650 °C, although it is possible to obtain it at lower temperatures (> 550 °C) with prolonged permanence at these temperatures (> 4 h). Ping et al. remarked that the time for the synthesis of the MgAl_2O_4 spinel is a relevant issue [46]. Within this line, routes proposed at laboratory scale by different authors are still time consuming and, therefore, synthesizing the spinel in short times is still a challenge. The low temperature synthesis by sol–gel process proposed by Pei and researchers [64] lasts at least 6 h, the process of modified sol–gel process proposed by Sanjabi and Obeydavi [65] also lasted at least 6 h, Meng and colleagues [66] indicate that their process took about 3 h. On the other hand, Bocanegra and co-authors [67] proposed different routes of synthesis that took > 36 h (ceramic method), > 48 h (mechanomechanical synthesis) and > 30 h (co-precipitation). In the field of mechanomechanical synthesis too, Kong et al. [50] required more than 14 h to sinter MgAl_2O_4 spinel, with 12 h of milling in planetary ball milling and 2 h of sintering in furnace. Zhang in the hydrothermal route, required more than 31 h to synthesize the spinel [49]. On the other hand,

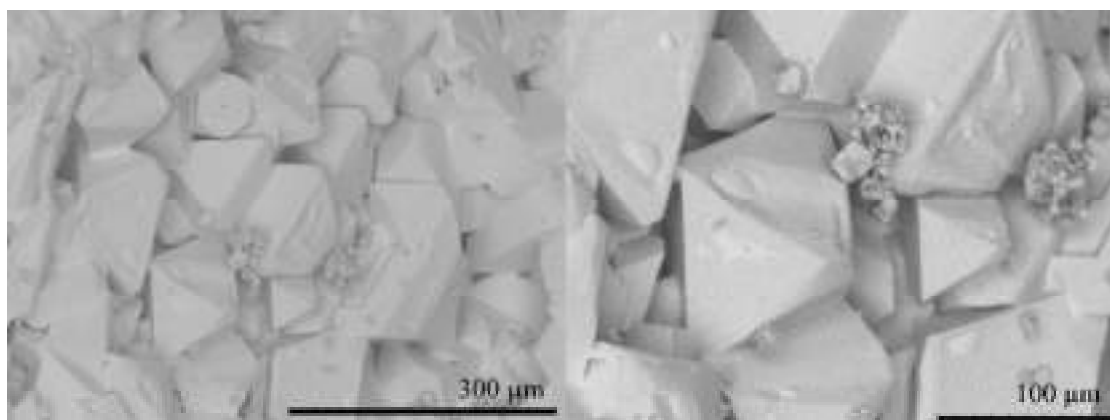


Fig. 5 Details of MgAl_2O_4 spinel crystals

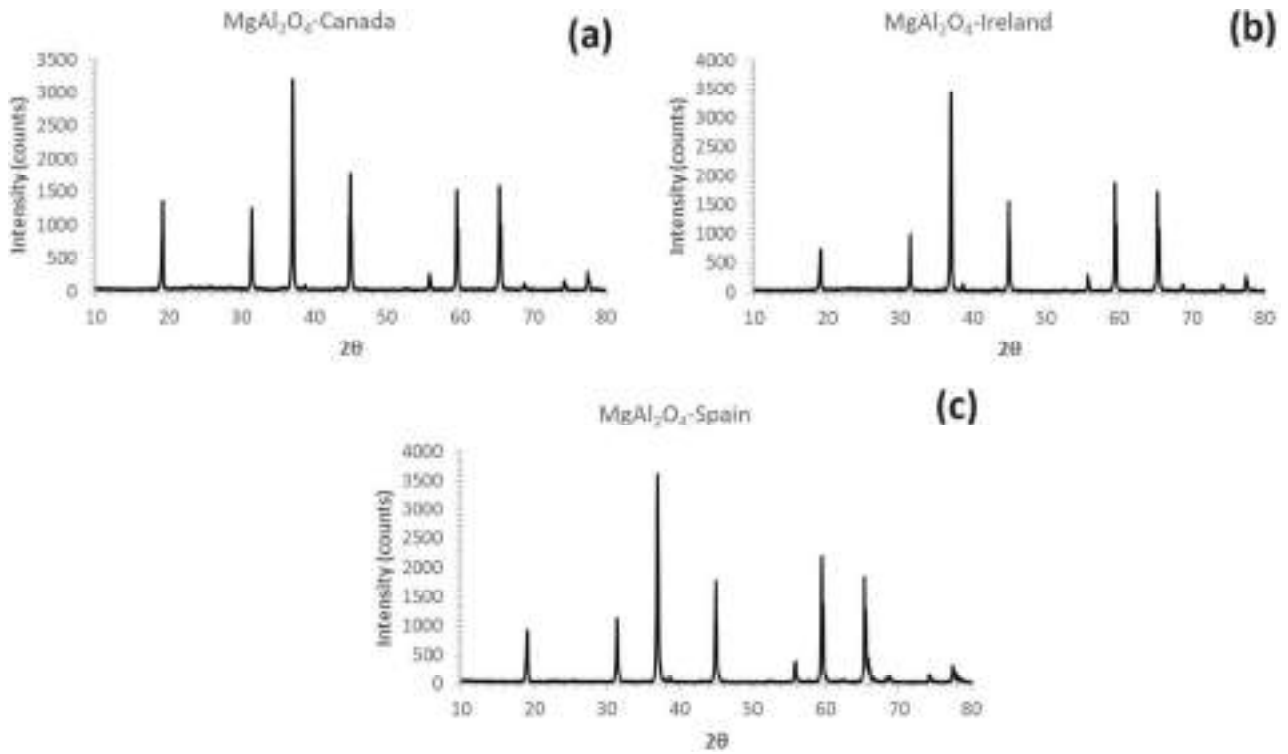


Fig. 6 X-ray diffraction of MgAl_2O_4 spinel using **a** Canadian BPEFs, **b** Irish BPEFs, and **c** Spanish BPEFs

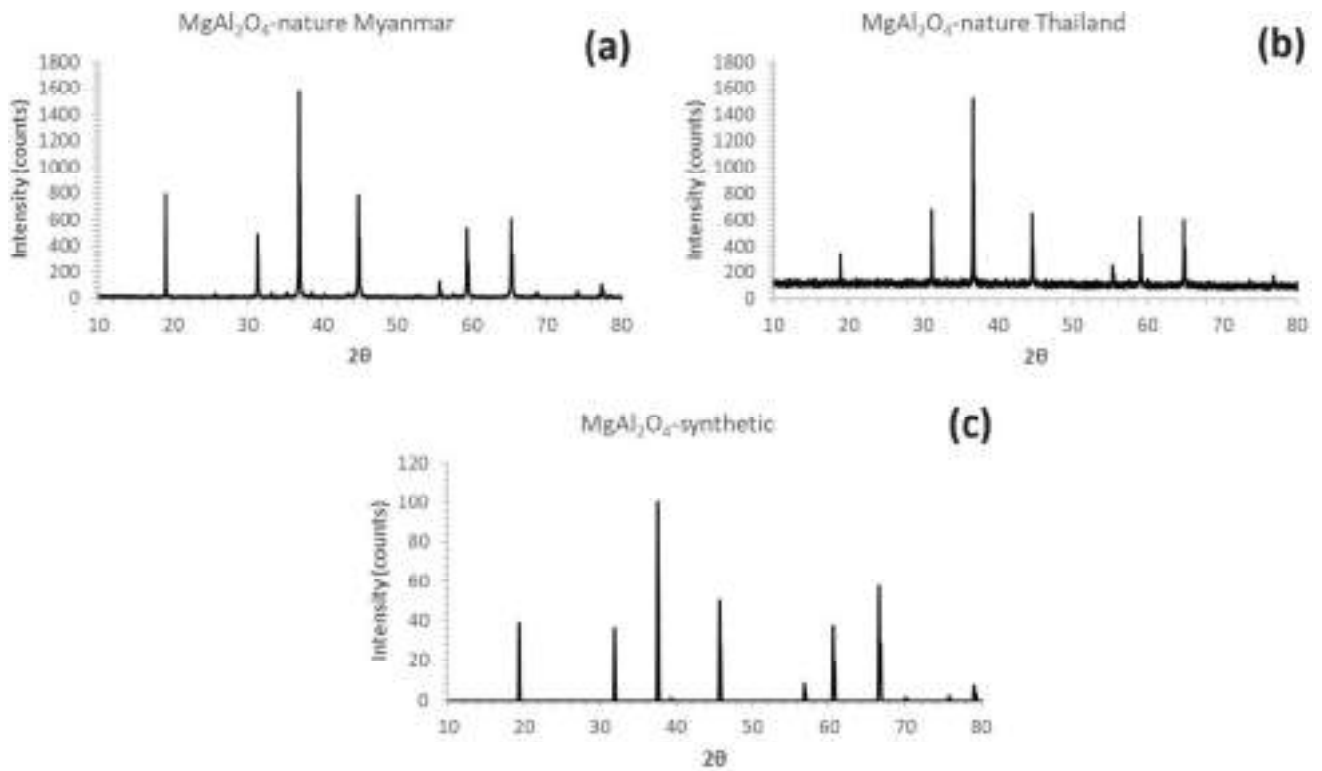


Fig. 7 X-ray diffraction of MgAl_2O_4 spinel found in nature (Myanmar) (a), nature (Thailand) (b), and synthesized in laboratory (c)

Table 5 Position of the peaks in the X-ray diffraction pattern of solar MgAl₂O₄ spinel compared with those obtained by Paterson et al., (1991) [58] and some other spinels either found in the nature or synthesized in the laboratory

	MgAl ₂ O ₄ -from Pein Pyit, Mogok, Myanmar (natural) [58]	MgAl ₂ O ₄ -from Bo Phloi, Kanchoutabori Province, Thailand (natural) [63]	MgAl ₂ O ₄ — (synthetic) [58]	MgAl ₂ O ₄ -Canadian BPEFs	MgAl ₂ O ₄ -Irish BPEFs	MgAl ₂ O ₄ -Spanish BPEFs
20	19.02		19.37	19.183	19.103	19.083
	31.28	31.11	31.89	31.446	31.386	31.366
	36.85	36.65	37.58	37.048	36.968	36.968
	38.55		39.32		38.688	
	44.81	44.56	45.72	44.990	44.930	44.950
	55.64	55.33	56.82	55.973	55.793	55.833
	59.34	59.01	60.61	59.574	59.494	59.514
	65.21	64.84	66.65	65.436	65.376	65.376
	68.60		70.14	68.917	68.777	
	74.09	73.65	75.79	74.298	74.238	74.238
	77.30	77.90	79.11	77.519	77.459	77.459

Table 6 D-spacing of the hkl planes of the peaks in the X-ray diffraction pattern of solar MgAl₂O₄ spinel compared with those obtained by Paterson et al., (1991) [58] and some other spinels either found in the nature or synthesized in the laboratory

	hkl	MgAl ₂ O ₄ -from Pein Pyit, Mogok, Myanmar (natural) [58]	MgAl ₂ O ₄ -from Bo Phloi, Kanchoutabori Province, Thailand (natural) [63]	MgAl ₂ O ₄ — (synthetic) [58]	MgAl ₂ O ₄ -Canadian BPEFs	MgAl ₂ O ₄ -Irish BPEFs	MgAl ₂ O ₄ -Spanish BPEFs
d-spacing	111	4.6706		4.5830	4.6231	4.6423	4.6471
	220	2.8602	2.8743	2.8065	2.8426	2.8479	2.8496
	311	2.4392	2.4512	2.3934	2.4246	2.4297	2.4297
	222	2.3353		2.2915		2.3255	
	400	2.0224	2.0324	1.9845	2.0133	2.0159	2.0150
	422	1.6513	1.6595	1.6203	1.6442	1.6464	1.6453
	333	1.5569	1.5646	1.5277			
	511	1.5569	1.5646	1.5277	1.5506	1.5525	1.5520
	440	1.4301	1.4371	1.4033	1.4252	1.4263	1.4263
	531	1.3674		1.3418	1.3631	1.3638	
	620	1.2791	1.2854	1.2551	1.2756	1.2764	1.2764
	533	1.2337	1.2398	1.2105	1.2304	1.2312	1.2312

Bai and researchers [68] employed more than 4 h in the combustion method. Citric acid–ethylene glycol route was used for the synthesis of MgAl₂O₄ nano-powder, involving a synthesis time of 40 h [69]. The solar process could be competitive with microwave sintering, as irradiation lasts less than 1 h [51], although the process has the inconvenient of using electricity for the microwave equipment. From the perspective of synthesis, Tripathy and Bhattacharya [70] indicated that it is still an important challenge to synthesize mesoporous MgAl₂O₄ in a single step under rapid and economically viable approach. Their process required only 2 h to be completed by the flash pyrolysis route. Nevertheless, the process proposed in this manuscript might be seen as a competing alternative to produce MgAl₂O₄ spinel in a single step. The flow diagram of the solar process is presented in the Fig. 8.

It is important to remark that process proposed in this manuscript at laboratory scale required a maximum of 15 min for the process in the solar furnace. Even when the blending and crushing might be time consuming, the proposed route might represent a competitive alternative to produce the MgAl₂O₄ spinel.

The processing times might be significantly reduced as well as the productivity of the process might be increased in further steps aimed at the scalation of the process. The direct application of the solar energy, as a process like that conducted in electric furnaces where the heating is punctual, is a potential alternative to produce MgAl₂O₄ spinel although research conducted with other materials-processes might be potentially applied in this case. The production of lime by calcination of limestone and the thermal decomposition and reduction of zinc oxide with

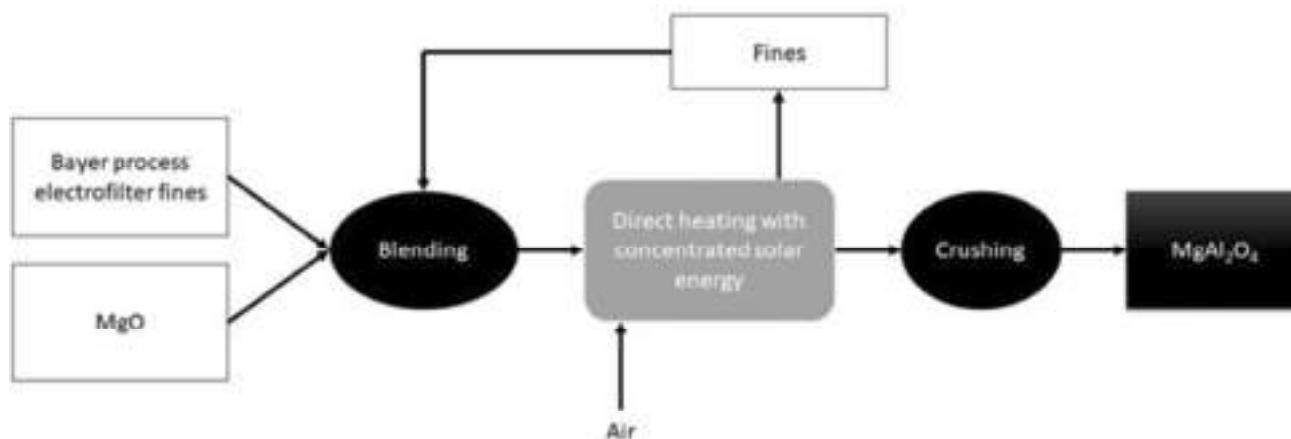


Fig. 8 Flow diagram of the solar process to produce MgAl_2O_4 spinel

solar energy have been significantly studied using solar for the process [12]. The first investigations in this line were conducted by direct application of the solar beam to the samples in a laboratory scale but soon research acquired a greater dimension and investigators started to think about the increase of the productivity. Within this line, reactors are a key point and, therefore, have been significantly reviewed in the literature [71–73]. However, the importance of directly processing powders might be considered as one of the key points. Pilot plant scale studies have already validated the possibility of processing powders of limestone to produce lime, or reducing different metal oxides to obtain metal fuels, where the Paul Scherrer Institute has played an important role in the last 30 years [74]. Nevertheless, these indirectly heated reactors have never been applied in the synthesis MgAl_2O_4 spinel. Thus, the following investigations in this line should be oriented to the synthesis of the compound in the form of powders, which would reduce even more the processing times as the steps of blending and crushing may be eliminated. There is not too much information about the world production-consumption of MgAl_2O_4 spinel. Ganesh and collaborators indicated that the world consumption of spinel exceeded the 205,000 tons in 2004 [75]. This production, updated to current levels of consumption, might be easily covered with 10 solar factories considering that the conditions of production proposed by Meier and coauthors to produce lime (plant design of 25 MW_{th} operating for around 2700 h per year to produce 27,000 tons) [76] are applicable in the case of the MgAl_2O_4 spinel synthesis, although other researchers, as Purohit and researchers [77], increase the capacity of production (in this case for iron nuggets) to 200,000 tons/year. These technoeconomic studies, together with others reported in the review of Fernández-González [12] for different processes, suggest that the deployment of this technology at

larger scale is only related with economic issues due to the lack of a plant operating for long periods of time under real conditions. Once validated in a real environment that it is possible to reach such capacities of production, plants to produce different materials will appear in countries with the suitable sun conditions.

Regarding the environmental issues, solar energy has a great potential in reducing carbon dioxide emissions. The energy demand required in the synthesis of the MgAl_2O_4 spinel was determined by means of the software HSC Chemistry 5.1. Calculations include heating from the room temperature (25 °C) to the synthesis temperature (assumed to be 1700 °C) and energy required for the formation of the compound. It is important to indicate that the formation of the spinel occurs partially through intermediate decomposition of the gibbsite with a Al_2O_3 to MgO molar ratio 1:1. Therefore, it is important to consider the gibbsite content in the thermodynamic calculations. Results are collected in the Table 7 for each residue of the aluminum industry, which indicates the energy required from the theoretical point of view.

Concentrated solar energy was directly applied to the sample. Power during the experiments was 900 W for a Direct Normalized Irradiation of around 1000 W/m^2 and a parabolic concentrator of 1.5 m in diameter with a concentration ratio of 15,000, a distance to the focal point of 65 cm, a maximum angle of incidence of 56° and a focal point of 1 cm in diameter. Therefore, the energy consumed during the experiments, which lasted for 5 min, is approximately 0.075 kWh to produce 2.4 g (31.25 kWh/kg, 112,500 kJ/kg). The efficiency of the process (η), defined as $\eta = (E_{\text{Spinel}}/E_{\text{Total}}) \cdot 100$, is $< 5\%$ in this case. In fact, Flamant and coauthors estimated that the energy conversion efficiency from the primary energy source to the useful energy beam reaches the 60% in the case solar furnaces [78]. It is necessary to remark at this point that there was not a strict control of the energy

Table 7 Thermodynamic calculations for the formation of the MgAl₂O₄ spinel

Reaction	Energy demand (kJ/kg MgAl ₂ O ₄)		
MgO + Al(OH) ₃ → MgAl ₂ O ₄ + H ₂ O	6047.7		
MgO + Al ₂ O ₃ → MgAl ₂ O ₄	1979.3		
Energy demand (kJ/kg MgAl ₂ O ₄)			
Canada	Ireland	Spain	
3159.1	2569.2	2711.6	

requirements in the process proposed in this manuscript as the objective was to demonstrate the feasibility of synthesizing the MgAl₂O₄ spinel.

The potential reduction in carbon dioxide emissions was calculated. The efficiency of the electric arc furnace was assumed to be in the range 40–75% [79], which would be the energy source replaced by the solar energy. The plant sizes were assumed to be of 1000, 5000 and 25,000 tons MgAl₂O₄ spinel per year, in agreement with the reference plant production sizes proposed by Meier and colleagues [76] for limestone calcination. Moreover, the carbon intensity of electricity in Spain in 2022 was 217 g CO_{2eq}/kWh, according to the Energy Institute Statistical Review of World Energy. Results of the carbon dioxide avoidance are collected in Table 8. It is possible to see that the utilization of concentrated solar energy in the production of MgAl₂O₄ spinel would promote a significant reduction in the greenhouse

gas emissions and can contribute to the energy transition in the field of raw materials production for the manufacture of advanced ceramics.

Conclusions

The synthesis of ceramic materials still involves processes that generate significant quantities of greenhouse gases, thus contributing to the climate change. Within this context, solar energy, when it is adequately concentrated, emerges as a suitable alternative for high temperature processes. Therefore, this renewable energy source has been applied in the synthesis of MgAl₂O₄ spinel, where the source of alumina was a residue from the aluminum metallurgy called Bayer process electrofilter fines.

Table 8 Carbon dioxide emissions avoidance considering the data collected in Table 7

	Efficiency (%)	Canada	Ireland	Spain
Energy demand (theoretical) (kJ/kg)		3159.1	2569.2	2711.6
Energy demand (real) (kJ/kg)	40	7897.8	6423.0	6779.0
	75	4212.1	3425.6	3615.5
Plant size (t/y)		Energy demand (kWh)		
1000	40	2,193,835.1	1,784,168.1	1,883,057.1
	75	1,170,028.7	951,556.3	1,004,306.4
5000	40	10,969,175.4	8,920,840.5	9,415,285.3
	75	5,850,143.6	4,757,781.6	5,021,531.8
25,000	40	54,845,877.2	44,604,202.4	47,076,426.6
	75	29,250,717.8	23,788,907.9	25,107,659.0
Plant size (t/y)		CO ₂ emissions avoidance (t/y)		
1000	40	476.1	387.2	408.6
	75	253.9	206.5	217.9
5000	40	2380.3	1935.8	2043.1
	75	1269.5	1032.4	1089.7
25,000	40	11,901.6	9679.1	10,215.6
	75	6347.4	5162.2	5448.4

The synthesis of the spinel was conducted in very short times, not exceeding the 5 min under the action of the solar beam. The solar spot was at temperatures clearly exceeding 1700 °C, as it was reported by mathematical simulations, which is sufficient for the formation of the compound. The formation of the MgAl_2O_4 spinel occurred partially through an intermediate process of decomposition of the gibbsite.

The fine particles of the residue together with the high heating rates and the water content produced certain mass losses that in a possible industrial process could be collected and sent back to the beginning of the treatment. Within this context, the direct application of the solar energy might be a technology that imitates the processes conducted in the electric arc furnaces in terms of direct application of the heat, although the processing of powders in indirectly solar heated furnaces might be a suitable alternative to directly process powder and reduce even more the processing times.

There is neither difference in terms of crystallinity nor phases when considering the three residues: Canada, Ireland, and Spain. The direct application of the solar radiation to the sample and the temperatures in excess to those required for the synthesis of the spinel hinder the possible influence of impurities in terms of reducing the synthesis temperature.

Three different scenarios were analyzed to evaluate the potential reduction in the carbon dioxide emissions. The values ranged from the 200 t/year in the case of small plants (1000 tons/year) to 12,000 t/year in the case of commercial plants (25,000 tons/year). This also translates into economics in terms of reducing the impact of the CO_2 emissions taxes.

Acknowledgements Daniel Fernández-González acknowledges the grant (Juan de la Cierva-Formación program) FJC2019-041139-I funded by the Ministerio de Ciencia e Innovación, Agencia Estatal de Investigación. Juan Piñuela Noval acknowledges the Programa “Severo Ochoa” of Grants for Research and Teaching of the Principality of Asturias for the funds received for the elaboration of the Ph. D. Thesis (Ref: BP20 041). We thank the PROMES-CNRS (PROcédés Matériaux et Energie Solaire- Centre National de la Recherche Scientifique) for providing access to its installations, the support of its scientific and technical staff, and the financial support of the SFERA-III project (Grant Agreement No 823802).

Declarations

Conflict of interest The authors have no competing interests to declare that are relevant to the content of this article.

References

1. Pero-Sanz JA, Fernández-González D, Verdeja LF (2019) Structural materials. Properties and selection. Springer, Cham
2. Sancho JP, Verdeja LF, Ballester A (2000) Metalurgia extractiva. Síntesis, Madrid
3. Sancho J, Fernández Pérez B, Ayala J, Garcia, P, Verdeja LF (2009) The recycling of Bayer electrofilter fines for diverse applications, 1st Spanish National Conference on Advances in Materials Recycling and Eco – Energy, Madrid, 12–13, November 2009, S04–9, pp. 123–125.
4. Tutic E, Jovanovic M, Mujkanovic A (2016) Preparation of mul-lite ceramics from Bayer electrofilter fines and low kaolinite clay. *Sci Sinter* 48:247–257. <https://doi.org/10.2298/SOS1602247T>
5. Sancho-Gorostiaga J, Bernardo-Sánchez A, Sancho-Martínez JP, Fernández-González D, Verdeja LF (2021) Manufacture of a High Temperature Structural Insulator (HTSI) using electrofilter powders generated in the Bayer process. *T Indian Ceram Soc* 80:163–173. <https://doi.org/10.1080/0371750X.2021.1915872>
6. Okudan MD, Akcil A, Tuncuk A, Devenci H (2015) Recovery of gallium and aluminum from electrofilter dust of alumina calcination plant in Bayer process. *Sep Sci Technol* 50:2596–2605. <https://doi.org/10.1080/01496395.2015.1062027>
7. Ayala J, Fernández B (2015) Bayer electrofilter fines as potential Se(VI) adsorbents. *JOM* 67:2727–2732. <https://doi.org/10.1007/s11837-015-1616-0>
8. Sancho JP, Ayala J, García MP, Pérez B, Alonso D (2006) The sulfuric acid leaching of Bayer electrofilter fines: a practical kinetical approach. *JOM* 58:58–62. <https://doi.org/10.1007/s11837-006-0055-3>
9. Ayala JM, Sancho JP, García-Coque MP (2008) The Recycling of Electrofilter Fines to Produce Aluminum Sulfate. In: Proc. 2008 Global Symposium on Recycling, Waste Treatment and Clean Technology, REWAS 2008, Cancún, México, 2008: 419–426.
10. Sancho-Gorostiaga J, Bernardo-Sánchez A, Sancho-Martínez JP, Fernández-González D, Verdeja LF (2021) Study of copper fixation mechanisms on Bayer process electrostatic precipitator microparticles (BPEM) using ^1H and ^{27}Al NMR spectroscopy. *J Water Process Eng* 39:101872. <https://doi.org/10.1016/j.jwpe.2020.101872>
11. Fernández-González D, Ruiz-Bustinza I, González-Gasca C, Piñuela-Noval J, Mochón-Castaños J, Sancho-Gorostiaga J, Verdeja LF (2018) Concentrated solar energy applications in materials science and metallurgy. *Sol Energy* 170:520–540. <https://doi.org/10.1016/j.solener.2018.05.065>
12. Fernández-González D (2023) A state-of-the-art review on materials production and processing using solar energy. *Mineral Proc Extr Metall Rev*. <https://doi.org/10.1080/08827508.2023.2243008>
13. Fernández-González D, Prazuch J, Ruiz-Bustinza I, González-Gasca C, Piñuela-Noval J, Verdeja LF (2019) Transformations in the Si-O-Ca system: silicon-calcium via solar energy. *Sol Energy* 181:414–423. <https://doi.org/10.1016/j.solener.2019.02.026>
14. Fernández-González D, Prazuch J, Ruiz-Bustinza I, González-Gasca C, Piñuela-Noval J, Verdeja LF (2019) Transformations in the Mn-O-Si system using concentrated solar energy. *Sol Energy* 184:148–152. <https://doi.org/10.1016/j.solener.2019.04.004>
15. Fernández-González D, Prazuch J, Ruiz-Bustinza I, González-Gasca C, Piñuela-Noval J, Verdeja LF (2018) Solar synthesis of calcium aluminates. *Sol Energy* 171:658–666. <https://doi.org/10.1016/j.solener.2018.07.012>
16. Fernández-González D, Prazuch J, Ruiz-Bustinza I, González-Gasca C, Piñuela-Noval J, Verdeja LF (2018) Iron metallurgy via concentrated solar energy. *Metals* 8:873. <https://doi.org/10.3390/met8110873>
17. Fernández-González D, Piñuela-Noval J, Ruiz-Bustinza I, González-Gasca C, Gómez-Rodríguez C, García Quiñonez LV, Fernández A, Verdeja LF (2023) Solar dissociation of zirconium silicate sand: a clean alternative to obtain zirconium dioxide. *J Clean Prod* 420:138371. <https://doi.org/10.1016/j.jclepro.2023.138371>
18. Murray JP (1999) Aluminum production using high-temperature solar process heat. *Sol Energy* 66:133–142. [https://doi.org/10.1016/S0038-092X\(99\)00011-0](https://doi.org/10.1016/S0038-092X(99)00011-0)

19. Murray JP (1999) Aluminum-silicon carbothermal reduction using high-temperature solar process heat, 128th TMS Annual Meeting, San Diego, CA, 28 de February-4 de March, 1999 pp. 399–405.
20. Murray JP (2001) Solar production of aluminum by direct reduction: Preliminary results for two processes. *J Sol Energ -T ASME* 123:125–132. <https://doi.org/10.1115/1.1351809>
21. Kruesi M, Galvez ME, Halmann M, Steinfeld A (2011) Solar aluminum production by vacuum carbothermal reduction of alumina-Thermodynamic and experimental analyses. *Metall Mater Trans B* 42B:254–260. <https://doi.org/10.1007/s11663-010-9461-6>
22. Vishnevetsky I, Ben-Zvi R, Epstein M, Barak S, Rubin R (2013) Solar carboreduction of alumina under vacuum. *JOM* 65:1721–1732. <https://doi.org/10.1007/s11837-013-0777-y>
23. Puig J, Balat-Pichelin M (2016) Production of metallic nanopowders (Mg, Al) by solar carbothermal reduction of their oxides at low pressure. *J Mag Alloy* 4:140–150. <https://doi.org/10.1016/j.jma.2016.05.003>
24. Puig J, Balat-Pichelin M (2020) Experimental carbothermal reduction of Al₂O₃ at low pressure using concentrated solar energy. *J Sustain Metall* 6:161–173. <https://doi.org/10.1007/s40831-020-00266-7>
25. Lytvynenko YM (2013) Obtaining aluminum by the electrolysis with the solar radiation using. *Appl Sol Energy* 49:4–6. <https://doi.org/10.3103/S0003701X13010088>
26. Davis D, Müller F, Saw WL, Steinfeld A, Nathan G (2017) Solar-driven alumina calcination for CO₂ mitigation and improved product quality. *Green Chem* 19:2992–3005. <https://doi.org/10.1039/C7GC00585G>
27. Kakosimos KE, Fhatima N, Al-Rawashdeh M (2022) Alrawashdeh M (2022) Conversion of boehmite to higher alumina phases by direct irradiation with concentrated light: numerical modelling and experimental verification. *AIP Conf Proc* 2445:130005
28. Fernández-González D, Prazuch J, Ruiz-Bustanza I et al (2021) Recovery of copper and magnetite from copper slag using concentrated solar power (CSP). *Metals* 11:1032. <https://doi.org/10.3390/met11071032>
29. Fernández-González D, Prazuch J, Ruiz-Bustanza I, González-Gasca C, Gómez-Rodríguez C, Verdeja LF (2019) The treatment of basic oxygen furnace (BOF) slag with concentrated solar energy. *Sol Energy* 180:372–382. <https://doi.org/10.3390/met11071032>
30. Binner P, Plötz F, Funken KH, Knoche KF (1995) The evaluation of a solar process for the high temperature treatment of hazardous wastes with solar energy. In: *Proceedings of 7th Int. Symp. Solar Thermal Conc. Technol.*, Moscow, Russia, 1994: 497–508.
31. Funken KH, Pohlmann B, Lüpfer E, Dominik R (1999) Application of concentrated solar radiation to high temperature detoxification and recycling processes of hazardous wastes. *Sol Energy* 65:25–31. [https://doi.org/10.1016/S0038-092X\(98\)00089-9](https://doi.org/10.1016/S0038-092X(98)00089-9)
32. Navarro A, Cañadas I, Martínez D, Rodríguez J, Mendoza JL (2009) Application of solar thermal desorption to remediation of mercury-contaminated soils. *Sol Energy* 83:1405–1414. <https://doi.org/10.1016/j.solener.2009.03.013>
33. Navarro A, Cañadas I, Rodríguez J, Martínez D (2012) Leaching characteristics of mercury mine wastes before and after solar thermal desorption. *Environ Eng Sci* 29:915–928. <https://doi.org/10.1089/ees.2010.0017>
34. Navarro A, Cardellach E, Cañadas I, Rodríguez J (2013) Solar thermal vitrification of mining contaminated soils. *Int J Miner Process* 119:65–74. <https://doi.org/10.1016/j.minpro.2012.12.002>
35. Navarro A, Cañadas I, Rodríguez J (2014) Thermal treatment of mercury mine wastes using a rotary solar kiln. *Minerals* 4:37–51. <https://doi.org/10.3390/min4010037>
36. Schaffner B, Höffelner W, Sun H, Steinfeld A (2000) Recycling of hazardous solid waste material using high-temperature solar process heat. 1 thermodynamic analysis. *Environ Sci Technol* 34:4177–4184. <https://doi.org/10.1021/es0000495>
37. Schaffner B, Meier A, Wuillemin D, Höffelner W, Steinfeld A (2003) Recycling of hazardous solid waste material using high-temperature solar process heat. 2. Reactor design and experimentation. *Environ Sci Technol* 37:165–170. <https://doi.org/10.1021/es020056o>
38. Tzouganatos N, Matter R, Wieckert C, Antrekowitsch J, Gamroth M, Steinfeld A (2013) Thermal recycling of waelz oxide using concentrated solar energy. *JOM* 65:1733–1743. <https://doi.org/10.1007/s11837-013-0778-x>
39. Funken KH, Roeb M, Schwarzboezl P, Warnecke H (2001) Aluminum remelting using directly solar-heated rotary kilns. *J Sol Energ-T ASME* 123(2):117–124. <https://doi.org/10.1115/1.1355242>
40. Roeb M, Monnerie N, Schäfer R, Rohner N (2003) Thermal treatment of industrial residues using concentrated sunlight. *Int. Symp. on Recycling and Reuse of Waste Materials*, Dundee, Scotland, UK, 9-11 Sep. 2003
41. Puttkamer MNV, Roeb M, Tescari S, de Oliveira L, Breuer S, Sattler C (2016) Solar aluminum recycling in a directly heated rotary kiln. *REWAS* 2016:233–240
42. Demirtas C, Ozcan AK (2021) The experimental thermal analysis of aluminum metal melting with concentrated solar energy. *Sol Energ Mat Sol C* 222:11094010. <https://doi.org/10.1016/j.solmat.2020.110940>
43. Padilla I, López-Delgado A, López-Andrés S, Álvarez M, Galindo R, Vázquez-Vaamonde AJ (2014) The application of thermal solar energy to high temperature processes: case study of the synthesis of alumina from boehmite. *Sci World J* 2014:825745. <https://doi.org/10.1155/2014/825745>
44. Padilla I, Romero M, Robla JJ, López-Delgado A (2021) Waste and solar energy: an eco-friendly way for glass melting. *ChemEngineering* 5:16. <https://doi.org/10.3390/chemengineering5020016>
45. Ganesh I (2013) A review on magnesium aluminate (MgAl₂O₄) spinel: synthesis, processing and applications. *Int Mater Rev* 58:63–112. <https://doi.org/10.1179/1743280412Y.0000000001>
46. Ping LR, Azad AM, Dung TW (2001) Magnesium aluminate (MgAl₂O₄) spinel produced via self-heat-sustained (SHS) technique. *Mater Res Bull* 36:1417–1430. [https://doi.org/10.1016/S0025-5408\(01\)00622-5](https://doi.org/10.1016/S0025-5408(01)00622-5)
47. Li H, Wei HY, Cui Y, Sang RL, Bu JL, Wei YN, Lin J, Zhao JH (2017) Synthesis and characterisation of MgAl₂O₄ spinel nanopowders via nonhydrolytic sol-gel route. *J Ceram Soc Jpn* 125:100–104. <https://doi.org/10.2109/jcersj2.16297>
48. Figueredo GP, Carvalho AFM, Medeiros RLBA, Silva FM, de Macedo HP, de Freitas Melo MA, de Araujo Melo DM (2017) Synthesis of MgAl₂O₄ by gelatin method: effect of temperature and time of calcination in crystalline structure. *Mat Res* 20:254–259. <https://doi.org/10.1590/1980-5373-MR-2017-0105>
49. Nuernberg GDB, Foletto EL, Probst LFD, Campos CEM, Carreño NLV, Moreira MA (2012) A novel synthetic route for magnesium aluminate (MgAl₂O₄) particles using metal-chitosan complexation method. *Chem Eng J* 193–194:211–214. <https://doi.org/10.1016/j.cej.2012.04.054>
50. Miroliaee A, Salehirad A, Rezvani AR (2015) Ion-pair complex precursor approach to fabricate high surface area nanopowders of MgAl₂O₄ spinel. *Mater Chem Phys* 151:312–317. <https://doi.org/10.1016/j.matchemphys.2014.11.072>
51. Zhang X (2009) Hydrothermal synthesis and catalytic performance of high-surface-area mesoporous nanocrystallite MgAl₂O₄ as catalyst support. *Mater Chem Phys* 116:415–420. <https://doi.org/10.1016/j.matchemphys.2009.04.012>
52. Kong LB, Ma J, Huang H (2002) MgAl₂O₄ spinel phase derived from oxide mixture activated by a high-energy ball milling

- process. *Mater Lett* 56:238–243. [https://doi.org/10.1016/S0167-577X\(02\)00447-0](https://doi.org/10.1016/S0167-577X(02)00447-0)
53. Ganesh I, Johnson R, Rao GVN, Mahajan YR, Madavendra SS, Reddy BM (2005) Microwave-assisted combustion synthesis of nanocrystalline MgAl_2O_4 spinel powder. *Ceram Int* 31:67–74. <https://doi.org/10.1016/j.ceramint.2004.03.036>
 54. Pacurariu C, Lazau I, Ecsedi Z, Lazau R, Barvinschi P, Marginean G (2007) New synthesis methods of MgAl_2O_4 spinel. *J Eur Ceram Soc* 27:707–710. <https://doi.org/10.1016/j.jeurceramsoc.2006.04.050>
 55. Troia A, Pavese M, Geobaldo F (2009) Sonochemical preparation of high surface area MgAl_2O_4 spinel. *Ultrason Sonochem* 16:136–140. <https://doi.org/10.1016/j.ultsonch.2008.06.001>
 56. Suyama Y, Kato A (1982) Characterization and sintering of Mg-Al spinel prepared by spray-pyrolysis technique. *Ceram Int* 8:17–21. [https://doi.org/10.1016/0272-8842\(82\)90010-4](https://doi.org/10.1016/0272-8842(82)90010-4)
 57. Montouillout V, Massiot D, Douy A, Coutures JP (2004) Characterization of MgAl_2O_4 precursor powders prepared by aqueous route. *J Am Ceram Soc* 82:3299–3304. <https://doi.org/10.1111/j.1151-2916.1999.tb02243.x>
 58. Sarkar R, Banerjee G (1999) Effect of compositional variation and fineness on the densification of $\text{MgO-Al}_2\text{O}_3$ compacts. *J Eur Ceram Soc* 19:2893–2899. [https://doi.org/10.1016/S0955-2219\(99\)00078-3](https://doi.org/10.1016/S0955-2219(99)00078-3)
 59. Tong ZF, Qiao JL, Jiang XY (2017) Kinetics of Na_2O evaporation from $\text{CaO-Al}_2\text{O}_3\text{-SiO}_2\text{-MgO-TiO}_2\text{-Na}_2\text{O}$ slags. *Ironmak Steelmak* 44:237–245. <https://doi.org/10.1080/03019233.2016.1210354>
 60. Meier A, Bonaldi E, Cella GM, Lipinski W, Wuillemain D (2006) Solar chemical reactor technology for industrial production of lime. *Sol Energ* 80:1355–1362. <https://doi.org/10.1016/j.solener.2005.05.017>
 61. Hauter P, Moeller S, Palumbo R, Steinfeld A (1999) The production of zinc by thermal dissociation of zinc oxide—solar chemical reactor design. *Sol Energ* 67:161–167. [https://doi.org/10.1016/S0038-092X\(00\)00037-2](https://doi.org/10.1016/S0038-092X(00)00037-2)
 62. Peterson RC, Lager GA, Hitterman RL (1991) A time-of-flight neutron powder diffraction study of MgAl_2O_4 at temperatures up to 1273 K. *Am Mineral* 76:1455–1458
 63. Lucchesi S, Russo U, Della Giusta A (1997) Crystal chemistry and cation distribution in some Mn-rich natural and synthetic spinel. *Eur J Mineral* 9:31–42
 64. Pei LZ, Yin WY, Wang JF, Chen J, Fan CG, Zhang QF (2010) Low temperature synthesis of magnesium oxide and spinel powders by a sol-gel process. *Mater Res* 13:339–343. <https://doi.org/10.1590/S1516-14392010000300010>
 65. Sanjabi S, Obeydavi A (2015) Synthesis and characterization of nanocrystalline MgAl_2O_4 spinel via modified sol-gel method. *J Alloy Compd* 645:535–540. <https://doi.org/10.1016/j.jallcom.2015.05.107>
 66. Meng J, Chen W, Zhao J, Liu L (2017) Study of the high-temperature synthesis of MgAl_2O_4 spinel refractory raw materials from chromium slag. *High Temp Mater Proc* 37:581–586. <https://doi.org/10.1515/htmp-2016-0254>
 67. Bocanegra SA, Ballarini AD, Scelza OA, de Miguel SR (2008) The influence of the synthesis routes of MgAl_2O_4 on its properties and behavior as support of dehydrogenation catalysts. *Mater Chem Phys* 111:534–541. <https://doi.org/10.1016/j.matchemphys.2008.05.002>
 68. Bai J, Liu J, Li C, Li G, Du Q (2011) Mixture of fuels approach for solution combustion synthesis of nanoscale MgAl_2O_4 powders. *Adv Powder Technol* 22:72–76. <https://doi.org/10.1016/j.apt.2010.03.013>
 69. Lee PY, Suematsu H, Yano T, Yatsui K (2006) Synthesis and characterization of nanocrystalline MgAl_2O_4 spinel by polymerized complex method. *J Nanopart Res* 8:911–917. <https://doi.org/10.1007/s11051-005-9055-4>
 70. Tripathy S, Bhattacharya D (2013) Rapid synthesis and characterization of mesoporous nanocrystalline MgAl_2O_4 via flash pyrolysis route. *J Asian Ceram Soc* 1:328–332. <https://doi.org/10.1016/j.jascer.2013.08.006>
 71. Abbas SA, Eidan AA, Al Sahlani A (2022) Solar reactor review. *Solar reactor review*. *Int J Heat Technol* 40(3):671–84. <https://doi.org/10.18280/ijht.400303>
 72. Ekman BM, Brooks G, Rhamdhani MA (2014) A review: Solar thermal reactors for materials production (Chapter 1). In: Wang C, de Bakker J, Belt CK, Jha A, Neelameggham NR, Pati S, Prentice LH, Tranell G, Brinkman KS (eds) *Energy technology 2014: Carbon dioxide management and other technologies*. John Wiley, London. <https://doi.org/10.1002/9781118888735.ch1>
 73. Guerra-Rosa L (2019) Solar heat for materials processing: a review on recent achievements and a prospect on future trends. *Chemengineering* 3(4):83. <https://doi.org/10.3390/chemengineering3040083>
 74. Koepf E, Alxneit I, Wieckert C, Meier A (2017) A review of high temperature solar driven reactor technology: 25 years of experience in research and development at the Paul Scherrer Institute. *Appl Energ* 188:620–651. <https://doi.org/10.1016/j.apenergy.2016.11.088>
 75. Ganesh I, Srinivas B, Johnson R, Saha BP, Mahajan YR (2004) Microwave assisted solid state reaction synthesis of MgAl_2O_4 spinel powders. *J Eur Ceram Soc* 24:201–207. [https://doi.org/10.1016/S0955-2219\(03\)00602-2](https://doi.org/10.1016/S0955-2219(03)00602-2)
 76. Meier A, Gremaud N, Steinfeld A (2005) Economic evaluation of the industrial solar production of lime. *Energ Convers Manage* 46:905–926. <https://doi.org/10.1016/j.enconman.2004.06.005>
 77. Purohit S, Ekman B, Mejias R, Brooks G, Rhamdhani MA (2018) Solar processing of composite iron ore pellets: preliminary assessments. *J Clean Prod* 205:1017–1028. <https://doi.org/10.1016/j.jclepro.2018.09.112>
 78. Flamant G, Ferriere A, Laplace D, Monty C (1999) Solar processing of materials: opportunities and new frontiers. *Sol Energ* 66:117–132. [https://doi.org/10.1016/S0038-092X\(98\)00112-1](https://doi.org/10.1016/S0038-092X(98)00112-1)
 79. Kirschen M, Risonarta V, Pfeifer H (2009) Energy efficiency and the influence of gas burners to the energy related carbon dioxide emissions of electric arc furnaces in steel industry. *Energy* 34:1065–1072. <https://doi.org/10.1016/j.energy.2009.04.015>






Publisher's Note Springer Nature remains neutral with regard to jurisdictional claims in published maps and institutional affiliations.

Springer Nature or its licensor (e.g. a society or other partner) holds exclusive rights to this article under a publishing agreement with the author(s) or other rightsholder(s); author self-archiving of the accepted manuscript version of this article is solely governed by the terms of such publishing agreement and applicable law.

Artículo 3: MgO–ZrO₂ ceramic composites for silicomanganese production.

Article

MgO–ZrO₂ Ceramic Composites for Silicomanganese Production

Cristian Gómez-Rodríguez ^{1,2}, Linda Viviana García-Quiñonez ^{3,*}, Josué Amilcar Aguilar-Martínez ⁴ ,
Guadalupe Alan Castillo-Rodríguez ⁴ , Edén Amaral Rodríguez-Castellanos ⁴, Jesús Fernando López-Perales ⁴ ,
María Isabel Mendivil-Palma ⁵ , Luis Felipe Verdeja ² and Daniel Fernández-González ^{6,*} 

¹ Faculty of Engineering, University of Veracruz, Coatzacoalcos 96535, Mexico; crisgomez@uv.mx

² Departamento de Ciencia de los Materiales e Ingeniería Metalúrgica, Escuela de Minas, Energía y Materiales, Universidad de Oviedo, 33004 Oviedo, Asturias, Spain; lfv@uniovi.es

³ CONACYT-Centro de Investigación Científica y de Educación Superior de Ensenada B.C. (CICESE), Unidad Monterrey, Apodaca 66629, Mexico

⁴ Facultad de Ingeniería Mecánica y Eléctrica (FIME), Universidad Autónoma de Nuevo León (UANL), San Nicolás de los Garza 66450, Mexico; josue.aguilarmrt@uanl.edu.mx (J.A.A.-M.); alan.castillo.rdz@gmail.com (G.A.C.-R.); eden.rodriguezcs@uanl.edu.mx (E.A.R.-C.); jlopezp@uanl.edu.mx (J.F.L.-P.)

⁵ Centro de Investigación en Materiales Avanzados, S.C. (CIMAV-Sede Monterrey), Alianza Norte 202, Parque de Investigación e Innovación Tecnológica, Apodaca 66600, Mexico; maria.mendivil@cimav.edu.mx

⁶ Centro de Investigación en Nanomateriales y Nanotecnología (CINN), Consejo Superior de Investigaciones Científicas (CSIC), Universidad de Oviedo (UO), Principado de Asturias (PA), Avda. de la Vega, 4-6, 33940 San Martín del Rey Aurelio, Asturias, Spain

* Correspondence: linda@cicese.mx (L.V.G.-Q.); d.fernandez@cinn.es (D.F.-G.)



Citation: Gómez-Rodríguez, C.; García-Quiñonez, L.V.; Aguilar-Martínez, J.A.; Castillo-Rodríguez, G.A.; Rodríguez-Castellanos, E.A.; López-Perales, J.F.; Mendivil-Palma, M.I.; Verdeja, L.F.; Fernández-González, D. MgO–ZrO₂ Ceramic Composites for Silicomanganese Production. *Materials* **2022**, *15*, 2421. <https://doi.org/10.3390/ma15072421>

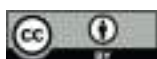
Academic Editor: Lidija Čurković

Received: 11 March 2022

Accepted: 24 March 2022

Published: 25 March 2022

Publisher's Note: MDPI stays neutral with regard to jurisdictional claims in published maps and institutional affiliations.



Copyright: © 2022 by the authors. Licensee MDPI, Basel, Switzerland. This article is an open access article distributed under the terms and conditions of the Creative Commons Attribution (CC BY) license (<https://creativecommons.org/licenses/by/4.0/>).

Abstract: The deterioration of the refractory lining represents a significant problem for the smooth operation in the ferroalloys industry, particularly in the production of silicomanganese, due to the periodic requirements of substitution of the damaged refractory. Within this context, magnesia refractories are commonly employed in the critical zones of the furnaces used in silicomanganese production since the slag involved in the process has a basic character. The behavior of MgO–ZrO₂ ceramic composites with different ZrO₂ nanoparticles (0, 1, 3, and 5 wt.%) contents in the presence of silicomanganese slags is proposed in this manuscript. XPS, XRD and SEM–EDX were used to evaluate the properties of the ceramic composite against the silicomanganese slag. The static corrosion test was used to evaluate the corrosion of the refractory. Results suggest that corrosion is controlled by the change in slag viscosity due to the reaction between CaZrO₃ and the melted slag. Besides, ZrO₂ nanoparticles located at both triple points and grain boundaries act as a barrier for the slag advance within the refractory. The utilization of MgO refractories with ZrO₂ nanoparticles can extend the life of furnaces used to produce silicomanganese.

Keywords: sintering; slag; corrosion; spectroscopy; chemical properties; mechanical properties; MgO; silicomanganese; nanomaterials; refractories; ceramics

1. Introduction

Materials used in furnaces must withstand the adverse conditions during the operation at high temperatures required to produce metals, which include: (i) corrosion and erosion by solids, liquids, fumes, and gases; (ii) thermo-mechanical loads generated in different parts of the furnace [1–5]. Refractory ceramics are used with this aim in the refractory lining of furnaces, and, within this context, around 70% of the worldwide refractory production is used by the metallurgy industry [2,6]. Basic refractory ceramics (mainly magnesia ceramics) are, from those used in metallurgy, one of the most important families of refractories, since they are used in metallurgical ladles, electric arc furnaces (EAF), basic oxygen furnace (BOF), and in special furnaces for non-ferrous metallurgy. The problem arises from the soon deterioration (wear, cracks, spalling due to chemical corrosion produced during the

metal smelting) of the refractory resulting from operation under extreme conditions, which requires year by year, from large amounts of money for maintenance or total replacement of damaged refractory linings.

Silicomanganese (17–20% Si and 1.5–2.0% C) is mainly consumed in electric arc furnace steel production [7–10]. Its utilization is expected to advance at a faster rate than ferromanganese and ferrosilicon because it adds less phosphorus, carbon, aluminum, and nitrogen [7–10] to the steel. It is also an effective deoxidizer, which results in cleaner steel. Low and ultra-low carbon silicomanganese alloys (26–31% Si and 0.05–0.5% C) are used in the manufacture of stainless steels and special steels [7–10].

Silicomanganese alloy is produced by carbothermal reduction in raw materials (manganese ores, quartzite, (Fe)Si-remelts, coke (1.5–2%), and high carbon ferromanganese production slag (35–45% MnO), since both types of alloys are produced in the same factory) in a Submerged Arc Furnace (SAF) at temperatures within 1600 °C and 1700 °C [11]. One of the critical issues during the silicomanganese production is the refractory lining damage in the tap-hole area and the furnace hearth due to the wear and chemical corrosion caused by molten metal and slag [11], which involves a non-smooth production process and economic and environmental impacts resulting from the periodic replacement of the refractory. Silicomanganese slag (around 1225 kg slag per ton) is disregarded when it contains 6 to 12% of dissolved MnO, where the other main constituents are SiO₂ (38–44%), CaO (20–35%), MgO (5–15%), and Al₂O₃ (10–25%). Within this context, little literature is available about the deterioration of the refractories in the presence of silicomanganese slag, and this is limited to SiC-based and C-based refractories [11–14]. However, the improvement of refractories for the SiMn alloy production is essential due to the technological importance (23.5 Mt are expected for 2025) of this material alloy in the steelmaking process [7–10].

Historically, MgO-based refractories have fulfilled the requirements of the metallurgical and steel industries. The addition of different additives, particularly oxides, has been subject of research for more than 10 years. C [15–17], Al₂O₃ [18], Cr₂O₃ [19–21], MgAl₂O₄ [22,23], ZrSiO₄ [24], ZrO₂ [25], TiO₂ [26], FeAl₂O₄ [27], or CaZrO₃ [28] were added to improve the properties of MgO-based refractories, and considering nanoparticles, it is possible to point out Fe₂O₃ [29,30], Al₂O₃ [30–32], ZrO₂ [33,34], ZrSiO₄ [35,36], C [37,38], MgAl₂O₄ [39], TiO₂ [40,41], Cr₂O₃ [42,43], and SiO₂ [44].

This manuscript presents an innovative study about the behavior of MgO reinforced with ZrO₂ nanoparticles in the presence of silicomanganese slag. The influence of different contents of ZrO₂ nanoparticles (0, 1, 3, and 5 wt.%) is discussed together with the effect of the method of obtaining the green compacts (cold uniaxial pressing or cold uniaxial pressing and cold isostatic pressing) and also the sintering temperature (1550 °C or 1650 °C). The results of this research work could represent a potential benefit for the industry of SiMn alloy production from the environmental and economic points of view.

2. Materials and Methods

2.1. Materials

Sintered magnesia (MgO) with an average particle size < 45 µm (98.5% MgO, 1% CaO, 0.2% SiO₂, 0.15% Al₂O₃, 0.13% Fe₂O₃, 0.01% B₂O₃, 3.48–3.52 g/cm³ bulk density, supplied by Grupo Peñoles company (Laguna del Rey, Coahuila, México) was used as starting material. It is well known that the fine fraction is considered the weakest constituent of a refractory matrix. Therefore, it has to be reinforced by a strong bond development. The bonding strength represents one of the main microstructural characteristics contributing to the reliable refractory matrix establishment. Increasing the bonding strength, the resistance against many kinds of stresses during the performance, and structural spalling would be improved. Fine fraction study is important since it is the one that has the highest reactivity in a refractory system. Besides, the aggregates are the main refractory constituent that supports the mechanical, thermal, and chemical changes in a system. On the other hand, there are many studies focused on the fine elements of a refractory (matrix and bonding structure), as was cited below. Through these studies, it was found that reducing the

particle size (<45 μm) helps the thermal sintering process by improving the morphology and microstructure of sintered composites with a beneficial impact on the mechanical, physical, and chemical properties [17,28,30,34].

High purity zirconia (ZrO_2) nanoparticles (<100 nm, >99.9% purity, 5.89 g/cm^3 relative density, $\geq 25 \text{ m}^2/\text{g}$ specific surface area, supplied by Skyspring Nanomaterials Inc., (Houston, TX, USA) were also used as starting raw material. ZrO_2 nanoparticles used in this manuscript had a monoclinic structure. Zirconium oxide (ZrO_2) is a phase that characterizes by exhibiting three polymorphic transformations. It is monoclinic from room temperature up to 1170 $^\circ\text{C}$, tetragonal from 1171 $^\circ\text{C}$ to 2370 $^\circ\text{C}$, and cubic above 2370 $^\circ\text{C}$ and until the melting point (2715 $^\circ\text{C}$). It is well known that there are several phases that, as the MgO, CaO, and Y_2O_3 are adequate to stabilize a single crystalline structure of ZrO_2 , that is to say, they would remain with a certain crystalline structure form from room temperature to the melting point. Thus, without polymorphic changes (monoclinic–tetragonal–cubic, or vice versa) and, therefore, volume changes that could involve cracks in the parts.

Silicomanganese slag from the metallurgical process was used to assess the chemical resistance of experimental refractory compositions (wt.%): 26.88% SiO_2 , 24.85% CaO, 24.56% MnO, 12.41% Al_2O_3 , 4.55% MgO, 1.21% BaO, 0.76% Na_2O , 0.80 K_2O , and balanced others (Fe, P, Ti, Sr). Silicomanganese slag was milled and screened to <38 μm . The slag chemical composition was determined by an Axios, a PANalytical wavelength-dispersive X-ray fluorescence spectrometer (Servicios Científico-Técnicos, Universidad de Oviedo, Oviedo, Asturias, Spain) with an Rh-anode X-ray tube as a radiation source (4 kW as maximum power). Samples were measured in a vacuum with a 15–50 eV energy resolution. For the quantitative analysis of the spectra, the Omnian software was used.

The slag is considered basic when $\text{BI} > 1$ considering the basicity index $\text{BI} = (\% \text{CaO} + \% \text{MgO})/(\% \text{SiO}_2)$ [45,46]. Therefore, the SiMn slag is a basic slag (1.09), so the chemical compatibility with MgO-based refractories is high.

2.2. Sample Preparation

Weight percentages of ZrO_2 nanoparticles were added to magnesia powders considering the following relation: $(100 - X) \text{ wt.\% MgO} + X \text{ wt.\% of ZrO}_2$, where $X = 0, 1, 3$ and 5. Table 1 shows the experimental design and physical properties carried out in this research. Bulk density and porosity tests were developed in accordance with the ASTM-C830-00 Standard and as described in the same standard [45].

The nanoparticle's dispersion was obtained using Zephrim PD3315 as a dispersant and acetone as a dispersion medium. A 1/10 ratio (nanoparticles/dispersant) was used. Afterward, the powders with the specific nanoparticle concentration and ethylene glycol (2 wt.% of the total mass) as a binder were mixed for 15 min by a mechanical method using an Alghamix II-Zhermack mechanical mixer (Facultad de Ingeniería Mecánica y Eléctrica, San Nicolás de los Garza, Nuevo León, México) at 100 rpm to obtain a suitable homogeneity.

Then, the resulting powder mixtures were formed in green cylinder samples (25 mm in diameter and 30 mm in height) using two options: cold uniaxial pressing (CUP) at 100 MPa for 2 min; cold uniaxial pressing (CUP) at 100 MPa for 2 min and cold isostatic pressing (CIP) in an autoclave (Autoclave Engineers, Inc. P-419 (located in Centro de Investigación en Nanomateriales y Nanotecnología (CINN), L'Entregu, Asturias, Spain) at 200 MPa for 5 min.

All the experimental samples were dried in a muffle (Departamento de Ciencia de los Materiales e Ingeniería Metalúrgica, Escuela de Minas, Energía y Materiales, Universidad de Oviedo, Oviedo, Asturias, Spain) at 250 $^\circ\text{C}$ for 24 h to evaporate moisture. After the drying process, sintering was carried out in a Lindberg Blue M/1700 Thermo Fisher Scientific electric furnace (Escuela Politécnica de Mieres, Universidad de Oviedo, Mieres, Asturias, Spain) using a heating rate of 5 $^\circ\text{C}/\text{min}$ with a dwell time of 4 h at maximum temperature (1550 $^\circ\text{C}$ or 1650 $^\circ\text{C}$, depending on the sample). Cooling down to room temperature was carried out in the furnace.

Table 1. Sintering temperature, pressing method (cold uniaxial pressing (CUP) or cold uniaxial pressing (CUP) + Cold Isostatic Pressing (CIP)), batch composition and physical properties of samples analyzed.

Sintering Temperature	Pressing Method	Batch Composition			Physical Properties	
		Simple Code	ZrO ₂ Nanoparticles (wt.%)	MgO (wt.%)	Density (g/cm ³)	Porosity (%)
1550 °C	CUP Batch 1	XL1	0	100	2.62	28.46
		XL2	1	99	2.66	27.21
		XL3	3	97	2.88	20.83
		XL4	5	95	2.89	20.90
1550 °C	CUP + CIP Batch 3	XL5	0	100	2.67	27.03
		XL6	1	99	2.67	26.79
		XL7	3	97	2.90	19.69
		XL8	5	95	2.90	20.24
1650 °C	CUP Batch 2	XL9	0	100	2.65	27.54
		XL10	1	99	2.83	21.73
		XL11	3	97	2.95	18.27
		XL12	5	95	3.01	17.22
1650 °C	CUP + CIP Batch 4	XL13	0	100	2.71	26.25
		XL14	1	99	2.88	20.57
		XL15	3	97	2.99	16.43
		XL16	5	95	3.06	14.49

2.3. Methods

2.3.1. Microstructural Analysis

The microstructural analysis was carried out using a Philips X'Pert diffractometer (Servicios Científico-Técnicos, Universidad de Oviedo, Oviedo, Asturias, Spain) equipped with Cu anode tube and K α 1 radiation ($\lambda = 1.54056 \text{ \AA}$) to investigate the crystallographic information, in the range of 2θ from 15° to 90° at a scan speed of $1^\circ/\text{s}$. Data analysis and the peak profile fitting were carried out using the X Powder program. The main crystalline phases of the silicomanganese slag are gehlenite ($\text{Ca}_2\text{Al}(\text{SiAl})\text{O}_7$), kirschsteinite ($\text{CaFe}^{2+}\text{SiO}_4$), and fukalite ($\text{Ca}_4[\text{Si}_2\text{O}_6][\text{CO}_3](\text{OH})_2$) with an average phase percentage of around 22%. Melilite phase ($(\text{Ca}, \text{Na})_2(\text{Al}, \text{Mg})(\text{Si}, \text{Al})_2\text{O}_7$) represents a phase percentage of 14%, and other phases that represent less than 10% were detected (rhodochrosite— MnCO_3 , goethite— $(\alpha\text{-Fe}^{3+}\text{O}(\text{OH}))$, tephroite— Mn_2SiO_4 and mozartite— $\text{CaMn}^{3+}(\text{SiO}_4)(\text{OH})$).

2.3.2. Morphological Analysis

The morphological analysis of the MgO refractory reinforced with ZrO₂ nanoparticles, sintered at 1550 °C and 1650 °C, was carried out by a JEOL-6610LV scanning electron microscopy (Servicios Científico-Técnicos, Universidad de Oviedo, Oviedo, Asturias, Spain) equipped with an electron dispersive X-ray spectroscopy (EDX) detector (Inca energy-200).

2.3.3. Mechanical Properties

Mechanical resistance of the composites was determined by cold crushing strength in specimens of sintered samples corresponding to cylindrical specimens with a diameter of 24 mm and a height of 11 mm.

An ELE-INTERNATIONAL hydraulic universal press machine (Departamento de Ciencia de los Materiales e Ingeniería Metalúrgica, Escuela de Minas, Energía y Materiales, Universidad de Oviedo, Oviedo, Asturias, Spain), model ABR-AUTO with a maximum load set at 200 tons, was used for the evaluation. The compressive load was applied parallel to the cylindrical samples at a speed of 50 kgf/s and at room temperature.

2.3.4. Chemical State Analyses

The elemental composition and oxidation state analyses of sintered samples were carried out by a Thermo Scientific X-ray photoelectron spectroscopy (XPS, Facultad de Ingeniería Mecánica y Eléctrica, San Nicolás de los Garza, Nuevo León, México) using a K-alpha X-ray photoelectron spectrometer system. The samples were excited by a monochromatized Al K α X-ray radiation of energy of 1486.6 eV.

Cleaning by a soft surface etching step was performed to remove superficial impurities from the sample during the analysis. Binding energies of all the peaks were corrected using C 1s energy at 284.6 eV corresponding to adventitious carbon. Moreover, the charge compensation was corrected by the flood gun associated with the spectrometer. The peaks were deconvoluted using a Shirley type background calculation and peak fitting using the Gaussian–Lorentzian sum function.

2.3.5. Chemical Properties

A measurement of slag penetration by a static corrosion test (finger test method) was performed to determine the chemical resistance of the sintered refractory samples against SiMn slag corrosion. The test consists of drilling a hole (~3.5 mm in diameter with 2.5 mm in depth) in the center of the upper face of the cylindrical sample and filling it with powder slag (5 g). The sintered samples analyzed in this chemical test were 25 mm in diameter and 6 mm in height. The experiment was carried out in an electric furnace for 4 h at 1550 °C. Both the heating and cooling rates were 5 °C/min. Afterward, samples were transversely cut using a diamond disc. After cutting, the surfaces of interest were polished for microscopy evaluation.

Figure 1 shows a scheme of the slag penetration analysis carried out in the refractories. Points A, B, and C represent zones where the morphological analyses by SEM were carried out. These zones correspond to the slag zone (top area), interphase slag/refractory (middle area), and the refractory zone (bottom area). The dotted red line indicates the path followed in all the samples corresponding to the chemical semi-quantitative analysis of elements (wt.%) by the EDX technique.

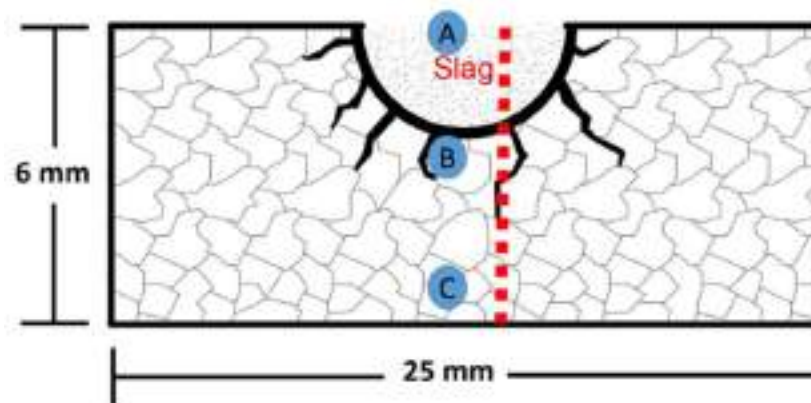


Figure 1. Scheme representing the chemical resistance test of silicomanganese slag on refractory samples where: A = slag zone, B = slag/refractory interface, and C = refractory zone.

3. Results and Discussion

3.1. Microstructural Analysis

Figure 2 shows the XRD patterns of the reference sample (100 wt.% of MgO) and the MgO sample containing 5 wt.% of ZrO₂ nanoparticles. This XRD analyses compare the influence of the sintering temperature (1550 °C and 1650 °C) as well as the effect of the method of obtaining the green compacts (CUP or CUP + CIP). These two compositions were chosen as the most representative to identify the crystalline phases in the samples.

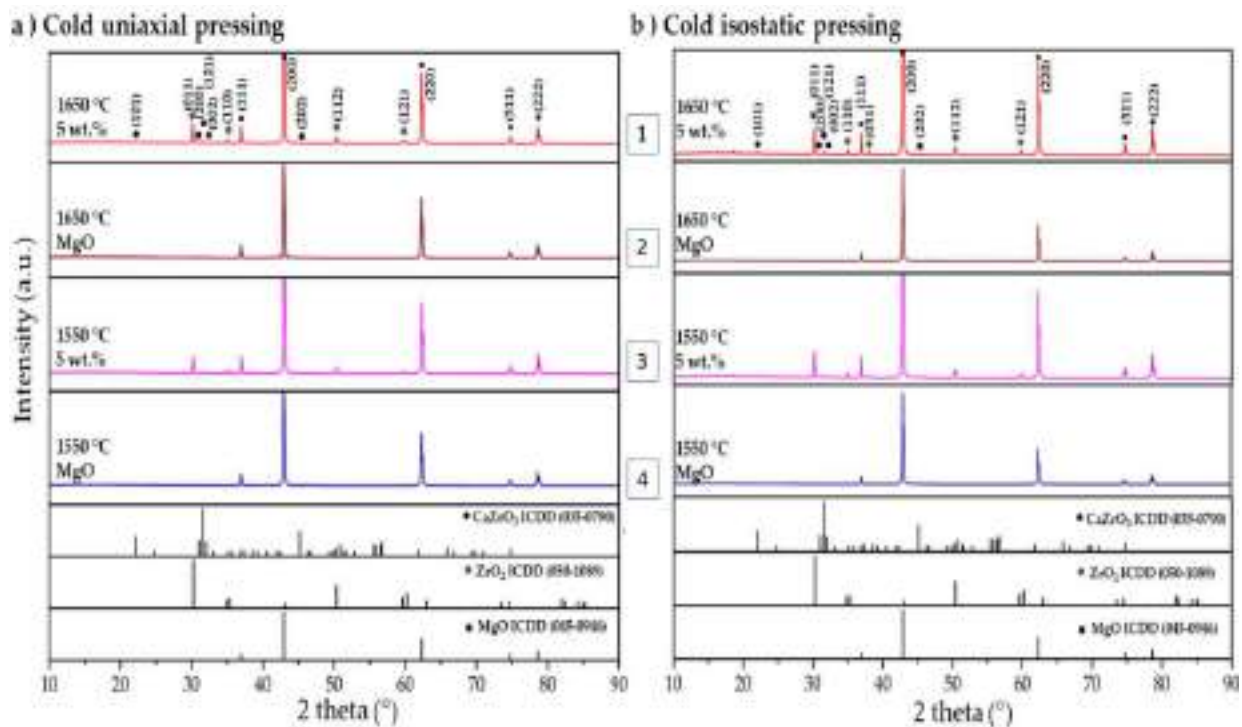


Figure 2. XRD pattern of the sample 100 wt.% MgO (brown and blue line, 2 and 4) and MgO sample containing 5 wt.% of ZrO₂ nanoparticles (red and pink line, 1 and 3) sintered at 1550 °C and 1650 °C, pressed by: (a) Cold uniaxial pressing (CUP) and (b) cold isostatic pressing after cold uniaxial pressing (CUP + CIP).

As can be observed, the reference samples (100 wt.% of MgO) exhibited in all conditions the same crystalline phase (2nd and 4th diagrams), corresponding to periclase (ICDD 45-0946). The patterns show the characteristic peaks located in 2θ equal to 36.93°, 42.91°, 62.3°, 74.64°, and 78.63° with preferential orientations in the crystallographic planes in (111), (200), (220), (311), and (222), respectively.

Meanwhile, samples with 5 wt.% of ZrO₂ nanoparticles (1st and 3rd diagrams) display diffraction planes corresponding to magnesium oxide (MgO) (ICDD 45-0946). Moreover, the zirconium oxide phase (ZrO₂) (ICDD 50-1089) is identified in 2θ equal to 30.27°, 35.25°, 50.37°, and 60.20° with planes diffracted in (011), (110), (112), and (121). Moreover, it was observed in this research that the ZrO₂ nanoparticles were completely surrounded by MgO particles (matrix constituent). In agreement with the MgO–ZrO₂ binary diagram, the ZrO₂ tetragonal phase admits 10% of MgO, and the cubic phase admits up to 27% MgO in solid solution. Thus, there was a change from monoclinic to tetragonal when the composites were sintered at 1600 °C, and this crystallographic change was maintained down to room temperature as the MgO acted as a stabilizer. This can be checked in the X-ray diffraction results in Figure 2 as with 5 wt.% of ZrO₂, peaks corresponding to the tetragonal ZrO₂ were observed (ICDD 50-1089). Small peaks with low-intensity corresponding to the calcium zirconate phase (CaZrO₃) (ICDD 35-0790) were detected. This phase is attributed to the in situ reaction between CaO (phase detected as an impurity of MgO) and the additions of ZrO₂ nanoparticles.

3.2. Morphological Analyses

Figure 3 shows scanning electron microscope images of the reference sample (100 wt.% of MgO) and of the sample with 5 wt.% of ZrO₂ nanoparticles formed by CUP or CUP + CIP and sintered at 1550 °C or 1650 °C.

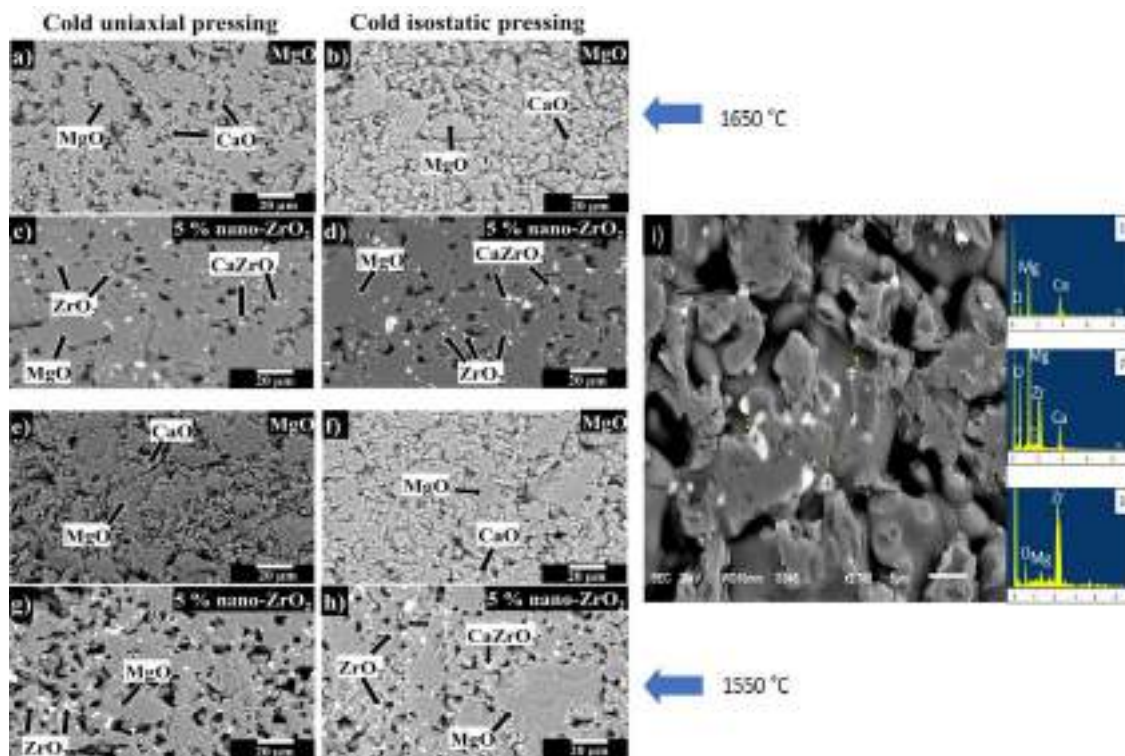


Figure 3. SEM images. (a,b) 100 wt.% MgO samples and (c,d) specimens MgO containing 5 wt.% of ZrO_2 nanoparticles, all sintered at 1650 °C. (e,f) 100 wt.% MgO and (g,h) MgO containing 5 wt.% of ZrO_2 nanoparticles, all sintered at 1550 °C. (i) shows the shape of each of the phases identified as point 1 (CaO), point 2 ($CaZrO_3$), point 3 (ZrO_2). (a,c,e,g) correspond to samples pressed by CUP. (b,d,f,h) correspond to samples pressed by a CUP + CIP.

Figure 3a,b shows the microstructures of MgO samples formed by CUP or CUP + CIP (XL9 and XL13 samples, sintered at 1650 °C, respectively), where MgO grains (dark gray phase) and small CaO particles (blurred white color phase with a particle size $\sim 3 \mu m$) are observed. The MgO aggregates (10 to 40 μm in size) have an angular morphology, while the MgO particles that form the matrix have a quasi-spherical morphology ($< 5 \mu m$ in size). The CaO particles also have an angular morphology.

Figure 3c,d shows the microstructures of the sample with 5 wt.% of ZrO_2 nanoparticles formed by CUP or CUP + CIP techniques and sintered at 1650 °C (XL12, and XL16 samples, respectively). Three main phases corresponding to magnesia (MgO), zirconia (ZrO_2) (circular morphology, bright, intense white color with a particle size $< 3 \mu m$), and calcium zirconate ($CaZrO_3$) (rounded light gray particles with a particles size around 5 μm), were observed. As can be observed, ZrO_2 nanoparticles and $CaZrO_3$ particles are at the grain boundaries and triple points. This microstructural characteristic might lead to the development of a pinning effect that allows not only to reduce the porosity but also to increase the density. The XL16 sample (Figure 3d) developed the highest density value (3.05 g/cm^3) and the lowest porosity percentage (14.48%).

Figure 3e,f, corresponds to the microstructure of MgO samples sintered at 1550 °C (formed by CUP or CUP + CIP techniques, respectively), where MgO grains (dark gray phase) have an irregular shape. Moreover, some CaO particles (soft gray phase) are observed as impurities from raw material. In both microstructures (XL1 and XL5 samples), it is evident a deficit of cohesion between particles develops a dense matrix. This feature opens the opportunity to use a bond phase that allows a better cohesion between particles.

Similar microstructural characteristics were observed in 100 wt.% MgO samples sintered at 1550 and 1650 °C. The highest density (2.71 g/cm^3) and the lowest porosity (26.24%)

were reached by the XL13 sample (100 wt.% MgO) formed by CUP + CIP and sintered at 1650 °C.

Figure 3g,h shows the microstructure of the MgO sample with 5 wt.% ZrO₂ nanoparticles formed by CUP or CUP + CIP techniques and sintered at 1550 °C (XL4 and XL8 samples, respectively). The microstructural analysis revealed the same phases as those identified in the samples sintered at 1650 °C, i.e., MgO, ZrO₂, and CaZrO₃. However, the presence of CaZrO₃ is lower compared with the samples sintered at 1650 °C. The ZrO₂ nanoparticles and CaZrO₃ particles are also located at the grain boundaries and triple points. Figure 3i shows the shape of the phases detected in the XL4 sample: Point 1: CaO, it is possible to see that they are bigger than the nanoparticles, and they appear in blurred white color. Point 2: CaZrO₃, this phase appears with acicular shape with a color intermediate between the bright, intense white points of ZrO₂ and the blurred white color of the CaO. Point 3: ZrO₂ nanoparticles, circular morphology, bright, intense white color.

The difference in density and porosity between the MgO sample that contains 5 wt.% of ZrO₂ nanoparticles sintered at 1550 and 1650 °C (formed by CUP or CUP + CIP techniques) is remarkable. The combined effect of temperature and forming method leads to higher densification and higher reduction in porosity. Besides, a pinning effect through the addition of ZrO₂ nanoparticles might contribute to reaching a higher density and an effective porosity reduction.

In general, some mechanisms might promote the densification of the MgO microstructure through the addition of ZrO₂ nanoparticles [47]: (i) an in situ CaZrO₃ phase formation with a higher density (4.95 g/cm³) than that of the matrix of MgO (3.58 g/cm³), (ii) the development of a ceramic bonding through the CaZrO₃ formation, (iii) a pinning effect due to the specific location of ZrO₂ and CaZrO₃ at the grain boundaries and triple points. It is well known that the pinning effect contributes to the porosity elimination, and thus higher densification is obtained. The pinning effect (through ZrO₂ and CaZrO₃) avoids the grain boundary movement, allowing the porosity elimination. However, that phenomenon does not mean that the grain size cannot grow since all that is happening during sintering is cohesion between particles that leads to the grain growth. That is why MgO grains grow through the pinning effect. Below we demonstrated this effect graphically. Details of the mechanism are indicated in Figure 4.

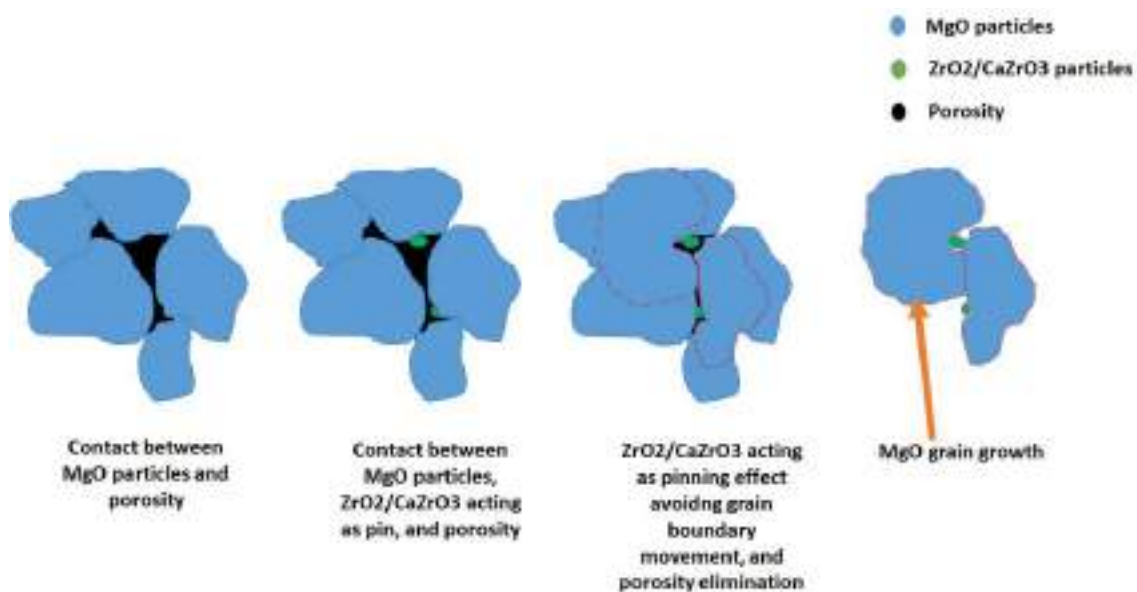


Figure 4. Influence of ZrO₂ nanoparticles on the densification of the samples.

3.3. Mechanical Properties

Figure 5 shows the variation in the cold crushing strength of the magnesia samples reinforced with ZrO₂ nanoparticles (1, 3, 5 wt.%) and the reference sample of MgO (100 wt.%

of MgO). The increase in the ZrO₂ nanoparticles content leads to an increase in mechanical resistance since, in all compositions, an increasing tendency in CCS (Cold Crushing Strength) values can be observed. The sample was made with 100 wt.% MgO formed by CUP and sintered at 1550 °C (XL1, reference sample) reached a mechanical resistance of 60.94 MPa. The sample with 5 wt.% of ZrO₂ nanoparticles formed by CUP and sintered at 1550 °C reached the maximum value of CCS (180.32 MPa, corresponding to the XL4 sample), with an improvement of 66.2% with respect to the reference sample of 100 wt.% MgO, curve 1. Meanwhile, the samples formed by CUP + CIP and sintered at 1550 °C (curve 2) were more sensitive to the forming method since 5 wt.% of ZrO₂ nanoparticles in the composite resulted in a remarkable improvement of 80.44% with respect to the reference sample of 100 wt.% MgO (maximum value of 311.61 MPa, corresponding to the XL8 sample). For the samples formed by CUP and sintered at 1650 °C (XL12 sample), the maximum CCS value was 318.72 MPa, which corresponds to an improvement of 80.87% with respect to the reference sample of 100 wt.% MgO. Finally, the highest cold crushing strength was reached by the sample XL16, which was formed by CUP + CIP and sintered at 1650 °C, 323.78 MPa, corresponding to an improvement of 80.87% with respect to the reference sample of 100 wt.% MgO.

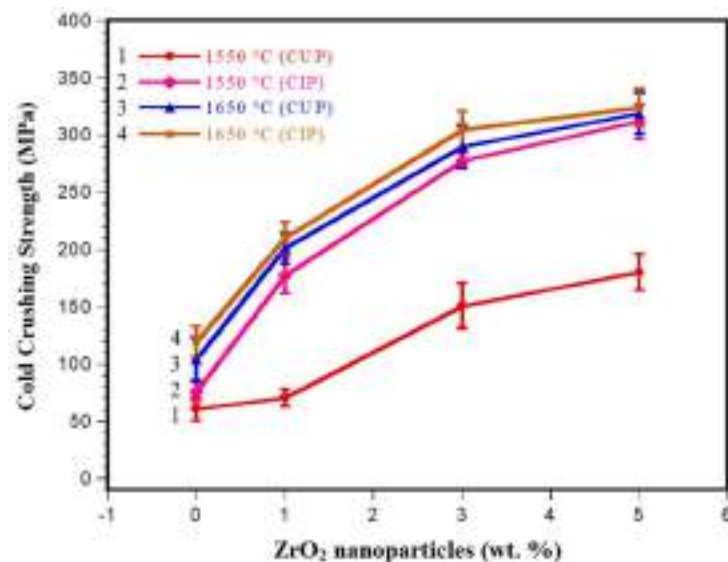


Figure 5. Variations in the cold crushing strength (CCS) of magnesia refractories with different contents of ZrO₂ nanoparticles formed by CUP or CUP + CIP and sintered at 1550 °C and 1650 °C.

As it is known, the temperature is the main factor in a ceramic system that leads to a correct sintering process, thus increasing the mechanical properties among other properties, as was corroborated in these refractory systems. However, at low sintering temperatures (1550 °C), it was confirmed that the forming method controls the increase in mechanical resistance.

In these samples, three mechanisms were present as the concentration of ZrO₂ increased: (i) a crystalline structure change mechanism with energy absorption, i.e., at a high concentration of ZrO₂ nanoparticles, more particles undergo a structural change, which helps to stop the crack propagation. When a crack approaches a ZrO₂ particle (tetragonal zirconia), it is transformed into a new crystalline structure (monoclinic structure) by displacement transformation. This structure change implies energy absorption, causing the crack to slow down and stop [48].

This transformation is not only induced by temperature change but also occurred by a diffusionless shear process at near sonic velocities [3,49,50]. (ii) A volumetric expansion mechanism is believed to be another factor that helps stop cracks. A volumetric expansion (3–5%) is generated by the ZrO₂ phase transition from tetragonal to monoclinic. This transition occurs by displacement transformation induced by pressure [3,51–54]. The

expansion is carried out in the periphery of the ZrO_2 particles. Since these particles increase in volume, they help to deflect or break the cracks [3]. (iii) With an increase in ZrO_2 nanoparticles content and with the CUP + CIP method, samples densified with homogenous pore dispersion into the MgO matrix (isolated pores) were obtained, helping to increase the mechanical resistance.

3.4. Chemical States Analyses

An XPS analysis was carried out in this work to corroborate the results obtained in XRD analysis. According to the best results in previous analyses, the samples pressed by CUP + CIP (XL5, XL8, XL13, and XL16 samples) were studied by XPS high-resolution spectra after the sintering process (Figure 6). Figure 6a–f corresponds to peaks of the binding energy of Mg 1 s, Ca 2 p, and O 1 s for MgO samples sintered at 1550 °C and 1650 °C, respectively. Figure 6g shows high-resolution spectra of zirconia nanoparticles powders before being incorporated into the matrix (MgO). In this case, two peaks can be observed, which are accredited to Zr 3 d components of spin-orbit splitting (three $d_{5/2}$ and three $d_{3/2}$ orbitals), with binding energies of 181.92 eV and 184.29 eV, respectively. The energy difference ΔE , between the Zr 3 d doublets, corresponds to 2.4 eV [55]. The image inserted in Figure 6g shows the high-resolution O 1 s peaks in the binding energies at 529.85 eV [56] and 531.02 eV [57,58], corresponding to ZrO_2 nanoparticles and the carbon tape, respectively. Figure 6h–o corresponds to high-resolution XPS of Mg 1 s, Ca 2 p, O 1 s, and Zr 3 d for samples with 5 wt.% of ZrO_2 nanoparticles sintered at 1550 °C and 1650 °C, respectively.

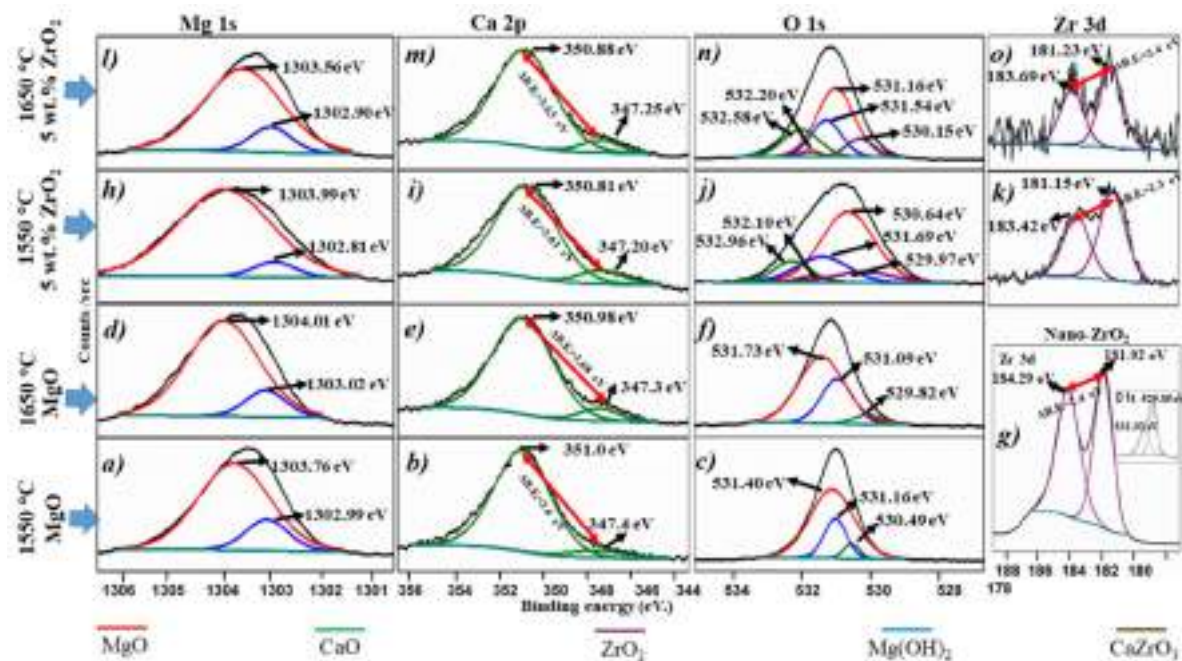


Figure 6. XPS high-resolution spectra of (a) Mg 1 s, (b) Ca 2 p, and (c) O 1 s of MgO sintered a 1550 °C, (d) Mg 1 s, (e) Ca 2 p and (f) O 1 s of MgO sintered a 1650 °C. Spectra in (g) correspond to Zr 3 d for nanoparticles of ZrO_2 . The image in the inset in (g) shows two peaks; one corresponds to the O 1 s spectra of nano- ZrO_2 (higher peak) and the other to C 1 s corresponding to carbon tape. (h–o) Spectra of Mg 1 s, Ca 2 p, O 1 s, and Zr 3 d correspond to samples with 5 wt.% of ZrO_2 nanoparticles sintered at 1550 °C and 1650 °C, respectively.

The deconvoluted core-level spectrum of Figure 6a,d,h,l corresponds to peaks of the binding energy of Mg 1 s of the MgO and Mg(OH)_2 phases. The corresponding binding energy for MgO (red line) was 1303.76, 1304.01, 1303.99, and 1303.56 eV. Meanwhile, the binding energy of Mg(OH)_2 (blue line) was detected at 1302.99, 1303.02, 1302.81, and

1302.90 eV. This phase was detected due to a reaction on the sample surface with the environment humidity.

The deconvoluted core-level spectrum of Figure 6b,e,i,m corresponds to peaks of the binding energy of Ca 2p of the CaO phase, identified by green lines. In the samples with ZrO₂ nanoparticles at 1550 °C and 1650 °C (Figure 6i,m), a chemical shift towards lower binding energies was evident in comparison with those obtained in samples of MgO (Figure 6b,e) sintered at 1550 °C and 1650 °C, respectively. The above is attributed to the formation of the CaZrO₃ phase with binding energies at 347.20 (2 p_{3/2}) and 350.81 (2 p_{1/2}) at 1550 °C, and 347.25 (2 p_{3/2}) and 350.88 (2 p_{1/2}) eV at 1650 °C. These results agree with binding energies values reported in other works [59,60]. XPS analysis confirmed the presence of CaZrO₃ formed in the sample when the ZrO₂ nanoparticles were added, as was observed in XRD analyses [42]. The energy difference (ΔE) was ~3.6 eV and corresponded to Ca 2p doublets, which agrees with the literature [60]. The CaO is an impurity in the raw material that reacts with the ZrO₂ to form CaZrO₃ in MgO samples containing ZrO₂ nanoparticles [3,47].

Figure 6c,f,j,n shows the deconvolution of binding energies of O 1s for MgO (Figure 6c,f) and MgO containing 5 wt.% of ZrO₂ nanoparticles (Figure 6j,n), each sintered at 1550 and 1650 °C. In general, three peaks associated with the phases MgO, Mg(OH)₂, and CaO phases are observed. However, with ZrO₂ nanoparticles, two more peaks corresponding to ZrO₂ and CaZrO₃ (violet and brown line, respectively) are observed. The different binding energies values of O 1s eV peaks of MgO, Mg(OH)₂, CaO, ZrO₂, and CaZrO₃ phases are listed in Table 2. Besides, a comparison is made with those values found in the literature.

Table 2. Binding energy corresponds to O 1s eV peaks of MgO, Mg(OH)₂, ZrO₂, CaO, and CaZrO₃ phases for samples of 100 wt.% MgO sintered a 1550 °C (XL5) and 1650 °C (XL13), samples of MgO containing 5 wt.% of ZrO₂ nanoparticles sintered at 1550 °C (XL8) and 1650 °C (XL16).

Sample	O 1s eV				
	MgO	Mg (OH) ₂	ZrO ₂	CaO	CaZrO ₃
ZrO ₂ nanoparticles			529.85		
XL5	531.4	531.16		530.49	
XL8	530.64	531.69	529.97	532.96	532.1
XL13	531.73	531.09		529.82	
XL16	531.16	531.54	530.15	532.58	532.2
From the literature	529.2 [58], 530.4 [57,58], 531.2 [61].	531.15 [58], 531.5 [58], 531.6 [61], 532.5 [58].	527.1 [62], 529.7 [63], 530.0 [63].	530.10 [64], 532.5 [59].	531.9 [65], 532.2 [59]

Figure 6k,o, shows the deconvolution of the Zr 3d core level spectrum for the sample with 5 wt.% ZrO₂. A doublet in their high-resolution spectra due to spin-orbital coupling is shown. The binding energies correspond to 181.15 (Zr 3d_{5/2}) and 183.42 eV (Zr 3d_{3/2}) (Figure 6k) for samples sintered at 1550 °C and 181.23 (Zr 3d_{5/2}) and 183.69 eV (Zr 3d_{3/2}) (Figure 6o) for samples sintered at 1650 °C. The energy difference (ΔE) between the peaks is ~2.4 eV, which completely agrees with the raw material analyzed of ZrO₂ nanoparticles (Figure 6g).

Table 3 presents the XPS binding energies for high-resolution analysis of Mg 1s, Ca 2p, and Zr 3d of each sample analyzed.

In summary, the changes in chemical states in the elements (Mg, Ca, O, Zr) of the analyzed samples were identified by the XPS technique. The major change was detected in Ca, O, and Zr due to the CaZrO₃ phase formed during the sintering process. According to the literature in Table 2, the bond energies detected in 532.2 and 532.1 eV for oxygen

represents the formation of the CaZrO_3 phase. Meanwhile, the Ca and Zr displayed shifts towards lower bond energies corresponding to a reduction in each element.

Table 3. Binding energy corresponds to Mg 1 s, Ca 2 p, and Zr 3 d of MgO, $\text{Mg}(\text{OH})_2$, CaO, CaZrO_3 , and ZrO_2 phases, corresponding to samples of 100 wt.% MgO sintered at 1550 °C (XL5) and 1650 °C (XL13), MgO containing 5 wt.% of ZrO_2 nanoparticles sintered at 1550 °C (XL8) and 1650 °C (XL16).

Sample	Mg 1 s eV		Ca 2 p eV		Zr 3 d eV	
	MgO	$\text{Mg}(\text{OH})_2$	CaO 2p _{1/2}	CaO 2p _{3/2}	ZrO_2 3d _{3/2}	ZrO_2 3d _{5/2}
ZrO ₂ nanoparticles					184.29	181.92
XL5	1303.76	1302.99	351.00	347.40		
XL8	1303.99	1302.81	350.81	347.20	183.42	181.15
XL13	1304.01	1303.02	350.98	347.30		
XL16	1303.56	1302.90	350.88	347.25	183.69	181.23
From the literature	1303.8 [66], 1303.9 [57,58], 1303.4 [67].	1301.1 [57], 1301.98 [58], 1302.2 [66], 1302.7 [68].	348 [59], 349.7 [64], 351.0 [59,60].	346.5 [59], 347.7 [59].	183 [59], 184.9 [69].	181.1 [70], 182 [63].

3.5. Chemical Properties

3.5.1. MgO Sample Tested with Silicomanganese Slag

Figure 7 shows the morphological analysis of the XL13 sample once it was chemically attacked with silicomanganese slag. The XL13 sample corresponds to MgO formed by CUP + CIP and sintered at 1650 °C. Moreover, a graph corresponding to the concentration of silicomanganese slag elements as a function of the penetration distance is plotted. As a guidance, a schematic representation of the cross-cut section of the specimen used for chemical analysis is observed.

Figure 7a shows the SEM micrograph corresponding to the upper area of the sample (lateral wall of the hole) where the slag was placed. Strong adhesion of silicomanganese slag to the MgO grains is observed, as indicated by the crusts shown in the image. Figure 7b shows the interface between magnesia refractory/silicomanganese slag, where the first contact between MgO grains and slag is displayed. A dense microstructure can be observed due to a slag infiltration into the pores.

Figure 7c corresponds to the sample's lower area, where silicomanganese slag penetration into the matrix can be observed. The slag is located both at the grain boundaries and triple points. The results of the semi-quantitative analysis (EDX) are presented in Figure 7d.

The plotted graph shows the concentration of slag elements associated with the slag (Mn, Ca, Si, and Al) ordered from highest to lowest traces as a function of the penetration distance concerning the height of the sample (6 mm). The letters marked as A (upper area of the sample), B (interface, magnesia refractory/silicomanganese slag), and C (lower area of the sample) and the red dotted lines on the graph correspond to the place (distance from $y = 0$) where the morphological SEM study of the samples was performed. A concentration of 1.11% of slag elements was detected at 181 μm from the bottom of the sample. Likewise, another significant concentration of 7.26% of slag elements was observed at around 763 μm to the bottom of the sample. The slag concentration was 7.63% at a distance from 1927 μm to 3381 μm to the bottom of the sample. This zone represents the boundary between MgO grains and the bottom of the hole where the silicomanganese slag was placed. The slag concentration decreased (~2.94%) due to a slag penetration towards the bottom and walls of the refractory at the zone covered by the hole (3490 μm to 6000 μm distance). Figure 7e shows the cross-section sample and the zones where the SEM micrograph analyses were made (indicated by letters A, B, and C). The path followed to perform the chemical microanalysis by EDX is indicated by the dotted red line.

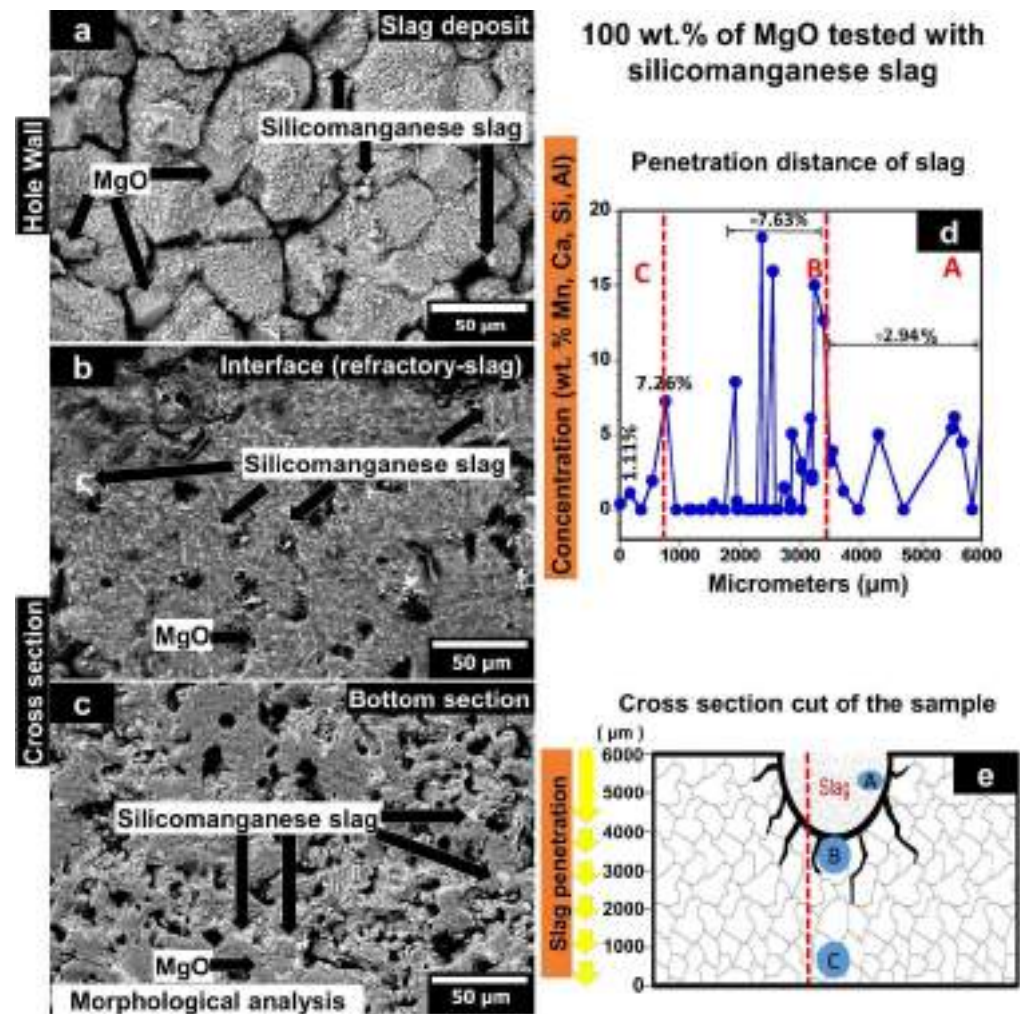


Figure 7. (a–c) SEM images of 100 wt.% MgO sample sintered at 1650 °C and chemically attacked with silicomanganese slag. (d) The concentration of silicomanganese slag elements as a function of the penetration distance. (e) Schematic representation of the cross-cut section of the sample used for chemical analysis.

3.5.2. MgO Containing 5 wt.% of ZrO₂ Nanoparticles Tested with Silicomanganese Slag

Figure 8 shows the morphological analysis of the sample XL16 chemically attacked with silicomanganese slag. The sample XL16 corresponds to the MgO sample that contains 5 wt.% of ZrO₂ nanoparticles formed by CUP + CIP and sintered at 1650 °C. The graph corresponding to the concentration of silicomanganese slag elements as a function of the penetration distance is also plotted. A schematic representation of the cross-cut section of the specimen used for chemical analysis is observed.

In Figure 8a, the wall of the hole where the silicomanganese slag powders were placed to carry out the chemical corrosion analysis is observed. The image shows the molten slag strongly adhered to the MgO and ZrO₂ grains. In some cases, a strong slag adherence leads to the development of a crust that protects the refractory to direct contact with the melted slag, gas, and fluxes. Figure 8b shows a micrograph corresponding to the area below the interface refractory/slag, i.e., the lowest area where the slag was deposited. Slag penetration was mainly observed at the grain boundaries of magnesia. However, some slag penetrated closed pores inside the MgO grains, as was observed in the micrograph. Some agglomerates composed of ZrO₂ nanoparticles are surrounded by some elements from the slag (Mn, Ca, Al, Si, Ti). ZrO₂ nanoparticles might be a barrier at both triple points and grain boundaries to avoid the advance of the SiMn slag in the refractory. As was analyzed, no CaZrO₃ traces were found.

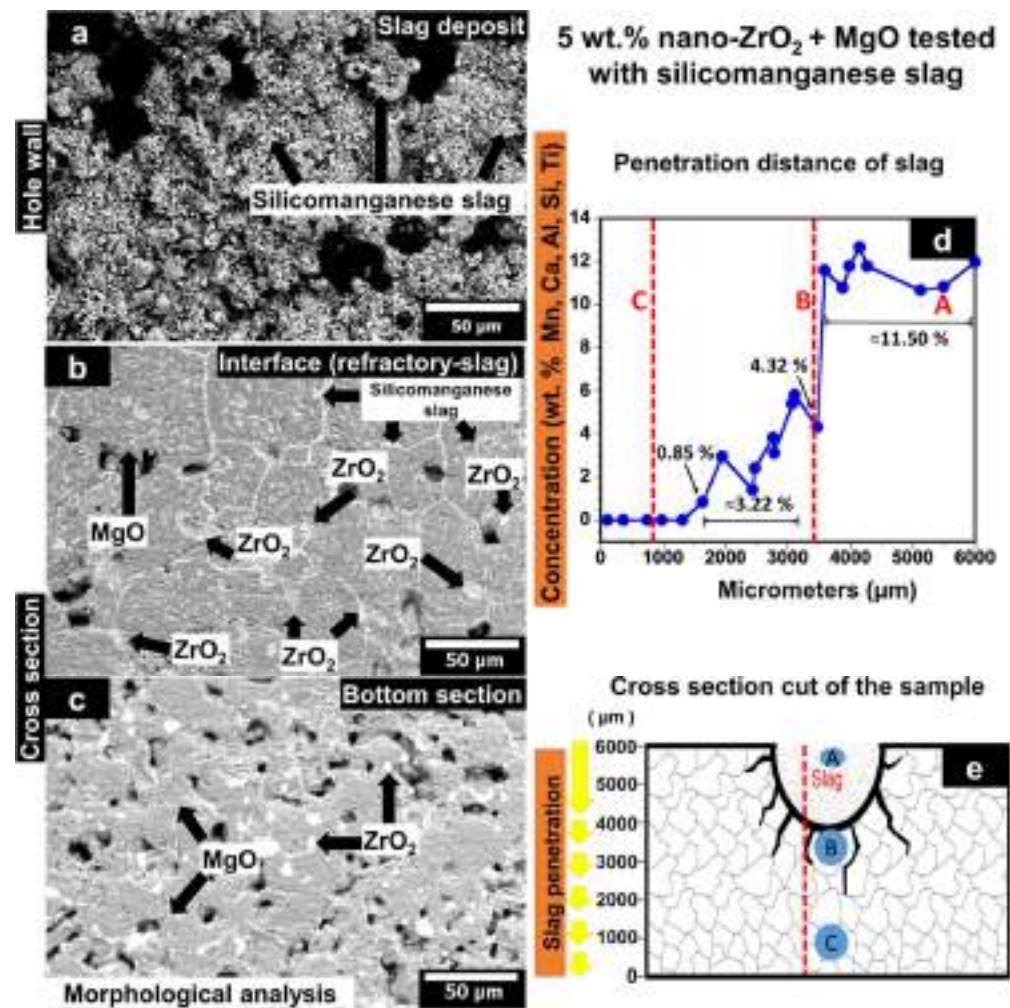


Figure 8. (a–c) SEM images of the MgO sample that contains 5 wt.% of ZrO₂ nanoparticles sintered at 1650 °C and chemically attacked with silicomanganese slag. (d) The concentration of silicomanganese slag elements as a function of the penetration distance. (e) Schematic representation of the cross-cut section of the sample used for chemical analysis.

This phenomenon can be attributed to a possible interaction between CaZrO₃ and the slag. This reaction might change the slag viscosity that prevents slag penetration, i.e., a higher viscosity will help to control or stop the slag infiltration, as reported in other CaZrO₃ refractory systems [23].

The formation of CaZrO₃ was not the objective of the present research work. However, magnesia raw material included CaO among its impurities (up to 1 wt.%), which by reaction with the zirconia nanoparticles lead to the CaZrO₃ formation. CaZrO₃ is located at the grain junctions and triple points since ZrO₂ nanoparticles react with CaO forming CaZrO₃ at these points, also promoted by the utilization of fine particles. The reaction of CaZrO₃ formation is widely reported in the literature [71–73]:

On the other hand, calcium zirconate, due to its beneficial properties, such as high melting point (2345 °C), low linear thermal expansion coefficient ($11.05 \cdot 10^{-6} \text{ K}^{-1}$), high hardness (9.5 GPa), low thermal conductivity, high chemical stability, and corrosion resistance to alkalis (especially KOH), alkaline earth metals, slags [74–76] and other environments such as NaVO₂–Na₂SO₄ mixture [77], can be applied in numerous fields of industry. This chemical compound is stable up to the temperature of 1800 °C, at which the transformation from orthorhombic to cubic phase takes place [78]. CaZrO₃ is also a promising candidate for use in titanium metallurgy. Meanwhile, CaZrO₃ is considered a material for refractory linings in cement kilns when is added to the MgO refractories [28,79,80]. CaZrO₃ was

successfully verified as a competitive refractory material for the melting process of titanium and the production of cement clinker. However, only a few research works concerned the interaction of this refractory compound with steelmaking and ironmaking slags.

Although CaZrO_3 is stable at $1550\text{ }^\circ\text{C}$ in contact with the slag, it is suggested in the present study (considering the chemical composition of the silicomanganese slag (wt.%): 26.88% SiO_2 , 24.85% CaO , 24.56% MnO , 12.41% Al_2O_3 , 4.55% MgO , 1.21% BaO , 0.76% Na_2O , 0.80 K_2O , and balanced others (Fe, P, Ti, Sr)) that the following products can be formed by reaction with the metallurgical slag: calcium zirconate (CaZrO_3), zirconium oxide stabilized with Ca^{2+} ($\text{ZrO}_2\text{stab.}$, Zstab.), gehlenite (C_2AS), and baghdadite ($\text{Ca}_3\text{Zr}[\text{O}_2\text{I Si}_2\text{O}_7]$, C_3ZS_2). These phases coexist in the four-component diagram A–C–Z–S (Al_2O_3 – CaO – ZrO_2 – SiO_2) [81]. The suggested reaction is attributed to the exposure time in contact with slag and the main chemical compounds that constituted the silicomanganese slags.

In Figure 8c, a slag-free microstructure is observed since, in the EDX analysis, only MgO and ZrO_2 are found.

Figure 8d shows the results of the semi-quantitative analysis by the EDX technique. The plotted graph shows the concentration of slag elements (Mn, Ca, Al, Si, and Ti) ordered from highest to lowest traces as a function of the penetration distance concerning the height of the sample (6 mm). The letters (A, B, and C) and red dotted lines on the graph correspond to the area where the morphological study was carried out on the sample. The analysis allowed us to observe that there was no slag penetration at the bottom of the refractory specimen. A slag concentration of 0.85% was detected above $1636\text{ }\mu\text{m}$ concerning the bottom of the sample.

This concentration might result from the slag infiltration into the residual open pores after the sintering process. The slag concentration was 3.22% at a distance from $1945\text{ }\mu\text{m}$ to $3109\text{ }\mu\text{m}$ with respect to the bottom of the sample. This concentration might be due to the slag infiltration through the MgO grain boundaries. At the interface between magnesia refractory/silicomanganese slag ($\sim 3467\text{ }\mu\text{m}$ concerning the bottom of the sample), the concentration of slag elements was 4.32%. The first contact and infiltration of the slag took place in this zone of the refractory. The slag concentration was $\sim 11.5\%$ in the wall of the hole where slag was deposited (at a distance from $3500\text{ }\mu\text{m}$ to $6000\text{ }\mu\text{m}$). This value was higher concerning the sample of 100 wt.% of MgO due to a higher dense refractory matrix that retained more slag elements in this zone. Figure 8e shows the cross-section sample and the zones where the SEM micrograph analyses were made, indicated by letters (A, B, and C). The path followed to perform the chemical microanalysis by EDX is indicated by the dotted red line.

In summary, the change in slag viscosity (a higher slag viscosity) due to the reaction between CaZrO_3 and the melted slag is the main mechanism that leads to a decrease in corrosion attack. Moreover, the addition of ZrO_2 nanoparticles represents a barrier at triple points and grain boundaries to avoid the advance of the slag in the refractory. These two mechanisms help to control or stop the slag penetration.

4. Conclusions

The behavior of MgO ceramics reinforced with ZrO_2 nanoparticles against SiMn slag was studied in this manuscript. Different contents of ZrO_2 nanoparticles (0, 1, 3, and 5 wt.%) were considered, as well as different methods of obtaining green compacts (CUP and CUP + CIP) and sintering temperatures ($1550\text{ }^\circ\text{C}$ and $1650\text{ }^\circ\text{C}$).

Three mechanisms promote the densification of the MgO microstructure through the addition of ZrO_2 nanoparticles: (i) CaZrO_3 phase formation (formed due to in situ reaction between CaO (1 wt.%) and the ZrO_2 nanoparticles) with a higher density (4.95 g/cm^3) than the MgO matrix (3.58 g/cm^3); (ii) development of a ceramic bonding through the CaZrO_3 formation; (iii) pinning effect due to the specific location of ZrO_2 and CaZrO_3 at the grain boundaries and triple points. The lowest values of porosity (14.485%) and the highest value of density (3.0599 g/cm^3) were measured in the samples with 5 wt.% of ZrO_2 nanoparticles formed by CUP + CIP and sintered at $1650\text{ }^\circ\text{C}$.

The main change by the XPS technique was detected in Ca, O, and Zr due to the CaZrO₃ phase formed during the sintering process. The bond energies detected in 532.2 and 532.1 eV for oxygen correspond to the formation of the CaZrO₃ phase.

The increase in mechanical resistance for samples with ZrO₂ nanoparticles is a consequence of this phase. The maximum value of CCS is observed when 5% ZrO₂ nanoparticles are added. Samples were obtained by CUP + CIP and sintered at 1650 °C. The value of cold crushing strength is 80.87% greater than the reference sample with only MgO.

The corrosion resistance is controlled by the CaZrO₃ but also by the decreased porosity, which difficulties the advance of the slag in the refractory. Similarly, ZrO₂ nanoparticles act as a barrier both at the triple points and the grain boundaries, avoiding the advance of silicomanganese slag in the magnesia refractory.

Author Contributions: Conceptualization, C.G.-R. and D.F.-G.; methodology, C.G.-R., D.F.-G., L.F.V., L.V.G.-Q. and G.A.C.-R.; validation, C.G.-R., D.F.-G. and L.F.V.; formal analysis, C.G.-R., D.F.-G., J.A.A.-M. and L.F.V.; investigation, C.G.-R., J.F.L.-P., E.A.R.-C. and M.I.M.-P.; resources, G.A.C.-R.; writing—original draft preparation, C.G.-R., D.F.-G. and L.V.G.-Q.; writing—review and editing, C.G.-R., J.A.A.-M., D.F.-G. and L.V.G.-Q.; visualization, C.G.-R., D.F.-G., L.F.V. and G.A.C.-R.; supervision, D.F.-G. and L.F.V.; project administration, C.G.-R., E.A.R.-C., M.I.M.-P., J.F.L.-P., J.A.A.-M. and G.A.C.-R.; funding acquisition, C.G.-R. and D.F.-G. All authors have read and agreed to the published version of the manuscript.

Funding: Guadalupe Alan Castillo-Rodríguez and Cristian Gómez-Rodríguez thank for the support PAICYT-UANL 2020, IT1382-20. Daniel Fernández-González acknowledges the grant (Juan de la Cierva-Formación program) FJC2019-041139-I funded by MCIN/AEI/10.13039/501100011033 (Ministerio de Ciencia e Innovación, Agencia Estatal de Investigación).

Institutional Review Board Statement: Not applicable.

Informed Consent Statement: Not applicable.

Data Availability Statement: Not applicable.

Acknowledgments: The authors acknowledge the support of Grupo Peñoles (Laguna del Rey, Coahuila, México).

Conflicts of Interest: The authors declare no conflict of interest.

References

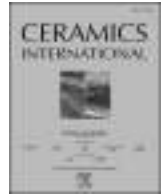
1. Walker, H. *Handbook of Refractory Practice*; Harbinson-Walker: Pittsburgh, PA, USA, 1979.
2. Banerjee, S. Properties of refractories. In *Refractories Handbook*; Schacht, C., Ed.; CRC Press: New York, NY, USA, 2004; pp. 1–10.
3. Verdeja, L.F.; Sancho, J.P.; Ballester, A.; González, R. *Refractory and Ceramic Materials*; Síntesis: Madrid, Spain, 2014.
4. Cardarelli, F. Ceramics, refractories, and glasses. In *Materials Handbook: A Concise Desktop Reference*; Cardarelli, F., Ed.; Springer: London, UK, 2008; pp. 593–689.
5. Sadik, C.; Moudden, O.; El Bouari, A.; El Amranic, A.I.-E. Review on the elaboration and characterization of ceramics refractories based on magnesite and dolomite. *J. Asian Ceram. Soc.* **2016**, *4*, 219–233. [[CrossRef](#)]
6. Horcksmans, L.; Nielsen, P.; Dierckx, P.; Ducastel, A. Recycling of refractory bricks used in steelmaking: A review. *Resour. Conserv. Recycl.* **2019**, *140*, 297–304. [[CrossRef](#)]
7. Verdeja, J.I.; Fernández-González, D.; Verdeja, L.F. *Operations and Basic Processes in Ironmaking*; Springer: Cham, Switzerland, 2020. [[CrossRef](#)]
8. Verdeja, L.F.; Fernández-González, D.; Verdeja, J.I. *Operations and Basic Processes in Steelmaking*; Springer: Cham, Switzerland, 2021. [[CrossRef](#)]
9. Olsen, S.E.; Tangstad, M.; Lindstad, T. *Production of Manganese Ferroalloys*; Tapir Academic Press: Trondheim, Norway, 2007.
10. Thomas, K.; Gunderwar, C.S. *Manganese Ore: Vision 2020 and Beyond*; IBM Press: Nagpur, India, 2014.
11. Steenkamp, J.D.; Pistorius, P.C.; Tangstad, M. Chemical wear analysis of a tap-hole on a SiMn production furnace. *J. S. Afr. Inst. Min. Metal.* **2015**, *115*, 199–208. [[CrossRef](#)]
12. Steenkamp, J.D.; Gous, J.P.; Pistorius, P.; Tangstad, M.; Zietsman, J.H. Wear analysis of a tap-hole from A SiMn production furnace. In *Furnace Tapping Conference 2014*; Steenkamp, J.D., Ed.; The Southern African Institute of Mining and Metallurgy: Johannesburg, South Africa, 2014; pp. 51–64.
13. Sutherland, J.J.; Gous, J.P. Managing the tap-hole life-cycle at five submerged arc furnaces producing silicomanganese at trasalloys. *J. S. Afr. I. Min. Met.* **2019**, *119*, 563–571. [[CrossRef](#)]

14. Banda, W.K.; Steenkamp, J.D.; Matinde, E. An investigation into the wear mechanisms of carbon- and silicon carbide-based refractory materials by silicomanganese alloy. *J. S. Afr. Inst. Min. Metal.* **2020**, *120*, 333–344. [[CrossRef](#)]
15. Borges, R.A.A.; Lenz e Silva, G.F.B. A statistical and post-mortem study of wear and performance of MgO-C resin bonded refractories used on the slag line ladle of a basic oxygen steelmaking plant. *Eng. Fail. Anal.* **2017**, *78*, 161–168. [[CrossRef](#)]
16. Han, B.; Ke, C.; Wei, Y.; Yan, W.; Wang, C.; Chen, F.; Li, N. Degradation of MgO-C refractories corroded by SiO₂-Fe₂O₃-V₂O₅-TiO₂-MnO-MgO slag. *Ceram. Int.* **2015**, *41*, 10966–10973. [[CrossRef](#)]
17. Gómez, C.; Castillo, G.A.; Rodríguez, E.A.; Vázquez-Rodríguez, F.J.; López-Perales, J.F.; Aguilar-Martínez, J.A.; Fernández-González, D.; García-Quiñonez, L.V.; Das-Roy, T.K.; Verdeja, L.F. Development of an ultra-low carbon MgO refractory doped with α -Al₂O₃ nanoparticles for the steelmaking Industry: A microstructural and thermo-mechanical study. *Materials* **2020**, *13*, 715. [[CrossRef](#)] [[PubMed](#)]
18. Muñoz, V.; Galliano, P.G.; Brandaleze, E.; Martínez, A.G.T. Chemical wear of Al₂O₃-MgO-C bricks by air and basic slag. *J. Eur. Ceram. Soc.* **2015**, *35*, 1621–1635. [[CrossRef](#)]
19. Chen, L.; Guo, M.; Shi, H.; Scheunis, L.; Jones, P.T.; Blanpain, B.; Malfliet, A. The influence of ZnO in fayalite slag on the degradation of magnesia-chromite refractories during secondary Cu smelting. *J. Eur. Ceram. Soc.* **2015**, *35*, 2641–2650. [[CrossRef](#)]
20. Chen, L.; Guo, M.; Shi, H.; Huang, S.; Jones, P.T.; Blanpain, B.; Malfliet, A. Effect of ZnO level in secondary copper smelting slags on slag/magnesia-chromite refractory interactions. *J. Eur. Ceram. Soc.* **2016**, *36*, 1821–1828. [[CrossRef](#)]
21. Chen, L.; Li, S.; Jones, P.T.; Guo, M.; Blanpain, B.; Malfliet, A. Identification of magnesia-chromite refractory degradation mechanisms of secondary copper smelter linings. *J. Eur. Ceram. Soc.* **2016**, *36*, 2119–2132. [[CrossRef](#)]
22. Jeon, J.; Kang, Y.; Park, J.H.; Chung, Y. Corrosion-erosion behavior of MgAl₂O₄ spinel refractory in contact with high MnO slag. *Ceram. Int.* **2017**, *43*, 15074–15079. [[CrossRef](#)]
23. Rodríguez, E.A.; Castillo, G.A.; Das, T.K.; Puente-Ornelas, R.; González, Y.; Arato, A.M.; Aguilar-Martínez, J.A. MgAl₂O₄ spinel as an effective ceramic bonding in a MgO-CaZrO₃ refractory. *J. Eur. Ceram. Soc.* **2013**, *33*, 2767–2774. [[CrossRef](#)]
24. Ceylantekin, R.; Aksel, C. Improvements on corrosion behaviours of MgO-spinel composite refractories by addition of ZrSiO₄. *J. Eur. Ceram. Soc.* **2012**, *32*, 727–736. [[CrossRef](#)]
25. Szczerba, J. Chemical corrosion of basic refractories by cement kiln materials. *Ceram. Int.* **2010**, *36*, 1877–1885. [[CrossRef](#)]
26. Aneziris, C.G.; Hubáľková, J.; Barabás, J. Microstructure evaluation of MgO-C refractories with TiO₂- and Al-additions. *J. Eur. Ceram. Soc.* **2007**, *27*, 73–78. [[CrossRef](#)]
27. Ding, X.; Zhao, H.; Xiang, Z.; Zhang, H.; He, Q.; Li, J. Effect of hercynite content on the properties of magnesia-spinel composite refractories sintered in different atmospheres. *Ceram. Int.* **2016**, *42*, 19058–19062. [[CrossRef](#)]
28. Serena, S.; Sainz, M.A.; Caballero, A. Corrosion behavior of MgO/CaZrO₃ refractory matrix by Clinker. *J. Eur. Ceram. Soc.* **2004**, *24*, 2399–2406. [[CrossRef](#)]
29. Kahrizsang, S.G.; Nemati, A.; Shahraki, A.; Farooqhi, M. Effect of nano-sized Fe₂O₃ on microstructure and hydration resistance of MgO-CaO refractories. *Int. J. Nanosci. Nanotechnol.* **2016**, *12*, 19–26.
30. Gómez-Rodríguez, C.; Das, T.K.; Shaji, S.; Castillo-Rodríguez, G.A.; García-Quiñonez, L.; Rodríguez, E.; González, J.O.; Aguilar-Martínez, J.A. Effect of addition of Al₂O₃ and Fe₂O₃ nanoparticles on the microstructural and physico-chemical evolution of dense magnesia composite. *Ceram. Int.* **2015**, *41*, 7751–7758. [[CrossRef](#)]
31. Ghasemi, S.; Gheisari, H.; Boroujerdnia, M. Effect of micro and nano-Al₂O₃ addition on the microstructure and properties of MgO-C refractory ceramic composite. *Mater. Chem. Phys.* **2016**, *189*, 545–551. [[CrossRef](#)]
32. Shahraki, A.; Ghasemi-Kahrizsang, S.A.; Nemati, A. Performance improvement of MgO-CaO refractories by the addition of nano-sized Al₂O₃. *Mater. Chem. Phys.* **2017**, *198*, 354–359. [[CrossRef](#)]
33. Dudczig, S.; Veres, D.; Aneziris, C.G.; Sierra, E.; Steinbrech, R.W. Nano- and micrometre additions of SiO₂, ZrO₂ and TiO₂ in fine grained alumina refractory ceramics for improved thermal shock performance. *Ceram. Int.* **2012**, *38*, 2011–2019. [[CrossRef](#)]
34. Ghasemi-Kahrizsang, S.; Sedeh, M.B.; Dehsheikh, H.G.; Shahraki, A.; Farooqhi, M. Densification and properties of ZrO₂ nanoparticles added magnesia-dolomite refractories. *Ceram. Int.* **2016**, *42*, 15658–15663. [[CrossRef](#)]
35. Dehsheikh, G.H.; Ghasemi-Kahrizsang, S. Performance improvement of MgO-C refractory bricks by the addition of Nano-ZrSiO₄. *Mater. Chem. Phys.* **2017**, *202*, 369–376. [[CrossRef](#)]
36. Ghasemi-Kahrizsang, S.; Karamian, E.; Dehsheikh, H.G. The impact of ZrSiO₄ nanoparticles addition on the microstructure and properties of dolomite based refractories. *Ceram. Int.* **2017**, *43*, 13932–13937. [[CrossRef](#)]
37. Bag, M.; Adak, S.; Sarkar, R. Study on low carbon containing MgO-C refractory: Use of nano carbon. *Ceram. Int.* **2012**, *38*, 2339–2346. [[CrossRef](#)]
38. Dehsheikh, H.G.; Ghasemi-Kahrizsang, S.; Karamian, E. Addition impact of nano-carbon black on the performance of MgO-CaO compounds. *Ceram. Int.* **2018**, *44*, 5524–5527. [[CrossRef](#)]
39. Ghasemi-Kahrizsang, S.; Dehsheikh, H.G.; Karamian, E.; Boroujerdnia, M.; Payandeh, K. Effect of MgAl₂O₄ nanoparticles addition on the densification and properties of MgO-CaO refractories. *Ceram. Int.* **2017**, *43*, 5014–5019. [[CrossRef](#)]
40. Ghasemi-Kahrizsang, S.; Dehsheikh, H.G.; Karamian, E. Impact of Titania nanoparticles addition on the microstructure and properties of MgO-C refractories. *Ceram. Int.* **2017**, *43*, 15472–15477. [[CrossRef](#)]
41. Ghasemi-Kahrizsang, S.; Shahraki, A.; Farooqhi, M. Effect of Nano-TiO₂ Additions on the Densification and Properties of Magnesite-Dolomite Ceramic Composites. *Iran J. Sci. Technol. Trans. A Sci.* **2018**, *42*, 567–575. [[CrossRef](#)]

42. Zargar, H.R.; Oprea, C.; Oprea, G.; Troczynski, T. The effect of nano-Cr₂O₃ on solid-solution assisted sintering of MgO refractories. *Ceram. Int.* **2012**, *38*, 6235–6241. [[CrossRef](#)]
43. Ghasemi-Kahrizsangi, S.; Dehsheikh, H.G.; Boroujerdnia, M. MgO-CaO-Cr₂O₃ composition as a novel refractory brick: Use of Cr₂O₃ nanoparticles. *Bol. Soc. Esp. Ceram. V.* **2017**, *56*, 83–89. [[CrossRef](#)]
44. Dehsheikh, H.G.; Ghasemi-Kahrizsangi, S. The influence of silica nanoparticles addition on the physical, mechanical, thermo-mechanical as well as microstructure of Mag-Dol refractory composites. *Ceram. Int.* **2017**, *43*, 16780–16786. [[CrossRef](#)]
45. Puertas, F. Cementos de escorias activadas alcalinamente: Situación actual y perspectivas de futuro. *Mater. Construcc.* **1995**, *45*, 53–64. [[CrossRef](#)]
46. Ballester, A.; Verdeja, L.F.; Sancho, J.P. *Metalurgia Extractiva: Fundamentos*, 1st ed.; Síntesis: Madrid, Spain, 2000; Volume I.
47. Gómez-Rodríguez, C.; Fernández-González, D.; García-Quiñonez, L.V.; Castillo-Rodríguez, G.A.; Aguilar-Martínez, J.A.; Verdeja, L.F. MgO Refractory Doped with ZrO₂ nanoparticles: Influence of cold isostatic and uniaxial pressing and sintering temperature in the physical and chemical properties. *Metals* **2019**, *9*, 1297. [[CrossRef](#)]
48. Ashby, J.M. *Engineering Materials 2: An Introduction to Microstructures, Processing and Design*; Butterworth-Heinemann: Burlington, VT, USA, 2005.
49. Stevens, R. *Magnesium Elektron, Zirconia and Zirconia Ceramics*; Magnesium Elektron: Manchester, UK, 1986.
50. Wolten, G.M. Diffusionless phase transformations in zirconia and hafnia. *J. Am. Ceram. Soc.* **1963**, *46*, 418–422. [[CrossRef](#)]
51. Platt, P.; Frankel, P.; Gass, M.; Howells, R.; Preuss, M. Finite element analysis of the tetragonal to monoclinic phase transformation during oxidation of zirconium alloys. *J. Nucl. Mater.* **2014**, *454*, 290–297. [[CrossRef](#)]
52. Bailey, J.E. The monoclinic-tetragonal transformation and associated twinning in thin films of zirconia. *Proc. R. Soc. Lond. Ser. A Math. Phys. Sci.* **1964**, *279*, 395–412. [[CrossRef](#)]
53. Qingping, S.; Shouwen, Y.; Kehchih, H. A micromechanics constitutive model for pure dilatant martensitic transformation of ZrO₂-containing ceramics. *Acta Mech. Sin.* **1990**, *6*, 141–150. [[CrossRef](#)]
54. Stam, G.T.; Van der Giessen, E.; Meijers, P. Effect of transformation-induced shear strains on crack growth in zirconia-containing ceramics. *Int. J. Solids Struct.* **1994**, *31*, 1923–1948. [[CrossRef](#)]
55. Moulder, J.F. *Handbook of X-ray Photoelectron Spectroscopy: A Reference Book of Standard Spectra for Identification and Interpretation of XPS Data*; Physical Electronics: Chanhassen, MN, USA, 1995.
56. Reddy, C.V.; Babu, B.; Reddy, I.N.; Shim, J. Synthesis and characterization of pure tetragonal ZrO₂ nanoparticles with enhanced photocatalytic activity. *Ceram. Int.* **2018**, *44*, 6940–6948. [[CrossRef](#)]
57. García, L.V.; Mendivil, M.I.; Roy, T.K.; Castillo, G.A.; Shaji, S. Laser sintering of magnesia with nanoparticles of iron oxide and aluminum oxide. *Appl. Surf. Sci.* **2015**, *336*, 59–66. [[CrossRef](#)]
58. García-Quiñonez, L.V.; Mendivil-Palma, M.I.; Das Roy, T.K.; Castillo-Rodríguez, G.A.; Gómez-Rodríguez, C.; Fernández-González, D.; Shaji, S. Effects of irradiation energy and nanoparticle concentrations on the structure and morphology of laser sintered magnesia with alumina and iron oxide nanoparticles. *Ceram. Int.* **2020**, *46*, 7850–7860. [[CrossRef](#)]
59. Koirala, R.; Gunugunuri, K.R.; Pratsinis, S.E.; Smirniotis, P.G. Effect of zirconia doping on the structure and stability of CaO-based sorbents for CO₂ capture during extended operating cycles. *J. Phys. Chem. C* **2011**, *115*, 24804–24812. [[CrossRef](#)]
60. Cabello, G.; Lillo, L.; Caro, C.; Buono-Core, G.E.; Chornik, B.; Flores, M.; Carrasco, C.; Rodríguez, C.A. Photochemical synthesis of AZrO_{3-x} thin films (A = Ba, Ca and Sr) and their characterization. *Ceram. Int.* **2014**, *40*, 7761–7768. [[CrossRef](#)]
61. Inoue, Y.; Yasumori, I. Catalysis by alkaline earth metal oxides. III. X-ray photoelectron spectroscopic study of catalytically active MgO, CaO, and BaO surfaces. *Bull. Chem. Soc. Jpn.* **1984**, *54*, 1505–1510. [[CrossRef](#)]
62. Shah, D.; Bahr, S.; Dietrich, P.; Mayer, M.; Thiben, A.; Linford, M.R. Zirconium oxide particles, by near-ambient pressure XPS. *Surf. Sci. Spectra.* **2019**, *26*, 024001. [[CrossRef](#)]
63. Bumajdad, A.; Nazeer, A.A.; Al Sagheer, F.; Nahar, S.; Zaki, M.I. Controlled synthesis of ZrO₂ nanoparticles with tailored size, morphology and crystal phases via organic/inorganic hybrid films. *Sci. Rep.* **2018**, *8*, 3695. [[CrossRef](#)]
64. Sosulnikov, M.I.; Teterin, Y.A. X-ray photoelectron studies of Ca, Sr and Ba and their oxides and carbonates. *J. Electron Spectrosc.* **1992**, *59*, 111–126. [[CrossRef](#)]
65. Reddy, G.K.; Quillin, S.; Smirniotis, P. Influence of the synthesis method on the structure and CO₂ adsorption properties of Ca/Zr sorbents. *Energ. Fuel.* **2014**, *28*, 3292–3299. [[CrossRef](#)]
66. Zhang, J.Y.; Wu, Z.L.; Wang, S.G.; Zhao, C.J.; Yang, G.; Zhang, S.L.; Liu, Y.; Liu, S.; Teng, J.; Yu, G.H. Effect of interfacial structures on anomalous Hall behavior in perpendicular Co/Pt multilayers. *Appl. Phys. Lett.* **2013**, *102*, 102404. [[CrossRef](#)]
67. Wan, Y.; Samundsett, C.; Bullock, J.; Hettick, M.; Allen, T.; Yan, D.; Peng, J.; Wu, Y.; Cui, J.; Javey, A.; et al. Conductive and stable magnesium oxide electron-selective contacts for efficient silicon solar cells. *Adv. Energy Mater.* **2017**, *7*, 1601863. [[CrossRef](#)]
68. Haycock, D.E.; Kasrai, M.; Nicholls, C.J.; Urch, D.S. The electronic structure of magnesium hydroxide (brucite) using X-ray emission, X-ray photoelectron, and Auger spectroscopy. *J. Chem. Soc. Dalton Trans.* **1978**, *12*, 1791–1796. [[CrossRef](#)]
69. Li, W.; Liu, X.; Huang, A.; Chu, P.K. Structure and properties of zirconia (ZrO₂) films fabricated by plasma-assisted cathodic arc deposition. *J. Phys. D: Appl. Phys.* **2007**, *40*, 2293–2299. [[CrossRef](#)]
70. Rameshan, C.; Li, H.; Anic, K.; Roiiaz, M.; Pramhaas, V.; Rameshan, R.; Blume, R.; Hëvecker, M.; Knudsen, J.; Knop-Gericke, A. In Situ NAP-XPS spectroscopy during methane dry reforming on ZrO₂/Pt (1 1 1) inverse model catalyst. *J. Chem. Soc. Dalton Trans.* **2018**, *30*, 264007. [[CrossRef](#)]

71. Angers, R.; Tremblay, A.; Chaklader, A.C.D. Formation of CaZrO_3 by solid-state reaction between CaO and ZrO_2 . *J. Am. Ceram. Soc.* **1972**, *55*, 425. [[CrossRef](#)]
72. Serena, S. Modelización Termodinámica y Cálculo del Diagrama de Equilibrio de Fases ZrO_2 - CaO - MgO : Aplicación al Diseño y Obtención de Materiales de MgO - CaZrO_3 . Ph.D. Thesis, Universidad Autónoma de Madrid, Facultad de Ciencias and Instituto de Cerámica y Vidrio (C.S.I.C.), Madrid, Spain, 21 March 2002. Available online: <http://hdl.handle.net/10486/673998> (accessed on 10 March 2022).
73. De la Lastra, C.B.; Pena, P.; Obregón, A.; Rodríguez-Galicia, J.L. Mechanical behaviour of MgO - CaZrO_3 -based refractories for cement kilns. *Adv. Sci. Technol.* **2010**, *70*, 47–52. [[CrossRef](#)]
74. Schafföner, S.; Aneziris, C.G.; Berek, H.; Hubálková, J.; Priese, A. Fused calcium zirconate for refractory applications. *J. Eur. Ceram. Soc.* **2013**, *33*, 3411–3418. [[CrossRef](#)]
75. Hou, Z.F. Ab initio calculations of elastic modulus and electronic structures of cubic CaZrO_3 . *Phys. B Condens. Matter.* **2008**, *403*, 2624–2628. [[CrossRef](#)]
76. Szczerba, J. Modyfikowane magnezjowe materiały ogniotrwałe. *Pol. Tow. Ceram.* **2007**, *99*, 1–204.
77. Silva, A.; Booth, F.; Garrido, L.; Aglietti, E.; Pena, P.; Baudín, C. Sliding wear of CaZrO_3 - MgO composites against ZrO_2 and steel. *J. Eur. Ceram. Soc.* **2017**, *37*, 297–303. [[CrossRef](#)]
78. Szczerba, J. Wyroby magnezjowe z cyrkonianem wapnia w osnowie. *Mater. Ceram.* **2009**, *61*, 7–11.
79. Lang, J.F.; You, J.G.; Zhang, X.F.; Luo, X.D.; Zheng, S.Y. Effect of MgO on thermal shock resistance of CaZrO_3 ceramic. *Ceram. Int.* **2018**, *44*, 22176–22180. [[CrossRef](#)]
80. Ewais, E.M.M.; Bayoumi, I.M.I. Fabrication of MgO - CaZrO_3 refractory composites from Egyptian dolomite as a clinker to rotary cement kiln lining. *Ceram. Int.* **2018**, *44*, 9236–9246. [[CrossRef](#)]
81. Pena, P.; De Aza, S. Compatibility relations of Al_2O_3 in the system ZrO_2 - Al_2O_3 - SiO_2 - CaO . *J. Am. Ceram. Soc.* **1984**, *67*, C3–C5.

Artículo 4: Selective laser sintering of alumina-molybdenum nanocomposites.



Selective laser sintering of alumina-molybdenum nanocomposites

C. Gómez-Rodríguez^{a,b}, L.V. García-Quiñonez^c, L.F. Verdeja^b, G.A. Castillo-Rodríguez^d,
J.A. Aguilar-Martínez^d, A.E. Mariño-Gámez^d, D. Fernández-González^{e,*}

^a Departamento de Mecánica, Facultad de Ingeniería, Campus Coatzacoalcos, Universidad Veracruzana, Av. Universidad Km 7.5 Col. Santa Isabel, Coatzacoalcos, 6535, Veracruz, Mexico

^b Departamento de Ciencia de los Materiales e Ingeniería Metalúrgica, Escuela de Minas, Energía y Materiales, Universidad de Oviedo, 33004, Oviedo/UViú, Asturias, Spain

^c CONACYT-Centro de Investigación Científica y de Educación Superior de Ensenada, B.C (CICESE), Parque de Innovación e Investigación, Carretera Aeropuerto, 66612, Apodaca, Mexico

^d Facultad de Ingeniería Mecánica y Eléctrica, Universidad Autónoma de Nuevo León, Av. Pedro de Alba s/n, 66455, San Nicolás de los Garzas, Mexico

^e Nanomaterials and Nanotechnology Research Center (CINN-CSIC), Universidad de Oviedo (UO), Principado de Asturias (PA), Avda. de la Vega, 4-6, 33940, El Entrego, Spain

ARTICLE INFO

Keywords:

Selective laser sintering
Molybdenum
Alumina
Refractories
Nanocomposite
Toughness

ABSTRACT

Alumina/molybdenum nanocomposites were obtained from alumina and molybdenum particles. Alumina with different molybdenum contents (0, 1, 2.5, 5, 10 and 20 wt %) was first uniaxially pressed at 100 MPa to obtain green compacts that were later sintered using a carbon dioxide (CO₂) laser. Samples were characterized by X-ray diffraction and Scanning Electron Microscope to evaluate the morphological and microstructural characteristics of the composites. SEM results show that for mixtures with 1, 2.5, 5 and 10 wt % Mo, metallic Mo appears dispersed within the alumina grains (grain boundaries and triple points). Nevertheless, for the mixture with 20 wt % Mo, it also appears in the alumina matrix as Mo in triple points and grain boundaries, although MoO₃ is also identified (as inclusion). The presence of these phases was confirmed by X-ray Diffraction technique. These metallic molybdenum particles distributed in the alumina matrix at triple points and grain boundaries promote the densification of the composite. Metallic molybdenum has also a pinning effect, which drastically affects the microstructural evolution during the sintering, mainly on the grain size of alumina. The best results were observed for the composite Al₂O₃-10 wt % Mo, with an average alumina grain size <10 μm and few pores.

1. Introduction

High alumina bricks are widely used in industrial furnaces due to the great characteristics of high temperature performance, great corrosion and wear resistances, among others. However, fracture toughness is sometimes a problem for certain engineering applications. For that reason, several methods have been proposed to improve the fracture toughness in ceramics, mainly based on the crack deflection, which can be made with fibers or whiskers, nacre-like structure or hard second phases. The incorporation of a second phase, such as metallic particles, to the alumina matrix has been subject of research for many years [1]. This way, Matteazzi and Le Caër synthesized nanometric α-Al₂O₃-M composites, where M was Fe, V, Cr, Mn, Co, Ni, Cu, Zn, Nb, Mo, W, Si and Fe alloys [2], which were sintered by aluminothermic reduction. Waku and co-workers also investigated Al₂O₃-Mo, -Ta, -Nb composites

prepared by hot pressing [3]. Other composites Al₂O₃-metal have been proposed to improve the fracture toughness: Al₂O₃-Ni [4–7] and Al₂O₃-W [4,8]. However, molybdenum appears as the metal with the greatest interest to reinforce alumina ceramics when fracture toughness is considered. It has been added in the form of metallic powders, MoO₃ or Mo fibers [9–11]. Nawa and collaborators sintered Al₂O₃-Mo composites by hot pressing under vacuum conditions [12]. Wang and co-authors prepared Al₂O₃-Mo composites by different methods: dissolution of MoO₃ powder in ammonia solution followed by spray-drying or hot-plate drying before hot pressing under hydrogen reductant atmosphere; mechanical mixing and hot pressing [13]. Lada and others prepared Al₂O₃-10 vol % Mo composites by aqueous gel casting method and sintering in argon atmosphere at 1600 °C for 2 h with very slow heating and cooling rates [14]. Broniszewski et al. sintered alumina-molybdenum composites from powders by hot pressing at

* Corresponding author.

E-mail address: d.fernandez@cinn.es (D. Fernández-González).

<https://doi.org/10.1016/j.ceramint.2022.08.058>

Received 27 April 2022; Received in revised form 1 July 2022; Accepted 6 August 2022

Available online 11 August 2022

0272-8842/© 2022 The Authors. Published by Elsevier Ltd. This is an open access article under the CC BY-NC-ND license (<http://creativecommons.org/licenses/by-nc-nd/4.0/>).

1350 °C for 1 h under a pressure of 20 MPa in argon atmosphere [15]. Zyguntowicz and researchers obtained Al₂O₃–Mo composites by centrifugal slip casting method and sintering at 1400 °C for 2 h under 20 vol % H₂–80 vol % N₂ atmosphere [16]. Several questions arise from the above-mentioned research: the improvement of the fracture toughness resulted from both the second phase (molybdenum) on the composite and the inhibition of the alumina grain growth, and the requirement of long sintering processes under special atmosphere (in general reductant) to avoid the oxidation of the molybdenum (to form molybdenum (VI) oxide (MoO₃)), whose boiling point is at 1155 °C.

On the other hand, selective laser sintering (SLS) is a technique that allows the consolidation of powder layers, sintering layer after layer, to obtain three-dimensional parts with fine finishes and complex shapes, being an efficient, economical, high-precision and fast process. Two different types of lasers are commonly used Nd:YAG and carbon dioxide (CO₂). The type of material that can be studied with each laser mainly depends on both the wavelength that each laser generates (1.64 μm and 10.64 μm, respectively) and the wavelength that each material can absorb. Different materials have been treated using laser as heat source for the selective sintering of metallic, ceramic and polymer powders, or mixes between them [17–20]. Great part of the studies in the sintering using laser have focused on the variables that depend on the laser and have direct influence in the properties of the obtained parts: scanning speed [21], scan spacing [22,23], energy density [24,25], laser scanning strategy [26], layer thickness [22,27], laser power [24], particle size and distribution [28].

There is little research about the selective laser sintering of alumina parts. Part of this research focuses on the preparation of powders for later sintering in furnace [29,30]. Regarding direct sintering of alumina (or alumina with additives) using selective laser sintering, it is possible to report the research of Fayed et al. [31] that employed Nd:YAG laser to sinter alumina parts; Shishkovsji and collaborators reported alumina-zirconium porous ceramics manufactured by selective laser sintering using Nd-YAG laser [32]; Subramanian and Marcus sintered alumina with aluminum by Nd-YAG selective laser sintering with subsequent treatment in furnace at different temperatures and times to study the effect [33]. Alumina-molybdenum cermet manufactured using selective laser sintering was not yet reported in the literature.

Despite the significant interest of the alumina-metal composites to obtain alumina-base refractories with improved the fracture toughness (and flexural strength), and the potential advantages of laser sintering technique related with the economization of the processing time, this technique has not been already applied to manufacture such composites. This way, considering the high melting points of the considered materials (Al₂O₃, 2072 °C; Mo, 2623 °C), a heating source as the CO₂ laser was employed. Therefore, we present in this manuscript novel research about the utilization of the selective laser sintering to obtain alumina-Mo composites. The influence of the molybdenum content (0, 1, 2.5, 5, 10 and 20 wt %) on the microstructure and morphology of the

composite was studied when the green compacts were irradiated with carbon dioxide laser.

2. Experimental

2.1. Raw materials and sample preparation

Powders of aluminum oxide (Al₂O₃, 99.9% purity, J.T. Baker) and molybdenum (Mo, 99.9% trace metals basis, Sigma Aldrich) were used as raw materials. SEM images of the initial powders are reported in Fig. 1. These images indicate that most of the molybdenum initial particles are nanometric while the size of the alumina initial particles is in the range 20–100 μm. Six compositions of Al₂O₃ and Mo samples were prepared with the objective of studying the influence of the molybdenum content on the microstructure of the ceramic-metal composite. The samples were prepared considering the following relation: (100–X) wt. % Al₂O₃ + X wt. % of Mo, where X = 0, 1, 2.5, 5, 10 and 20). Once weighted the starting materials in the above-indicated proportion, raw materials were loaded in an attrition mill with alumina balls (3 mm in diameter) in a ratio of 10 to 1 and using isopropyl alcohol as milling medium. Blending was carried out for 5 h in order to ensure a homogeneous mixture. Powder mixtures were treated at 120 °C for 24 h to remove any traces of alcohol and dry powders were sieved by 180 μm. Powders mixture (1 g) were uniaxially pressed in a metallic mold to obtain cylindrical samples of 7 mm in height and 12 mm in diameter using a pressure of 100 MPa for 2 min. A SEM image of the green

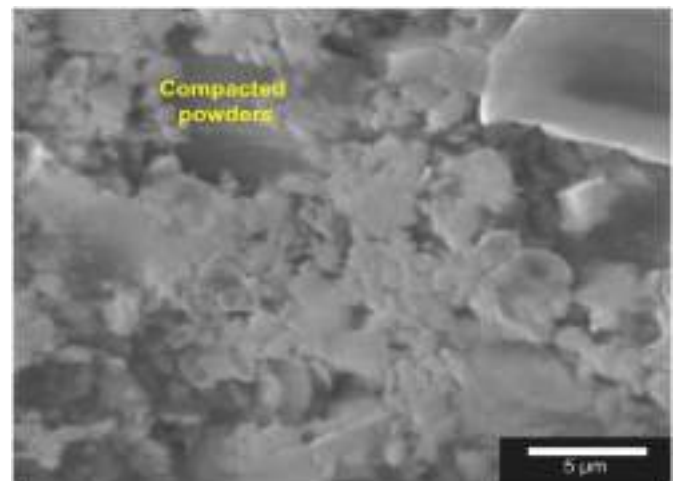


Fig. 2. SEM image of the green compacts. (For interpretation of the references to colour in this figure legend, the reader is referred to the Web version of this article.)

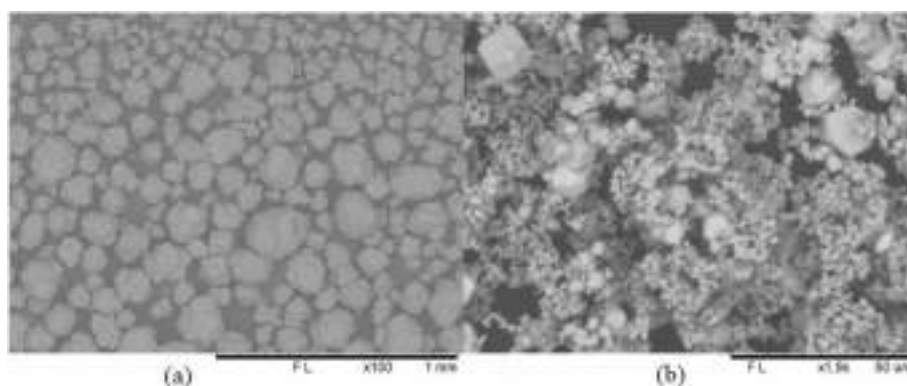


Fig. 1. SEM images of the initial powders of alumina (a) and molybdenum (b).

compacts is reported in Fig. 2 to check the difference with the specimen sintered using laser of CO₂.

2.2. Laser sintering

Green compacts were sintered by means of a CO₂ laser equipment (Coherent, Diamond k-150 model with a wave length $\lambda = 10.64 \mu\text{m}$), where the laser irradiation was perpendicular to the circular surface of the samples. The laser nozzle is fixed in this equipment and the sample was placed on the translation system, which was programmed to move longitudinally, so a parallel radiation was achieved on the diameter of the samples. Subsequently, two more irradiation routes were assigned one next to the other. The sintering resulted on morphological and microstructural changes of the sample.

The following selective laser sintering parameters were considered in this investigation: laser power of 79.5 W, spot diameter of the laser beam of 3 mm and scanning distance of 12 mm. Moreover, the irradiation power density is $Q = 70.29 \text{ W/cm}^2$ and the translation speed was 1.25 mm/s. There is a distance between the laser nozzle and the surface of the sample of 35 mm. Green compacts are located on the surface of the translation equipment and experiments were carried out at room temperature and under ambient atmosphere.

2.3. Characterization

X-ray diffraction technique was used to identify the crystalline phases at the end of the selective laser sintering process. The equipment where the diffraction patterns were obtained was a PANalytical EMPYREAN diffractometer with a target of metal cobalt (radiation $K_{\alpha} = 1.5406 \text{ \AA}$) operated at 40 kV, 40 mA and an X'Celerator detector in Bragg-Brentano geometry. The scans were carried out over a 2θ range from 5° to 120° with a step scan of 0.013° and 25.5 s per step in a continuous mode. Peak fitting was carried out with the commercial software X Powder12.

3. Results

3.1. X-ray diffraction

Results of the X-ray diffraction analyses of laser sintered samples are summarized in Fig. 3. The oxidation of molybdenum has been subject of significant research throughout the years [34,35], because metallic molybdenum exhibits good mechanical properties at high temperatures but the resistance to oxidation is really poor. This way, at temperatures greater than 400°C oxidizes to form MoO₃, which easily volatilizes

(1155°C). This is a problem in the manufacture of composites with molybdenum as this element is lost during their manufacture, as for instance in the case of graphite-molybdenum composites sintered at high temperatures (2600°C [36]). X-ray diffraction analyses suggest that oxidation of molybdenum for contents $<10 \text{ wt } \%$ is not relevant and peaks correspond to only molybdenum and aluminum oxide, which might be associated to the sintering speed. X-ray diffraction analysis of alumina-20 wt % molybdenum composite indicates the presence of molybdenum (VI) oxide, which as it is later observed in SEM-EDX analyses, tends to agglomerate and the pinning effect of the molybdenum microparticles disappear.

3.2. SEM-EDX

The morphological characterization was performed by Field Emission Scanning Electron Microscopy (FESEM) using a FEI Nova Nano SEM 200, with an acceleration voltage of 10–15 kV in low vacuum mode and an Helix detector; additionally, energy dispersive X-ray microanalysis, EDX (Oxford, model INCA X-Sight) was also carried out for semi-quantitative chemical microanalysis. Images are collected in Fig. 4. It is possible to see that molybdenum clearly appears at grain boundaries and triple points, particularly for the composite Al₂O₃-10 wt % Mo. It is precisely in this sample where few pores are identified in the micrographs, which suggest high densification rates. In other cases, there are empty spaces at triple points and grain boundaries that suggest that the sintering of the composite was not complete. It is also possible to see in these cases that grain has grown during the selective laser sintering process, probably due to the insufficient quantity of molybdenum in some cases (when Mo content is $<10 \text{ wt } \%$) and to the significant oxidation of the molybdenum (when Mo content is $>10 \text{ wt } \%$). The sample with 10 wt % has the smallest grain size ($<10 \mu\text{m}$), precisely promoted by the fine molybdenum particles located at triple points and grain boundaries that have a pinning effect. As it was observed in the X-ray diffraction analyses, molybdenum (VI) oxide appears as inclusions in several points of the microstructure for the greatest molybdenum contents (20 wt %). This question is highly relevant for the mechanical properties of the composite as these inclusions appear as stress concentration sites in the composite. In the other cases, metallic molybdenum particles clearly appear at triple points and grain boundaries (see Fig. 4).

3.3. Discussion

The reinforcement of ceramic materials, and in particular alumina ceramics, has always attracted significant interest in an attempt to promote the mechanical properties (as well as the slag corrosion resistance in other cases) by second phases located at triple points and grain boundaries that could divert the crack during its propagation. These second phases also avoid the grain growth and, in this way, a fine grained structure has a significant length of grain boundary, which is beneficial to avoid crack propagation. This manuscript collects a novel research about the application of selective laser sintering to manufacture Al₂O₃-Mo ceramic materials with the aim of studying the microstructure and analyzing how this could have influence on the mechanical properties, in particular on the fracture toughness.

The main problem of the molybdenum is that it easily oxidizes under sintering conditions and this habitually requires sintering the molybdenum-based composites, and Al₂O₃-Mo, under special atmospheres as Ar/H₂ [37], vacuum [12,38], argon [14,15] or H₂/N₂ [16]. In this way, the utilization of fast sintering techniques, as laser, might be useful to minimize the losses of molybdenum as molybdenum (VI) oxide during the sintering process and, at the same time, obtain dense composites. It was possible to see for molybdenum contents $<10 \text{ wt } \%$ that molybdenum (VI) oxide does not appear during the X-ray diffraction analyses (this phase appears in the sample with 20 wt % molybdenum), although this is not indicative of potential minimum losses of this

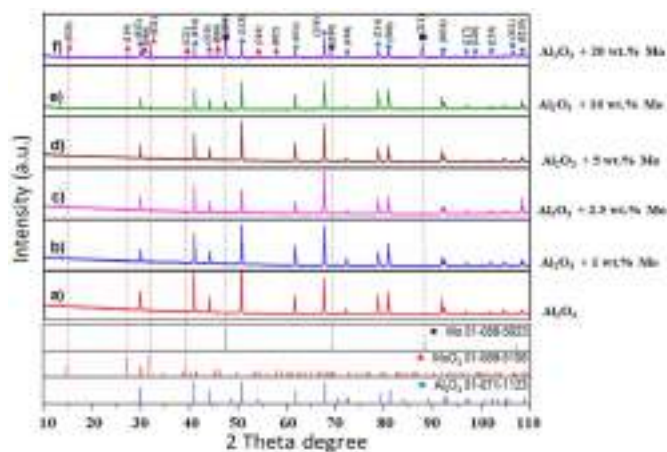


Fig. 3. XRD patterns of: (a) Aluminium oxide (Al₂O₃) sample and (b–f) samples containing 1, 2.5, 5, 10 and 20 wt % of Mo, respectively. At the bottom, the diffraction patterns of Al₂O₃, MoO₃ and Mo are observed.

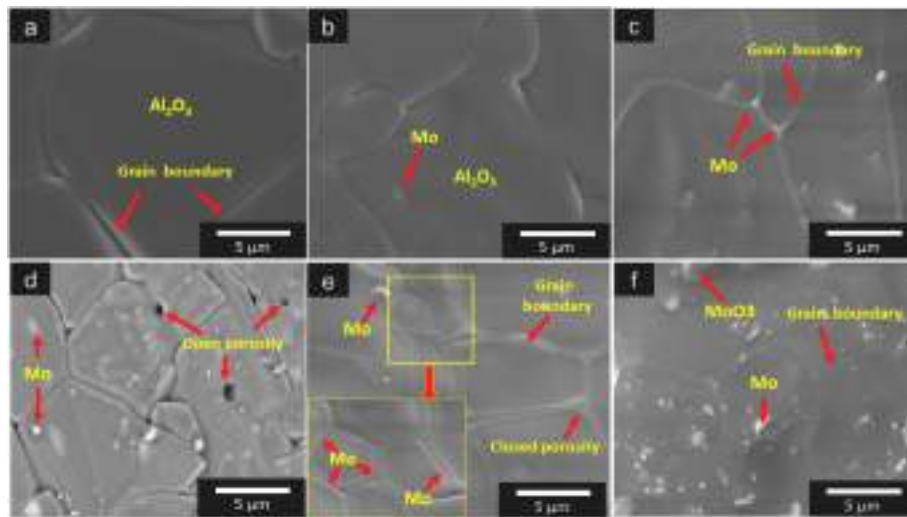


Fig. 4. SEM images of irradiated samples, where: (a) corresponds to Al₂O₃ particles and (b–f) corresponds to 1, 2.5, 5, 10 and 20 wt% of Mo, respectively.

element during the sintering process of the composites with <10 wt % Mo. SEM technique suggests pinning effect promoted by the metallic molybdenum and few pores, which indicates that sintering of the Al₂O₃–Mo composite could be achieved without special atmosphere for these contents of molybdenum. This is potentially beneficial because near-net shape sintered samples could be obtained in very short times without using any special atmosphere, which otherwise could complicate the process. Therefore, laser sintering of ceramic materials arises as a technology that could compete with other novel high energy density technologies as solar energy [39–46] or spark plasma sintering [47,48]. This way, competitiveness of ceramic industry could increase because sintered ceramic materials might be obtained in shorter times. Selective laser sintering technique is a good option to sinter ceramics because it is a versatile technique, which is one of the aspects that is being searched by the industry and, particularly by the additive manufacturing industry. The reason is that this technology allows the rapid fabrication of functional parts, in addition to having the ability to process a wide range of materials (polymers, ceramics and metals) [49], although the manufacture of dense alumina ceramics is still to be studied. Therefore, this manuscript could be a starting point to study the obtaining of dense ceramics using laser technology. There is currently a wide variety of manufacturing techniques, but the most attractive and of greatest importance to the industrial sector are, naturally, those that provide high efficiency in production output without neglecting quality standards. Therefore, one of the most cost-effective methods for manufacturing complex 3D parts is the selective laser sintering technique, which has achieved the highest market share growth since 1997 [50].

Based on several studies [51–56], selective laser sintering could provide a number of advantages as the selection of any specific area, sintering at room temperature (with the sintering temperature being reached only in the surface of the beam), sintering of layers of microns in thickness, selection of the area that is to be irradiated, among others as the possibility of operating under two methods of irradiation, punctual or translational, where in this last case, it is possible to adjust the speed of the beam and the direction of irradiation. Moreover, it is possible to process parts of considerable size. Anyway, the greatest interest of this technology arises from the possibility of obtaining microstructures and morphologies of sintered refractories in seconds, which are comparable with those obtained by means of other sintering methods (as the sintering in furnace) that require hours. This could relate with the productivity but also with the savings in manufacturing costs, the reduction in energy consumption, and, therefore, this process could be environmentally friendly and could attract interest of the industry of ceramics in

general.

There are two laser sources used for the Selective Laser Sintering of materials which are, continuous wave CO₂ with a wavelength of 10.6 μm, and Nd:YAG laser of wavelength 1.06 μm with pulsed or continuous mode [57]. The use of the laser source for each material is mainly governed by the percentage of energy absorption of each material. In the research presented in this manuscript, laser of CO₂ was chosen because we know that the matrix of the composite (Al₂O₃) has high absorption (96% of wavelength of 10.6 μm with CO₂ laser) with long wavelengths [50]. In the case of metals, as molybdenum, it is known that they absorb shorter wavelengths. This way, a sufficient amount of energy was supplied to induce high local temperature leading the beginning of the solid-state sintering. Thus, when the Al₂O₃ atoms were irradiated, they had sufficient energy to make that the vacancies of the Al₂O₃, which are in the hexagonal structure of the aluminum oxide, were replaced at high temperature by other cations that are inside of the volume of the crystal of the aluminum oxide. Therefore, there is a migration towards the grain boundaries, making the grain boundaries to start to move and grow due to the cationic movement, which takes place in the same direction. This growth associated to the movement of cations is drastically affected by the molybdenum particles, located at triple points and grain boundaries, avoiding the growth of the grains and the movement of the grain boundaries.

4. Conclusions

Alumina-molybdenum composites sintered by selective laser sintering were proposed in this manuscript. Different molybdenum contents were studied: 0, 1, 2.5, 5, 10 and 20 wt %. It was possible to see that increasing the molybdenum content resulted in composites with less percentage of porosity. It is possible, for that reason, to say that increasing the molybdenum content results in greater densification rates, which could ensure the good characteristics of the alumina. The best results were observed in the case of the composite Al₂O₃-10 wt % Mo, with an average alumina grain size <10 μm and few pores. It is also observed for this molybdenum content that this element drastically affects the microstructural evolution during the sintering, mainly the final size of alumina, as this element, located at triple points and grain boundaries, inhibits the grain growth. On the other hand, results suggest that laser sintering could be an attractive method to sinter Al₂O₃–Mo ceramics in short times. This is particularly relevant when the molybdenum content is < 10 wt % Mo as greater contents involve the appearance of significant quantities of molybdenum (VI) oxide, which, apart from its potential volatilization and, thus losses of molybdenum, is

detrimental for the mechanical properties of the composite when it appears as inclusion.

Declaration of competing interest

The authors declare that they have no known competing financial interests or personal relationships that could have appeared to influence the work reported in this paper.

Acknowledgements

Daniel Fernández-González acknowledges the grant (Juan de la Cierva-Formación program) FJC2019-041139-I funded by MCIN/AEI/10.13039/501100011033 (Ministerio de Ciencia e Innovación, Agencia Estatal de Investigación).

We thank Dra. Nayely Pineda Aguilar for her support in the utilization of the Scanning Electron Microscope equipment.

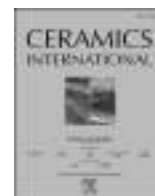
Cristian Gómez-Rodríguez acknowledges the Universidad Veracruzana (Vicerrectoría Coatzacoalcos and Facultad de Ingeniería) for allowing him to make a short stay in the Nanomaterials and Nanotechnology Research Center (CINN-CSIC) and the University of Oviedo (Asturias, Spain) for research activities.

References

- [1] J.S. Moya, S. López-Esteban, C. Pecharrómán, The challenge of ceramic/metal microcomposites and nanocomposites, *Prog. Mater. Sci.* 52 (2000) 1017–1090, <https://doi.org/10.1016/j.pmatsci.2006.09.003>.
- [2] P. Matteazzi, G. Le Caër, Synthesis of nanocrystalline alumina-metal composites by room-temperature ball-milling of metal oxides and aluminum, *J. Am. Ceram. Soc.* 75 (1992) 2749–2755, <https://doi.org/10.1111/j.1151-2916.1992.tb05499.x>.
- [3] Y. Waku, M. Suzuki, Y. Oda, Y. Kohtoku, Improvement of fracture toughness of Al₂O₃ composites by micro-dispersion of flaky refractory metals Mo, Ta and Nb, *J. Ceram. Soc. Jpn.* 103 (1995) 713–719, <https://doi.org/10.2109/jcersj.103.713>.
- [4] T. Sekino, T. Nakajima, S. Ueda, K. Niihara, Reduction and sintering of a nickel-dispersed-alumina composite and its properties, *J. Am. Ceram. Soc.* 80 (1997) 1139–1148, <https://doi.org/10.1111/j.1151-2916.1997.tb02956.x>.
- [5] W.G. Fahrenholtz, D.T. Ellerby, R.E. Loehman, Al₂O₃-Ni composites with high strength and fracture toughness, *J. Am. Ceram. Soc.* 83 (2004) 1279–1280, <https://doi.org/10.1111/j.1151-2916.2000.tb01368.x>.
- [6] E. Breval, G. Dodds, C.G. Pantano, Properties and microstructure of Ni-alumina composite materials prepared by the sol/gel method, *Mater. Res. Bull.* 20 (1985) 1191–1205, <https://doi.org/10.1007/BF00542904>.
- [7] A. Miazga, K. Konopka, M. Gizowska, M. Szafran, Preparation of Al₂O₃-Ni cermet composites by aqueous gelcasting, *Powder Metall. Met* 52 (2014) 567–571, <https://doi.org/10.1007/s11106-014-9561-y>.
- [8] T. Sekino, K. Niihara, Microstructural characteristics and mechanical properties for Al₂O₃/metal nanocomposites, *Nanostruct. Mater.* 6 (1995) 663–666, [https://doi.org/10.1016/0965-9773\(95\)00145-X](https://doi.org/10.1016/0965-9773(95)00145-X).
- [9] W.-C.J. Wei, S.C. Wang, F.H. Cheng, Characterization of Al₂O₃ composites with fine Mo particulates, I Microstructural development, *Acta Metall.* 10 (1998) 965–981, <https://doi.org/10.3390/ma14123398>.
- [10] L.A. Simpson, A. Wasylshyn, Fracture energy of Al₂O₃ containing Mo fibers, *J. Am. Ceram. Soc.* 54 (1971) 56–57, <https://doi.org/10.1111/j.1151-2916.1971.tb12171.x>.
- [11] D.T. Rankin, J.J. Stiglich, D.R. Petrak R. Ruh, Hot-pressing and mechanical properties of Al₂O₃ with a Mo-dispersed phase, *J. Am. Ceram. Soc.* 54 (1971) 277–281, <https://doi.org/10.1111/j.1151-2916.1971.tb12290.x>.
- [12] N. Nawa, T. Sekino, K. Niihara, Fabrication and mechanical behaviour of Al₂O₃/Mo nanocomposites, *J. Mater. Sci.* 29 (1994) 3185–3192, <https://doi.org/10.1007/BF00356661>.
- [13] S.-C. Wang, W.-C.J. Wei, Characterization of Al₂O₃ composites with Mo particulates, II. Densification and mechanical properties, *Nanostruct. Mater.* 10 (1998) 983–1000.
- [14] P. Lada, A. Miazga, M. Zagorska, J. Zygmontowicz, K. Konopka, Characterization of alumina-molybdenum composites prepared by gel casting method, *Powder Metall. Met* 58 (2019) 295–300, <https://doi.org/10.1007/s11106-019-00073-0>.
- [15] K. Broniszewski, J. Wozniak, K. Czechowski, L. Jaworska, A. Olszyna, Al₂O₃-Mo cutting tools for machining hardened stainless steel, *Wear* 303 (2013) 87–91, <https://doi.org/10.1016/j.wear.2013.03.002>.
- [16] J. Zygmontowicz, A. Baczynska, A. Miazga, W. Kaszuwara, K. Konopka, Al₂O₃-Mo functionally graded material obtained via centrifugal slip casting, *Ceram. Mater.* 69 (2017) 73–77.
- [17] Y.P. Kuthuria, Microstructuring by selective laser sintering of metallic powder, *Surf. Coating Technol.* 116–119 (1999) 643–649, [https://doi.org/10.1016/S0257-8972\(99\)00266-2](https://doi.org/10.1016/S0257-8972(99)00266-2).
- [18] P. Bertrand, F. Bayle, C. Combe, P. Goeuriot, I. Smurov, Ceramic components manufacturing by selective laser sintering, *Appl. Surf. Sci.* 254 (2007) 989–992, <https://doi.org/10.1016/j.apsusc.2007.08.085>.
- [19] K. Wudy, L. Lanzl, D. Drummer, Selective laser sintering of filled polymer systems: bulk properties and laser beam material interaction, *Phys. Procedia* 83 (2016) 991–1002, <https://doi.org/10.1016/j.phpro.2016.08.104>.
- [20] K. Murali, A.N. Chatterjee, P. Saha, R. Palai, S. Kumar, S.K. Roy, P.K. Mishra, A. R. Choudhury, Direct selective laser sintering of iron-graphite powder mixture, *J. Mater. Process. Technol.* 136 (2003) 179–185, [https://doi.org/10.1016/S0924-0136\(03\)00150-X](https://doi.org/10.1016/S0924-0136(03)00150-X).
- [21] L.V. García, M.I. Mendivil, T.K.D. Roy, G.A. Castillo, S. Shaji, Laser sintering of magnesia with nanoparticles of iron oxide and aluminum oxide, *Appl. Surf. Sci.* 336 (2015) 59–66, <https://doi.org/10.1016/j.apsusc.2014.09.140>.
- [22] S.K. Ghosh, K. Bandyopadhyay, P. Saha, Development of an in-situ multi-component reinforced Al-based metal matrix composite by direct metal laser sintering technique — optimization of process parameters, *Mater. Char.* 93 (2014) 68–78, <https://doi.org/10.1016/j.matchar.2014.03.021>.
- [23] W.N. Su, P. Erasenthiran, P.M. Dickens, Investigation of fully dense laser sintering of tool steel powder using a pulsed Nd: YAG (neodymium-doped yttrium aluminium garnet) laser, *P. I. Mech. Eng. C- J. Mec.* 217 (2003) 127–138, <https://doi.org/10.1243/095440603762554677>.
- [24] E.O. Olakanmi, R.F. Cochrane, K.W. Dalgarno, Densification mechanism and microstructural evolution in selective laser sintering of Al–12Si powders, *J. Mater. Process. Technol.* 211 (2011) 113–121, <https://doi.org/10.1016/j.jmatprotec.2010.09.003>.
- [25] B. Zhang, H. Liao, C. Coddet, Effects of processing parameters on properties of selective laser melting Mg–9%Al powder mixture, *Mater. Des.* 34 (2012) 753–758, <https://doi.org/10.1016/j.matdes.2011.06.061>.
- [26] X. Su, Y. Yang, Research on track overlapping during selective laser melting of powders, *J. Mater. Process. Technol.* 212 (2012) 2074–2079, <https://doi.org/10.1016/j.jmatprotec.2012.05.012>.
- [27] M. Agarwala, D. Bourell, J. Beaman, H. Marcus, J. Barlow, Direct selective laser sintering of metals, *Rapid Prototyp. J.* 1 (1995) 26–36, <https://doi.org/10.1108/13552549510078113>.
- [28] E.O. Olakanmi, K.W. Dalgarno, R.F. Cochrane, *Rapid Prototyp. J.* 18 (2012) 109–119, <https://doi.org/10.1108/13552541211212096>.
- [29] K. Subramanian, N. Vail, J. Barlow, H. Marcus, Selective laser sintering of alumina with polymer binders, *Rapid Prototyp. J.* 1 (1995) 24–35, <https://doi.org/10.1108/13552549510086844>.
- [30] J. Deckers, J.-P. Kruth, K. Shahzad, J. Vleugels, Density improvement of alumina parts produced through selective laser sintering of alumina-polyamide composite powder, *CIRP Annals* 61 (2012) 211–214, <https://doi.org/10.1016/j.cirp.2012.03.032>.
- [31] E.M. Fayed, A.S. Elmesalamy, M. Sobih, Y. Elshaer, Characterization of direct selective laser sintering of alumina, *Int. J. Adv. Manuf. Technol.* 94 (2018) 2333–2341, <https://doi.org/10.1007/s00170-017-0981-y>.
- [32] I. Shishkovsky, I. Yadroitsev, Ph Bertrand, I. Smurov, Alumina-zirconium ceramics synthesis by selective laser sintering/melting, *Appl. Surf. Sci.* 254 (2007) 966–970, <https://doi.org/10.1016/j.apsusc.2007.09.001>.
- [33] P.K. Subramanian, H.L. Marcus, Selective laser sintering of alumina using aluminum binder, *Mater. Manuf. Process.* 10 (1995) 689–706, <https://doi.org/10.1080/10426919508935060>.
- [34] E.A. Gulbransen, K.F. Andrew, F.A. Brassart, Oxidation of molybdenum 550° to 1700°C, *J. Electrochem. Soc.* 110 (1963) 952, <https://doi.org/10.1149/1.2425918>.
- [35] G. de Micco, H. Nassini, A.E. Bohé, Kinetics of molybdenum oxidation between 375 and 500°C, in: V.S. Saji, S.I. Lopatin (Eds.), *Molybdenum and its Compounds: Applications, Electrochemical Properties and Geological Implication*, Nova Publishers, New York, 2014, pp. 313–339.
- [36] J. Guardia-Valenzuela, A. Bertarelli, F. Carra, N. Mariani, S. Bizzaro, R. Arenal, Development and properties of high thermal conductivity molybdenum carbide-graphite composites, *Carbon* 135 (2018) 72–84, <https://doi.org/10.1016/j.carbon.2018.04.010>.
- [37] L.A. Diaz, A.F. Valdés, C. Díaz, A.M. Espino, R. Torrecillas, Alumina/molybdenum nanocomposites obtained in organic media, *J. Eur. Ceram. Soc.* 23 (2003) 2829–2834, [https://doi.org/10.1016/S0955-2219\(03\)00295-4](https://doi.org/10.1016/S0955-2219(03)00295-4).
- [38] A. Heidarpour, F. Karimzadeh, M.H. Enayati, Fabrication and characterisation of bulk Al₂O₃/Mo nanocomposite by mechanical milling and sintering, *Powder Metall.* 54 (2011) 513–517, <https://doi.org/10.1179/003258910X12740974839585>.
- [39] D. Fernández-González, I. Ruiz-Bustinza, C. González-Gasca, J. Piñuela-Noval, J. Mochón-Castaños, J. Sancho-Gorostiaga, L.F. Verdeja, Concentrated solar energy applications in materials science and metallurgy, *Sol. Energy* 170 (2018) 520–540, <https://doi.org/10.1016/j.solener.2018.05.065>.
- [40] G. Flamant, A. Ferriere, D. Laplace, C. Monty, Solar processing of materials: opportunities and new frontiers, *Sol. Energy* 66 (1999) 117–132, [https://doi.org/10.1016/S0038-092X\(98\)00112-1](https://doi.org/10.1016/S0038-092X(98)00112-1).
- [41] D. Fernández-González, J. Prazuch, I. Ruiz-Bustinza, C. González-Gasca, J. Piñuela-Noval, L.F. Verdeja, Iron metallurgy via concentrated solar energy, *Metals* 8 (2018) 873, <https://doi.org/10.3390/met8110873>.
- [42] D. Fernández-González, J. Prazuch, I. Ruiz-Bustinza, C. González-Gasca, J. Piñuela-Noval, L.F. Verdeja, Solar synthesis of calcium aluminates, *Sol. Energy* 171 (2018) 658–666, <https://doi.org/10.1016/j.solener.2018.07.012>.
- [43] D. Fernández-González, J. Prazuch, I. Ruiz-Bustinza, C. González-Gasca, J. Piñuela-Noval, L.F. Verdeja, Transformations in the Mn-O-Si system using concentrated

- solar energy, *Sol. Energy* 184 (2019) 148–152, <https://doi.org/10.1016/j.solener.2019.04.004>.
- [44] D. Fernández-González, J. Prazuch, I. Ruiz-Bustanza, C. González-Gasca, J. Piñuela-Noval, L.F. Verdeja, Transformations in the Si-O-Ca system: silicon-calcium via solar energy, *Sol. Energy* 181 (2019) 414–423, <https://doi.org/10.1016/j.solener.2019.02.026>.
- [45] D. Fernández-González, J. Prazuch, I. Ruiz-Bustanza, C. González-Gasca, J. Piñuela-Noval, L.F. Verdeja, The treatment of Basic Oxygen Furnace (BOF) slag with concentrated solar energy, *Sol. Energy* 180 (2019) 372–382, <https://doi.org/10.1016/j.solener.2019.01.055>.
- [46] D. Fernández-González, J. Prazuch, I. Ruiz-Bustanza, C. González-Gasca, C. Gómez-Rodríguez, L.F. Verdeja, Recovery of copper and magnetite from copper slag using concentrated solar power (CSP), *Metals* 11 (2022) 1032, <https://doi.org/10.3390/met11071032>.
- [47] M. Suárez, D. Fernández-González, L.A. Díaz, A. Borrell, J.S. Moya, A. Fernández, Synthesis and processing of improved graphite-molybdenum-titanium composites by colloidal route and spark plasma sintering, *Ceram. Int.* 47 (2021) 30993–30998, <https://doi.org/10.1016/j.ceramint.2021.07.267>.
- [48] M. Suárez, D. Fernández-González, C.F. Gutiérrez-González, L.A. Díaz, A. Borrell, J. S. Moya, R. Torrecillas, A. Fernández, Effect of green body density on the properties of graphite-molybdenum-titanium composite sintered by spark plasma sintering, *J. Eur. Ceram. Soc.* 42 (2022) 2048–2054, <https://doi.org/10.1016/j.jeurceramsoc.2021.12.073>.
- [49] S.J.J. Kumar, Selective laser sintering: a qualitative and objective approach, *JOM-J. Min. Met. Mat. S.* 55 (2003) 43–47, <https://doi.org/10.1007/s11837-003-0175-y>.
- [50] J.P. Kruth, X. Wang, T. Laoui, L. Froyen, Lasers and materials in selective laser sintering, *Assemb. Autom.* 23 (2003) 357–371, <https://doi.org/10.1108/01445150310698652>.
- [51] E.M. Mohamed, S.F. Barakh Ali, Z. Rahman, S. Dharani, T. Ozkan, M. A. Kuttolamadom, M.A. Khan, Formulation optimization of selective laser sintering 3D-Printed tablets of clindamycin palmitate hydrochloride by response surface methodology, *AAPS PharmSciTech* 21 (2020) 232, <https://doi.org/10.1208/s12249-020-01775-0>.
- [52] Y.A. Gueche, N.M. Sanchez-Ballester, S. Cailleaux, B. Bataille, I. Soulairol, Selective laser sintering (SLS), a new chapter in the production of solid oral forms (SOFs) by 3D printing, *Pharmaceutics* 13 (2021) 1212, <https://doi.org/10.3390/pharmaceutics13081212>.
- [53] P. Muthuswamy, Additive manufacturing of tungsten carbide hardmetal parts by selective laser melting (SLM), selective laser sintering (SLS) and binder jet 3D printing (BJ3DP) techniques, *Lasers Manuf. Mater. Process.* 7 (2020) 338–371, <https://doi.org/10.1007/s40516-020-00124-0>.
- [54] F. Fina, A. Goyanes, S. Gaisford, A.W. Basit, Selective laser sintering (SLS) 3D printing of medicines, *Int. J. Pharm. (Amst.)* 529 (2017) 285–293, <https://doi.org/10.1016/j.ijpharm.2017.06.082>.
- [55] E. Balliu, H. Andersson, M. Engholm, T. Öhlund, H.-E. Nilsson, H. Olin, Selective laser sintering of inkjet-printed silver nanoparticle inks on paper substrates to achieve highly conductive patterns, *Sci. Rep.* 8 (2018), 10408, <https://doi.org/10.1038/s41598-018-28684-4>.
- [56] A. Franco, M. Lanzetta, L. Romoli, Experimental analysis of selective laser sintering of polyamide powders: an energy perspective, *J. Clean. Prod.* 18 (2010) 1722–1730, <https://doi.org/10.1016/j.jclepro.2010.07.018>.
- [57] J.P. Kruth, M.C. Leu, T. Nakagawa, Progress in additive manufacturing and rapid prototyping, *CIRP Annals* 47 (1998) 525–540, [https://doi.org/10.1016/S0007-8506\(07\)63240-5](https://doi.org/10.1016/S0007-8506(07)63240-5).

Artículo 5: Alumina/molybdenum nanocomposites obtained by colloidal synthesis and spark plasma sintering.



Alumina/molybdenum nanocomposites obtained by colloidal synthesis and spark plasma sintering

D. Fernández-González^{a,*}, M. Suárez^{a,**}, J. Piñuela-Noval^a, L.A. Díaz^a, C. Gómez-Rodríguez^b, L.V. García Quiñonez^c, A. Borrell^d, A. Fernández^a

^a *Nanomaterials and Nanotechnology Research Center (CINN-CSIC), Universidad de Oviedo (UO), Principado de Asturias (PA), Avda. de la Vega, 4-6, 33940, El Entrego, Spain*

^b *Departamento de Mecánica, Facultad de Ingeniería, Campus Coatzacoalcos, Universidad Veracruzana, Av. Universidad Km 7.5 Col. Santa Isabel, Coatzacoalcos, 96535, Veracruz, Mexico*

^c *CONACYT-Centro de Investigación Científica y de Educación Superior de Ensenada, B.C (CICESE), Parque de Innovación e Investigación, Carretera Aeropuerto, 66612, Apodaca, Mexico*

^d *Instituto de Tecnología de Materiales, Universitat Politècnica de València (UPV), Camino de Vera S/N, 46022, Valencia, Spain*

ARTICLE INFO

Keywords:

Ceramics
Composite materials
Sintering
Mechanical properties
Spark plasma sintering
Alumina
Cermets

ABSTRACT

Alumina/molybdenum nanocomposites were prepared by colloidal synthesis from alumina powder and molybdenum (V) chloride using ethanol as dispersion medium. Modified alumina was calcined at 450 °C in air atmosphere to remove chlorides, and then treated in a tubular furnace at 850 °C under Ar/H₂ to reduce the MoO₃ formed in the previous stage and obtain Al₂O₃ with molybdenum nanoparticles on the surface. Three different molybdenum contents were proposed (1, 5 and 10 wt % Mo), and pure alumina was used as reference, that were sintered by spark plasma sintering (SPS) under vacuum atmosphere at 1400 °C for 3 min with an applied pressure of 80 MPa. Composites were characterized by microstructure, hardness, toughness, and three-point bending test. The presence of molybdenum nanoparticles resulted in a fine-grained structure promoted by the presence of molybdenum at grain boundaries and triple points, as well as by the utilization of the SPS equipment. Hardness is at least a 20% greater and fracture toughness 30% larger in the composites than in the monolithic alumina.

1. Introduction

One of the main interests of ceramic materials is the wear resistance together with the thermal and chemical stabilities [1]. These properties are important for some engineering applications [2]. The main problem of ceramic materials arises from the mechanical properties. These materials are, in general, brittle, since they are easily broken by crack propagation. Several methods have been proposed to improve fracture toughness of ceramics. One of these is based on the crack deflection, which can be made with fibers or whiskers, with a nacre-like structure or with hard second phases. The incorporation of a second phase, such as metallic particles, to improve the mechanical properties of the alumina has been proposed for years [3]. This way, Mattecazzi and Le Caër synthesized nanometric α -Al₂O₃-M composites, where M was Fe, V, Cr, Mn, Co, Ni, Cu, Zn, Nb, Mo, W, Si and Fe alloys [4]. They prepared the composites by room temperature ball milling of mixtures of the

above-mentioned metal oxides and aluminum and, nanocomposites were obtained by aluminothermic reduction in different times (1.5–24 h) using different powder-to-ball weight ratio (1:30 to 1:40 in the planetary, and 1:10 to 1:5 in the vibratory) under pure nitrogen or argon atmosphere depending on the mixture. They satisfactorily produced nanocomposites to be used as dispersoids in high temperature metals and alloys to improve the properties. Other researchers also investigated the composites Al₂O₃-metal. Within this line, Waku and co-workers also investigated Al₂O₃-Mo, -Ta, -Nb composites prepared by hot pressing [5], which resulted in a significant increase of the flexural strength and fracture toughness of the composite.

Some other Al₂O₃-metal composites were studied by different researchers:

- Al₂O₃-Ni. Within this topic, Sekino and collaborators studied high-density nickel-dispersed-alumina (Al₂O₃/Ni) composites with

* Corresponding author.

** Corresponding author.

E-mail addresses: d.fernandez@cinn.es (D. Fernández-González), m.suarez@cinn.es (M. Suárez).

<https://doi.org/10.1016/j.ceramint.2022.11.108>

Received 25 August 2022; Received in revised form 27 October 2022; Accepted 8 November 2022

Available online 10 November 2022

0272-8842/© 2022 Elsevier Ltd and Techna Group S.r.l. All rights reserved.

excellent mechanical properties (high strength and high-temperature hardness) by reduction with hydrogen and hot pressing of $\text{Al}_2\text{O}_3/\text{NiO}$ mixed powders [6]. Also in this line, Fahrenholtz and colleagues reported $\text{Al}_2\text{O}_3\text{-Ni}$ composites, prepared by reactive hot pressing of aluminum and NiO, with high strength and toughness [7]. Additionally, Breval and coauthors studied the properties (hardness, stiffness, and toughness) and microstructure of $\text{Ni-Al}_2\text{O}_3$ composite materials prepared by sol/gel method [8]. Miazga et al. prepared $\text{Al}_2\text{O}_3\text{-Ni}$ composites, with improved fracture toughness of the matrix, by aqueous gel casting process and sintering in reducing atmosphere [9]. And, finally, Rodríguez-Suárez et al. studied $\text{Al}_2\text{O}_3\text{-Ni}$ composites sintered by conventional route and spark plasma sintering [10].

- $\text{Al}_2\text{O}_3\text{-W}$: Also, Sekino, and collaborators, prepared two types of $\text{Al}_2\text{O}_3\text{-W}$ composites by hot pressing of $\alpha\text{-Al}_2\text{O}_3$ and $\gamma\text{-Al}_2\text{O}_3$ and tungsten powders resulting in improved fracture toughness (1.6 times) compared with the monolithic Al_2O_3 [11]. Moreover, Sekino and Niihara studied the mechanical properties of high density $\text{Al}_2\text{O}_3\text{-W}$ nanocomposites prepared by controlled reduction and hot pressing of $\text{Al}_2\text{O}_3\text{-WO}_3$ mixtures [12]. Finally, Rodríguez-Suárez et al. [13] prepared $\text{Al}_2\text{O}_3\text{-nW}$ composites by colloidal processing route and spark plasma sintering and obtained full dense compacts with high hardness.
- $\text{Al}_2\text{O}_3\text{-Fe}$: This family of composites was few studied; only the research of Konopka and Oziębło can be found in the literature [14]. The methodology that they used to prepare the composite (with different iron contents (10, 30 and 50 wt %)) consisted in: wet mixing of reactants in ethanol for 2 h in agate mill; application of uniaxial (20 MPa) and isostatic (120 MPa) pressing to obtain the green compacts; and, sintering in two stages (900 °C and 1700 °C in vacuum for 1.5 h). They observed that the improvement of mechanical properties was limited by the appearance of FeAl_2O_4 spinel.

However, molybdenum is the metallic phase that has attracted the greatest interest due to its refractory character to improve the mechanical properties of the alumina, particularly the fracture toughness, and the composite being suitable to be used at high temperatures. Molybdenum has been added in the form of metallic powders, MoO_3 or Mo fibers [15]. Different techniques and molybdenum contents (up to a maximum of 26.6 vol % [16]) have been proposed to prepare $\text{Al}_2\text{O}_3\text{-Mo}$ composites: spray-drying, hydrogen reduction and sintering with or without hot-pressing [15]; hot-pressing under vacuum conditions [17, 18]; conventional powder metallurgy technique [19]; dissolution of MoO_3 powder in ammonia solution, followed by spray-drying or hot-plate-drying to obtain ammonium molybdate/ Al_2O_3 granules that were subsequently reduced in hydrogen atmosphere and hot-pressed to obtain $\text{Mo}/\text{Al}_2\text{O}_3$ composites [20]; aqueous gel casting method and sintering in argon atmosphere at 1600 °C with 2 h of retention and slow heating and cooling rates (3 and 5 °C/min) [21]; or consolidation by centrifugal slip casting at 3000 rpm for 1.5 h (slurry containing 50 vol % solid phase including 10 vol % molybdenum particles), drying at 30 °C for 48 h and sintering at 1400 °C for 2 h in 20 vol % $\text{H}_2\text{-80 vol % N}_2$ [22]. And, much more recently, Gómez-Rodríguez and coauthors reported the possibility of sintering $\text{Al}_2\text{O}_3\text{-Mo}$ composites using laser of CO_2 as heat source [23]. However, spark plasma sintering technique has yet to be reported in the manufacture of $\text{Al}_2\text{O}_3\text{-Mo}$ composites.

On another note, the improvement of the mechanical properties of the monolithic alumina, apart from the addition of the metal, requires a nanometric size and a homogenous distribution in the matrix. Within this line, it was observed that fine dispersoids resulted in the grain growth restrain due to pinning effect at grain boundaries [16], which is positive for the fracture toughness and hardness of the composite [16, 20]. Moreover, the homogeneity of the microstructure of the composite has a critical influence on the properties [20]. Therefore, colloidal processing method has been seen as a technology very suitable to obtain homogeneous distribution of nanoparticles in ceramic materials [24].

Already published research reported that it is possible to obtain a very homogeneous distribution of very small molybdenum nanoparticles in an alumina matrix using this technique [25]. On the other hand, Spark Plasma Sintering (SPS) is a relatively novel technique that is attracting significant interest because it allows a high-speed of powder consolidation [26]. This technique has not been applied in the manufacture of $\text{Al}_2\text{O}_3\text{-Mo}$ composites, as it was already indicated. Therefore, the synthesis of alumina/molybdenum nanocomposites starting from a modified alumina powder in a solution of molybdenum (V) chloride in ethanol and subsequent sintering in spark plasma apparatus is proposed in this manuscript. The presence of molybdenum nanoparticles has significant influence in the microstructural evolution during sintering and, as a result, mechanical properties are significantly affected.

2. Experimental procedure

2.1. Processing of alumina/molybdenum composites

Alumina/molybdenum nanocomposites were prepared using $\alpha\text{-alumina}$ (Al_2O_3) powder (Taimei Chemicals Co., Ltd, Tokyo, Japan) with $d_{50} = 0.153 \mu\text{m}$, a specific surface area of $14.5 \text{ m}^2/\text{g}$ and 99.99% purity (8 ppm Na, 10 ppm Si, 8 ppm Fe), and molybdenum (V) chloride (Sigma Aldrich, Madrid, Spain) as molybdenum precursor.

The preparation of the composite is detailed in the following lines. The procedure was the same for the three compositions that were chosen (1 wt % Mo, 5 wt % Mo and 10 wt % Mo), apart from the monolithic alumina. First, alumina powders and molybdenum (V) chloride were dispersed in ethanol (anhydrous 99.97% ethanol) separately. Later, molybdenum (V) chloride solution in ethanol was added dropwise into the alumina solution. The slurry was first heated at 80 °C under magnetic stirring. After that, it was heated at 120 °C for 24 h in air atmosphere to start the nucleation of the composite and remove the ethanol. Dried powders were sieved under 180 μm , and they were later treated at 450 °C for 2 h in air atmosphere to remove chlorides and reduced afterwards under Ar/H_2 atmosphere at 850 °C for 2 h to obtain molybdenum nanoparticles. Treated powders were sieved under 63 μm . Finally, the powders were sintered using the spark plasma sintering apparatus.

Powders were first placed into a graphite die (20 mm inner diameter) and uniaxial pressure of 80 MPa was used at the same time that temperature was applied. The cycle of the process consisted in heating at a rate of 100 °C/min from room temperature to the sintering temperature (1400 °C), and finally, sample was sintered for 3 min of dwell time at 1400 °C. Cooling was carried out inside of the equipment at a cooling rate of around 500 °C/min. Temperature was controlled by a pyrometer.

2.2. Characterization techniques

X-ray diffraction analyses of the powders as well as of the sintered samples were carried out using a Bruker D8 Advance Powder X-ray Diffractometer with $\text{Cu-K}\alpha$ radiation ($\lambda = 0.15406 \text{ nm}$). Working conditions included a copper anticathode cooled with water with an intensity of 40 mA and a voltage of 40 kV, a sweep between 5 and 70° with a step size of 0.03° and a step time of 0.5 s.

The relative density of the sintered samples was calculated using Eq. (1).

$$\rho(\%) = d/d_m \cdot 100 \quad (1)$$

where d is the density measured using the Archimedes method and d_m is the real density obtained by helium pycnometry using Accupyc 1330 V2.04 N on samples previously grounded below 63 μm to increase the accuracy of the measurement.

High-resolution transmission electron microscopy (HRTEM) was used to evaluate the adherence of the molybdenum nanoparticles to the surface of the alumina particles. The equipment was a JEOL JEM 2100F

with an acceleration voltage of 200 kV with a field emission gun.

Microstructural characterization and fracture surface of the sintered samples was performed by Field Emission Scanning Electron Microscopy (FESEM) on a Quanta FEG 650.

Vickers microhardness was determined using a Buehler Micromet 5103 microindenter. Measurements were made by applying loads of 1000 gf, with an indentation time of 10 s, on samples polished down to a roughness of 1 μm . The applied load was worked out considering the Kick Law. Hardness was determined according to Eq. (2).

$$H_v = 1.853 P/d^2 \quad (2)$$

where P stands for the applied load (in N) and d is the diagonal length of the indentation (in mm).

Fracture toughness, K_{IC} , was determined by means of the indentation method using Eq. (3):

$$K_{IC} = \frac{P}{C^{3/2}} \quad (3)$$

where P is the applied load using the indenter, and C is the length of the crack.

Mechanical properties were tested in mechanical tests machine Instron 8562. Samples of 3 mm x4 mm x20 mm were prepared to evaluate the flexural resistance. Mechanical resistance of materials after the three-point bending test was evaluated using Eq. (4):

$$\sigma_f = \frac{3 \cdot P \cdot L}{2 \cdot w \cdot b^2} \quad (4)$$

where σ_f is the mechanical resistance of the material in MPa, P is the load the sample supports in N, L is the distance between supports in mm, w is the width of the sample in mm and b is the thickness of the sample in mm.

3. Results and discussion

3.1. Nanocomposite powders

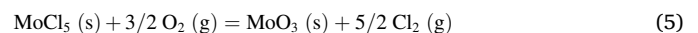
3.1.1. Sintering curve in the SPS

Fig. 1 shows the linear shrinkage and speed curve for the Al_2O_3 and Al_2O_3 -Mo composites in the spark plasma sintering apparatus. The material starts to exhibit a significant shrinkage at 1075 $^\circ\text{C}$, particularly in the case of the monolithic Al_2O_3 , while in the case of the Al_2O_3 -Mo composites, this happens at around 1100 $^\circ\text{C}$. Therefore, the

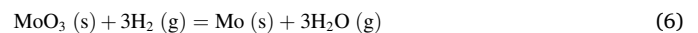
molybdenum content seems to have influence on the beginning of the sintering process. On the contrary, the sintering of the alumina ends at 1280 $^\circ\text{C}$ while the final sintering temperature is approximately 1350 $^\circ\text{C}$ for Al_2O_3 -Mo composites. The maximum speed is reached at 1130 $^\circ\text{C}$, which is analogous in all the compositions. Therefore, it is possible to say that molybdenum produces a delay in the sintering process. This temperature is 200 $^\circ\text{C}$ below than in the case of Díaz et al. [24], where composites were cold isostatically pressed (CIP) at 200 MPa and sintered in Ar/H_2 atmosphere at 1600 $^\circ\text{C}$ for 2 h in conventional furnace. The selected sintering temperature is the same used in the case of Wang and Wei [20], where composites were manufactured by hot-pressing at 1400 $^\circ\text{C}$ with an applied uniaxial pressure of 30 MPa for 1 h under vacuum atmosphere. Sintering conditions in this manuscript are, therefore, comparable with those employed in Wang and Wei [20] in shorter sintering times (3 min in spark plasma sintering against 1 h in hot pressing) and with fast heating and cooling rates that have influence on the final microstructure of the composite.

3.1.2. Phase identification

Fig. 2 shows the X-ray diffraction patterns of pure alumina (Fig. 2a), Al_2O_3 -Mo powder treated at 450 $^\circ\text{C}/2\text{h}$ in air (Fig. 2b), Al_2O_3 -Mo powder after reduction in Ar/H_2 atmosphere at 850 $^\circ\text{C}$ for 2 h (Fig. 2c) and Al_2O_3 -Mo composite after sintering in the SPS equipment (Fig. 2d). Fig. 2 b-d correspond to the composite Al_2O_3 -5 wt % Mo. X-ray diffraction patterns for the other composites were analogous. According to XRD, the main constituents of the powders after the treatment in furnace at 450 $^\circ\text{C}$ for 2 h under air atmosphere (78 vol % N_2 -21 vol % O_2 - 1 vol % Ar) (Fig. 2b) are Al_2O_3 and MoO_3 . The second phase is formed by oxidation of the molybdenum (V) chloride used as precursor of molybdenum during the colloidal processing. Reaction is indicated in Eq. (5).



After a reduction treatment in furnace at 850 $^\circ\text{C}$ for 2 h under Ar/H_2 atmosphere (Fig. 2c) the main mineralogical phases are Al_2O_3 and Mo since a reduction the molybdenum (VI) oxide to Mo by the hydrogen has happened according to the reaction indicated in Eq. (6).



Finally, the SPS sintered sample is composed only by α - Al_2O_3 and Mo particles (Fig. 2d).

A detailed microstructural characterization was made by HRTEM. Images corresponding to Al_2O_3 with 5 wt % molybdenum are shown in

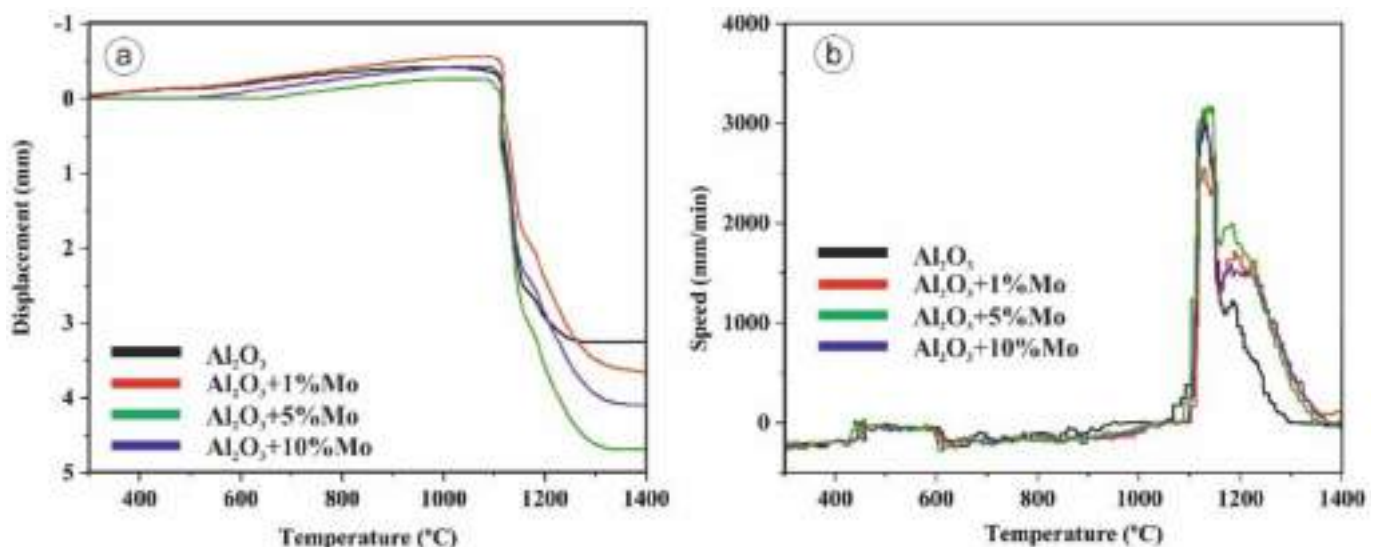


Fig. 1. Linear shrinkage and speed curve for Al_2O_3 and Al_2O_3 -Mo powders during the spark plasma sintering.

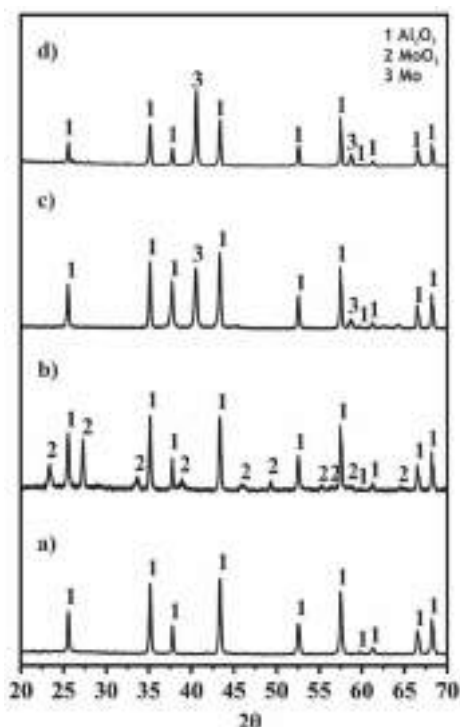


Fig. 2. XRD pattern of pure alumina (a), Al_2O_3 -5 wt-% Mo 450 °C/2h in air (b), Al_2O_3 -5 wt-% Mo 850 °C/2h (c) in Ar/H_2 and Al_2O_3 -5 wt-% Mo SPSed (d).

Fig. 3. It is possible to see that molybdenum nanoparticles (in black color) have an average grain size of around 20 nm and appear superficially adhered to the surface of the alumina (in light grey color).

3.2. Dense nanocomposites

Dense composites are formed as a result of the treatment in the spark plasma sintering apparatus. The values of the densification of the sample because of the sintering process are collected in Table 1.

It is possible to see that all the sintered samples show high density values, being close to 99% or even higher, as reported by other authors

for Al_2O_3 -Mo composites (i. e. Simpson and Wasylyshyn obtained values of relative density >98% by hot-pressing at 1400 °C and 35 MN m^{-2} for 1–2 h [27]). These values of density could be related to the fact that during the sintering process the porosity in the samples was reduced due to the homogeneity and size of the particles, resulted from of a combination of pressure and temperature in the spark plasma sintering apparatus.

3.2.1. Microstructural analysis

Fig. 4 shows a FESEM general view of the microstructure of the different composites, Al_2O_3 , Al_2O_3 -1 wt % Mo, Al_2O_3 -5 wt % Mo and Al_2O_3 -10 wt % Mo, sintered at 1400 °C for 3 min obtained on fracture surfaces. Molybdenum appears homogeneously distributed in the matrix of alumina as it is clearly appreciated in Fig. 4.

According to the type of fracture, it is observed that pure alumina shows a clear intergranular fracture. However, when molybdenum is added, two types of fracture appear in the composite: intergranular and transgranular. It could be associated to a possible toughening mechanism, as the nano-sized particles are far smaller than the critical particle size of initiating microcracking around [28].

Molybdenum nanoparticles appear preferentially located at triple points and grain boundaries, as reported in Fig. 5. Rounded in red color, it is possible to see these molybdenum nanoparticles located at grain boundaries and triple points for the sample with 1 wt % Mo (Fig. 5). Similar situation is observed in the case of samples with greater molybdenum content, although the size of the molybdenum nanoparticles is greater, as it is possible to see in Fig. 4, which is detrimental to the mechanical properties of the composite.

Increasing the molybdenum content involves that more particles appear, and these particles grow, the more the greater the molybdenum

Table 1

Density of the SPS sintered samples.

	Apparent density (g/cm^3)	Real density (g/cm^3) helium pycnometry	Relative sample density (%)
Al_2O_3	3.9369	4.0054	98.29
Al_2O_3 -1 wt % Mo	3.9898	4.0456	98.62
Al_2O_3 -5 wt % Mo	4.0897	4.1102	99.50
Al_2O_3 -10 wt % Mo	4.2167	4.2531	99.14

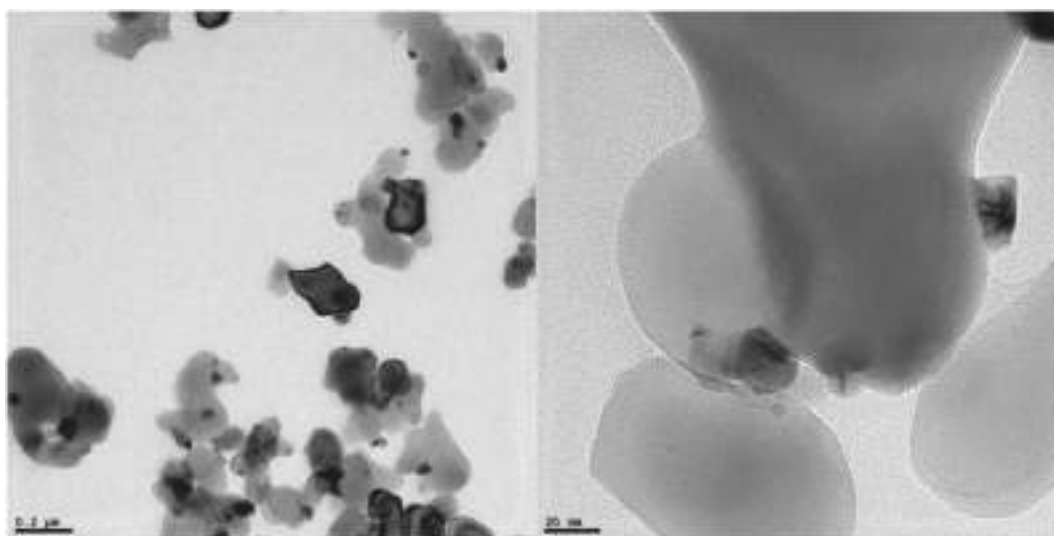


Fig. 3. TEM image of reduced modified powder at 850 °C/2 h of the Al_2O_3 -5 wt % Mo. (a) Left image corresponds to a general view of the powders. (b) Right image corresponds to a detail view of the powders (black color: molybdenum nanoparticles, <20 nm; light grey: alumina particles, >200 nm).

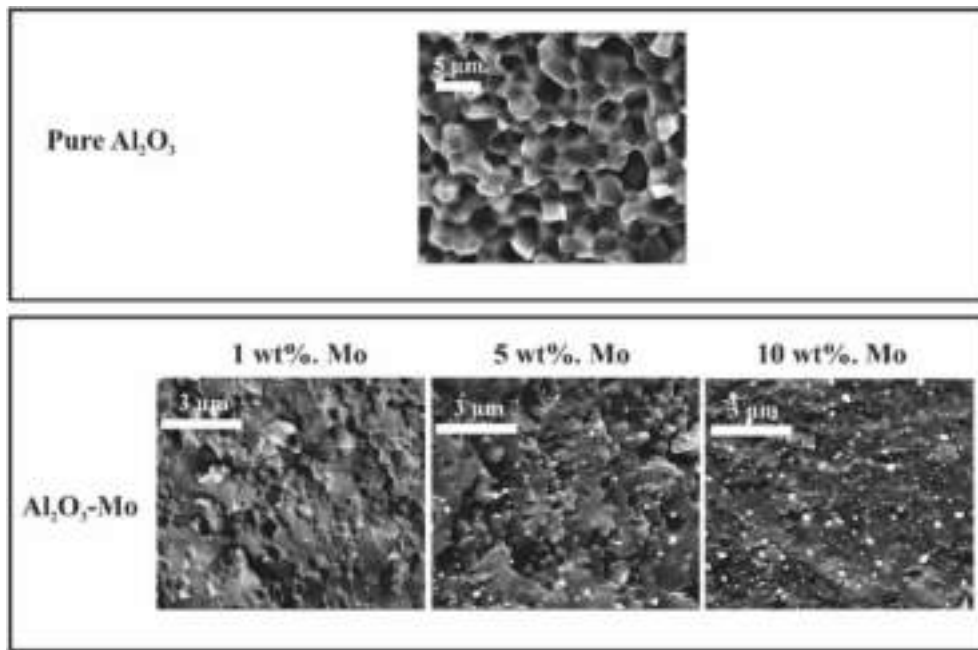


Fig. 4. FESEM images of the fracture surface of pure and Al_2O_3 -Mo SPS sintered samples.

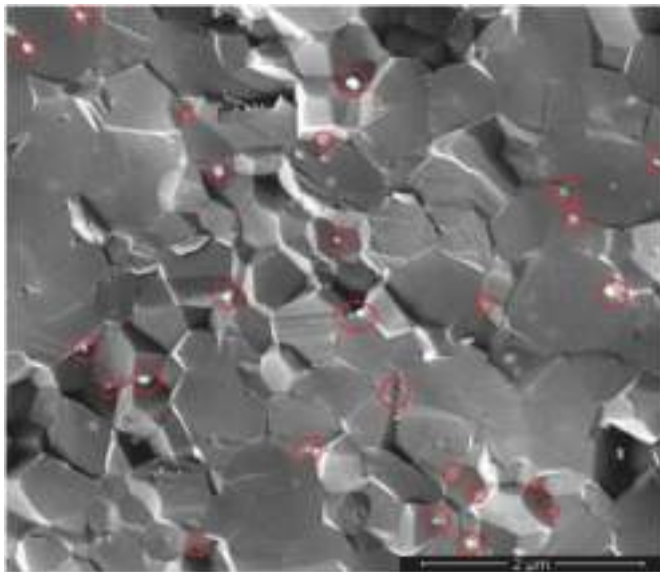


Fig. 5. FESEM image of the fracture surface of Al_2O_3 -Mo SPS sintered samples. Rounded in red color, molybdenum particles appear preferentially located at triple points and grain boundaries for the sample Al_2O_3 -1 wt% Mo. (For interpretation of the references to color in this figure legend, the reader is referred to the Web version of this article.)

content. The size of the molybdenum nanoparticles ranges from 40 nm to 450 nm, although differences are observed depending on the sample. In the case of the sample Al_2O_3 -1 wt % Mo, molybdenum nanoparticles have a size <200 nm, with particles as small as 40 nm. Nevertheless, in the case of the composites Al_2O_3 -5 wt % Mo and Al_2O_3 -10 wt % Mo, small particles are also identified but molybdenum nanoparticles with a size >250 nm are around 30% and 45%, respectively. There is a histogram of the size distribution of the alumina and molybdenum in Fig. 6. Regarding the size of the alumina particles, the pinning effect produced by the presence of molybdenum is clearly observed. Monolithic Al_2O_3 ranging from 2 to 6 μm is $>70\%$. Nevertheless, the size of Al_2O_3 particles is always <1.6 μm in presence of molybdenum. The influence of the

molybdenum content must be also considered, as when the molybdenum content is 1 wt %, the percentage of Al_2O_3 grains with a size in the range 0.2–0.6 μm is as high as 54%. On the contrary, when the molybdenum content is 10 wt %, the percentage of Al_2O_3 grains with a size in the range 0.2–0.6 μm reduces to 26% (for 5 wt % Mo, the fraction of Al_2O_3 grains in this range is 40%). Within this context, increasing the molybdenum content does not involve an Al_2O_3 grain refinement but molybdenum particles grow instead of promoting a finer microstructure in the composite.

3.2.2. Mechanical properties

3.2.2.1. Hardness. Hardness of the composite was measured to analyze the influence of the molybdenum addition. Pure alumina shows a low hardness value due to the grain growth during sintering. The addition of molybdenum nanoparticles produces an increase of the hardness of the composite with respect to the monolithic alumina (Table 2) showing the positive effect of the molybdenum nanoparticles in the composites. However, this improvement is not observed when the molybdenum content increases for the composites. This could be justified by trade-off between the grain refinement effect and metal phase addition effect. The increase of the hardness can be explained by means of the reduction in the grain size produced by the addition of the nanoparticles [29], due to the pinning effect of them on the alumina matrix. The above-mentioned is complemented with the advantage of the SPS, which are the fast heating (100 $^\circ\text{C}/\text{min}$) and cooling (500 $^\circ\text{C}/\text{min}$) rates and the short sintering times, resulting in the possibility of avoiding the grain growth. Therefore, the sintering technique also plays a role as grain-growth inhibitor to obtain a grain size smaller than in conventional sintering. Increasing the molybdenum content does not involve a growth of the hardness value, as it was already indicated. This is consistent with results obtained by other authors using different sintering techniques, see Fig. 7. If the microstructural analysis is considered, the minimum grain sizes are measured in the case of the composite Al_2O_3 -1 wt % Mo. Increasing the molybdenum content does not improve the refinement of the alumina grain as the percentage of alumina grains in the smaller range in Fig. 6 is lower as the molybdenum grain size increases. At the same time, molybdenum size is greater the greater the molybdenum content.

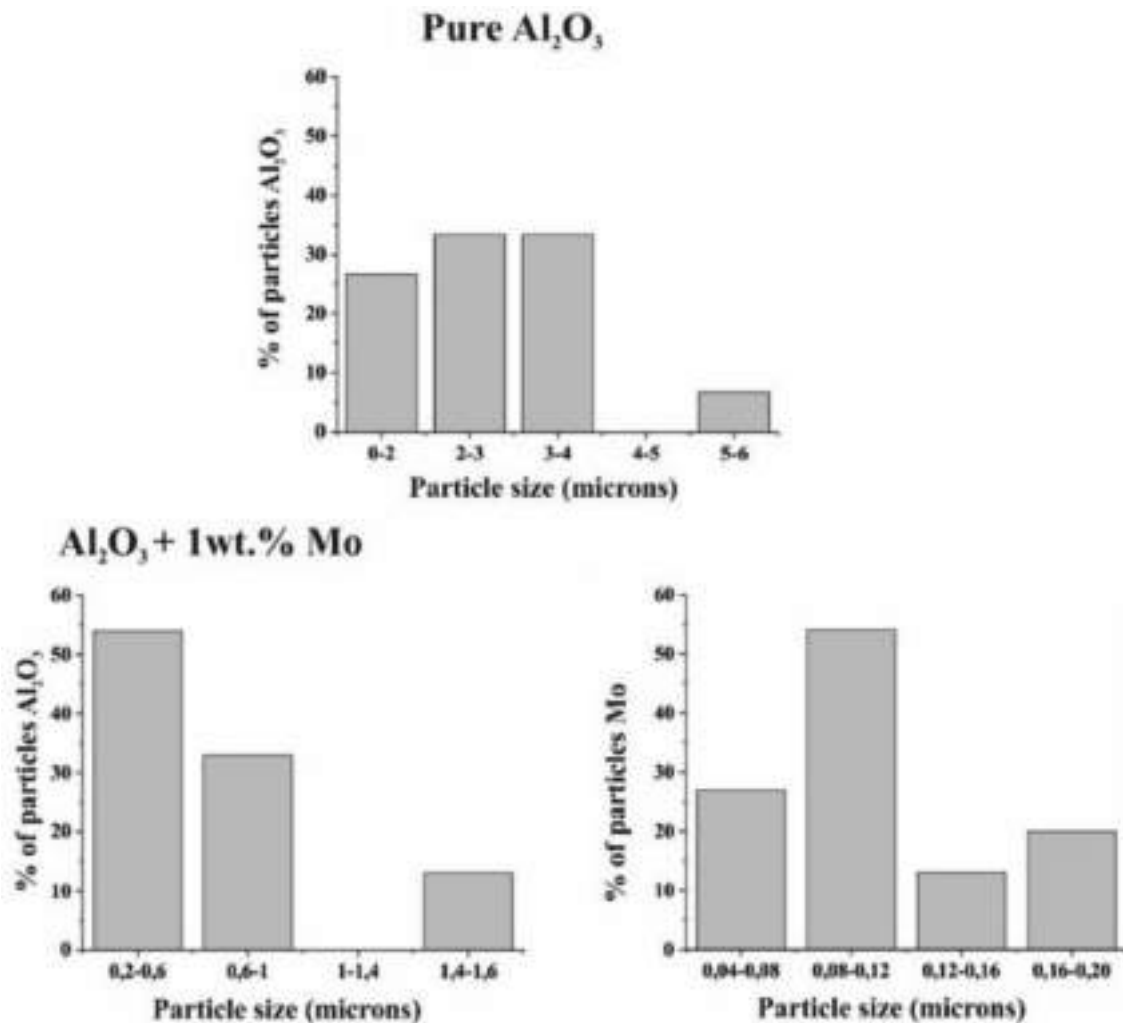


Fig. 6. Alumina and molybdenum histogram of particles' sizes distribution for the different molybdenum contents.

The values of hardness obtained in this research are significantly greater than those obtained by other authors as Zygmuntowicz et al. [22] (9.72 GPa for Al₂O₃ and 9.25 GPa for Al₂O₃-10 vol % Mo) or Lada and collaborators [21] (7.39–10.44 GPa for Al₂O₃-10 vol % Mo). A graphical representation of the results obtained by other authors compared with those obtained in this research appears in Fig. 7. In the first case [22], the composite was obtained by centrifugal slip casting and sintering at 1400 °C for 2 h under H₂-80 vol % N₂ atmosphere with 5 °C/min of heating rate. In the second case [21], the composite was obtained by gel casting method and sintering under argon atmosphere at 1600 °C for 2 h and 3 °C/min of heating rate and 5 °C/min of cooling rate. In the case of Rankin and collaborators [30], they obtained a value of 22.4 GPa for the monolithic Al₂O₃ sintered by hot pressing at 1600 °C under an applied pressure of 55 MPa. Nevertheless, they were not able to appreciate an improvement in the hardness as the molybdenum content increased (22.6 GPa for Al₂O₃-0.5 vol % Mo; 20.25 GPa for Al₂O₃-3 vol % Mo; 19.10 GPa for Al₂O₃-5 vol % Mo). Values in this manuscript are also better than those of Wang and Wei [20], which obtained hardness for the monolithic alumina of around 16 GPa with the greatest values of hardness being measured in the case of the composite with 1 vol % Mo, which approaches 19 GPa. In this second case, composites were manufactured by hot pressing at 1400 °C with an applied uniaxial pressure of 30 MPa for 1 h under vacuum atmosphere, as it was already pointed out. Sintering conditions in the spark plasma sintering apparatus allows a

better control of the microstructure, which usually results in fine-grained microstructures. The size of the molybdenum nanoparticles is in all compositions of this manuscript within the range 40–450 nm, with smaller sizes for the composition Al₂O₃-1 wt % Mo, which provides the best values of hardness. Previous research in this line report values of molybdenum particle sizes of: 7.79 μm ± 0.85 μm–13.90 μm ± 1.03 μm in the case of Zygmuntowicz et al. [22]; 4.35 μm in the case of Lada et al. [21]; or 0.08–0.28 μm in the case of Wang and Wei [20], which correlates with the above indicated values of hardness.

3.2.2.2. Fracture toughness. Table 3 collects the variation of fracture toughness (K_{IC}) as a function of the molybdenum content for the alumina/molybdenum composites obtained by spark plasma sintering and colloidal processing method. It is possible to appreciate that small quantities of molybdenum involve significant improvements in the fracture toughness, from 3.17 MPa m^{1/2} in the case of the monolithic Al₂O₃ to >4.14 MPa m^{1/2} in the case of Al₂O₃ with different molybdenum contents. Fig. 8 collects a comparison of the fracture toughness obtained by different researchers using different sintering techniques. The value of the fracture toughness of the composite is at least 30% greater than that of the monolithic alumina, with the best results being obtained for the composite with Al₂O₃-5 wt % Mo (4.84 MPa m^{1/2}), where the improvement is >50%. This improvement is consistent with that observed by Rankin and co-workers [30], which obtained that

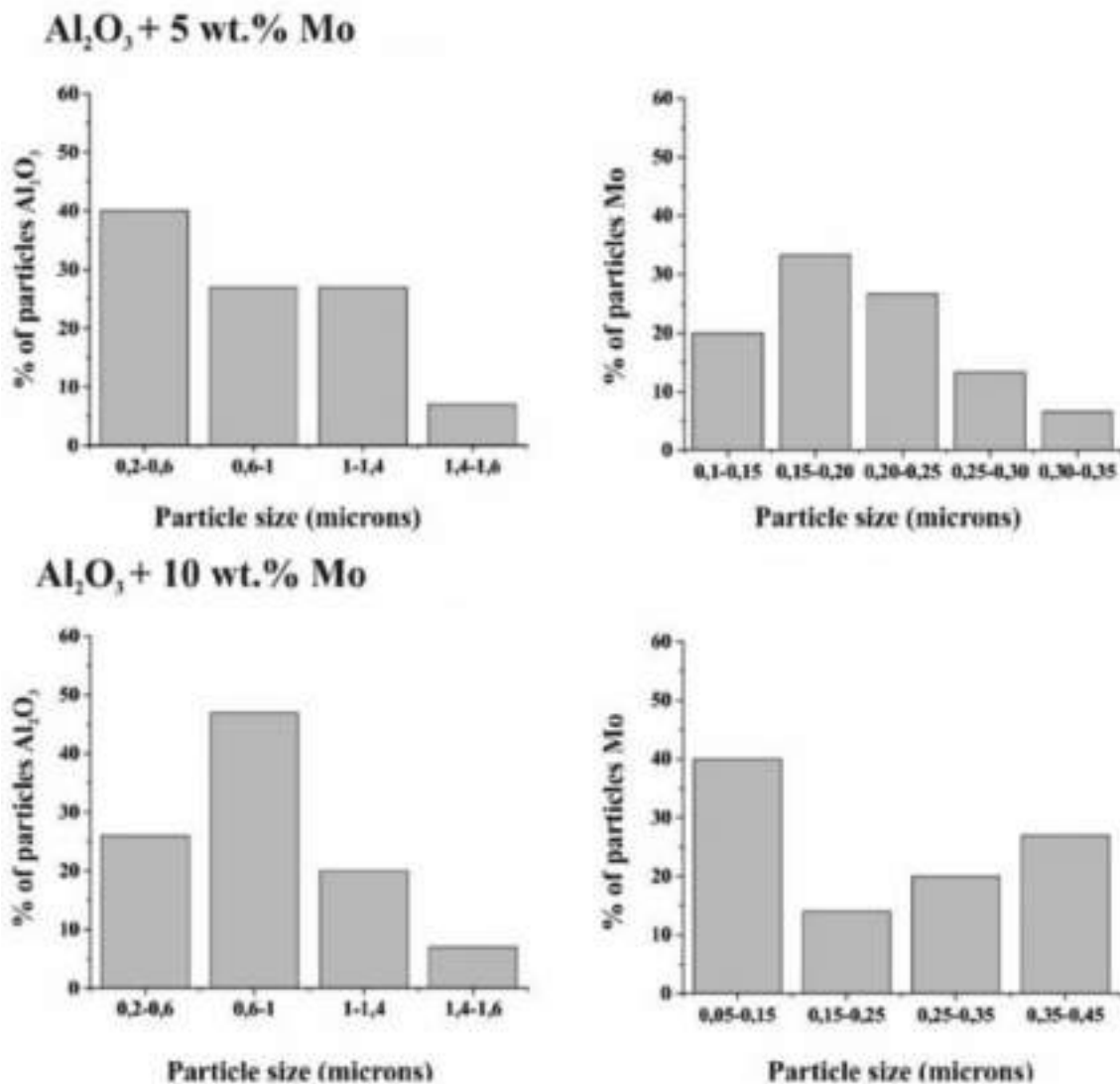


Fig. 6. (continued).

Table 2
Hardness as a function of the molybdenum content.

	Hardness (GPa)
Al ₂ O ₃	18.91 ± 0.61
Al ₂ O ₃ -1 wt % Mo	24.12 ± 0.87
Al ₂ O ₃ -5 wt % Mo	23.49 ± 0.75
Al ₂ O ₃ -10 wt % Mo	23.16 ± 1.15

fracture energy for the composite with 5 vol % Mo (0.5 wt % of MgO to inhibit the grain growth) was 50% greater than that of the monolithic alumina (5.26 MPa m^{1/2}, Al₂O₃; 6.03–6.73 MPa m^{1/2}, Al₂O₃-5 vol. % Mo). Wang and Wei also observed that toughness increased by 32% with the addition of molybdenum, with molybdenum grains of micrometric and nanometric size at grain boundaries and entrapped within alumina [20] (3.40 MPa m^{1/2}, Al₂O₃; ~3.6 MPa m^{1/2}, Al₂O₃-1 vol % Mo; and ~4.5 MPa m^{1/2}, Al₂O₃-5, 10 and 20 vol % Mo). Díaz and collaborators observed that fracture toughness was ~40% greater (1 wt % Mo) than that of the monolithic alumina (4 MPa m^{1/2}, Al₂O₃; 6.26 MPa m^{1/2}, Al₂O₃-1 wt % Mo; ~5.75 MPa m^{1/2}, Al₂O₃-5 wt % Mo; and, ~4.00 MPa m^{1/2}, Al₂O₃-20 wt % Mo). Finally, Broniszewski et al. also observed that molybdenum had a positive influence for the fracture toughness in Al₂O₃-Mo composites [31] (3.5 MPa m^{1/2}, Al₂O₃; 3.64 MPa m^{1/2},

Al₂O₃-5 wt % Mo; 3.95 MPa m^{1/2}, Al₂O₃-10 wt % Mo). Values of fracture toughness in the above referenced research are on the same order of magnitude than those obtained in this research. These values of the fracture toughness seem to be strongly related with the molybdenum grain size: from hundreds of nanometers in the case of Díaz et al. [24] to ~3 μm in the case of Broniszewski et al. [31]. According to the density values and the microstructure obtained by FESEM, the improvement in fracture toughness could be also associated to the presence of a very small grain sizes of molybdenum and the homogeneous distribution of this reinforcing phase in the matrix. All the composites exhibit in this case an improvement of the fracture toughness in comparison with the monolithic alumina. This improvement seems to be more related with the crack deflection or crack detention by absorption of the energy by the molybdenum particle. The influence of alumina grain size on the improvement of the fracture toughness is not clear. Even when the microstructural analysis in Fig. 6 in relation with the values of fracture toughness in Table 3 clearly evidences that fracture toughness is greater in the samples with molybdenum, this relation is not so evident when only considering the samples containing molybdenum. It is possible to see in the microstructural analysis in Fig. 6 that the greatest refinement is produced by the molybdenum nanoparticles in the specimen Al₂O₃-1 wt % Mo. Nevertheless, this sample does not report the greatest value of fracture toughness, which corresponds to the sample Al₂O₃-5 wt % Mo.

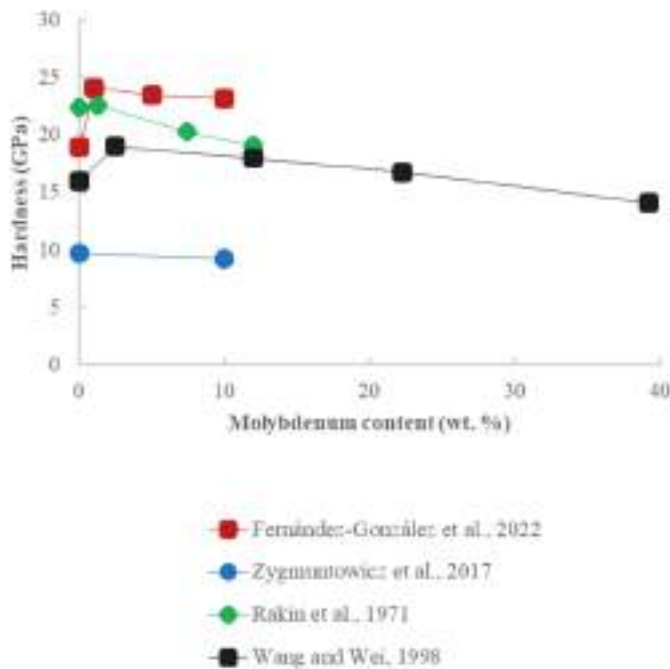


Fig. 7. Comparison of the hardness values obtained in this research with those obtained by other researchers using different sintering techniques.

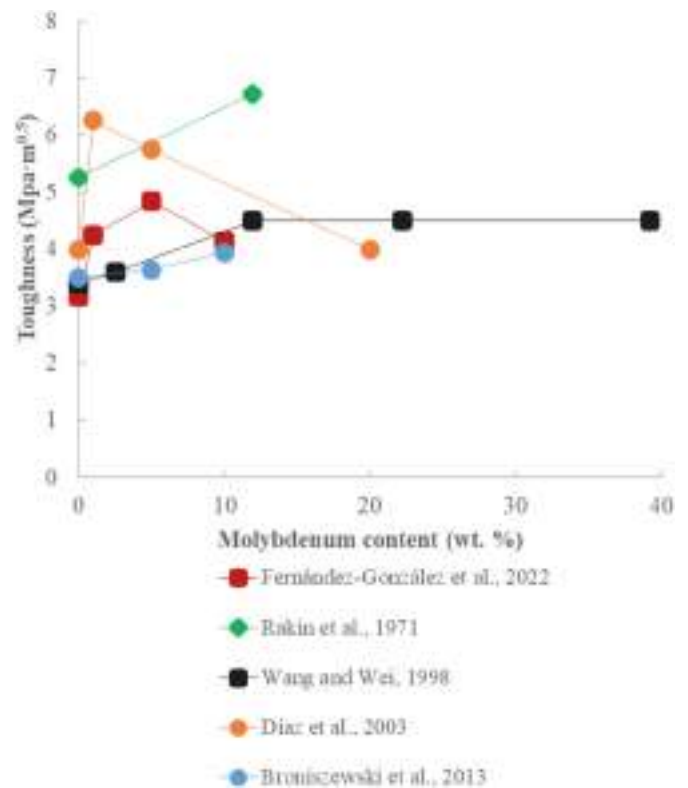


Fig. 8. Comparison of the fracture toughness values obtained in this research with those obtained by other researchers using different sintering techniques.

Table 3

Fracture toughness as a function of the molybdenum content.

	Fracture toughness (MPa·m ^{1/2})
Al ₂ O ₃	3.17 ± 0.25
Al ₂ O ₃ -1 wt % Mo	4.25 ± 0.22
Al ₂ O ₃ -5 wt % Mo	4.84 ± 0.16
Al ₂ O ₃ -10 wt % Mo	4.14 ± 0.32

As the molybdenum content increases further (Al₂O₃-10 wt % Mo), the fracture toughness is even worse than in the composite Al₂O₃-1 wt. % Mo. There is some discussion about the influence of the alumina grain size on the improvement of fracture toughness. Most of research studies were focused on alumina with grain size in the micron scale, where there was an evident improvement of fracture strength when the grain size decreased [32–34]. Nevertheless, Yao et al. found that fracture toughness in fine grained alumina was independent of the grain size in a study made on submicron alumina grain sizes [35]. In this line, it is possible to see that the addition of molybdenum produces a refinement of the alumina grain size from the scale of microns to nanometers, which has influence on the improvement of the fracture toughness. However, if we consider the study of Yao et al. [35], once the alumina grain size is in the scale of nanometers (as happens in the case of the samples with molybdenum), the improvement of the fracture toughness should be consequence of the presence of the molybdenum nanoparticles. In this case, it is necessary to consider that the number of molybdenum particles increases as the molybdenum content increases, which promotes the effect of crack deflection produced by the second phase (a method that is usually employed to improve the fracture toughness in the field of ceramics [1]) or the detention of the crack as plastic deformation of the molybdenum particles. This suggests that the improvement of the fracture toughness is result of the combined effect of the grain size (refinement of the alumina grain size from the microns to the nanometers) but also by the crack deflection or crack absorption as plastic deformation produced by the molybdenum nanoparticles.

3.2.2.3. *Flexural strength.* Flexural strength does not improve with the addition of molybdenum (Table 4). The reasons to explain this behavior

are not clear and require from further studies. Other research with these types of composites showed different behaviors. For instance, Díaz et al. [24] reported a maximum of flexural strength for the composition Al₂O₃-1 wt % Mo (0.69 vol %) with a fast deterioration of this property for greater compositions, reaching values of 700 MPa for this composition while for 5 wt % Mo the value was <600 MPa and for the 20 wt % Mo was <400 MPa. On the other hand, Nawa et al. [17] appreciated that the best results were obtained in the case of Al₂O₃-5 vol % Mo (600 MPa), although the flexural strength did not deteriorate as fast as in Díaz et al. [24] since the flexural strength was close to 575 MPa for the composite Al₂O₃-20 vol % Mo. This situation was not observed by Wang and Wei [20]. They appreciated different behaviors depending on the processing method: mechanical mixing of Mo-Al₂O₃, spray drying process to prepare molybdate/Al₂O₃ granules subjected later to reduction with hydrogen and dissolution of MoO₃ in ammonia solution and dry on a hot plate subjected later the molybdate/Al₂O₃ granules to reduction with hydrogen. The values of flexural strength were in this case far from those obtained by Nawa et al. and Díaz et al., as the maximum strength was 530 MPa, while the values of the maximum flexural strength for samples prepared by dissolving-precipitation/spray-drying was in the range 300–346 MPa. These last values are consistent with the values of flexural strength obtained in this manuscript. Wang and Wei [20] indicated that these low values of flexural strength may be due to the lower sintering density of the two composites. Other reasons may be provided to explain these poor values of flexural strength. On the one

Table 4

Flexural strength as a function of the molybdenum content.

	Flexural strength (MPa)
Al ₂ O ₃	425.02 ± 7.45
Al ₂ O ₃ -1 wt % Mo	349.68 ± 40.35
Al ₂ O ₃ -5 wt % Mo	305.59 ± 46.11
Al ₂ O ₃ -10 wt % Mo	326.15 ± 4.83

hand, the presence of second phases that even when improve the toughness as they are obstacles for the crack propagation, they are points where stresses can concentrate making the composite to break at lower stresses than in the case of the alumina refractory [1]. This is also observed in surface of fracture, since the mechanism of fracture changes from intergranular in the case of monolithic alumina to intergranular and transgranular combined mechanisms in the case of the composites. Therefore, during the crack propagation, this finds a point for the stress concentration in the molybdenum nanoparticles, which are bigger the greater the molybdenum content.

This way, Griffith equation for brittle fracture establishes that:

$$\sigma_f = \sqrt{\frac{2 \cdot E \cdot \gamma}{\pi \cdot c}} \quad (7)$$

where E is the young modulus, γ is the surface energy and c is the crack size. Therefore, the addition of molybdenum nanoparticles involves the addition of “defects” to the alumina matrix, which even grow as the molybdenum content increases. As the flexural strength is inversely proportional to the crack size, the presence of molybdenum nanoparticles may produce a deterioration of the value of the flexural strength of the composite.

On the other hand, another reason that may explain the deterioration of bending strength would be the problem of the weak interfacial bonding between Al₂O₃ ceramic matrix and molybdenum metal phase. This question was already identified by other researchers in the field Mo-Al₂O₃ composites [36]. Although further study should be carried out in this line, if Fig. 9 is considered, it is possible to clearly see from the surface of fracture that many molybdenum grains detach from the composite when the specimen is broken by three-points bending test, which indicates that there is weak interfacial bonding between Al₂O₃ ceramic matrix and molybdenum metal phase. Therefore, it seems that there is not good crystalline interaction between the alumina and the molybdenum. This is, the metal does not enter in the lattice of the alumina, and for that reason, both phases remain independent at the end of the sintering process (there is not strong consistence between the matrix and the disperse constituent).

4. Conclusions

Colloidal processing is an effective method to produce alumina-molybdenum composites. Using this method, molybdenum nanoparticles are homogeneously distributed at the alumina grain boundaries, which is beneficial to obtain a homogeneous small grain size. On another note, spark plasma sintering technique allows fast sintering of the particles. This allows obtaining Al₂O₃-Mo composites in very short times (3 min at sintering temperature) at lower temperature (1400 °C) than other conventional methods. Several additional conclusions can be deduced from the research:

- The addition of molybdenum nanoparticles involves an improvement of the hardness and toughness with respect to the alumina ceramic without nanoparticles. Hardness and toughness increase at least a 25%. Hardness is a 28% greater in the case of the Al₂O₃-1 wt % Mo (without significant differences with the values measured in the other compositions) and toughness is a 50% greater in Al₂O₃-5 wt % Mo with respect to the Al₂O₃.
- The addition of molybdenum nanoparticles inhibits the grain growth of the Al₂O₃. The grain of alumina in the Al₂O₃-Mo composite is < 1.6 μ m, while in the case of the monolithic alumina, > 70% of the alumina grains have a size >2 μ m.
- The addition of molybdenum nanoparticles is deleterious for the flexural strength. The presence of molybdenum particles (that grow as the Mo content increase) act as stress concentration sites where the brittle failure can take place. Other justifications may be associated to the poor interaction between the alumina and molybdenum

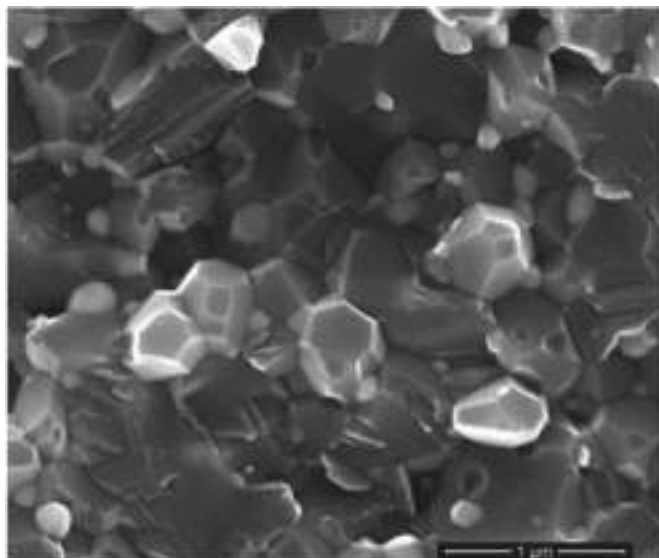


Fig. 9. Fracture surface of the sample Al₂O₃-10 wt % Mo.

nanoparticles. Flexural strength is at least 18% lower in the composite with respect to the monolithic alumina.

- The utilization of the spark plasma sintering technique allows, apart from the already mentioned reduction of processing times, obtaining very fine-grained structures, which is beneficial for the hardness of the composite because of the fast heating and cooling rates. This influence in the microstructure is combined with that of the molybdenum.

Declaration of competing interest

The authors declare that they have no known competing financial interests or personal relationships that could have appeared to influence the work reported in this paper.

Acknowledgements

Daniel Fernández-González acknowledges the grant (Juan de la Cierva-Formación program) FJC2019-041139-I funded by MCIN/AEI/10.13039/501100011033 (Ministerio de Ciencia e Innovación, Agencia Estatal de Investigación). The authors also acknowledge the financial support received from FICYT (IDI/2021/000106). Juan Piñuela Noval acknowledges the Programa “Severo Ochoa” of Grants for Research and Teaching of the Principality of Asturias for the funds received for the elaboration of the Ph. D. Thesis (Ref: BP20 041). Authors are grateful to Ainhoa Macías San Miguel from Nanomaterials and Nanotechnology Research Center (CINN) for providing excellent technical assistance.

References

- [1] L.F. Verdeja, J.P. Sancho, A. Ballester, R. González, *Refractory and Ceramic Materials*, first ed., Síntesis, Madrid, Spain, 2014.
- [2] J.A. Pero-Sanz, D. Fernández-González, L.F. Verdeja, *Structural Materials: Properties and Selection*, first ed., Springer International Publishing, Cham, Switzerland, 2019.
- [3] J.S. Moya, S. López-Esteban, C. Pecharrormán, The challenge of ceramic/metal microcomposites and nanocomposites, *Prog. Mater. Sci.* 52 (2007) 1017–1090, <https://doi.org/10.1016/j.pmatsci.2006.09.003>.
- [4] P. Matteazzi, G. Le Caër, Synthesis of nanocrystalline alumina-metal composites by room-temperature ball-milling of metal oxides and aluminum, *J. Am. Ceram. Soc.* 75 (1992) 2749–2755, <https://doi.org/10.1111/j.1151-2916.1992.tb05499.x>.
- [5] Y. Waku, M. Suzuki, Y. Oda, Y. Kohtoku, Improvement of fracture toughness of Al₂O₃ composites by micro-dispersion of flaky refractory metals Mo, Ta and Nb, *J. Ceram. Soc. Jpn.* 103 (1995) 713–719, <https://doi.org/10.2109/jcersj.103.713>.
- [6] T. Sekino, T. Nakajima, S. Ueda, K. Niihara, Reduction and sintering of a nickel-dispersed-alumina composite and its properties, *J. Am. Ceram. Soc.* 80 (1997) 1139–1148, <https://doi.org/10.1111/j.1151-2916.1997.tb02956.x>.

- [7] W.G. Fahrenholtz, D.T. Ellerby, R.E. Loehman, Al₂O₃-Ni composites with high strength and fracture toughness, *J. Am. Ceram. Soc.* 83 (2004) 1279–1280, <https://doi.org/10.1111/j.1151-2916.2000.tb01368.x>.
- [8] E. Brevail, G. Dodds, C.G. Pantano, Properties and microstructure of Ni-alumina composite materials prepared by the sol/gel method, *Mater. Res. Bull.* 20 (1985) 1191–1205, [https://doi.org/10.1016/0025-5408\(85\)90093-5](https://doi.org/10.1016/0025-5408(85)90093-5).
- [9] A. Miazga, K. Konopka, M. Gizowska, M. Szafran, Preparation of Al₂O₃-Ni cermet composites by aqueous gel-casting, *Powder Metall. and Met. C+* 52 (2014) 567–571, <https://doi.org/10.1007/s11106-014-9561-y>.
- [10] T. Rodríguez-Suarez, J.F. Bartolomé, A. Smimov, S. Lopez-Esteban, R. Torrecillas, J.S. Moya, Sliding wear behaviour of alumina/nickel nanocomposites processed by a conventional sintering route, *J. Eur. Ceram. Soc.* 31 (2011) 1389–1395, <https://doi.org/10.1016/j.jeurceramsoc.2011.02.011>.
- [11] T. Sekino, A. Nakahira, N. Nawa, K. Niihara, Fabrication of Al₂O₃/W nanocomposites, *J. Japan Soc. of Powd.* 38 (1991) 326–330.
- [12] T. Sekino, K. Niihara, Microstructural characteristics and mechanical properties for Al₂O₃/metal nanocomposites, *Nanostruct. Mater.* 6 (1995) 663–666, [https://doi.org/10.1016/0965-9773\(95\)00145-X](https://doi.org/10.1016/0965-9773(95)00145-X).
- [13] T. Rodríguez-Suarez, L.A. Díaz, R. Torrecillas, S. Lopez-Esteban, W.H. Tuan, M. Nygren, J.S. Moya, Alumina/tungsten nanocomposites obtained by spark plasma sintering, *Compos. Sci. Technol.* 69 (2009) 2467–2473, <https://doi.org/10.1016/j.compscitech.2009.06.022>.
- [14] K. Konopka, A. Ozieblo, Microstructure and the fracture toughness of the Al₂O₃-Fe composites, *Mater. Char.* 46 (2001) 125–129, [https://doi.org/10.1016/S1044-5803\(01\)00113-9](https://doi.org/10.1016/S1044-5803(01)00113-9).
- [15] W.-C.J. Wei, S.-C. Wang, F.-H. Cheng, Characterization of Al₂O₃ composites with fine Mo particulates, I. Microstructural development, *Nanostruct. Mater.* 10 (1998) 965–981, [https://doi.org/10.1016/S0965-9773\(98\)00130-5](https://doi.org/10.1016/S0965-9773(98)00130-5).
- [16] A. Heidarpour, F. Karimzadeh, M.H. Enayati, Fabrication and characterisation of bulk Al₂O₃/Mo nanocomposite by mechanical milling and sintering, *Powder Metall.* 54 (2011) 513–517, <https://doi.org/10.1179/003258910X12740974839585>.
- [17] M. Nawa, T. Sekino, K. Niihara, Fabrication and mechanical behaviour of Al₂O₃/Mo nanocomposites, *J. Mater. Sci.* 29 (1994) 3185–3192, <https://doi.org/10.1007/BF00356661>.
- [18] G. De Portu, S. Guicciardi, C. Melandri, F. Monteverde, Wear behaviour of Al₂O₃-Mo and Al₂O₃-Nb composites, *Wear* 262 (2007) 1346–1352, <https://doi.org/10.1016/j.wear.2007.01.010>.
- [19] C.O. McHugh, T.J. Whalen, M. Humenik, Dispersion-strengthened aluminum oxide, *J. Am. Ceram. Soc.* 49 (1966) 486–491, <https://doi.org/10.1111/j.1151-2916.1966.tb13305.x>.
- [20] S.-C. Wang, W.-C.J. Wei, Characterization of Al₂O₃ composites with Mo particulates, II. Densification and mechanical properties, *Nanostruct. Mater.* 10 (1998) 983–1000, [https://doi.org/10.1016/S0965-9773\(98\)00135-4](https://doi.org/10.1016/S0965-9773(98)00135-4).
- [21] P. Lada, A. Miazga, M. Zagorska, J. Zygmuntowicz, K. Konopka, Characterization of alumina-molybdenum composites prepared by gel casting method, *Powder Metall. Met. C+* 58 (2019) 295–300, <https://doi.org/10.1007/s11106-019-00073-0>.
- [22] J. Zygmuntowicz, A. Baczynska, A. Miazga, W. Kaszuwara, K. Konopka, Al₂O₃-Mo functionally graded material obtained via centrifugal slip casting, *Materiały Ceramiczne/Ceramic Materials* 69 (2017) 73–77.
- [23] C. Gómez-Rodríguez, L.V. García-Quiñonez, L.F. Verdeja, G.A. Castillo-Rodríguez, J.A. Aguilar-Martínez, A.E. Mariño-Gómez, D. Fernández-González, Selective laser sintering of alumina-molybdenum nanocomposites, *Ceram. Int.* 48 (2022) 29540–29545, <https://doi.org/10.1016/j.ceramint.2022.08.058>.
- [24] M. Suárez, D. Fernández-González, L.A. Díaz, A. Borrell, J.S. Moya, A. Fernández, Synthesis and processing of improved graphite-molybdenum-titanium composites by colloidal route and spark plasma sintering, *Ceram. Int.* 47 (2021) 30993–30998, <https://doi.org/10.1016/j.ceramint.2021.07.267>.
- [25] L.A. Díaz, A.F. Valdés, C. Díaz, A.M. Espino, R. Torrecillas, Alumina/molybdenum nanocomposites obtained in organic media, *J. Eur. Ceram. Soc.* 23 (2003) 2829–2834, [https://doi.org/10.1016/S0955-2219\(03\)00295-4](https://doi.org/10.1016/S0955-2219(03)00295-4).
- [26] M. Suárez, D. Fernández-González, L.A. Díaz, F. Diolgent, L.F. Verdeja, A. Fernández, Consolidation and mechanical properties of ZrCu₃₉.85Y₂.37Al₁₁.8 bulk metallic glass obtained from gas-atomized powders by spark plasma sintering, *A. Intermetallics* 139 (2021), 107366 <https://doi.org/10.1016/j.intermet.2021.107366>, 2021.
- [27] L.A. Simpson, A. Wasylshyn, Fracture energy of Al₂O₃ containing Mo fibers, *J. Am. Ceram. Soc.* 54 (1971) 56–57, <https://doi.org/10.1111/j.1151-2916.1971.tb12171.x>.
- [28] H. Wu, Understanding residual stresses and fracture toughness in ceramic nanocomposites, in: M.M. Shokrieh (Ed.), *Residual Stresses in Composite Materials*, Woodhead publishing, Boston, USA, 2014, pp. 256–292.
- [29] J. Silvestre, N. Silvestre, J. de Brito, An overview on the improvement of mechanical properties of ceramic nanocomposites, *J. Nanomater.* (2015) 13, <https://doi.org/10.1155/2015/106494>. Article ID 106494.
- [30] D.T. Rankin, J.J. Stiglich, D.R. Petrak, R. Ruh, Hot-pressing and mechanical properties of Al₂O₃ with a Mo-dispersed phase, *J. Am. Ceram. Soc.* 54 (1971) 277–281, <https://doi.org/10.1111/j.1151-2916.1971.tb12290.x>.
- [31] K. Broniszewski, J. Wozniak, K. Czechowski, L. Jaworska, A. Olszyna, Al₂O₃-Mo cutting tools for machining hardened stainless steel, *Wear* 303 (2013) 87–91, <https://doi.org/10.1016/j.wear.2013.03.002>.
- [32] T. Koyama, A. Nishiyama, K. Niihara, Effect of grain morphology and grain size on the mechanical properties of Al₂O₃ ceramics, *J. Mater. Sci.* 29 (1994) 3949–3954, <https://doi.org/10.1007/bf00355953>.
- [33] J. Seidel, N. Claussen, J. Rödel, Reliability of alumina ceramics: effect of grain size, *J. Eur. Ceram. Soc.* 15 (1995) 395–404, [https://doi.org/10.1016/0955-2219\(95\)91430-V](https://doi.org/10.1016/0955-2219(95)91430-V).
- [34] A. Mughtar, L.C. Lim, Indentation fracture toughness of high purity submicron alumina, *Acta Mater.* 46 (1998) 1683–1690, [https://doi.org/10.1016/S1359-6454\(97\)00371-6](https://doi.org/10.1016/S1359-6454(97)00371-6).
- [35] W. Yao, J. Liu, T.B. Holland, L. Huang, Y. Xiong, J.M. Schoenung, A.K. Mukherjee, Grain size dependence of fracture toughness for fine grained alumina, *Scripta Mater.* 65 (2011) 143–146, <https://doi.org/10.1016/j.scriptamat.2011.03.032>.
- [36] B. Chen, Z.-B. Li, G.-H. Zhang, K.-C. Chou, Fabrication and mechanical properties of Mo-Al₂O₃ cermets by using ultrafine molybdenum and nano-sized alumina powders, *J. Occup. Med.* 73 (2021) 3451–3459, <https://doi.org/10.1007/s11837-021-04848-y>.

Trabajo complementario 1: Morphological study of refractory composite materials based on magnesia (MgO) with additions of hercinite ($\text{Fe}_2\text{Al}_2\text{O}_4$).

Morphological study of refractory composite materials based on magnesia (MgO) with additions of hercynite (Fe₂Al₂O₄)

Cristian Gomez Rodriguez^{1,2}, Beatriz Escobedo-Trujillo, Luis Felipe Verdeja, Daniel Fernández-González³, Adolfo Fernández³, Linda-Viviana García-Quiñónez, Guadalupe Alan Castillo Rodríguez

1 Universidad de Oviedo

2 Universidad Veracruzana

3 Centro de Investigación en Nanomateriales y Nanotecnología

Abstract

Since the refractory materials are immersed in aggressive environments, the deterioration is evident because they are affected by slags, gases or liquids that corrode the material. Materials used in the refractory lining of the rotary furnace of cement are densified materials with high resistance, particularly magnesia bricks (MgO) with second phases to improve their characteristics. Within this investigation, formulations with refractory powders were developed, which were uniaxially pressed at 100 MPa and sintered at 1650 °C for four hours. Up to a maximum of 20 wt.% of hercynite (Fe₂Al₂O₄), was added as second phase to the refractory matrix of magnesia (MgO). The morphological characteristics as well as the mechanical properties of the sintered samples, in a conventional electric furnace, were studied by scanning electron microscopy (SEM) with Energy-dispersive X-ray spectroscopy (EDX). As a result, it was checked that, the temperature used in the experiments was not sufficient to obtain sintered specimens of the MgO powders (100 wt. %). The additions of Fe₂Al₂O₄ helped to obtain morphologically densified specimens. A 10 and 20 wt. % of Fe₂Al₂O₄ promoted the grain growth during the sintering process.

OPEN ACCESS

Accepted: 29/08/2023

Keywords:

Magnesia
Hercinita
Refractarios
Morfología
Microestructura
Sinterización

1. Introducción

Los materiales refractarios son ampliamente utilizados en procesos industriales. Son diseñados y fabricados con el objetivo de soportar elevadas temperaturas y ambientes agresivos de líquidos y gases [1]. Recientemente se han estudiado diferentes sistemas refractarios tomando en cuenta composiciones de nanopartículas, agregadas al óxido de magnesio (MgO). Estos estudios se han basado en mejorar principalmente propiedades físicas [2], [3], [4], mecánicas [5], térmicas [6] y químicas [5] [7] [8]. Los estudios anteriores se centran en explotar las capacidades de las nanopartículas (<100 nm) brindando efectos potenciadores en la matriz, debido al efecto del tamaño, área superficial, y efectos cuánticos de éstas. La desventaja principal es el coste elevado, y de esta manera resulta difícil escalar, de muestras de laboratorio a una producción industrial real. El óxido de magnesio (2800 °C) se utiliza como revestimiento de recipientes en procesos siderúrgicos y también en hornos rotatorios de cementos. Estos últimos consisten en un largo cilindro de acero el cual es forrado de material refractario, así mismo, tiene una ligera inclinación y se encuentra en constante movimiento por medio de rodillos. En este tipo de horno se produce el clínker para cemento Portland [9]. El horno se divide en tres zonas (zona fría, zona intermedia y zona caliente) donde las condiciones y la temperatura (400-550 °C, 660 -1100 °C, 1300- 1600 °C, respectivamente) varían de acuerdo con cada zona. Así mismo los materiales utilizados tanto para zona fría y zona intermedia son diferentes según el contenido de Al₂O₃, y arcilla refractaria densa. La zona caliente se divide a su vez en tres partes (zona de transición alta, zona de quemado y zona de transición baja). Los ladrillos refractarios utilizados en zonas de transición alta

son principalmente ladrillos de magnesia-espinela (MgO-MgAl₂O₄) y magnesia-zirconia (MgO-ZrO₂) [10] [11] [12]. La zona de quemado es la zona donde se encuentra la mayor temperatura. Esta zona es una de las más afectadas debido a las condiciones extremas en las cuales se encuentran inmersos los ladrillos refractarios, provocando cambios o remplazos de ladrillos refractarios periódicamente [13]. En esta zona, se utilizan refractarios básicos, principalmente magnesia-cromita (MgO-CrO₃) [14]. Pero se ha comprobado que con estos ladrillos refractarios se pueden llegar a formar fases de Cr³⁺ a Cr⁶⁺ (cromo hexavalente) cuando los refractarios son expuestos por encima de los 800 °C y debido al contacto de álcalis, siendo este compuesto (Cr⁶⁺) tóxico y cancerígeno [15]. Para remplazar estos ladrillos y para aumentar la seguridad ecológica en la industria, se han propuesto estudios de sistemas que son altamente resistentes a las temperaturas, y a los álcalis de esta zona y que ecológicamente son más limpios. Por lo que se ha optado por reemplazar estos refractarios (MgO-CrO₃) por dolomita- (CaCO₃·MgCO₃) agregando segundas fases como ZrO₂, MgO o MgO con espinela (MgAl₂O₄), inclusive MgO - zirconia. En este tipo de sistemas lo que se busca es formar una capa protectora (auto-revestimiento) que ayude a proteger al ladrillo refractario, pero muchos de ellos no logran formar la capa protectora, haciéndolo vulnerable al ataque químico de los álcalis, causando agrietamientos, spalling, y erosión. Inclusive se forman bajos puntos de fusión entre la materia prima y elementos que contienen estos ladrillos refractarios debilitando propiedades térmicas y, por consiguiente, afectando al objetivo para el cual fueron colocados en esa zona. En la zona de transición baja los ladrillos más utilizados son ladrillos de magnesia - espinela. En este sentido, se busca emplear ladrillos

con características específicas para uso en zonas de quemado. Como primera parte, la presente investigación se centra en el estudio de un sistema refractario magnesia-hercinita (MgO-Fe₂Al₂O₄), y brinda un estudio de características morfológicas (análisis elemental semicuantitativo), microestructural y mecánico, de probetas, para posible uso en parte importante del horno rotatorio de cemento.

2. Materiales y métodos

2.1. Materia prima

Se empleó magnesia calcinada (MgO) con un tamaño de partícula < 45 µm. Esta materia prima fue suministrada por la compañía Grupo Peñoles (Laguna del Rey, Coahuila, México). Polvos de hercinita (Fe₂Al₂O₄) con pureza del 99.9%, fueron suministrados por la empresa Maerz Ofenbau AG. La hercinita fue molida en un molino de bolas de alúmina durante 15 minutos. Posteriormente, los polvos fueron tamizados con malla 325, para obtener polvos de tamaño de partícula < 45 µm. La Figura 1 muestra la materia prima utilizada: (a) hercinita (antes de molerla), en la cual se observa, una fase oscura correspondiente al aluminio y una fase más clara la cual fue detectada como hierro. Las partículas de hercinita presentan un tamaño promedio entre 25 y 70 µm; y, (b) polvos de MgO, los cuales se observan en forma de polvo fino (≈ 1 µm) con las partículas de fase oscura correspondiendo al MgO y las partículas de color blanco, perteneciendo al CaO. La Tabla 1 muestra la composición química del óxido de magnesio (MgO).

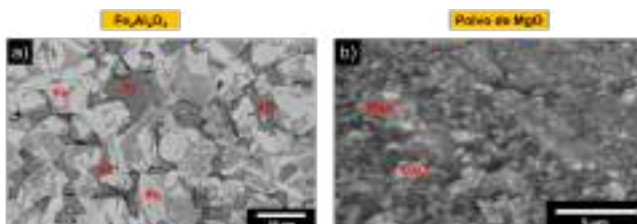


Figura 1. Micrográficas de SEM, correspondientes a materia prima utilizada, a) hercinita (Fe₂Al₂O₄) y b) óxido de magnesio (MgO).

Materia prima	Análisis químico						
	MgO	CaO	FeO	Fe ₂ O ₃	Al ₂ O ₃	SiO ₂	LOI
MgO	97.43	0.9	-	0.06	-	0.6	1.01

Tabla 1. Análisis químico de la materia prima utilizada (MgO).

2.2. Preparación de las muestras

Se agregaron porcentajes en peso de hercinita (Fe₂Al₂O₄) a la magnesia (MgO), considerando 0, 1, 2.5, 5, 10 y 20 % en peso. Para asegurar la correcta homogeneidad de mezclado se realizó una mezcla mecánica, en un mezclador (ALGHAMIX II-Zhermack) a 100 rpm, para cada concentración. Las mezclas de cada composición se vertieron en un molde metálico para obtener pastillas refractarias en verde. Éstas se obtuvieron mediante prensado uniaxial a 100 MPa en forma de discos de 10 mm de diámetro y 9 mm de altura. Las probetas refractarias fueron sinterizadas en un horno eléctrico a 1650 °C durante 4 horas con una rampa de calentamiento de 5 °C/min. Se realizaron 5 probetas para cada porcentaje en peso, los valores reportados pertenecen a la media de las probetas de cada composición.

El análisis microestructural se realizó con un FEI Nova, microscopio electrónico de barrido (MEB) NanoSEM 200

equipado con un detector de espectroscopia de rayos X de dispersión de electrones (EDX) (EDAX, modelo Apollo XP, número de serie 2930). La dureza de los materiales fue determinada por indentación de superficies pulidas con cargas de 300 gramos durante 10 segundos empleando el durómetro Buehler. Por razones estadísticas, se hicieron 5 indentaciones en cada probeta.

3. Resultados y discusión

3.1. Análisis morfológico

La Figura 2 muestra imágenes de (MEB), las cuales corresponden a superficies pulidas de probetas de MgO con diferentes concentraciones de hercinita (Fe₂Al₂O₄). En cada concentración se muestran tres diferentes magnificaciones. La Figura 2(a), corresponde a una muestra de 100 % de MgO, en esta probeta se observan porosidades, granos de óxido de magnesio y partículas de óxido de calcio. El óxido de calcio (CaO) se considera impureza el cual viene inmerso desde la materia prima, debido a la obtención del MgO. Ya que el MgO es obtenido desde dolomita CaMg(CO₃)₂. De acuerdo con la Tabla 1, el Ca, fue detectado desde la materia prima del MgO con una concentración de ≈ 0.9 %. La Figura 2 (b, c y d), corresponden a micrográficas de probetas del 1, 2.5 y 5 % en peso de Fe₂Al₂O₄, respectivamente. Así mismo, una fase blanca fue formada. Mediante análisis puntual EDX, se detectó en esta fase blanca la presencia de Ca y Fe. Con estas concentraciones se observaron porosidades redondas iguales a 5 µm. Con probetas del 10 % en peso de Fe₂Al₂O₄ (Figura 2 (e)), se observaron formaciones bien definidas de límites de grano, los cuales rodeaban a granos de MgO. Finalmente, con probetas con concentraciones del 20 % en peso de hercinita, se observaron límites de granos con formación de puntos triples con ángulos diédricos (ángulos de 120 °) que representan una buena sinterización entre los granos de MgO [16], por lo que, durante el proceso de sinterizado, la porosidad fue gradualmente disminuyendo lo que permitió que los granos también fueran creciendo y densificando.

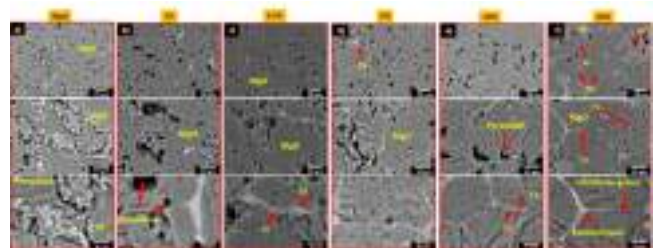


Figura 2. Micrográficas de probetas pulidas de MgO con diferentes composiciones de Fe₂Al₂O₄, donde: a) 100% MgO; b) 1%; c) 2.5%; d) 5%; e) 10%; y, f) 20% peso.

Con la probeta del 20% de Fe₂Al₂O₄, tres fases de color blanco fueron detectadas, las cuales tenían concentraciones de Mg, Fe, Al, Ca y Si (ver Figura 3). La primera fase, correspondía a fase blanca en límites de grano con concentraciones de Mg, Fe, Ca y Si. Sobre los granos se evidenciaron dos fases más, una con formación de pequeñas cruces blancas (con concentración de Mg y Fe), y otra fase blanca opaca la cual correspondió a Mg y Al.

En general algunos mecanismos que ocurrieron pudieron ayudar a promover la densificación de la microestructura de las probetas de MgO, a través de la adición de micropartículas de Fe₂Al₂O₄, a) Formación in situ de la fase magnesioferrita (MgFe₂O₄ = 4.51 gr/cm³) la cual tiene mayor densidad respecto a la matriz (MgO= 3.58 gr/cm³) (espectro 1, Figura 3). b) Las fases

formadas (entre Mg, Fe, Ca y Si, ver [Figura 3](#), espectro 3 y 4) en límites de grano, permitieron un sinterizado en estado líquido, de tal manera que los granos sólidos de MgO coexistieron con el líquido, actuando como enlazante entre las partículas sólidas, ayudando a densificar la pieza [17].

Otro mecanismo importante que pudo estar presente fue la formación insitu de la fase espinela MgAl₂O₄ (Ver, [Figura 2\(f\)](#), micrografía donde se observa fase blanca opaca y se señala al Al, la cual es una fase químicamente más estable a diferentes tipos de escorias. Se sabe que ladrillos refractarios con composición MgO- MgAl₂O₄ son utilizados en Zonas de Transición Alta y en Zonas de Quemado dentro del horno rotatorio de cemento. Además, que esta fase tiene una temperatura de fusión alta (2135 °C), se caracteriza por ser químicamente más estable y mucho más resistente a la rehidratación de la matriz del MgO.

En la probeta del 20% de hercinita, se evidenció la disminución de porosidades, respecto a las demás probetas. Como se sabe, un ladrillo refractario puede tener un porcentaje de porosidad permitido y que opere bajo condiciones normales en condiciones de trabajo bajo las cuales fue diseñado. En la probeta del 20% de hercinita, se observa porosidad remanente, se piensa que esta, podría ayudar para que cuando el Clinker penetre a través de la porosidad quede anclada una capa solidificada en las porosidades [18], y que posteriormente sirva de autoprotección contra el mismo Clinker de cemento [19]. Ya que la Zona de Quemado es donde se encuentra la mayor temperatura y es una de las más severas para los ladrillos refractarios dentro del horno rotatorio de cemento.

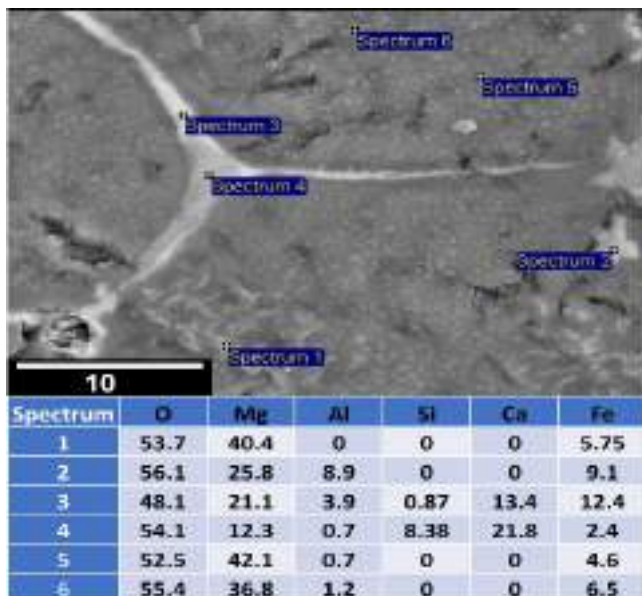


Figura 3. Micrografía correspondiente a probeta del 20% en peso de Fe₂Al₂O₄, analizada por EDX puntual en diferentes partes de la probeta.

3.2. Análisis de microdureza

En la [Figura 4](#) el efecto del porcentaje de hercinita (Fe₂Al₂O₄) sobre la dureza de las probetas, fue estudiado. Como se puede observar en la gráfica con adición de Fe₂Al₂O₄ se observan variaciones de dureza, en general un ligero aumento en la dureza fue evidente con adiciones de hercinita. En la gráfica se observa con 1% en peso de Fe₂Al₂O₄ una dureza de 204.7 HV, con 2.5, 5 y 10 % en peso de hercinita se observó que los valores se mantuvieron casi constantes con valores de 250.1,

239.5 y 228.86 HV, con la probeta del 20 % de Fe₂Al₂O₄ se observó un aumento en la microdureza (339.44 HV). Este aumento es consistente con la evolución microestructural presentada en la [Figura 2](#), en la cual se observó que con esta probeta se obtuvo una probeta densificada.

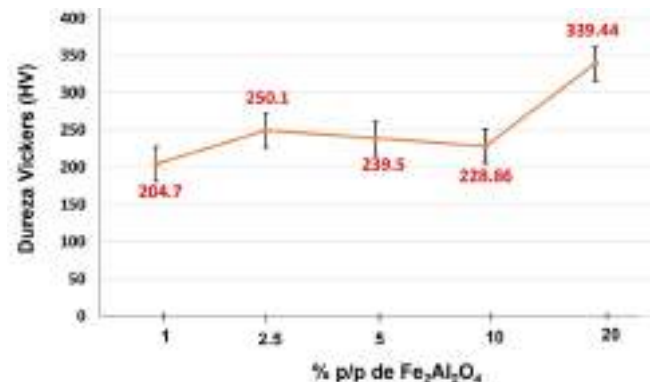


Figura 4. Variación de la dureza Vickers en función del porcentaje en peso de Fe₂Al₂O₄ agregado al MgO.

4. Conclusiones

En este trabajo se ha presentado un estudio morfológico y mecánico (microdureza) de probetas realizadas con magnesia (MgO) y adiciones de hercinita (Fe₂Al₂O₄). Esta investigación proporciona conocimiento en cuanto al desarrollo microestructural de este tipo probetas. De acuerdo con las micrografías del material sinterizado se puede observar que el mejor resultado en términos microestructurales, es decir, con menor porosidad, formación de límites de granos y piezas mejor densificadas, corresponde con las probetas de 20 % en peso de Fe₂Al₂O₄. Asimismo, esta probeta presentó mejor dureza en comparación a los otros porcentajes en peso de hercinita (339.44 HV).

Agradecimientos

Cristian Gómez-Rodríguez agradece a la AUIP (Asociación Universitaria Iberoamericana de Postgrado) por la beca autorizada (primer plazo 2023) para la estancia académica en la Universidad de Oviedo, así mismo agradece a la Universidad Veracruzana por otorgarle beca-HAPI 2023, para hacer estancia en la Universidad de Oviedo.

Bibliografía

- [1] L. Verdeja, J. Sancho, A. Ballester y R. González, *Refractory and Ceramic Materials*, Madrid: Síntesis, 2014.
- [2] H. Dehsheikh, S. Ghasemi-Kahrizsangi, E. Karamian y F. Shahmohammadian, «Hydration resistance improvement of doloma particles using different nanoparticles,» *Ceram. Int.*, vol. 45, n° 6, pp. 7390-7396, 2019.
- [3] H. Dehsheikh y S. Ghasemi-Kahrizsangi, «Performance improvement of MgO-C refractory bricks by the addition of Nano-ZrSiO₄,» *Mater. Chem. Phys.*, vol. 202, pp. 369-376, 2017.
- [4] S. Ghasemi-Kahrizsangi, M. Sedeh, H. Dehsheikh, A. Shahraki y M. Farooghi, «Densification and properties of ZrO₂ nanoparticles added magnesia-doloma refractories,» *Ceram. Int.*, vol. 42, n° 14, pp. 15658-15663, 2016.
- [5] C. Gómez-Rodríguez, D. Fernández-González, L. García-Quiñonez, G. Castillo-Rodríguez, J. Aguilar-Martínez y L. Verdeja, «MgO refractory doped with ZrO₂ nanoparticles:

Influence of cold isostatic and uniaxial pressing and sintering temperature in the physical and chemical properties,» *Metals*, vol. 9, p. 1297, 2019.

- [6] M. Hernández-Reséndiz, C. Gómez-Rodríguez, D. Fernández-González y G. Castillo-Rodríguez, «Synthesis and characterization of dense MgO-TiO₂ nanocomposites obtained by two novel processing routes,» *Ceram. Int.*, vol. 49, n° 8, pp. 12604-12614, 2023.
- [7] E. Benavidez, E. Brandaleze, L. Musante y P. Galliano, «Corrosion Study of MgO-C Bricks in Contact with a Steelmaking Slag,» *Procedia Materials Science*, vol. 8, pp. 228-235, 2015.
- [8] T. Xu, Y. Xu, Y. Li, S. Sang, Q. Wang, T. Zhu, M. Nath y B. Zhang, «Corrosion mechanisms of magnesia-chrome refractories in copper slag and concurrent formation of hexavalent chromium,» *J. Alloy Compd.*, vol. 786, pp. 306-313, 2019.
- [9] M. Sadeghian y A. Fatehi, «Identification, prediction and detection of the process fault in a cement rotary kiln by locally linear neuro-fuzzy technique,» *J. Process. Contr.*, vol. 21, n° 2, pp. 302-308, 2011.
- [10] S. Hong, Y. Li, Y. Liu, Y. Gao, G. Ma, J. Li, Z. Qian y J. Huang, «Investigation on the alkali resistance property of theoretical composition magnesia alumina spinel bricks,» *Adv. Mat. Res.*, Vols. %1 de %2503-504, pp. 533-537, 2012.
- [11] S. Hong y Y. Li, «The influences of zirconia on the properties of magnesia alumina spinel bricks,» *Adv. Mat. Res.*, Vols. %1 de %2690-693, pp. 369-642, 2013.
- [12] Z. Guo, S. Palco y M. Rigaud, «Reaction Characteristics of Magnesia-Spinel Refractories with Cement Clinker,» *Int. J. Appl. Ceram. Tec.*, vol. 2, n° 4, pp. 327-335, 2005.
- [13] W. Zhou, W. Yan, S. Ma, S. Schafföner, Y. Dai y Y. Li, «Degradation mechanisms of periclase-magnesium aluminat spinel refractory bricks used in the upper transition zone of a cement rotary kiln,» *Constr. Build. Mater.*, vol. 272, p. 121617, 2021.
- [14] Z. Qotaibi, A. Diouri, A. Boukhari, M. Taibi y J. *. a. Aride, «Analysis of magnesia chrome refractories weared in a rotary cement kilnAnalyse des réfractaires de magnésie-chrome dégradés dans un four à ciment,» *Ann. Chim.-Sci. Mat.*, vol. 23, n° 1-2, pp. 169-172, 1998.
- [15] M. Ludwig, E. Śnieżek, I. Jastrzębska, R. Prorok, Y. Li, N. Liao, M. Nath, J. Vlček y J. Szczerba, «Corrosion Resistance of MgO and Cr₂O₃-Based Refractory Raw Materials to PbO-Rich Cu Slag Determined by Hot-Stage Microscopy and Pellet Corrosion Test,» *Materials*, vol. 15, n° 3, p. 725, 2022.
- [16] C. Schacht, *Refractories Handbook. Mechanical engineering*, Londres: CRC Press, 2004.
- [17] R. German, P. Suri y S. Park, «Review: liquid phase sintering,» *J. Mater. Sci.*, vol. 44, pp. 1-39, 2009.
- [18] X. Lin, W. Yan, S. Ma, Q. Chen, N. Li, B. Han y Y. Wei, «Corrosion and adherence properties of cement clinker on porous periclase-spinel refractory aggregates with varying spinel content,» *Ceram. Int.*, vol. 43, n° 6, pp. 4984-4991, 2017.
- [19] S. Ma, W. Yan, S. Schafföner, X. Lin, N. Li, Y. Zhai, X. Liu y L. Xu, «Influence of magnesium aluminat spinel powder content on cement clinker corrosion and adherence properties of lightweight periclase-spinel refractories,» *Ceram. Int.*, vol. 43, n° 18, pp. 17026-17031, 2017.

Trabajo complementario 2: Nano-Oxide (SiO_2 and Fe_2O_3) effect on magnesium oxide compound (MgO).

3. NANO-OXIDE (SiO₂ AND Fe₂O₃) EFFECT ON MAGNESIUM OXIDE COMPOUND (MgO)

Cristian GÓMEZ-RODRÍGUEZ

Luis Felipe VERDEJA

Guadalupe Alan CASTILLO-RODRÍGUEZ

Eden Amaral RODRÍGUEZ-CASTELLANOS

Daniel FERNÁNDEZ-GONZÁLEZ

Adolfo COLLADO-HERNÁNDEZ

Linda Viviana GARCÍA-QUIÑONEZ

3.1. Introduction

3.1.1. Refractory materials

Refractory materials have many different definitions in the literature. However, one of the most common ways to define them is as materials that can withstand elevated temperatures and are subjected to different degrees of mechanical and thermal stress. Moreover, they resist corrosion and the erosion by solids, gases, and liquids as well. This definition is not unique, yet it can be taken as one that best describes the refractory materials.

3.1.2. General composition of refractory materials

A refractory material is generally composed of four structural units:

- a. Grains or aggregates: main element of refractory materials. They constitute near 70% of the product. Different grain sizes and aggregates are used to build and produce a dense texture.
- b. Matrix: materials with sizes smaller than 150 μm , which are used to fill up space between the aggregates.
- c. Binding material: structural unit that joins the aggregates with the matrix to form the refractory material.
- d. Pores: zones in the material where no material is found.

3.1.3. Recent studies on refractory materials: Investigation of their properties

Refractory materials play an important role on different industrial activities, specially where the production requires high temperatures, such as the melting of ferrous and non-ferrous metals. Different types of refractory materials have been employed as linings for walls, tiles, vaults for electric arc furnaces, metallurgical pots, basic oxygen furnaces, among others. These materials have been used due to their excellent thermal, chemical, and mechanical properties. Magnesite-carbon brick is taken as standard for the lining of ladle metallurgy furnaces for slag lines, basic oxygen furnaces, and electric arc furnaces for steel making and in secondary steel-making furnaces and equipment [1-3]. However, this refractory is a carbon-rich material, which makes it prone to oxidation and this condition leads to subsequent side effects. Recently, several efforts have been made to improve the performance of MgO bricks through the addition of different additives, such as TiO_2 , SiO_2 , Al_2O_3 , ZrO_2 , Fe_2O_3 , and ZnO [4, 5], but problems remain due to the increasing severity of the operating conditions. This fact has created enormous opportunities for further research in the field of refractory materials. Nanotechnology was introduced to the refractory industry some years ago, and nowadays it is an important tool included in many research projects [3, 6-8]. In their research work, Huizhong et al. reported on the addition of nano- Fe_2O_3 to a matrix of magnesite-chrome refractory and found that the sintering temperature was reduced about 150 $^\circ\text{C}$ [9]. Another interesting report comes from Min Chen et al., who studied different sizes of zirconia (micro-nano-powders) added to MgO-CaO refractories sintered at 1600 $^\circ\text{C}$. The results showed that densification was promoted by increasing the amount of nano- ZrO_2 . In addition, the formation of calcium zirconate (CaZrO_3) induced a volume expansion, which improved the thermal shock resistance, as well as an enhancement of the slag corrosion

resistance due to the chemical inertness of the CaZrO_3 phase [10]. Finally, Azhari et al. investigated the effect of nano- Fe_2O_3 up to 8 wt. % in $\text{MgO-Cr}_2\text{O}_3$ refractory matrix and established that the formation of magnesioferrite spinel was reached at 1350 °C [11]. On the other hand, as is known, the fine fraction is considered the weakest constituent of a refractory matrix. Therefore, it must be reinforced by the development of a strong bonding. The bonding strength represents one of the main microstructural characteristics that contributes to the development of a reliable refractory matrix. Increasing the bonding strength, the resistance against many kinds of stresses during performance and structural spalling would be improved. Considering the above mentioned, in the present research work, the effect of nanoparticles of Fe_2O_3 and SiO_2 as structural bonding on the sintering process of a dense magnesia composite was investigated.

3.2. Experimental procedure

3.2.1. Raw materials

Dead burnt magnesia (at industrial grade purity) with a particle size < 45 μm was used as raw material. Its chemical composition, determined by X-ray fluorescence technique, is given in Table 1. High-grade nano-iron oxide ($\alpha\text{-Fe}_2\text{O}_3$) and silicon oxide $\alpha\text{-SiO}_2$, with an average particle size in the range of 20–50 nm, were supplied by Skyspring Nanomaterials, Inc., USA (Table 2). The compositions investigated were 0, 1, 3, and 5 wt.% of nano- Fe_2O_3 and SiO_2 , which were added to magnesia powders. The $\alpha\text{-Fe}_2\text{O}_3$ (99.0 wt. %) and SiO_2 (99.9 wt. %) nano-raw materials in the present study were of analytical grade.

Tab. 1. Chemical analysis of magnesia.

Raw material	Chemical analysis (%)						
	MgO	CaO	FeO	Fe_2O_3	Al_2O_3	SiO_2	LOI
MgO	97.43	0.9	-	0.06	-	0.6	1.01

Tab. 2. Properties of the high-purity powders.

Powder	Purity (%)	Size nm	SSA m^2/g	Color
Fe_2O_3 (α)	99	20-40	40-60	Red brown
SiO_2	99.9	20-50	18	White

3.2.2. Dispersion test

The best dispersant for the nanoparticles was found by means of a dispersion test using acrylic copolymers as dispersant agents with acetone medium. This test consisted of mixing the nanoparticles inside of test tubes with six different dispersants in acetone and acetone alone. Once the nanoparticles were immersed in the liquid medium, the ultrasonic agitation method (Aquasonic TM 75 T model) was carried out during 1 hour for homogenization.

The tested dispersants were: Crodafos 010-LQ, Crodafos 03-LQ, Oratan 850, Oratan 681, Triton X-100, Zephyrym, and acetone. Figure 1 shows the test tubes with the mixtures of Fe_2O_3 or SiO_2 nanoparticles, acetone, and the dispersants. This analysis observed the settling time of the nanoparticles past 12 days. The best results were the essay tubes where the nanoparticles were dispersed in the liquid medium and not sedimented.

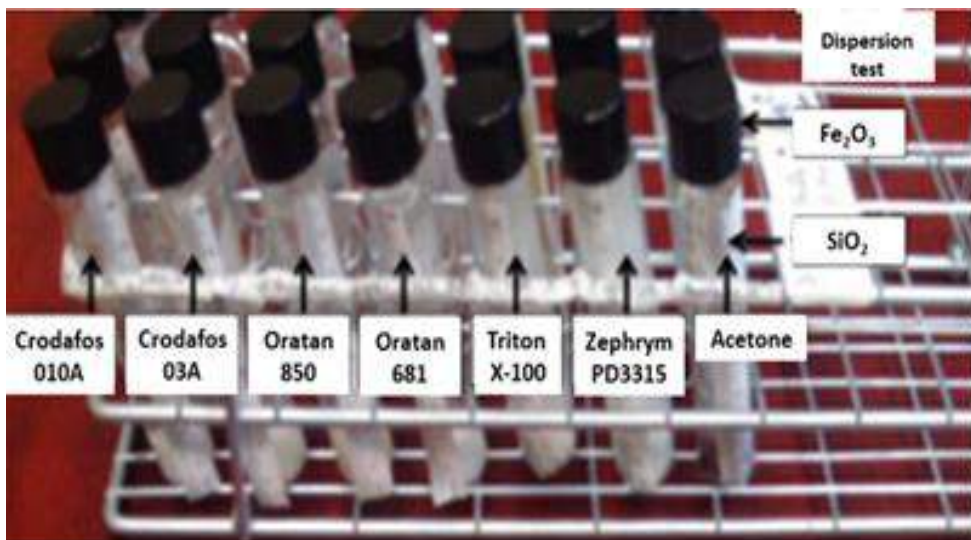


Fig. 1. Test tubes with the mixture of nanoparticles and dispersants used for the dispersion test.

3.2.3. Dispersion test of Fe_2O_3 nanoparticles

Figure 2 shows the dispersion percentage as a function of time for the Fe_2O_3 nanoparticles dispersed in acetone and the other dispersants. The results indicated that the dispersion volume was near 100% for Zephyrym during the first four days. Similarly, Oratan 681 and Triton X-100 had a high dispersion volume during the

first days, near 93% and 90%, respectively. As the days were passing, Fe_2O_3 nanoparticles were sedimenting on the test tube for all proposed mixtures, which was evidenced by the change in transparency of the liquid (acetone) used in each essay tube. After 12 days, Zephyrm dispersant helped to reduce the sedimentation of Fe_2O_3 nanoparticles.

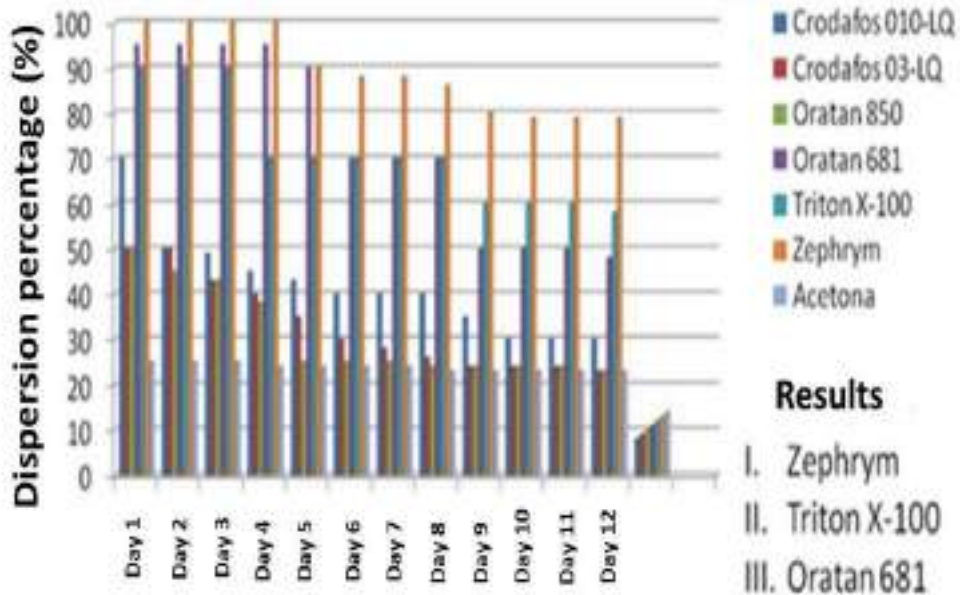


Fig. 2. Dispersion test of Fe_2O_3 nanoparticles. Zephyrm, Triton X-100 and Oratan 681 were the best dispersants used, these dispersants showed greater dispersion percentage past 12 days.

3.2.4. Dispersion test of SiO_2 nanoparticles

Figure 3 exhibits the dispersion percentage as a function of time for SiO_2 nanoparticles immersed in acetone and other dispersants. After 12 days, Zephyrm and Oratan 681 showed a higher dispersion volume, 65 and 60%, respectively. From day 5 to day 12, there is no significant change in the dispersion percentage for all dispersants and the sample that contained just acetone. After 12 days, Zephyrm dispersant also helped to reduce the sedimentation of SiO_2 nanoparticles and the dispersion volume in the liquid medium remained high, which was 65%.

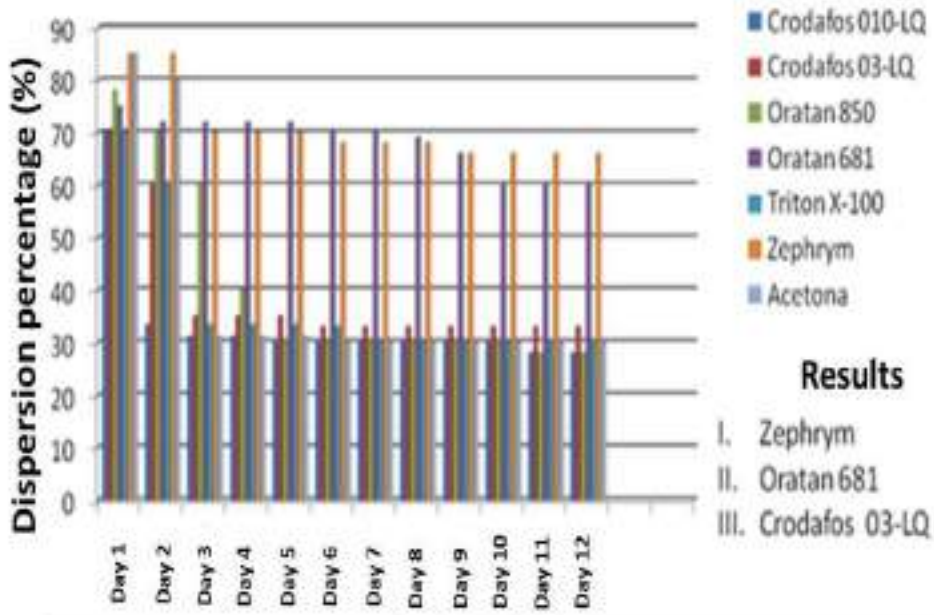


Fig. 3. Dispersion test of SiO_2 nanoparticles. Results considers the dispersants that showed greater dispersion percentage past 12 days

3.2.5. Use of pressure and temperature on refractory composites

Refractory mixtures were made based on the $\text{MgO} + \text{nano-Fe}_2\text{O}_3$ and $\text{MgO} + \text{nano-SiO}_2$ systems. To disperse the nanoparticles, we used Zephyr dispersant (based on the obtained results).

Refractory samples with a diameter of 25.4 mm and a height of 25.4 mm were obtained using a uniaxial pressure of 100 MPa. The refractory samples were sintered in an electric furnace at 1600 °C at a rate of 5 °C/min for 4 hours. Figure 4 displays the sintered samples of MgO and MgO with 1, 3 and 5 wt. % of nano- Fe_2O_3 and SiO_2 , as well as their dimensions before after sintering at 1600 °C.

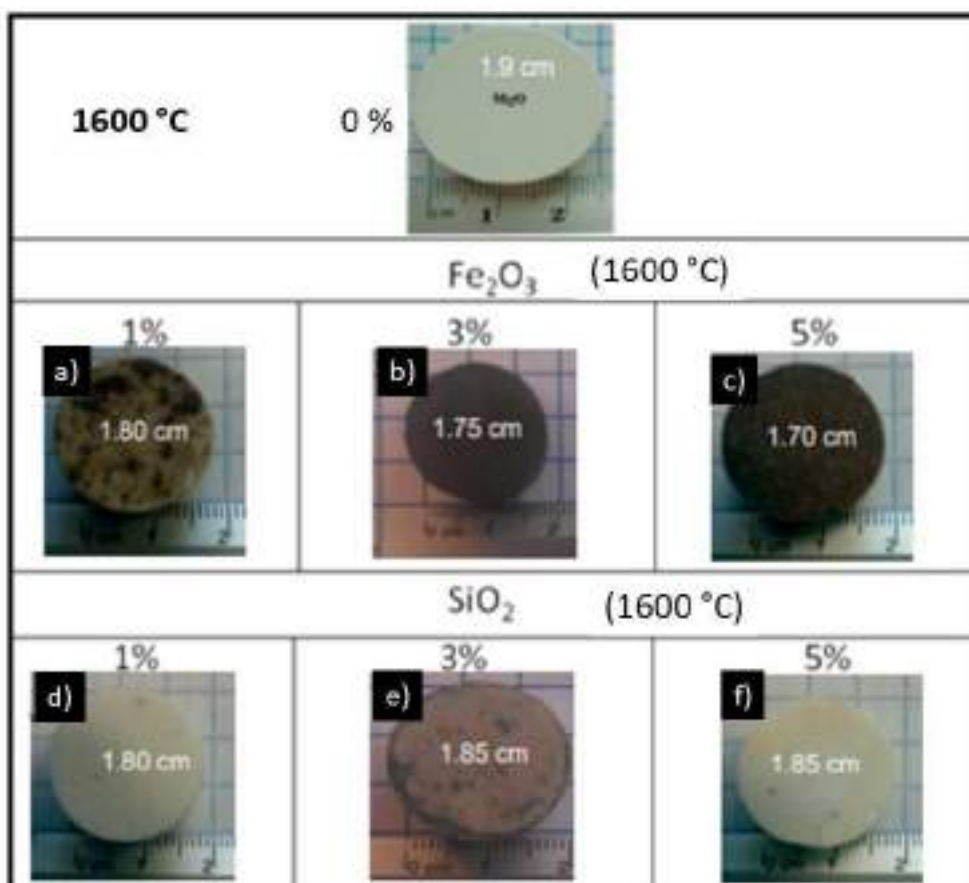


Fig. 4. Sintered samples at 1600 °C. MgO sample is located at the top part, corresponds to 0 wt. % of nanoparticles added to the matrix. (a-c) sintered samples with 1, 3 and 5 wt. % of nano-Fe₂O₃. (d-f) sintered samples with 1, 3 and 5 wt.% of nano-SiO₂.

3.2.6. Microstructural characterization and physical analysis of samples

The presence of ceramic phases was determined by X-ray diffraction technique (XRD; Bruker D8 Advance model) with CuK α radiation ($\lambda = 1.5406 \text{ \AA}$) operated at 40 kV and 30 mA. The scans were performed in the 2θ range from 10 to 90° with a step scan of 0.05° and 1.5 s per step in a continuous mode. The morphology analysis was performed using an FEI Nova NanoSEM 200 scanning electron microscope (SEM) equipped with an electron dispersive X-ray spectroscopy (EDX) detector (EDAX, Apollo XP model, 2930 serial number). The bulk density and apparent porosity were obtained using Archimedes' principle (according to

standard, ASTM C-20), reported values are the average of 10 determinations for each composition.

3.3. Results and discussion

Figure 5a shows the effect of Fe_2O_3 nanoparticle additions on the bulk density and apparent porosity of sintered specimens sintered at 1600 °C. It is observed that the bulk density begins to increase gradually starting from 1 wt. % of Fe_2O_3 , finding its highest value at 5 wt. %. This behavior can be attributed to the higher density of Fe_2O_3 (5.24 g/cm³) in comparison to the MgO (3.58 g/cm³) or by the new phase formation ($\text{MgFe}_2\text{O}_4 = 4.51 \text{ g/cm}^3$). In addition, it can be assuming a good dispersion in all the concentrations used, since the shown tendency is coherent with the increment in Fe_2O_3 nanoparticles addition. Another densification mechanism is correlated microstructurally with the low melting point belonging to the nano-iron oxide in comparison with magnesia oxide, which leads, several times, to the formation of an iron oxide bridge that permits a suitable mass transport between MgO particles. With a maximum increase of Fe_2O_3 nanoparticles, the bulk density increased appreciably, reaching a value of 3.37 g/cm³ at 5 wt. % of nano- Fe_2O_3 with a corresponding value of apparent porosity of 1.8%. Taking into account the porosity registered in the MgO matrix without the addition of nanoparticles (4 %), the porosity decreased substantially when the Fe_2O_3 nanoparticles were added.

Figure 5b shows the bulk density and the apparent porosity results of samples with nano- SiO_2 in the MgO matrix. From the analysis of results, it is observed that there is a tendency toward a decrease in bulk density, while at the same time there is an increase in apparent porosity when nano- SiO_2 is added. A higher apparent porosity was reached with the addition of 3 wt. % of nano- SiO_2 (7.3%). It is important to mention that the maximum density was registered in the sample without the addition of nano- SiO_2 , that is, in the MgO sample (a density of 3.29 g/cm³ with 4% apparent porosity). This behavior can be attributed to spinel formation (Mg_2SiO_4) along with the appearance of microcracks around this phase.

Figure 6a shows the XRD patterns of sintered samples with the addition of 1, 3, and 5 wt. % nano- Fe_2O_3 and without nano- Fe_2O_3 addition (reference). Samples with 1 wt. % of nano- Fe_2O_3 addition and without nano- Fe_2O_3 addition exhibit the existence of single-phase MgO (periclase) and no impurity peaks are observed. The diffraction patterns of samples with 3 and 5 wt. % of nano- Fe_2O_3 addition mainly consisted of MgO (periclase) and MgFe_2O_4 (magnesioferrite) phases.

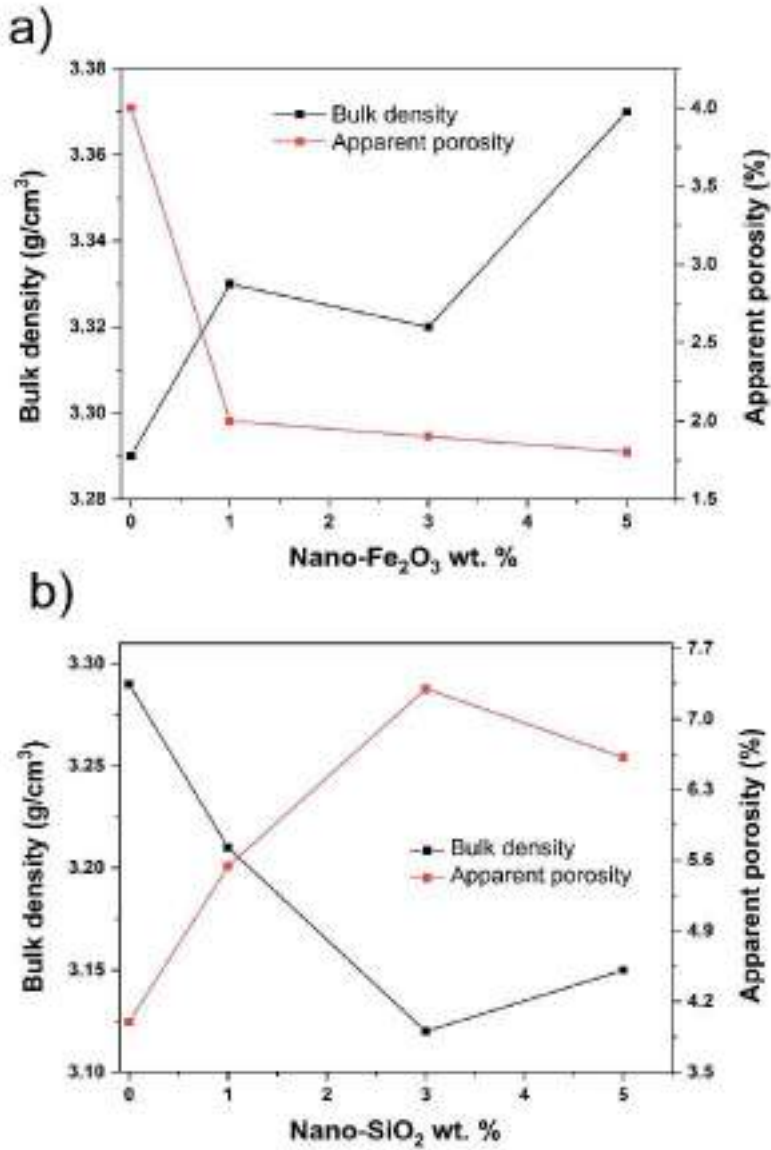


Fig. 5. Density and porosity as a function of weight percentage of: a) Fe₂O₃ nanoparticles, b) SiO₂ nanoparticles, sintered at 1600 °C.

Figure 6b shows the XRD patterns of sintered samples without and with the addition of 1, 3, and 5 wt. % of nano-SiO₂. In the samples without and with 1 wt. % of nano-SiO₂, MgO (periclase) was detected as the main crystalline phase.

Simultaneously, in the samples with 3 wt. % of nano-SiO₂, MgO (periclase) and Mg₂SiO₄ (forsterite) phases were detected

In the sample with the addition of 5 wt. % of nano-SiO₂, MgO (periclase) and Mg₂SiO₄ (forsterite) were observed once again. A greater number of peaks corresponding to the forsterite phase were detected when 5 wt. % nano-SiO₂ was added to the MgO matrix.

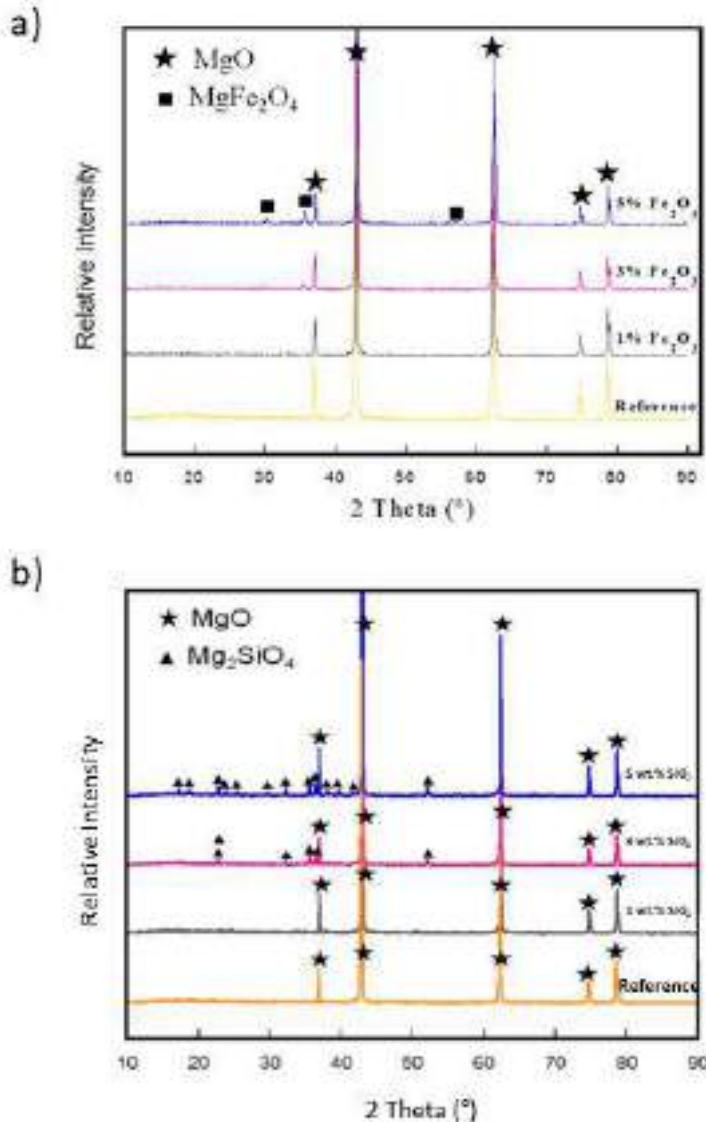


Fig. 6. XRD patterns of the samples sintered at 1600 °C. Yellow line corresponds to samples with 100 wt. % of MgO. Gray, pink, and blue lines correspond to 1, 3 and 5 wt. % of a) nano-Fe₂O₃ and b) nano-SiO₂, respectively.

Figure 7 shows the microstructure corresponding to the sample without the addition of nanoparticles. From the analysis, the typical microstructure of an MgO fractured surface is observed. In addition, porosity and a dark gray phase corresponding to MgO (magnesia) were identified as well as CaO (lime) particles as impurities (white phase).

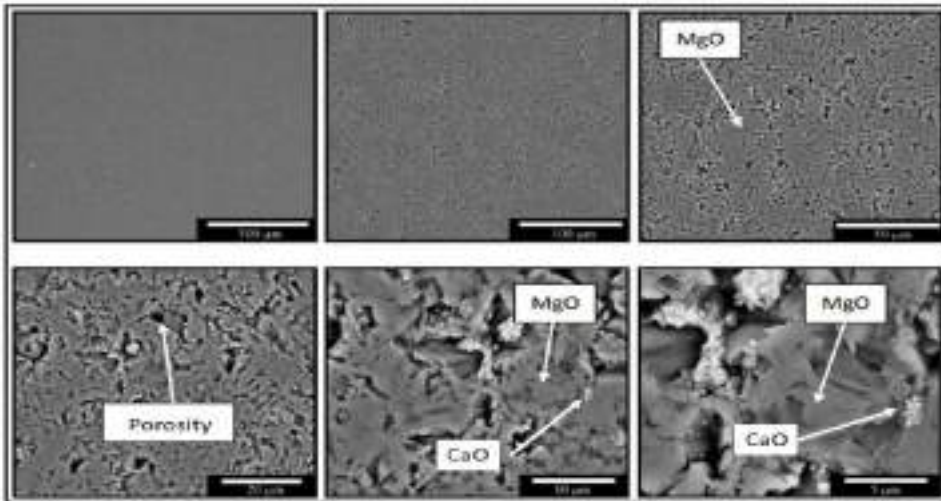


Fig. 7. SEM micrographs of sintered MgO (100%) specimens at 1600 °C.

Figure 8 displays SEM micrographs at different magnifications of samples with 1, 3, and 5 wt. % of nano-Fe₂O₃. With nano-Fe₂O₃ addition at 1 wt. % (micrographs at the top of Figure 8), the formation of phases with iron (Fe) and calcium (Ca) concentrations was observed. These phases formation take place during the reaction of nano-Fe₂O₃ with CaO impurities, resulting in calcium iron oxides. These oxides, characterized by low melting points, were found randomly in low proportion in the MgO matrix.

With the addition of nano-Fe₂O₃ at 3 wt. % (micrographs in the middle of Figure 8), a homogeneous microstructure with low apparent porosity (1.9%) and a phase corresponding to magnesioferrite (MgFe₂O₄) was found. Sample containing 5 wt. % of nano-Fe₂O₃, revealed magnesioferrite phase (MgFe₂O₄) in the grain boundaries as well as in the periclase grains, corroborated by XRD analysis. As claimed by some researchers, the high solubility of iron oxide (Fe₂O₃) in periclase (around 60 wt. % at 1500 °C) due to the near ionic radius of iron and magnesium (Mg²⁺: 0.65 Å; Fe³⁺: 0.6 Å) leads to the formation of cationic vacancies in magnesia [12]. This phenomenon results in high atomic mobility, encouraging precipitation of magnesioferrite spinel from periclase and enhancing the direct bond formation.

The white lines at the boundary and between periclase grains shown in Figure 8 (specifically in samples with 3 and 5 wt. % of nano- Fe_2O_3) indicate a spinel bond (magnesian ferrite spinel, MgFe_2O_4), which also plays an effective role in lowering the dihedral angle between periclase grains. As it is known, one of the key factors in reducing the sintering temperature of direct-bonded bricks, as reported nearly four decades ago, is lowering the dihedral angle between periclase grains [11].

Similarly, calcium (Ca) and iron (Fe) concentrations have been observed in the triple points as revealed by EDX analysis (white phase). Although this phase was not detected by XDR, it can be attributed to the calcium iron oxide phase (see point 1 and inserted table in Figure 8).

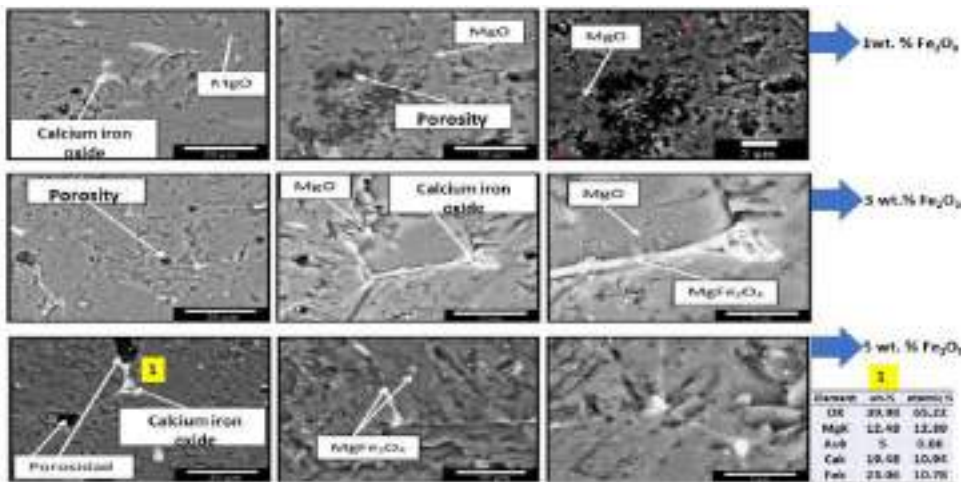


Fig. 8. SEM micrographs of sintered samples at 1600 °C with 1, 3, and 5 wt. % nano- Fe_2O_3 . Every composition has different magnifications, corresponding to 20, 10, and 5 μm .

The SEM analysis carried out on the samples with nano- SiO_2 content is shown in Figure 9. The EDX analysis indicated the presence of calcium magnesium silicate in the samples corresponding to the nano- SiO_2 additions at 1 and 3 wt. % (corresponding to the three micrographs in the top and the three in the middle of Figure 9, respectively). This phase has a low melting point and was formed by the reaction of nano- SiO_2 and CaO (as an impurity occurrence from magnesia).

Furthermore, Figure 9 shows the specimens with 5 wt. % additions of nano- SiO_2 , where the formation of magnesium silicates (Mg_2SiO_4) was identified. This phase was observed on the grains of magnesia, with a triangular morphology (white phase, see micrographs at the bottom of Figure 9). Magnesium silicate phase was identified by a punctual EDX analysis (see point 2 and inserted table in Figure 9) and was confirmed by XRD analysis.

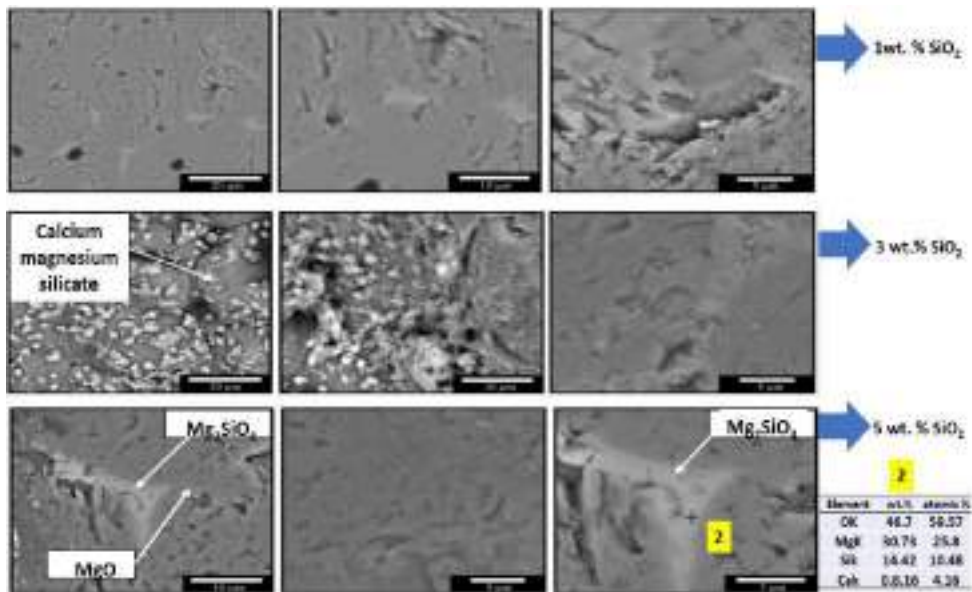


Fig. 9. SEM micrographs of sintered samples at 1600 °C with 1, 3, and 5 wt. % nano-SiO₂. Every composition has different magnifications, corresponding to 20, 10, and 5 μm.

3.4. Conclusions

The addition of nano-Fe₂O₃ leads to the formation of a magnesioferrite spinel bond that permits a suitable mass transport between MgO particles. The addition of nano-SiO₂ contributes to the formation of calcium magnesium silicates (which is a phase with low melting point). The high solubility of iron oxide (Fe₂O₃) in magnesia leads to the formation of cationic vacancies in magnesia, resulting in a high atomic mobility, encouraging the precipitation of magnesioferrite spinel from periclase, and enhancing the direct bond formation. The constitution of this phase aided the sintering process. Moreover, the density increased with the increment in concentration of nano-Fe₂O₃; best concentration corresponded to the sample with 5 wt. % of nano-Fe₂O₃, with a density of 3.37 g/cm³ and a porosity of 1.8%. On the other hand, density decreased with the increment of nano-SiO₂ concentrations in the sintered MgO samples; they have open porosities.

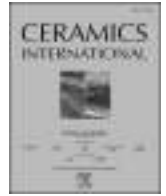
Acknowledgements

This research was supported by a Juan de la Cierva Formación grant from the Spanish Ministry of Science and Innovation (MCINN) to Daniel Fernández-González [FJC2019-041139-I].

3.5. Bibliography

- [1] Campos, K. S., Lenz e Silva, G.F.B., Nunes, E.H.M., Vasconcelos, W.L.: *The influence of B₄C and MgB₂ additions on the behavior of MgO–C bricks*. *Ceramics International*. 38 (7), p. 5661-5667, 2012.
- [2] Han, B., Li, Y., Guo, C., Li, N., Chen, F.: *Sintering of MgO-based refractories with added WO₃*. *Ceramics International*. 33 (8), p. 1563-1567, 2007.
- [3] Zargar, H. R., Oprea, C., Oprea, G., Troczynski, T.: *The effect of nano-Cr₂O₃ on solid-solution assisted sintering of MgO refractories*. *Ceramics International*. 38 (8) p. 6235-6241, 2012.
- [4] Martinac, V., Labor, M., Petric, N.: *Effect of TiO₂, SiO₂ and Al₂O₃ on properties of sintered magnesium oxide from sea water*. *Materials Chemistry and Physics*. 46 (1) p. 23-30, 1996.
- [5] Nelson, J. W., Cutler, I. B.: *Effect of oxide additions on sintering of magnesia*. *Journal of the American Ceramic Society*. 41 (10) p. 406-409, 1958
- [6] Dudczig, S., Veres, D., Aneziris, C. G. Skiera, E., Steinbrech, R. W.: *Nano- and micrometre additions of SiO₂, ZrO₂ and TiO₂ in fine grained alumina refractory ceramics for improved thermal shock performance*. *Ceramics International*. 38 (3) p. 2011-2019, 2012.
- [7] Bag, M., Adak, S., Sarkar, R.: *Nano carbon containing MgO-C refractory: Effect of graphite content*. *Ceramics International*. 38 (6) p. 4909-4914, 2012.
- [8] Sako, E. Y., Braulio, M. A. L., Pandolfelli, V. C.: *How effective is the addition of nanoscaled particles to alumina–magnesia refractory castables?*. *Ceramics International*. 38 (6) p. 5157-5164, 2012.
- [9] Huizhong, L. H., Jianxiu, W.: *Influence of nano-Fe₂O₃ on sintering and mechanical property of magnesia-chrome refractories*. *Refractories*. 5 p. 002, 2003.
- [10] Chen, M., Lu, C., Yu, J.: *Improvement in performance of MgO–CaO refractories by addition of nano-sized ZrO₂*. *Journal of the European Ceramic Society*. 27 (16) p. 4633-4638, 2007.
- [11] Azhari, A., Golestani-Fard, F., Sarpoolaky, H.: *Effect of nano iron oxide as an additive on phase and microstructural evolution of Mag-Chrome refractory matrix*. *Journal of the European Ceramic Society*. 29 (13) p. 2679-2684, 2009.
- [12] Ikesue, A., Yoshitomi, J., Shikano, H., Eguchi, T.: *Formation of precipitated-complex spinel in magnesia-chrome refractories and its characteristics*. *Interceram*. 41 (6), p. 406-412, 1992.

Trabajo complementario 3: Synthesis and characterization of dense MgO–TiO₂ nanocomposites obtained by two novel processing routes.



Synthesis and characterization of dense MgO–TiO₂ nanocomposites obtained by two novel processing routes

M. Hernández-Reséndiz^a, C. Gómez-Rodríguez^{b,c,*}, D. Fernández-González^{d,**},
G.A. Castillo-Rodríguez^{a,***}

^a Universidad Autónoma de Nuevo León, Av. Universidad No., 66451, San Nicolás de los Garza, Mexico

^b Departamento de Mecánica, Facultad de Ingeniería, Campus Coatzacoalcos, Universidad Veracruzana, Av. Universidad km 7.5 Col. Santa Isabel, Coatzacoalcos, 96535, Veracruz, Mexico

^c Departamento de Ciencia de los Materiales e Ingeniería Metalúrgica, Escuela de Minas, Energía y Materiales, Universidad de Oviedo, Calle Independencia, s/n, 33004, Oviedo/Uviéu, Asturias, Spain

^d Nanomaterials and Nanotechnology Research Center (CINN-CSIC), Universidad de Oviedo (UO), Principado de Asturias (PA), Avda. de la Vega, 4-6, 33940, El Entrego, Spain

ARTICLE INFO

Keywords:

Brucite (Mg(OH)₂)
Caustic magnesia (MgO)
TiO₂ nanoparticles
Calcination
Sintering

ABSTRACT

The aim of the present manuscript is to obtain dense MgO refractories by means of two novel different routes: TiO₂ nanoparticles in brucite (Mg(OH)₂, R1) and TiO₂ nanoparticles in caustic magnesia (MgO, R2). Therefore, contents of TiO₂ nanoparticles were added at 1, 3, and 5 wt % to brucite and caustic magnesia while the reference sample consisted in 100 wt % MgO (R0), which was obtained from calcined brucite. The nanoparticles were mixed with the brucite in the first route (R1), and the mixtures were first calcined at 960 °C and then cold uniaxially pressed at 150 MPa and subsequently sintered at 1600 °C for 4 h. Also, TiO₂ nanoparticles were mixed with the caustic magnesia in the second route (R2), and the mixtures were then cold uniaxially pressed and sintered at 1600 °C. Different techniques were considered to characterize the composites: Thermal Analysis, XRD, SEM, bulk density and porosity, and cold crushing strength (CCS). Results suggest that the route 1 produces MgO–TiO₂ composites with greater densification rate (density is at least a 3.29% greater) and better mechanical properties (CCS is at least a 20% better) than the route 2. Therefore, starting from brucite (Mg(OH)₂) to obtain MgO–TiO₂ composites is a better alternative to produce a material with greater densification and better mechanical properties.

1. Introduction

The study of MgO refractories adding second phases in micro and nanometric sizes has been widely reported in literature [1–20]. Part of these investigations focus on the structural changes generated by the second phases added to the matrix and on the obtained properties. Similar considerations could be applied to the study of TiO₂ nanoparticles on the structure and properties of MgO refractories. However, the novelty of this manuscript arises from the utilization of industrial grade brucite of synthetic origin doped with TiO₂ nanoparticles to obtain MgO–TiO₂ refractory composites and the comparison of the

results with those obtained for MgO–TiO₂ refractory composites directly obtained starting from caustic magnesia (MgO). Brucite, with the chemical formula Mg(OH)₂, is mainly used as precursor of magnesia (MgO) to manufacture refractory bricks. Nevertheless, it has some other uses as flame retardant, source of magnesium or, more recently, it was used as Mg(OH)₂/TiO₂ composite for catalytic degradation of chemical warfare agents [1]. Sintered magnesium oxide is one of the most important basic refractory materials used for many years worldwide by cement or different metallurgical industries, as the lining of ladles that transport the melt or used in walls, vaults, or floors of furnaces where different materials are melted [2,3]. Due to the demanding standards

* Corresponding author. Departamento de Mecánica, Facultad de Ingeniería, Campus Coatzacoalcos, Universidad Veracruzana, Av. Universidad km 7.5 Col. Santa Isabel, Coatzacoalcos, 96535, Veracruz, Mexico.

** Corresponding author.

*** Corresponding author.

E-mail addresses: crisgomez@uv.mx (C. Gómez-Rodríguez), d.fernandez@cinn.es (D. Fernández-González), alan.castillo.rdz@gmail.com (G.A. Castillo-Rodríguez).

<https://doi.org/10.1016/j.ceramint.2022.12.123>

Received 15 September 2022; Received in revised form 7 December 2022; Accepted 13 December 2022

Available online 14 December 2022

0272-8842/© 2022 Elsevier Ltd and Techna Group S.r.l. All rights reserved.

that they require in the fusion processes and obtaining of the finished products, these industries require refractory bricks of high purity and quality with exceptional properties. Recently, several researchers have reported the role of nano-additives or micro-particles on sintered magnesia, where Al_2O_3 [4–7], MgAl_2O_4 [8,9], SiO_2 [10], ZrO_2 [11–13], Fe_2O_3 [5,14], ZrSiO_4 [15], TiO_2 [16,17], C [18,19] or Cr_2O_3 [20] have been incorporated into the caustic magnesia and sintered magnesia matrix. Thermal, chemical, physical and mechanical properties have been substantially improved in these composites. Anyway, these investigations have centered on the impact that nano or micro-additions of ceramic oxides have on the sintered magnesia composite using caustic MgO as starting material. Nevertheless, the effect that TiO_2 nanoparticles addition on industrial grade brucite ($\text{Mg}(\text{OH})_2$) of synthetic origin may have on the final properties of sintered magnesia has not been yet studied.

There are different processes for obtaining high purity MgO, although it is commonly obtained from the precipitation of synthetic brine combined with calcined dolomite [4,21–23]. From brine, MgCl_2 is obtained in aqueous solution, which is introduced into a reactor and reacts with $\text{Ca}(\text{OH})_2$, where also there is a reaction between $\text{MgO}-\text{CaO}-\text{H}_2\text{O}$, from the calcination of dolomite. The $\text{Mg}(\text{OH})_2$ obtained by precipitation from the reactor is calcined in a Herreshoff kiln to produce high purity caustic MgO powder. The caustic MgO powder is then pressed (briquetted) to be sintered in a vertical furnace at 1800°C and produce sintered MgO.

Anyway, it is known that magnesium hydroxide is a chemically defined compound with hexagonal/rhombohedral crystal structure. When the brucite is calcined, during thermal decomposition at 960°C , a face-centered cubic crystalline transformation occurs, which yields caustic MgO [24]. In this transformation, the presence of Ti^{4+} ions could influence in the crystalline structure of brucite by substitution Mg^{2+} ions, finally impacting on the properties of the last stage to obtain the sintered MgO [25,26].

Within this manuscript, three routes (**R0**, **R1** and **R2**) are proposed to elaborate MgO– TiO_2 refractories:

- **R0** route, TiO_2 is not added (reference sample). Brucite was calcined at 960°C for 2 h, subsequently the obtained MgO powders were uniaxially pressed and green compacts were sintered at 1600°C for 4 h.
- **R1** route, TiO_2 nanoparticles are added before the calcination of the $\text{Mg}(\text{OH})_2$. Mixtures of $\text{Mg}(\text{OH})_2$ and TiO_2 nanoparticles were later calcined at 960°C for 2 h, then uniaxially pressed and, finally, green compacts were sintered at 1600°C for 4 h.
- **R2** route, TiO_2 is directly added to the caustic MgO (after the calcination of the $\text{Mg}(\text{OH})_2$ at 960°C for 2 h). Later, powders were uniaxially pressed and green compacts were sintered at 1600°C for 4 h.

The results of the formed phases, morphology, physical and mechanical properties such as density, porosity, and cold crushing strength of the three routes were investigated and discussed. Raw materials were analyzed by chemical composition and thermal analysis.

2. Experimental procedure

2.1. Calcined powders and sintered powders

Brucite ($\text{Mg}(\text{OH})_2$) industrial grade (Peñoles Group Inc.) was used as raw material. The chemical composition of the raw material was determined by inductively coupled plasma atomic emission spectroscopy (brand Thermo model iCAP 6500 Series): 0.03 wt % Al_2O_3 , 0.31 wt % CaO, 0.05 wt % SiO_2 , 0.02 wt % Fe_2O_3 , 46 wt % MgO, 53.59 wt % LOI. High purity nanoparticles of titanium dioxide, TiO_2 (Sigma-Aldrich, Inc., St. Louis, MO, USA), with particle size <21 nm, were used as a raw material. Other specifications of the TiO_2 - rutile/anatase phases are: $\geq 99.5\%$ of purity, 35–65 m^2/g of Specific Surface Area, 1850°C of

melting point, $4.26\text{ g}/\text{cm}^3$ of density. 1, 3, and 5 wt % TiO_2 nanoparticles were added to brucite ($\text{Mg}(\text{OH})_2$) and caustic magnesia (MgO) for route R1 and R2 respectively, where the MgO: TiO_2 ratio is equivalent in both routes (R1 and R2): 99:1 ratio (with sample codes BR1-1 and BR2-1 for route 1 and 2, respectively), 97:3 ratio (with sample code BR1-3 and BR2-3 for route 1 and 2, respectively) and 95:5 ratio (with sample code BR1-5 and BR2-5 for route 1 and 2, respectively). In the case of route 1, the formulations were calculated considering the content of the chemical water of brucite. Fig. 1 shows a flow diagram of the three routes (**R0**, **R1** and **R2**) proposed to elaborate raw materials for refractories based on MgO from brucite. In the **R1** route, TiO_2 is added to the brucite; in the **R2** route TiO_2 is added to the caustic MgO, which is obtained from brucite through calcination at 960°C for 2 h; in the **R0** route TiO_2 is not added.

Based on the above, the objective of the **R1** route is to prepare MgO– TiO_2 refractories from brucite by adding TiO_2 nanoparticles before the calcination of the $\text{Mg}(\text{OH})_2$. Mixtures of $\text{Mg}(\text{OH})_2$ and TiO_2 nanoparticles were later calcined at 960°C for 2 h, then uniaxially pressed and, finally, green compacts were sintered at 1600°C for 4 h. The objective of the **R2** route is to prepare refractories from brucite but adding TiO_2 nanoparticles after the calcination of the $\text{Mg}(\text{OH})_2$ at 960°C for 2 h (i.e. adding TiO_2 nanoparticles to the caustic MgO in the stage just after the calcination of the brucite). Later, the mixed powders of routes 1 and 2 were uniaxially pressed and green compacts were sintered at 1600°C for 4 h. Finally, the objective of the **R0** route is to prepare MgO refractories from $\text{Mg}(\text{OH})_2$ without TiO_2 nanoparticles. As in the other routes, MgO powders were uniaxially pressed and green compacts were sintered at 1600°C for 4 h.

All powder mixtures obtained by R0, R1 and R2 routes were uniaxially pressed (UP) in a steel mold at 150 MPa for 2 min to obtain compacted green samples. Then, green compacts were sintered at 1600°C for 4 h with a heating rate of $5^\circ\text{C}/\text{min}$ in a conventional furnace (KSL-1700X). Table 1 collects information about the samples used in this research, where the Stage 1 corresponds to the calcination of $\text{Mg}(\text{OH})_2$ or $\text{Mg}(\text{OH})_2 + \text{TiO}_2$ nanoparticles and Stage 2 is the sintering of the MgO or MgO + TiO_2 nanoparticles.

Fig. 2(a) shows a representative SEM micrograph of caustic magnesia powders (i.e., after the calcining of the brucite ($\text{Mg}(\text{OH})_2$) or before the sintering process), the particle sizes were <655 nm. Fig. 2(b) shows a

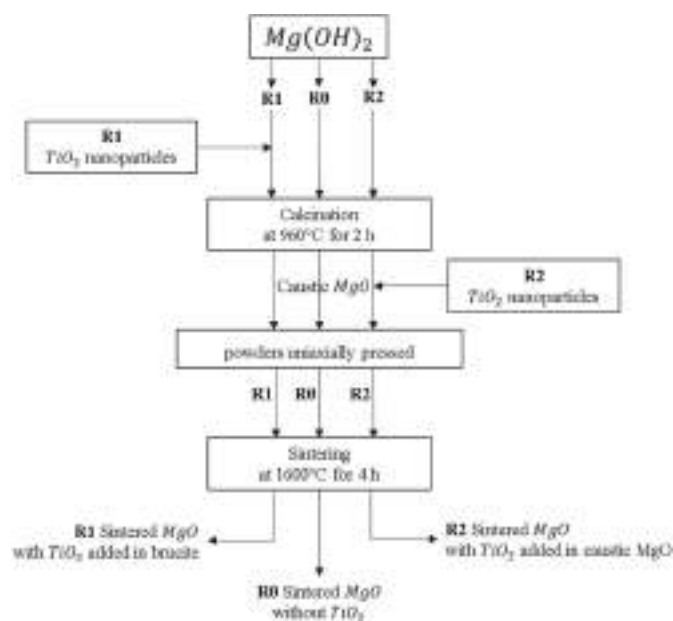
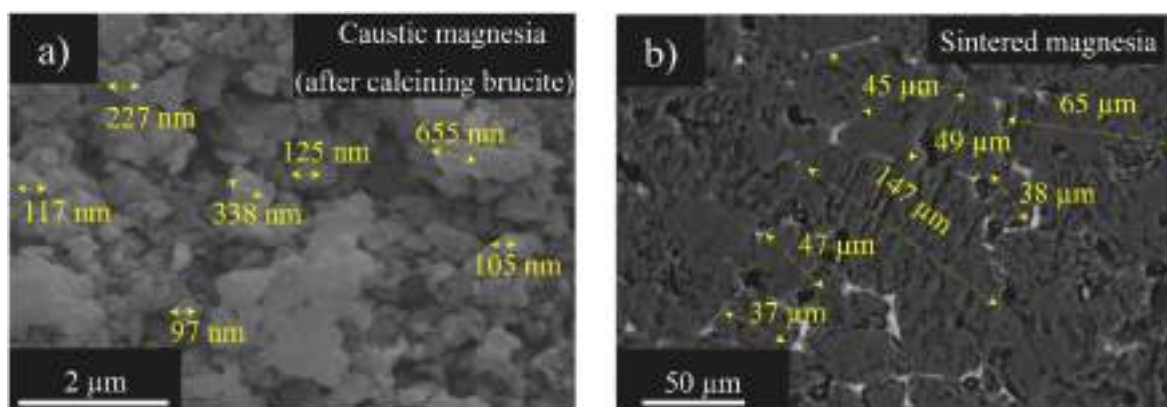


Fig. 1. Flow diagram of the preparation process of the samples. **R1** and **R2** indicate the followed route, where TiO_2 nanoparticles were added; **R0** indicates the route followed when TiO_2 was not added.

Table 1

Routes, samples code and parameter used in stage 1 and 2.

Routes/Samples ID		Stage 1			Stage 2		
Route	Sample code	Raw material (wt. %)		Temperature (°C)	Raw material (wt. %)		Temperature (°C)
		Brucite Mg (OH) ₂	Nano-TiO ₂ added in brucite	Calcination 2 h	Caustic magnesia (MgO)	Nano-TiO ₂ added in caustic MgO	Sintering 4 h
R0	BR0	100	–	960	–	–	1600
R1	BR1-1	99.31	0.69	960	–	–	1600
	BR1-3	97.91	2.09	960	–	–	1600
	BR1-5	96.49	3.51	960	–	–	1600
R2	BR2-1	100	–	960	99	1	1600
	BR2-3	100	–	960	97	3	1600
	BR2-5	100	–	960	95	5	1600

**Fig. 2.** SEM images of a) caustic magnesia powders and b) sintered magnesia sample at 1600 °C.

SEM image of the surfaces of a sample of sintered magnesia (MgO), where sintered grains with circular porosities were observed. The sizes of the grains varied significantly (37–147 μm).

2.2. Dispersion of nanoparticles

TiO₂ nanoparticles with anionic polymeric dispersant (10 wt % of crodafos 03A IQ in relation to the wt. % of nanoparticles, Croda Industrial Chemicals, Snaith, UK) were dispersed in acetone to avoid the agglomeration of the nanoparticles. The dispersion was subjected to magnetic stirring (Intillab Ms-500) for 15 min, and then the suspension was placed in an ultrasonic bath (VWR Scientific Aquasonic 75T) for 20 min. The dispersion was mechanically mixed with the brucite (Mg (OH)₂) (R1 route) (Alghamix II-Zhermack) for 15 min at 100 rpm to obtain a homogeneous mixture with the suspension of TiO₂ nanoparticles in brucite. The same procedure was carried out in the case of caustic magnesia (MgO) in R2 route. This methodology was applied for each content in TiO₂ nanoparticles.

2.3. Particle size after calcination

The particle size after calcination of brucite was calculated from the full width to half maximum (FWHM) peak of greatest diffraction for MgO (111) using the Scherrer equation [27].

$$D = \frac{K\lambda}{\beta \cos \theta} \quad (1)$$

where, D : sample particle size, K : factor (0.89), λ : x-ray wavelength, β : FWHM of the maximum diffraction peak in radians, θ : diffraction angle of the maximum peak. The results obtained are shown in Table 2.

Table 2

Parameters used in the Scherrer equation to obtain the particle size (D) after calcination of brucite (caustic magnesia (MgO)) and caustic magnesia samples with additions of nano-TiO₂.

	K	λ (Å)	FWHM (°2 θ)	B (FWHM in rad)	Θ (°)	D (nm)
MgO	0.89	1.78901	0.4809	0.004196654	25.1369	379
MgO-1 wt. % TiO ₂	0.89	1.78901	0.45	0.003927	25.1556	406
MgO-3 wt. % TiO ₂	0.89	1.78901	0.451	0.003935727	25.15955	405
MgO-5 wt. % TiO ₂	0.89	1.78901	0.4497	0.003924382	25.1916	406

2.4. Microstructural and morphological analysis

The crystal structure and identification of phases were carried out by X-ray diffraction technique (XRD; Panalytical Empyrean model) with Co-K α radiation ($\lambda = 1.79$ Å) operated with a voltage of 40 KV and a current of 40 mA. The scans were performed in the 2 θ range from 10 to 110° and 10 s per-step in a continuous mode. The morphology of all sintered samples was characterized by a Scanning Electron Microscope (JEOL JSM-6010 PLUS/LA) equipped with an electron dispersive X-ray spectroscopy (EDX) detector.

2.5. Physical and mechanical characterization, and thermal testing

The densification of the samples, bulk density (BD) and apparent porosity (AP), was studied by the Archimedes method (ASTM-C20). In other words, this test was carried out by immersing all the sintered

samples in a liquid medium (water), and by weighting the difference. Thus, BD and AP are obtained using formulas (2) and (3).

$$\text{Bulk density (g/cm}^3\text{)} = \left[\frac{M_1 - M_2}{M_3} \right] \quad (2)$$

$$\text{Apparent porosity (\%)} = \left[\frac{M_2 - M_3}{M_2 - M_1} \right] * 100 \quad (3)$$

where, M_1 is initial weight, M_2 is saturation weight and M_3 is immersion weight. The mechanical resistance was determined by the cold crushing strength (CCS) method. A mechanical testing machine (ELE-International, ABR-AUTO V2 model, with range up to 200 tons) was used. With a loading rate of 490 N/s. Samples of 25.4 mm in diameter and 25.4 mm in height were used in both evaluations and the reported values are the average of 13 measurements for each designed composition. The maximum loads per unit area that a refractory material support before failure occurs are obtained with CCS test. The refractory raw materials (brucite ($\text{Mg}(\text{OH})_2$) and caustic magnesia (MgO)) were subjected to simultaneous differential thermal analysis (DTA)/thermogravimetric (TGA) analyses (TA Instruments, model SDT Q600). The analysis was carried out up to 900 °C.

3. Results and discussions

3.1. Differential thermal analysis and thermogravimetric analysis of raw materials

Fig. 3 shows the simultaneous differential thermal analysis and thermogravimetric (DTA-TGA) curves of $\text{Mg}(\text{OH})_2$ and MgO . Brucite powders ($\text{Mg}(\text{OH})_2$) (Fig. 3 (a)) show an endothermic peak at 100 °C, with a weight loss of 31.44% which is attributed to the elimination of physical water in brucite [28]. Likewise, another important endothermic event occurs at 426.06 °C and a weight loss of 18.73% is observed. This thermal event corresponds to the dihydroxylation of ions (H^+ and OH^-) of brucite, which were chemically bound to Mg ions [7,29,30].

It is evident that the sample in this temperature remains with a mass of 49.83%. From 450 °C to 755 °C only a loss of mass of 2.40% occurs, attributed to the diffusion of water vapor trapped in the oxide, according to the literature [31].

Fig. 3 (b) depicts the simultaneous DTA/TGA curves of caustic magnesium oxide (MgO) (this compound was obtained from the calcination of brucite). As can be seen at 220 °C and 397 °C, mass losses corresponding to 1% and 1.7% are observed respectively, corresponding to evaporation of physical and chemical surface moisture that the sample absorbed due to its hygroscopic nature. Results show the presence of a large endothermic transition at 323 °C, which agrees with the dihydroxylation process reported in a range of 300–464 °C [32]. Up to 900 °C there is only a 0.6% in loss in weight which could be attributed to the release of Cl^- ions (which occurs at around 714 °C), since this element can be found in the raw material (in natural brine mantle, according to Brewer) [33].

3.2. Structural analysis

3.2.1. Raw materials and calcined powders

The phase composition of the raw materials was studied by XRD. Fig. 4 (a) shows the diffractogram of caustic magnesia (MgO), in which characteristic peaks of magnesium oxide (ICDD 01-077-2364) are evidenced. Fig. 4 (b) corresponds to the brucite ($\text{Mg}(\text{OH})_2$) sample where characteristic peaks of the brucite phase are evident (ICDD 04-016-3445). The TiO_2 nanoparticles showed two phases corresponding to rutile (ICDD 98-007-6734) and anatase (ICDD 98-009-7051) phase, both observed in Fig. 4 (c). To quantify the mass ratio of the phases in TiO_2 nanoparticles, a Rietveld analysis was performed, and 83.7% for Anatase and 16.3% for Rutile were obtained. Table 3 shows structural

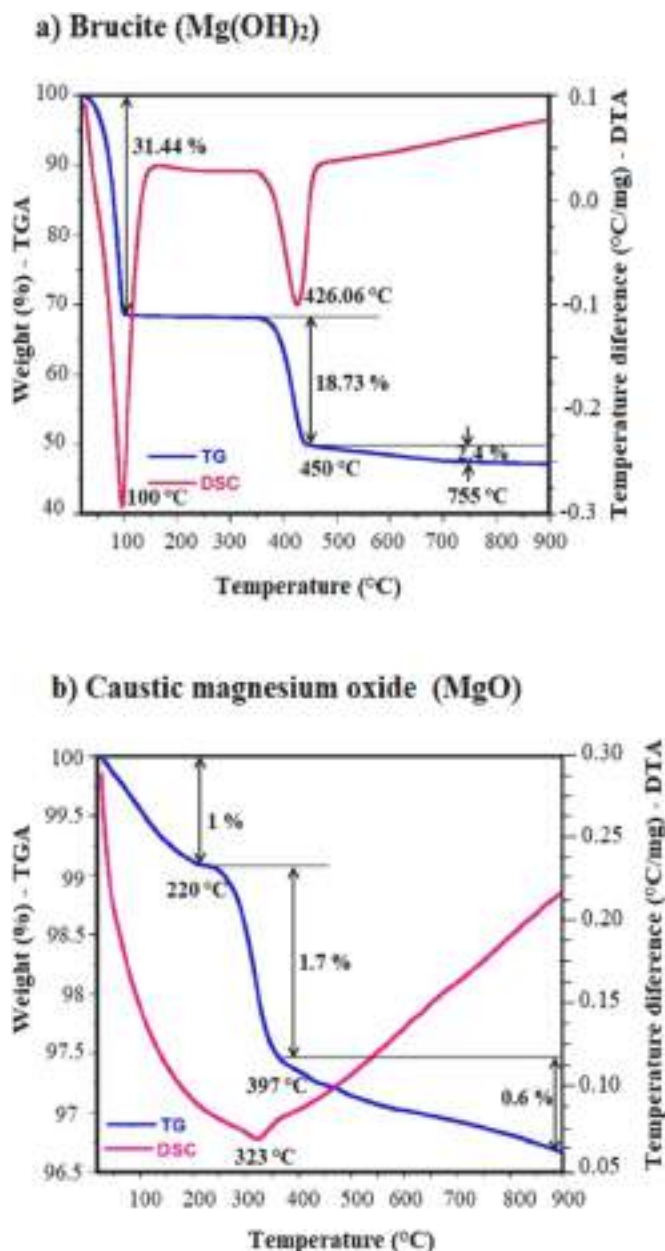


Fig. 3. DTA/TGA results of raw materials used: a) Brucite ($\text{Mg}(\text{OH})_2$) and b) Caustic magnesia (MgO).

parameters and mass ratio of the used raw materials. In all the experiments, the same TiO_2 nano powders were used, so the mass ratio was not modified.

Generally, rutile TiO_2 is a thermodynamically more stable phase at high temperatures and anatase TiO_2 is a thermodynamically more stable phase at low temperatures [34]. Likewise, it is known that the anatase phase transforms into the rutile phase above 750 °C according to the DeVries phase diagram [35] and according to other works [36,37], where they report that from 650 °C to 800 °C the phase transformation to rutile is completed. In the current work, the calcination and sintering temperatures were 960 °C and 1600 °C, respectively. Based on the above, it is assumed that in the aggregated TiO_2 nanoparticles, a transformation from anatase to rutile phase appeared at high temperatures. Therefore, it is considered that rutile was the one that was maintained during the sintering process.

After the calcining process (corresponding to Stage 1, at 960 °C), calcined brucite powders ($\text{Mg}(\text{OH})_2$) without TiO_2 (BR0 sample) and

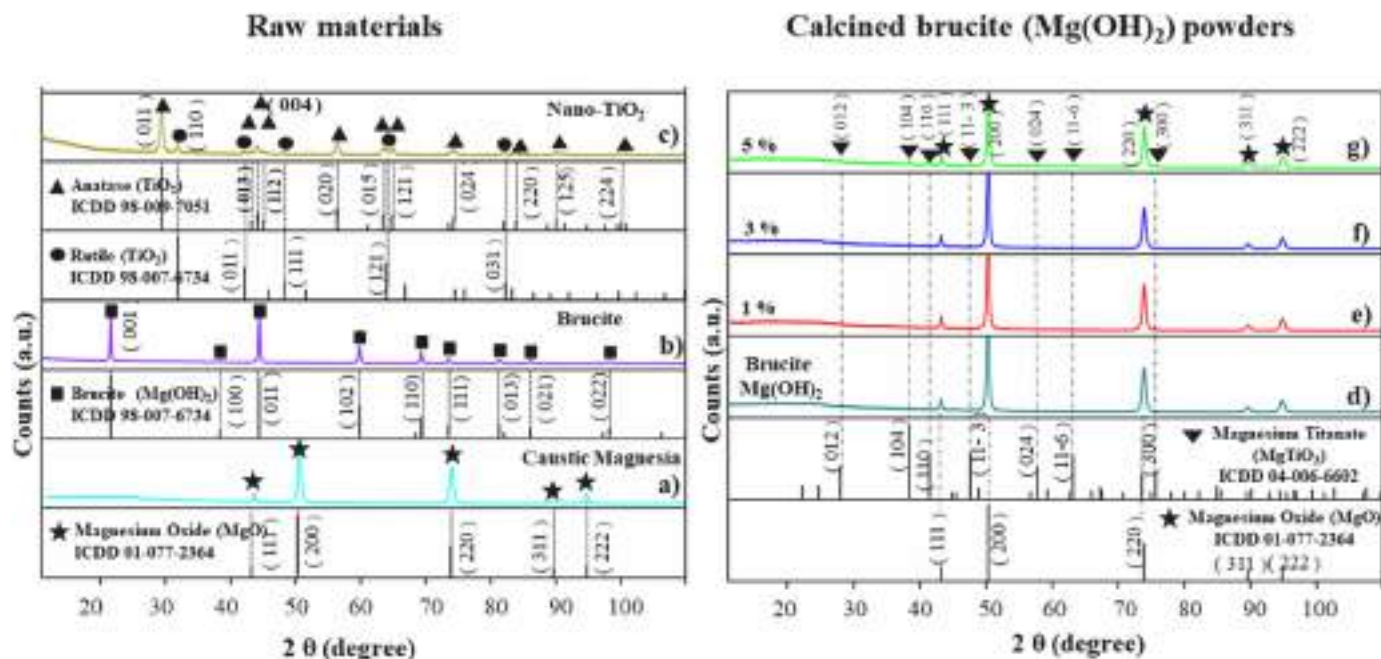


Fig. 4. XRD patterns of raw materials (a–c) and calcined powders (d–g). (a) Powder of caustic magnesia, (b) brucite $\text{Mg}(\text{OH})_2$, (c) Nano- TiO_2 , (d) calcined brucite powder, (e–g) corresponds to calcined powders of brucite with $\text{MgO}:\text{TiO}_2$ ratio of (e) 99:1, (f) 97:3 and (g) 95:5 of wt. %.

Table 3

Structural parameters and mass ratio of the raw materials used.

Phase	Mass ratio (%)	Lattice parameters (Å)	Volume (Å^3)	Angles between axes
From TiO_2 nanoparticles	83.7	a	3.7863	$\alpha = \beta = \gamma = 90^\circ$
		b	3.7863	
		c	9.5108	
From TiO_2 nanoparticles	16.3	a	4.5949	$\alpha = \beta = \gamma = 90^\circ$
		b	4.5949	
		c	2.9587	
MgO	100	a	4.209	$\alpha = \beta = \gamma = 90^\circ$
		b	4.209	
		c	4.209	

with TiO_2 nano additions (BR1-1, BR1-3 and BR1-5 samples) were analyzed by X-ray diffraction (see Fig. 4 (d–g)).

Fig. 4 (d) corresponds to powders of calcined brucite (already converted to caustic magnesia), showing characteristic MgO peaks (ICDD 01-077-2364). Fig. 4 (e–g) show the XRD results of calcined brucite with nanoparticles of TiO_2 , where it is possible to identify magnesium titanium oxide (MgTiO_3) phase in agreement with ICDD 04-006-6602 file, and MgO phase according to the file ICDD 01-077-2364.

3.2.2. Sintered samples

Fig. 5 (a) shows the X-ray diffraction patterns of the BR0 sintered sample from 100% brucite (no $\text{Mg}(\text{OH})_2$ peaks were detected). These diffraction peaks agree with ICDD 01-077-2364 file corresponding to the MgO phase. Fig. 5 (b–d) show the X-ray diffraction patterns of the sintered samples from brucite with $\text{MgO}:\text{TiO}_2$ weight ratio of 99:1, 97:3 and 95:5 of the BR1-1, BR1-3 and BR1-5 samples, respectively. It is observed in these samples that with the increase in TiO_2 nanoparticles, 4 peaks intensify and are most prominent (particularly for the sample with 5 wt % of TiO_2 nanoparticles), corresponding to the phase Mg_2TiO_4 (ICDD 01-079-0830). Fig. 5 (e), like Fig. 5 (a), shows the X-ray diffraction patterns of the BR0 sintered samples of 100% brucite. Fig. 5 (f–h) show the X-ray diffraction patterns of the sintered samples of composition

from caustic magnesia with $\text{MgO}:\text{TiO}_2$ ratio wt. % of 99:1, 97:3 and 95:5 of the BR2-1, BR2-3 and BR2-5 samples, respectively. In these samples, similar crystallographic planes at the same positions (2θ) appeared as those with 1, 3 and 5 wt % of TiO_2 nanoparticles with $\text{Mg}(\text{OH})_2$. It is worth noting that all TiO_2 nanoparticles reacted with MgO phase and so were not detected by XRD, because TiO_2 appears as MgTiO_4 in the XRD pattern of the sintered samples (See Fig. 5 (d) and (h)).

3.3. Densification

Bulk density and porosity were measured by the Archimedes method, as described above, in accordance with the standard ASTM-C20. Fig. 6 (a) and (b) show the effect of TiO_2 nanoparticles on the bulk density and apparent porosity, respectively, of sintered samples. In Fig. 6 (a), the value of bulk density corresponding to the sample BR0 of R0 route (i.e., 0 wt % of TiO_2) was 3.34 g/cm^3 . The bulk density results for the R1 route, i.e., adding TiO_2 nanoparticles to the brucite, show values substantially increased to 3.46 g/cm^3 (i.e., 3.59% increase in density with respect to the reference sample R0) with the incorporation of 1 wt % of TiO_2 nanoparticles, which corresponds to the sample BR1-1. In the same route with 3 and 5 wt % of TiO_2 nanoparticles (i.e., the samples BR1-3 and BR1-5 respectively), the density values remained stable in 3.45 g/cm^3 , corresponding to an increase of 3.29% in the value of density with respect to the reference sample R0, for both concentrations.

The bulk density results for the R2 route, i.e., adding TiO_2 nanoparticles to caustic magnesia, appear substantially increased to 3.38 g/cm^3 (i.e., 1.19% increase in density with respect to the reference sample R0) in the case of incorporating 1 wt % of TiO_2 nanoparticles, which corresponds to the sample BR2-1. In the same route with 3 and 5 wt % of TiO_2 nanoparticles (i.e., the samples BR2-3 and BR2-5 respectively) the density remained stable with values of 3.35 and 3.36 g/cm^3 respectively, corresponding to 0.3% and 0.6% respectively increase in density with respect to the reference sample R0, for both concentrations.

If route 1 and route 2 are compared, it is possible to see that greater values of density are obtained in the case of the route 1. This involves that this route promotes the densification of the composite: density is at least a 3% greater in the samples obtained by the route 1 than those obtained in the route 2.

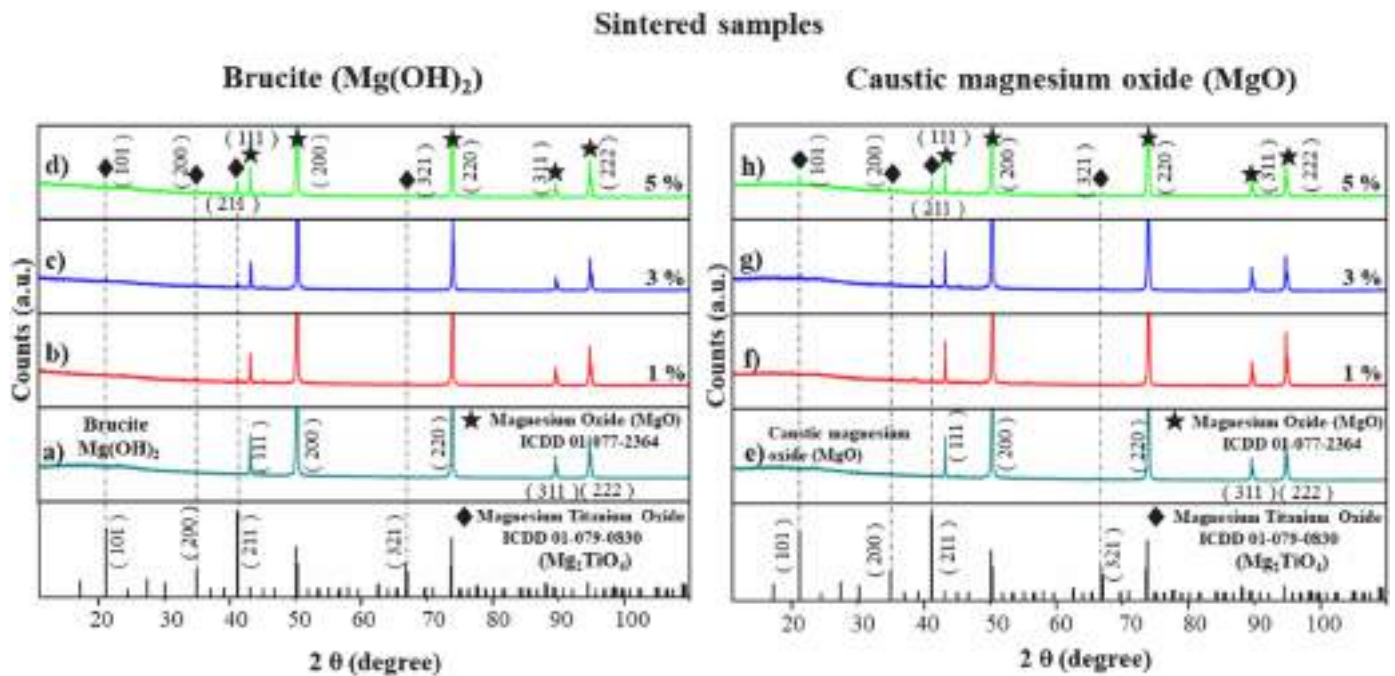


Fig. 5. XRD patterns of sintered samples at 1600 °C where: (a) Sample BR0, (b–d) Samples BR1-1, BR1-3, and BR1-5 respectively, (e) Sample BR0, (f–h) Samples BR2-1, BR2-3 and BR2-5, respectively.

The densification of the sintered samples can be explained as follows:

- From brucite by R1 route. It may be due to two important phenomena.
 - When TiO₂ nanoparticles were added to the brucite and calcined at 960 °C, the following occurred: Mg(OH)₂ has a hexagonal crystalline structure and when MgO dissociates from chemical water (300–464 °C [26,30]), a diffusion of Ti⁴⁺ ions (0.65 Å) [38] towards the crystalline structure brucite Mg²⁺ (0.68 Å) [13] occurs forming MgTiO₃ as confirmed by XRD analysis results (see Fig. 4 (e–g)) [26]. In this ionic migration, vacancies are also generated because the tetravalent ions of Ti that migrate towards spaces (of similar ionic radii) of Mg with bivalent valence ions cause a greater demand of oxygen ions, generating atomic vacancies, i.e., crystalline imperfections in the MgO network [26]. Therefore, this increases the internal energy of the network, which is a major cause of an atomic diffusion driving force, helping the mobility of the ionic transport of this material, which contributes to the densification of the MgO sample during the sintering process.
 - Furthermore, another important factor is that during calcination, the phase obtained (MgTiO₃) had a higher density (4.0 g/cm³) [39] compared to MgO phase (3.58 g/cm³) [2], hence, 1 wt % of TiO₂ nanoparticles helped to substantially increase the density of the sintered samples.
- From caustic magnesia by R2 route, the following happened:
 - When TiO₂ nanoparticles were added to caustic magnesia samples, they also helped to the densification, although they did not have the same effect as in samples of the R1 route, since the ionic mobility was lower in the sintering process, which caused a poorer densification compared with samples by R1 route. The main difference of the process is that by R1 route the Ti⁴⁺ ions occupied Mg²⁺ ion sites in the MgO crystal lattice during the transformation of hexagonal crystalline structure from brucite to crystalline structure of MgO (face centered-cubic) during heat treatment at 960 °C.

Fig. 6 (b) shows the porosity percentage of sintered samples without

and with TiO₂ nanoparticle additions. The R0 reference sample presented 0.6% porosity. In both R1 and R2 routes with TiO₂ nanoparticles additions, the porosity decreased compared to the R0 reference sample. However, with samples made by the R2 route, where TiO₂ nanoparticles were added to caustic magnesia, it is observed that porosity slightly increased with the TiO₂ content (1, 3 and 5 wt %) being 0.246, 0.257 and 0.258%, respectively. On the other hand, for samples made by R1 route, where brucite was doped with 1, 3 and 5 wt % TiO₂ nanoparticles, the porosity increased for the first compositions, 0.236 and 0.248%, respectively, and remained constant for the third composition, 0.243%. It is generally observed in Fig. 6 that the tendency of density in routes 1 and 2 is the same: the density is almost the same for the compositions with 3 and 5 wt % of TiO₂ nanoparticles while the highest density was obtained for 1 wt % TiO₂ nanoparticles. It is clearly observed that the density of the samples obtained by the route 1 is 2.5–3.0% greater than that of the samples obtained by the route 2. The above is consistent with the behavior of the porosity of the sintered samples, shown in Fig. 6, where it is observed for both R1 and R2 routes that the tendency is the same as the addition of TiO₂ increases. It is clearly observed that the porosity of the samples obtained by the route 2 is 4.0–6.0% greater than that of the samples obtained by the route 1. Summarizing, it should be noted that the samples produced by the R1 route obtained higher density and lower porosity than the samples of the R2 route. The increase in porosity could be explained by the microcracks caused during cooling due to the different thermal expansion coefficient between Mg₂TiO₄ formed and MgO obtained from brucite [7,40].

3.4. Morphology

A SEM micrograph of the MgO sample sintered at 1600 °C from brucite (Mg(OH)₂) by the R0 route is shown in Fig. 7. Fig. 7 reveals a sintering morphology with open porosity and traces of Ca and Si as impurities.

To understand the effect of the nanoparticles of TiO₂ on the morphological evolution of sintered MgO (by R1 and R2 route), the morphology was studied by SEM and EDX as shown in Fig. 8(a–f). Fig. 8 (a–c) correspond to samples of sintered MgO from brucite (R1 route) with 1, 3 and 5 wt % of TiO₂ nanoparticles, respectively. The sample

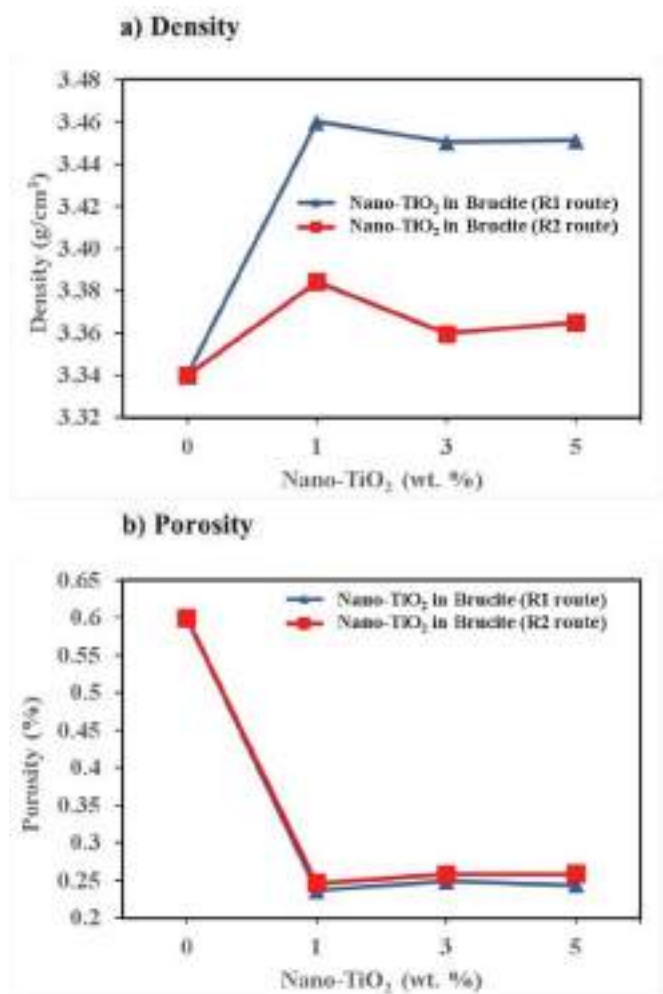


Fig. 6. Effect in sintered samples of 1, 3 and 5 wt % of nano-TiO₂ additions in brucite and caustic magnesia by the R1 and R2 routes, respectively; 0 wt % of nano-TiO₂ addition corresponds to the R0 route: a) variation of the bulk density, b) variation of the apparent porosity.

with 1 wt % of TiO₂ nanoparticles shows morphology of densified sintered MgO grains with closed porosity. Likewise, a white phase corresponding to magnesium titanate oxide phase (Mg₂TiO₄) is observed (see Fig. 8 (a)). It was appreciated with 3 and 5 wt % of TiO₂ nanoparticles

that white phase increased with the addition of TiO₂ nanoparticles to the sample, generating a greater amount of Mg₂TiO₄ (see Fig. 8 (b and c)). This agrees with the results obtained in XRD analysis, corresponding to Fig. 5 (c and d). Likewise, it was observed with 5 wt % of TiO₂ nanoparticles that they were homogeneously distributed within the MgO matrix. Based on the results obtained in XRD, it is known that the TiO₂ nanoparticles fully reacted with MgO, to form Mg₂TiO₄ (see Fig. 5 (d)).

Fig. 8 (d-f) correspond to samples of caustic magnesia (MgO) with 1, 3 and 5 wt % of TiO₂ nanoparticles, respectively. Fig. 8 (d) corresponds to 1 wt % of TiO₂ nanoparticles and shows morphology with growth of MgO grains, residual open porosity, and low formation of Mg₂TiO₄. Likewise, Fig. 8 (e and f) correspond to samples with 3 and 5 wt % of TiO₂ nanoparticles where the amount of Mg₂TiO₄ phase increased. All these samples had a lower density compared to samples of brucite with additions of nanoparticles. This was because with caustic magnesia and additions of TiO₂ nanoparticles, the driving force in atomic diffusion was not high enough for adequate sintering to take place, which results in morphologies with open porosities. Also, the formation of microcracks, when the spinel type phase (Mg₂TiO₄) was greater than 100 μm (see Fig. 8 (e)), is appreciated. This is due to the different coefficients of thermal expansion of the MgO matrix ($\sim 13.5 \times 10^{-6} \text{ }^\circ\text{C}^{-1}$) [40] and the spinel phase of Mg₂TiO₄ ($\sim 12 \times 10^{-6} \text{ }^\circ\text{C}^{-1}$) [40], which generates microcracks and porosity, resulting in a deterioration in the morphology and properties of the sample.

EDX punctual microanalysis was performed on the sample with 3 wt % of TiO₂ nanoparticles and it is shown in Fig. 8 (e). Point 1 (37.76 wt % O; 54.49 wt % Mg; 0.34 wt % Al; 1.33 wt % Si; 2.18 wt % P; 3.91 wt % Ca) corresponds to the MgO phase and point 2 (36.31 wt % O; 37.80 wt % Mg; 0.34 wt % Al; 0.12 wt % Si; 0.07 wt % P; 0.07 wt % Ca; 25.28 wt % Ti) corresponds to the Mg₂TiO₄ phase, according to the XRD results obtained in Fig. 5 (g). At both points, trace of elements such as Al, Si, P and Ca were detected (due to the process of the raw material obtaining).

Fig. 9 shows the evolution at higher magnification of the sintered microstructure at 1600 °C, corresponding to the reference sample and samples made by route 1 (a-c) and route 2 (d-f). The mapping of each sample is shown in each image of Fig. 9. This figure shows the morphology that the phases present and elemental analysis maps obtained by energy dispersive X-ray spectroscopy (EDX), in each sample. In the reference sample, grains of MgO are observed, identified as the dark grey phase. Likewise, different porosities and phases constituted by Ca and Si were observed, which are due to impurities from the raw material (brucite, Mg(OH)₂). Fig. 9 (a-c) corresponds to brucite samples with 1, 3, and 5 wt % of TiO₂ nanoparticles, respectively. In these micrographs, Ca phases were also identified, which had triangular shapes, light white in colour. Likewise, the Si phase was detected around porosities, this phase corresponded to phases of light grey colour. The Mg₂TiO₄ phase was

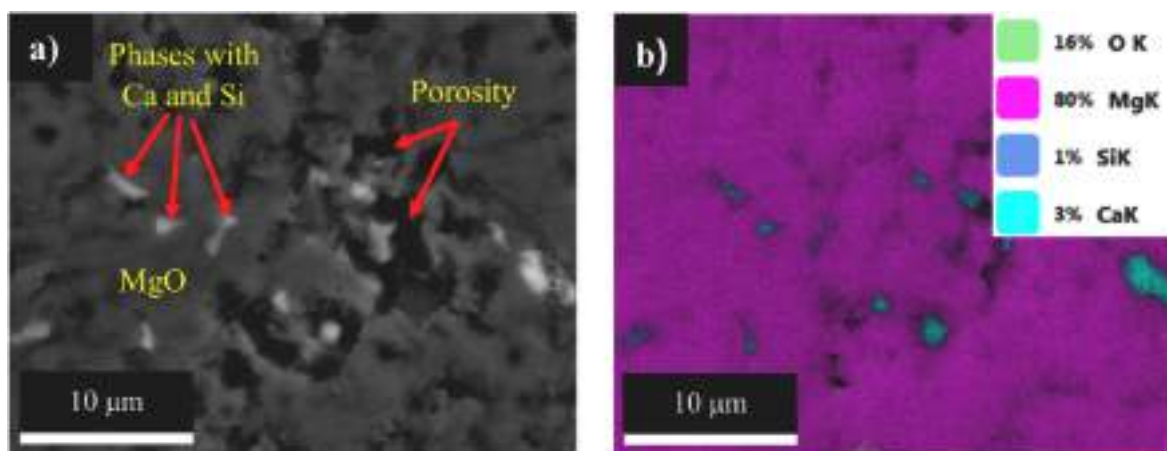


Fig. 7. SEM images of sintered MgO sample from brucite without TiO₂, a) morphology of the sample, b) area mapping, the inserted table corresponds to a semi-quantitative area analysis of the MgO sintered sample.

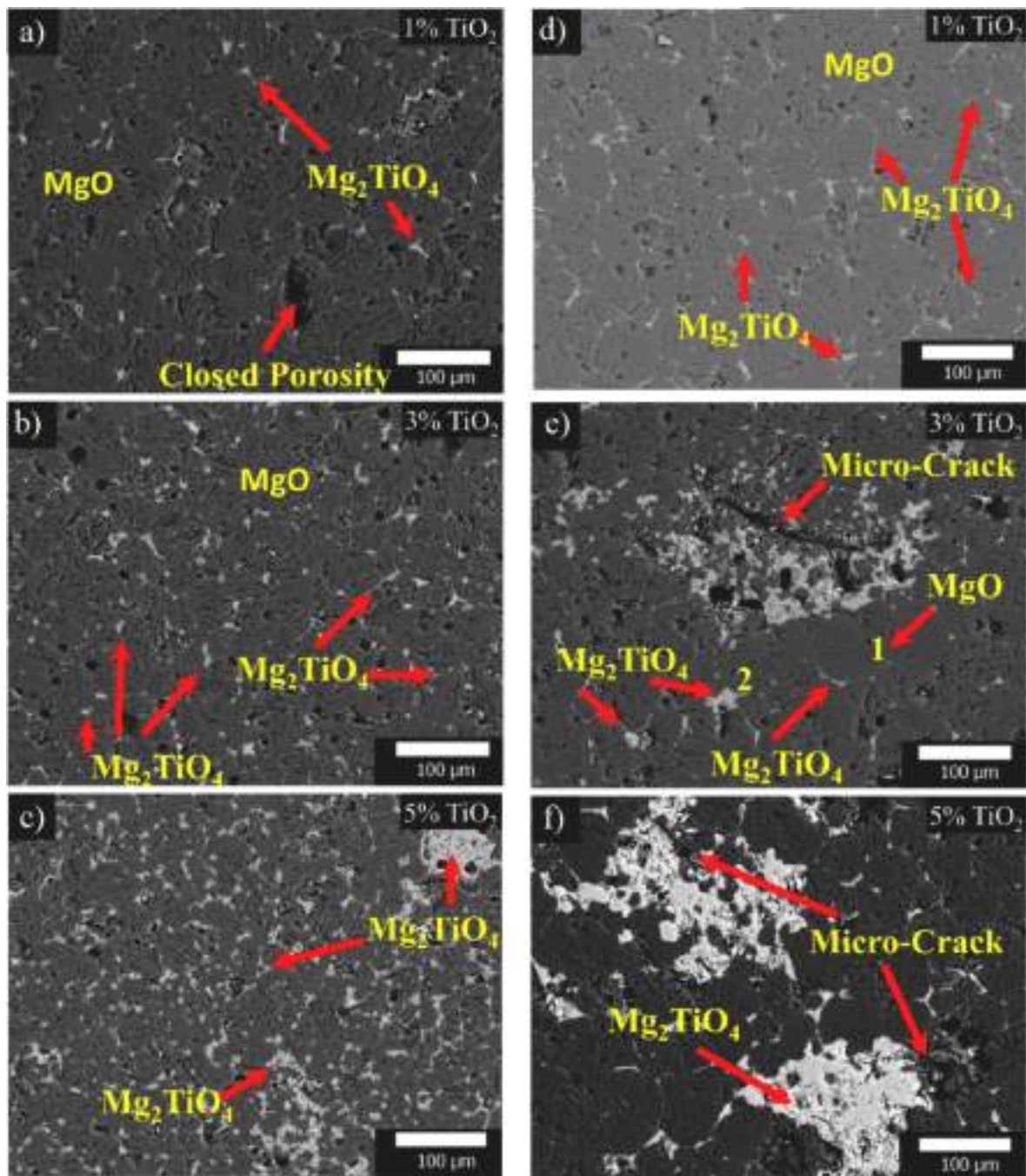


Fig. 8. SEM images of samples sintered at 1600 °C: (a–c) corresponds to samples of R1 route, i.e., brucite $\text{Mg}(\text{OH})_2$ with a) 1 wt%, b) 3 wt%, c) 5 wt% of nano TiO_2 . (d–f) corresponds to samples of R2 route, i.e., caustic magnesia (MgO) with d) 1 wt %, e) 3 wt %, f) 5 wt % of nano- TiO_2 . EDX points 1 and 2 correspond to detected phases of MgO and Mg_2TiO_4 , respectively.

identified as white phase with round shapes that grew with aggregates of nano- TiO_2 . Fig. 9 (d–f) corresponds to samples of caustic magnesia (MgO) with 1, 3, and 5 wt% of TiO_2 nanoparticles, respectively. Similarly, the same phases were identified, the microstructural difference was that with 5 wt % of nano- TiO_2 by route 1 (Fig. 9 (c)), smaller and very round porosities (almost closed) were observed, unlike with 5 wt% of nano- TiO_2 by route 2 (Fig. 9 (f)), which still showed large porosities and agglomerations of nano- TiO_2 that formed Mg_2TiO_4 phase.

3.5. Mechanical testing

Fig. 10 (a) shows the mechanical behavior of the nano- TiO_2 doped

sintered magnesia samples (from brucite and caustic magnesia) and the reference sample of MgO . The increase in TiO_2 nanoparticles leads to an increase in mechanical resistance, since an increasing tendency in Cold Crushing Strength (CCS) values was evident in all compositions, from 1 to 5 wt % of TiO_2 nanoparticles. As it can be seen in Fig. 10 (a), the samples made from brucite exhibited higher values of CCS, the highest value being 236 MPa (brucite sample + 5 wt % of TiO_2 nanoparticles). It is clearly appreciated that the cold crushing strength in the samples obtained by the route 1 is 16–23% greater than that of the samples obtained by the route 2. It is also concluded that during the sintering process a stronger bonding structure was created for the brucite samples. It is important to comment that both, in samples made with brucite or

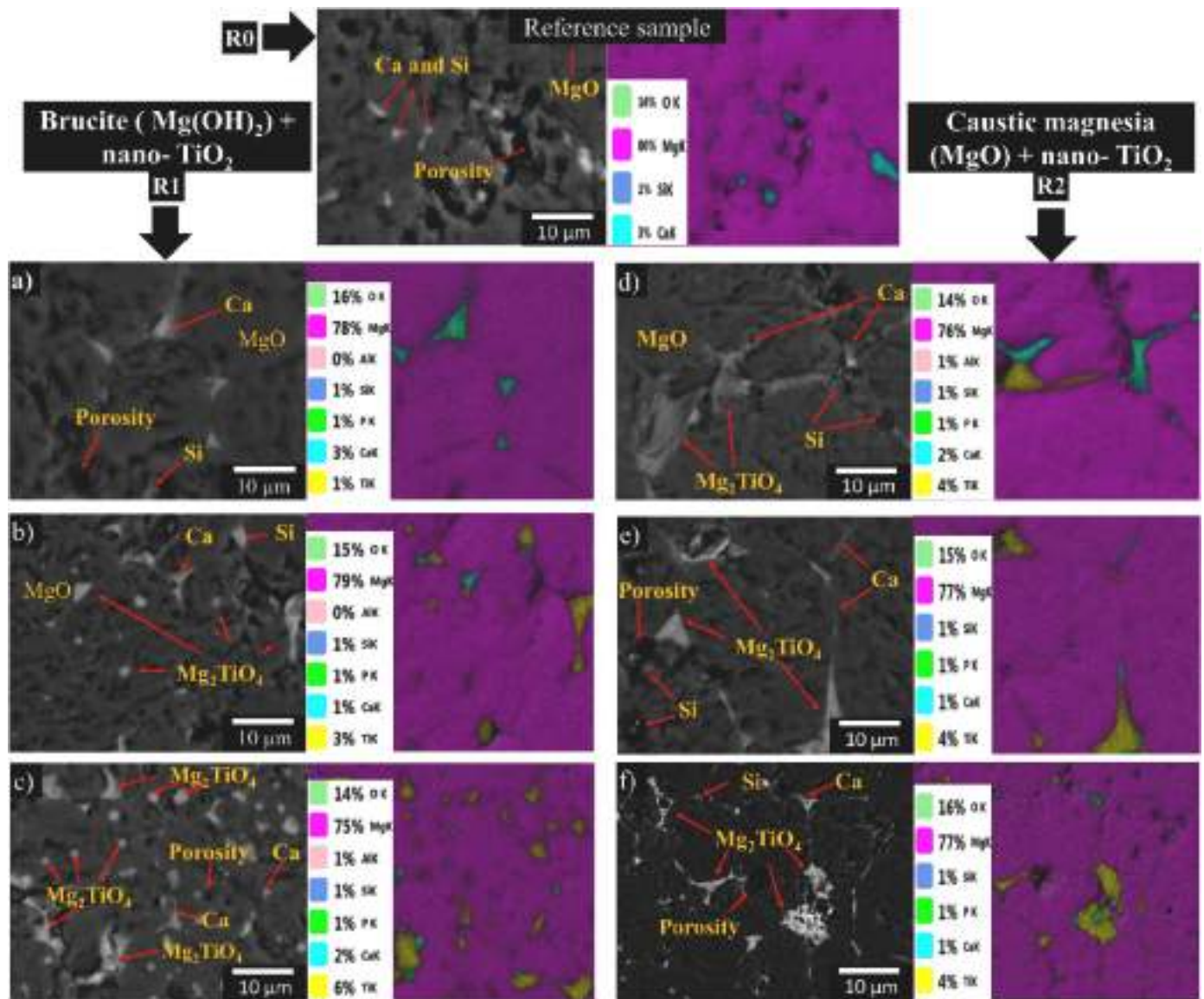


Fig. 9. SEM images and mapping of samples sintered at 1600 °C of samples made by: R0, (sample reference), R1, corresponds to samples of brucite Mg(OH)₂ with a) 1 wt %, b) 3 wt %, c) 5 wt % of nano TiO₂. R2, corresponds to samples of caustic magnesia (MgO) with d) 1 wt %, e) 3 wt %, f) 5 wt % of nano-TiO₂.

caustic magnesia, the density slightly decreased for composites with 3 and 5 wt % of TiO₂ nanoparticles whether compared with samples containing 1 wt % of TiO₂ nanoparticles. On the contrary, the CCS increased, which is attributed to the fact that with ceramic materials containing a range of porosity <30%. This can benefit the compressive strength since before the load acts on the ceramic particles, the pores absorb part of the mechanical energy that is dissipated through the sample [2,41]. As a result, an improvement of 36.5% and 26.1% (in samples with 5 wt % of TiO₂ nanoparticles corresponding to R1 and R2 routes, respectively) is observed, compared to the reference sample.

Fig. 10 (b) shows a micrograph corresponding to the fracture zone of the brucite Mg(OH)₂ sample with 5 wt % of nano-TiO₂ (236 MPa), where transverse microcracks are observed with respect to the applied load. These cracks are identified as intergranular cracks that advance through the grain boundaries with a size of less than 200 µm. Likewise, these correspond to thin cracks compared to those generated in the caustic magnesia sample +5 wt % of nano-TiO₂.

Fig. 10 (c), shows a micrograph corresponding to the fracture zone of the caustic magnesia (MgO) sample with 5 wt % of nano-TiO₂ (203 MPa), where macrocracks oriented in horizontal and vertical axes are

observed. This was since in route 2, a greater agglomeration of TiO₂ nanoparticles was observed (see Fig. 8 (f)), which caused that when the mechanical load was applied, cracks (transgranular) were formed in these phases and through grains of MgO. These macrocracks showed lengths greater than 200 µm and were wider than those generated with the brucite sample +5 wt % of nano-TiO₂. Both micrographs shown here are related to the results obtained from Fig. 10 (a).

4. Conclusions

In this work, a new route was proposed to obtain composites of densified refractories based on MgO. The effect of the addition of TiO₂ nanoparticles in brucite (route 1) or in caustic magnesia oxide (route 2) on the thermal, microstructure, morphological, physical, and mechanical properties was investigated. The results are shown below:

Thermal properties: Raw material dihydroxylation occurred at 426.06 °C and 323 °C for brucite and caustic magnesia, respectively.

Microstructural analysis: XRD analyses confirmed the formation of the MgTiO₃ phase in calcined brucite powders with TiO₂ nanoparticles. Also, during sintering the formation of Mg₂TiO₄ has taken place.

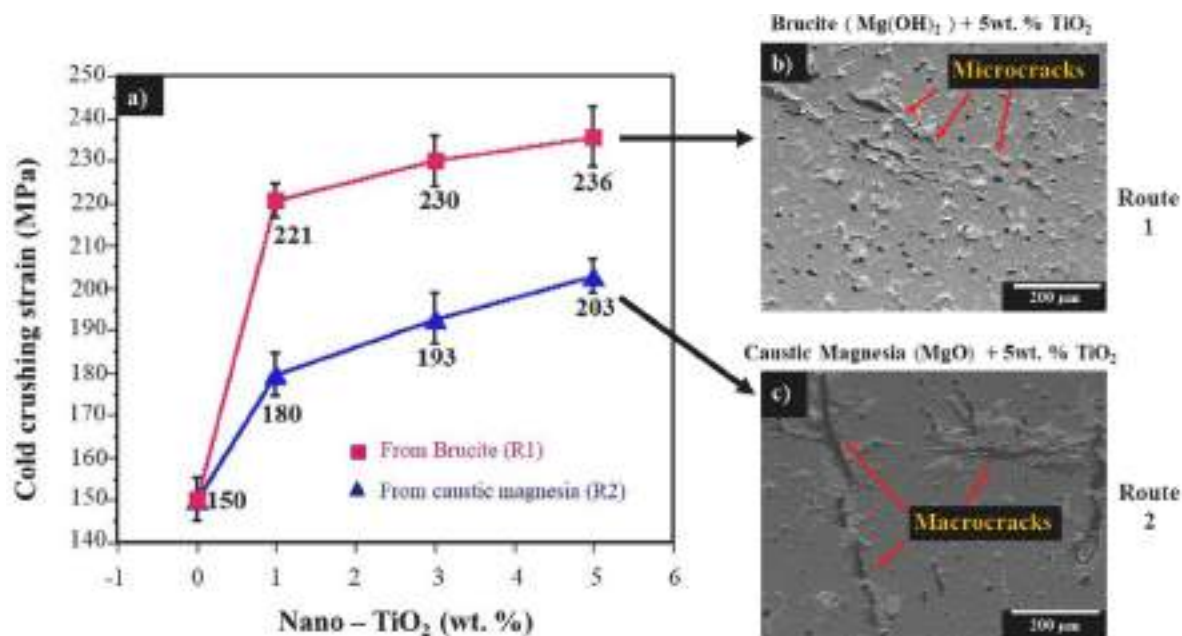


Fig. 10. (a) Cold crushing strength of magnesia sintered samples made from brucite (route 1, red line) or caustic magnesia (route 2, blue line) with 0, 1, 3 and 5 wt % of TiO₂ nanoparticles. (b) SEM image of fractured sample corresponding to brucite sample + 5 wt % of nano-TiO₂. (c) SEM image of fractured sample corresponding to caustic magnesia (MgO) sample with 5 wt % of nano-TiO₂. (For interpretation of the references to colour in this figure legend, the reader is referred to the Web version of this article.)

Physical properties: The results show that when TiO₂ nanoparticles were added to brucite paste (route 1), higher densities were obtained (from 1 to 5 wt % of TiO₂, the density remained stable at around ~3.46 g/cm³) with respect to when the TiO₂ was added to the caustic magnesia (route 2). The density of the samples obtained by the route 1 is 2.5–3.0% greater than that of the samples obtained by the route 2. Moreover, there was a 3.59% increase in density of the sample in route 1 with 1 wt % of TiO₂ nanoparticles with respect to the reference sample.

Morphological analysis: By SEM, in route 2, microcracks were observed around the Mg₂TiO₄ phase, when the size of this phase was equal to or greater than 100 μm. This affected the mechanical properties since cracks were evident in these phases when the load was applied.

Mechanical properties: There was an increase in CCS values with the content in TiO₂ nanoparticles for both routes. The samples fabricated by route 1 exhibited higher CCS values compared to route 2. The cold crushing strength in the samples obtained by the route 1 is 16–23% greater than that of the samples obtained by the route 2. If compared with the reference sample (0 wt % TiO₂), there is an improvement of 36.5% and 26.1% in samples with 5 wt % of TiO₂ of R1 and R2 routes, respectively.

In conclusion, the best route proposed for the elaboration of dense refractory materials based on MgO is that consisting in adding TiO₂ nanoparticles before the calcination of the Mg(OH)₂, calcination at 960 °C for 2 h, uniaxial pressing and, finally, sintering at 1600 °C for 4 h. The best values of mechanical properties were observed for the composite MgO-5 wt. % TiO₂ (cold crushing strength of 236 MPa).

Funding

M. Campos-Reséndiz thanks the support of the National Council of Science and Technology, Mexico, CONACYT.

Declaration of competing interest

The authors declare that they have no known competing financial interests or personal relationships that could have appeared to influence the work reported in this paper.

Acknowledgements

The authors are grateful for the contribution of the Centre for Research and Technological Development of Peñoles Group.

Two of the authors (G.A. Castillo-Rodríguez and C. Gómez-Rodríguez) thank for the support (PAICYT-UANL 2020, IT1382-20).

Daniel Fernández-González acknowledges the grant (Juan de la Cierva-Formación program) FJC2019-041139-I funded by MCIN/AEI/10.13039/501100011033 (Ministerio de Ciencia e Innovación, Agencia Estatal de Investigación).

Cristian Gómez-Rodríguez thanks the Vice-Rectoría of Veracruz for support during his academic stay at the University of Oviedo.

We thank Dra. Nayely Pineda Aguilar, for their help in the SEM (JEOL JSM-6010 PLUS/LA).

References

- [1] M. Stastny, V. Stengl, J. Henych, et al., Synthesis and characterization of TiO₂/Mg(OH)₂ composites for catalytic degradation of CWA surrogates, *RSC Adv.* 10 (2020) 19542–19552, <https://doi.org/10.1039/d0ra00944j>.
- [2] L.F. Verdeja, J.P. Sancho, A. Ballester, *Refractory and Ceramic Materials*, Sintesis, Madrid, 2008.
- [3] M.A. Shand, *The Chemistry and Technology of Magnesia*, John Wiley & Sons, Canada, 2006.
- [4] S. Ghasemi-Kahrizsangi, H. Gheisari, M. Boroujerdnia, Effect of micro and nano-Al₂O₃ addition on the microstructure and properties of MgO-C refractory ceramic composite, *Mater. Chem. Phys.* 189 (2016) 230–236, <https://doi.org/10.1016/j.matchemphys.2016.12.068>.
- [5] C. Gómez Rodríguez, T.K. Das Roy, S. Shaji, et al., Effect of addition of Al₂O₃ and Fe₂O₃ nanoparticles on the microstructural and physico-chemical evolution of dense magnesia composite, *Ceram. Int.* 41 (2015) 7751–7758, <https://doi.org/10.1016/j.ceramint.2015.02.107>.
- [6] L.V. García-Quiñonez, M.I. Mendivil-Palma, T.K. Das-Roy, et al., Effects of irradiation energy and nanoparticle concentrations on the structure and morphology of laser sintered magnesia with alumina and iron oxide nanoparticles, *Ceram. Int.* 46 (2020) 7850–7860, <https://doi.org/10.1016/j.ceramint.2019.12.004>.
- [7] Gómez-Rodríguez, G.A. Castillo-Rodríguez, E.A. Rodríguez-Castellanos, et al., Development of an ultra-low carbon MgO refractory doped with α-Al₂O₃ nanoparticles for the steelmaking industry: a microstructural and thermo-mechanical study, *Mater. Basel* 13 (2020) 1–22, <https://doi.org/10.3390/ma13030715>.
- [8] S. Ghasemi-Kahrizsangi, H.G. Dehsheikh, E. Karamian, et al., Effect of MgAl₂O₄ nanoparticles addition on the densification and properties of MgO-CaO

- refractories, *Ceram. Int.* 43 (2017) 5014–5019, <https://doi.org/10.1016/j.ceramint.2017.01.011>.
- [9] E. Rodríguez, G.A. Castillo, J.E. Contreras, et al., Desarrollo de un refractario MgO-CaZrO₃ dopado con MgAl₂O₄ para la industria cementera, *Ciencia UANL (Universidad Autónoma Nuevo León)* 14 (2011) 31–38.
- [10] Y. Han, Z. Li, Y. Zhu, Effect of MgO-TiO₂-SiO₂ additions on in-situ anisotropic grains growth and mechanical properties of corundum abrasive using pseudo-boehmite as raw material, *Ceram. Int.* 46 (2020) 1934–1939, <https://doi.org/10.1016/j.ceramint.2019.09.171>.
- [11] S. Ghasemi-Kahrizangi, M.B. Sedeh, H.G. Dehsheikh, et al., Densification and properties of ZrO₂ nanoparticles added magnesia-dolomite refractories, *Ceram. Int.* 42 (2016) 15658–15663, <https://doi.org/10.1016/j.ceramint.2016.07.021>.
- [12] S. Ghasemi-Kahrizangi, H. Gheisari-dehsheikh, M. Boroujerdnia, The effect of nano meter size ZrO₂ particles addition on the densification and hydration resistance of magnesite-dolomite refractories, *Iran, J. Mater. Sci. Eng.* 13 (2016) 33–40, <https://doi.org/10.22068/ijmse.13.4.33>.
- [13] C. Gómez-Rodríguez, D. Fernández-González, L.V. García-Quiñonez, et al., MgO refractory doped with ZrO₂ nanoparticles: influence of cold isostatic and uniaxial pressing and sintering temperature in the physical and chemical properties, *Met. Basel* 9 (2019) 1–20, <https://doi.org/10.3390/met9121297>.
- [14] S. Kahrizangi, A. Nemati, A. Shahraiki, et al., Effect of nano-sized Fe₂O₃ on microstructure and hydration resistance of MgO-CaO refractories, *Int. J. Nanosci. Nanotechnol.* 12 (2016) 19–26.
- [15] H.G. Dehsheikh, S. Ghasemi-Kahrizangi, Performance improvement of MgO-C refractory bricks by the addition of Nano-ZrSiO₄, *Mater. Chem. Phys.* 202 (2017) 369–376, <https://doi.org/10.1016/j.matchemphys.2017.09.055>.
- [16] C.G. Aneziris, J. Hubálková, R. Barabás, et al., Microstructure evaluation of MgO-C refractories with TiO₂- and Al-additions, *J. Eur. Ceram. Soc.* 27 (2007) 73–78, <https://doi.org/10.1016/j.jeurceramsoc.2006.03.001>.
- [17] S. Ghasemi-Kahrizangi, A. Shahraiki, M. Farooqi, Effect of nano-TiO₂ additions on the densification and properties of magnesite-dolomite ceramic composites, *Iran. J. Sci. Technol. Trans. A-Science* 42 (2018) 567–575, <https://doi.org/10.1007/s40995-016-0143-3>.
- [18] M. Bag, S. Adak, R. Sarkar, Study on low carbon containing MgO-C refractory: use of nano carbon, *Ceram. Int.* 38 (2012) 2339–2346, <https://doi.org/10.1016/j.ceramint.2011.10.086>.
- [19] H.G. Dehsheikh, S. Ghasemi-Kahrizangi, E. Karamian, Addition impact of nano-carbon black on the performance of MgO-CaO compounds, *Ceram. Int.* 44 (2018) 5524–5527, <https://doi.org/10.1016/j.ceramint.2017.12.195>.
- [20] S. Ghasemi-Kahrizangi, H.G. Dehsheikh, M. Boroujerdnia, MgO-CaO-Cr₂O₃ composition as a novel refractory brick: use of Cr₂O₃ nanoparticles, *Bol. Soc. Esp. Ceram. V.* 56 (2017) 83–89, <https://doi.org/10.1016/j.bsevcv.2016.11.002>.
- [21] G.A. Castillo-Rodríguez, Fusion of Magnesia in Electric Arc Furnace and its Characterization for the Refractory Industry, *Nuevo León: CIENCIA-UANL*, 1992.
- [22] G.A. Castillo-Rodríguez, Optimization of Magnesia Fusion Processes (MgO) by Electric Arc Furnace through the Validation of a Mathematical Model, *Nuevo León: CIENCIA-UANL*, 1992.
- [23] A. Ghaemi, M. Torab-Mostaedi, S. Shahhosseini, et al., Characterization of Ag(I), Co(II) and Cu(II) removal process from aqueous solutions using dolomite powder, *Kor. J. Chem. Eng.* 30 (2013) 172–180, <https://doi.org/10.1007/s11814-012-0113-1>.
- [24] J. Green, Calcination of precipitated Mg(OH)₂ to active MgO in the production of refractory and chemical grade MgO, *J. Mater. Sci.* 18 (1983) 637–651, <https://doi.org/10.1007/BF00745561>.
- [25] S.J. Gregg, R.K. Packer, The production of active solids by thermal decomposition. Part VI. The calcination of magnesium hydroxide, *J. Chem. Soc.* (1955) 51–55, <https://doi.org/10.1039/JR9550000051>.
- [26] K.S. Sanchez-Zambrano, M. Hernandez-Resendiz, C. Gomez-Rodriguez, et al., XPS study on calcining mixtures of brucite with titania, *Mater. Basel* 15 (2022) 1–20, <https://doi.org/10.3390/ma15093117>.
- [27] P. Scherrer, Nachrichten von der Gesellschaft der Wissenschaften zu Göttingen, *Mathematisch-Physikalische Klasse* 2 (1918) 98–100.
- [28] F.N. Jiménez-García, D.G. Espinosa-Arbeláez, C. Vargas-Hernández, et al., Characterization of nanostructures of ZnO and ZnMnO films deposited by successive ionic layer adsorption and reaction method, *Thin Solid Films* 519 (2011) 7638–7643, <https://doi.org/10.1016/j.tsf.2011.05.008>.
- [29] J. Wang, Y. Wei, J. Yu, Influences of polyhydric alcohol co-solvents on the hydration and thermal stability of MgAl-LDH obtained via hydrothermal synthesis, *Appl. Clay Sci.* 72 (2013) 37–43, <https://doi.org/10.1016/j.clay.2013.01.006>.
- [30] Z. Banu Bahşi, A.Y. Oral, Effects of Mn and Cu doping on the microstructures and optical properties of sol gel derived ZnO thin films, *Opt. Mater.* 29 (2007) 672–678, <https://doi.org/10.1016/j.optmat.2005.11.016>.
- [31] E.A. Barrera, Producción de polvos de óxido de magnesio con diferentes precursores. *Nuevo León, CIENCIA-UANL*, 1998.
- [32] P. Treviño, J.F. Perez-Robles, B. Millan-Malo, et al., Synthesis conditions of Mg (OH)₂ nanostructures by hydrothermal route, *Micro & Nano Lett.* 12 (2017) 404–407, <https://doi.org/10.1049/mnl.2016.0718>.
- [33] P.G. Brewer, D.W. Spencer, A note on the chemical composition of the red sea brines, in: E.T. Degens, D.A. Ross (Eds.), *Hot Brines and Recent Heavy Metal Deposits in the Red Sea: a Geochemical and Geophysical Account*, Springer Berlin, Berlin, 1969, pp. 174–179.
- [34] S.A.S. Nizar Kumar, J. Sundaramurthy, P. Ragupathy, V. Thavasi, S.G. Mhaisalkar, et al., Tunable hierarchical TiO₂ nanostructures by controlled annealing of electrospun fibers: formation mechanism, morphology, crystallographic phase and photoelectrochemical performance analysis, *J. Mater. Chem.* (2011) 9784–9790, <https://doi.org/10.1039/C1JM10859J>.
- [35] R.C. DeVries, R. Roy, The American ceramic society and the National institute of standards and Technology, NIST Standard Reference Database 31. Figure Number 22. 2014. Available online, www.nist.gov/srd/nist31.cfm. (Accessed 4 November 2022).
- [36] Baorang Li, Xiaohui Wang, Minyu Yan, Longtu Li, Preparation and characterization of nano-TiO₂ powder, *Mater. Chem. Phys.* (2002) 184–188, [https://doi.org/10.1016/S0254-0584\(02\)00226-2](https://doi.org/10.1016/S0254-0584(02)00226-2).
- [37] E. Haro-Poniatowski, R. Rodriguez, O. Cano-Corona, Crystallization of nanosized titania particles prepared by the sol-gel process, *J. Mater. Res.* (1994) 2102–2107, <https://doi.org/10.1557/JMR.1994.2102>.
- [38] N. Kuganathan, P. Iyngaran, R. Vovk, et al., Defects, dopants and Mg diffusion in MgTiO₃, *Sci. Rep.* 9 (2019) 1–9, <https://doi.org/10.1038/s41598-019-40878-y>.
- [39] Y.C. Chen, S.M. Tsao, C.S. Lin, et al., Microwave dielectric properties of 0.95MgTiO₃-0.05CaTiO₃ for application in dielectric resonator antenna, *J. Alloys Compd.* 471 (2009) 347–351, <https://doi.org/10.1016/j.jallcom.2008.03.118>.
- [40] H. Haefke, H.P. Lang, R. Sum, et al., Mg₂TiO₄ as a novel substrate for high-temperature superconducting thin films, *Appl. Phys. Lett.* 61 (1992) 2359–2361, <https://doi.org/10.1063/1.108243>.
- [41] W. Schulle, *Feuerfeste Werkstoffe*. Leipzig: Deustche Verlag für Grundstoffindustrie, 1990.

**Trabajo complementario 4: Desarrollo de un refractario de
MgO dopado con η -Al₂O₃.**

Desarrollo de un refractario de MgO dopado con η -Al₂O₃

C. Gómez-Rodríguez ^{1,*}, L. García-Quiñonez ², J. A. Aguilar-Martínez ³, F. J. Vázquez-Rodríguez ³, D. Fernández-González ⁴, L. F. Verdeja ⁴, J. F. López-Perales ³, A. Castillo-Rodríguez ³, Edén Rodríguez ^{3,*}

- 1 Facultad de Ingeniería, Universidad Veracruzana, Coatzacoalcos, Ver. México; cristiangu1983@hotmail.com (C. G.-R.)
 - 2 CONACYT-Centro de Investigación Científica y de Educación Superior de Ensenada B.C. (CICESE), Unidad Monterrey, Apodaca 66629, México; adnilanavivi_1984@hotmail.com (L. G.-Q.)
 - 3 Universidad Autónoma de Nuevo León (UANL); Facultad de Ingeniería Mecánica y Eléctrica (FIME); C.P. 66450, San Nicolás de los Garza, N.L., México; josue.aguilarmrt@uanl.edu.mx (J. A. A.-M.); fco-fimeuanl@gmail.com (F. J. V.-R.); lopez_perales_jesus@hotmail.com (J. F. L.-P.); alan.castillo.rdz@gmail.com (A. C.-R.); earc22@hotmail.com (E. R.)
 - 4 Department of Materials Science and Metallurgical Engineering, School of Mines, Energy and Materials, University of Oviedo, Oviedo/Uviéu, Asturias, Spain; fernandezgdaniel@uniovi.es (D.F.-G.); lfv@uniovi.es (L. F. V.)
- * Correspondencia: cristiangu1983@hotmail.com (D. G.-R.); earc22@hotmail.com (E. R.); Tel.: +52-8183294020 (ext. 1619)

Cita: C. Gómez-Rodríguez 1, L. García-Quiñonez, J. A. Aguilar-Martínez, F. J. Vázquez-Rodríguez 3, D. Fernández-González, L. F. Verdeja, J. F. López-Perales, A. Castillo-Rodríguez, Edén Rodríguez. Desarrollo de un refractario de MgO dopado con η -Al₂O₃. EYA ACADEMY 2023, 1, 1.

Editor Académico: Guadalupe Alan Castillo Rodríguez

Recibido: 30/01/2023

Aceptado: 27/02/2023

Publicación: 30/04/2023

Nota del editor: EYA ACADEMY se mantiene neutral con respecto a las reclamaciones jurisdiccionales en los mapas publicados y las afiliaciones institucionales.



Derechos de autor: © 2023 por los autores. Enviado para su posible publicación en acceso abierto bajo los términos y condiciones de la licencia Creative Commons Attribution (CC BY)

(<https://creativecommons.org/licenses/by/4.0/>).

Resumen: Se estudia el efecto de las nanopartículas de α -Al₂O₃ (hasta 5 % en peso) sobre las propiedades físicas, mecánicas y térmicas, así como sobre la evolución microestructural de un refractario de magnesia densa. Se utilizan temperaturas de sinterización a 1300°C, 1500°C y 1600°C. Las propiedades físicas de interés fueron la densidad y la porosidad aparentes, que se evaluaron mediante el método de Arquímedes. Las propiedades térmicas se examinaron mediante calorimetría diferencial de barrido. El comportamiento mecánico se estudió mediante pruebas de resistencia a la trituración en frío y micro dureza. Finalmente, la microestructura y las características cualitativas mineralógicas se estudiaron mediante microscopía electrónica de barrido y difracción de rayos X, respectivamente. El aumento de la temperatura de sinterización dio como resultado una densidad mejorada y una porosidad aparente reducida. Sin embargo, a medida que aumentaba el contenido de nanopartículas de α -Al₂O₃, la densidad y la micro dureza disminuían. Las observaciones microestructurales mostraron que la presencia de nanopartículas de α -Al₂O₃ en la matriz de magnesia indujo la formación de espinela de magnesio-aluminato (MgAl₂O₄), que mejoró la resistencia mecánica más significativamente a 1500°C.

Palabras llave: magnesia; Refractarios; Nanopartículas de Al₂O₃; espinela de magnesio-alúmina; sinterización

1. Introducción

Desde la introducción de la magnesia (MgO), su uso como refractario básico ha aumentado enormemente debido a su costo razonable, excelente resistencia química a escorias y fundentes básicos a altas temperaturas, así como un alto punto de fusión (2800°C). Estas propiedades se han convertido en refractarios a base de MgO en preferenciales para las industrias del hierro, no ferrosos y cemento [1-4]. En las industrias siderúrgicas, la magnesia se ha utilizado ampliamente en convertidores de acero, hornos de arco eléctrico y en revestimientos de cuchara para el proceso de fabricación de acero. Sin embargo, la conductividad térmica y el alto coeficiente de expansión térmica del MgO se ven afectados de tal manera por las altas temperaturas que inducen el desprendimiento térmico en condiciones de calentamiento [5]. Este efecto se ha mitigado desde el desarrollo del refractario de magnesia-carbono (MgO-C) en la década de 1970. Este fue un desarrollo tecnológico de gran importancia, ya que permitió controlar y mejorar las propiedades térmicas de la

magnesia. La mejora se debió a importantes ventajas como la alta conductividad térmica, la excelente resistencia al choque térmico (debido a su baja expansión térmica) y la buena resistencia a la corrosión [6-13].

Los refractarios de MgO-C típicamente contienen 7-20 % en peso de carbono [5, 14]. Pueden producirse serios inconvenientes con un mayor contenido de carbono, tales como: i) la oxidación del carbono da como resultado una estructura altamente porosa con una unión débil, poca resistencia mecánica que permite una fácil penetración y eventual corrosión por escoria y acero fundido; ii) aumento de la temperatura de la carcasa; iii) mayor consumo de energía originado por el aumento de la conductividad del refractario; iv) liberación de gases de dióxido de carbono o monóxido de carbono; y v) dificultad para controlar con precisión el contenido de carbono en el acero [5, 13, 15-18].

Para superar el fenómeno de oxidación, los investigadores refractarios han estado investigando el uso de diferentes óxidos y antioxidantes no óxidos como Al, Si, Mg, $Al_3B_4C_7$, SiC, SiB₄, CaB₆, ZrO₂, CaO, MgAl₂O₄ y Al₂O₃ para aumentar la resistencia a la oxidación de los refractarios de MgO-C [19-36]. Los antioxidantes pueden tener la capacidad de restringir y retrasar la oxidación del carbono, pero nunca hasta el punto de detenerlo por completo. Las nuevas tendencias se han centrado en la reducción del contenido de carbono (2-4%) y el desarrollo de refractarios de magnesia libres de carbono, pero con propiedades como el refractario de MgO-C [36, 37]. Este problema se ha convertido en un desafío difícil para los investigadores refractarios. La solución más atractiva a este desafío implica el uso de la nanotecnología, que es reconocida como el campo de investigación más prometedor del siglo 21. La nanotecnología se utiliza actualmente en muchas aplicaciones de investigación con resultados sobresalientes [38-63]. El uso de fuentes de nano carbono como [44-51]: negro (CB), nano fibras (CNF), nanotubos (CNT), grafito expandido (EG) y nano láminas de grafito u óxido de grafito (GON) muestran un alto potencial en el desarrollo de refractarios de MgO-C bajos en carbono. La investigación demuestra que la adición de CB en refractarios de MgO-C logró mejores propiedades mecánicas y termo mecánicas que los refractarios de MgO-C con alto contenido de carbono disponibles comercialmente.

Wei et al. [52] estudiaron el efecto de agregar nano láminas de Fe (de 0 a 1.0 % en peso) a la microestructura de refractarios de MgO-C bajos en carbono unidos con resina fenólica. Encontraron que las resistencias mecánicas y de choque térmico de los refractarios bajos en carbono con nano láminas de Fe al 0,5% en peso son altamente mejoradas en comparación con las muestras sin nano láminas de Fe, lo que se atribuye a la formación in situ de CNT y la aparición de puentes que inducen un mecanismo de desviación de grietas en la matriz. Matsuo et al. [53] informaron una mejora de 2,2 veces de la resistencia a la flexión cuando se agregó 0,4 % en peso de CNF a los refractarios de MgO-C. Zhu et al. [47, 48] informaron que los refractarios de MgO-C que contienen distribuciones homogéneas de nano carbonos, especialmente CNT y CB tienen un módulo de ruptura en frío residual (CMOR) más alto y una menor pérdida de resistencia que los refractarios convencionales de MgO-C después del choque térmico, ya que los materiales a nano escala pueden absorber y aliviar el estrés debido a la expansión térmica y la contracción de partículas refractarias. Además, los CNT y CB contribuyen a reducir la mala distribución del estrés térmico en los refractarios de MgO-C.

Salman Ghasemi-Kahrizangi et al. estudiaron el impacto de agregar nanopartículas de ZrSiO₄, Al₂O₃ y TiO₂ en las propiedades de los refractarios de MgO-C [54-56]. Descubrieron que el nano-ZrSiO₄ mejoró la resistencia mecánica y a la oxidación mediante la formación de cristales de forsterita, enstatita y en forma de aguja de fases de ZrC. La adición de Nano-Al₂O₃ promovió la densificación del refractario de MgO-C debido a la formación de fases de MgAl₂O₄, AlN y Al₄C₃; nano-Al₂O₃ también mejoró la resistencia a la oxidación de los refractarios de MgO-C. La adición de nano-TiO₂ condujo a la generación de fases de TiN, TiC y TiCN, mejorando las propiedades mecánicas, físicas y

termoquímicas. Zagar et al. [55] estudiaron el efecto del tamaño de partícula de Cr_2O_3 en la densificación de refractarios de magnesia. Los resultados mostraron que a medida que el tamaño de partícula de Cr_2O_3 se redujo (~ 20 nm), la densidad de los refractarios de MgO aumentó a temperaturas relativamente bajas ($\sim 850^\circ\text{C}$). Azhari et al. [56] investigaron el efecto de la adición de nano- Fe_2O_3 en la matriz refractaria magnesia-cromo; encontraron que la disolución de nano- Fe_2O_3 y la migración iónica mejoraron el proceso de sinterización, así como la estructura de enlace directo. Huizhong et al. [57] también estudiaron la adición de nano- Fe_2O_3 en la matriz refractaria magnesia-cromo. Informaron que la temperatura de sinterización puede reducirse ($\sim 150^\circ\text{C}$) [10]. Chen et al. [58] estudiaron refractarios de MgO-CaO con la adición de micro y nano polvos de ZrO_2 ; sus resultados mostraron que la densificación fue promovida por la adición de nano- ZrO_2 , lo que condujo a la formación de CaZrO_3 , mejorando así la resistencia al choque térmico y la resistencia a la corrosión de la escoria. Das [34] estudió el efecto de la micro y nano-espínela sobre refractarios de MgO-C sinterizados a 1000°C . Los resultados mostraron que la adición de 1 % en peso de nano-espínela obtuvo propiedades superiores en comparación con la muestra que contenía 10 % en peso de micro espínela. El efecto de la adición de nanopartículas de MgAl_2O_4 y Cr_2O_3 sobre las propiedades de los refractarios de MgO-CaO fue estudiado por Salman Ghasemi-Kahrizangi et al. [59, 60]. Las nanopartículas de Cr_2O_3 mejoraron la resistencia a la hidratación debido a la formación de fases de alta resistencia a la hidratación como CaCr_2O_4 y MgCr_2O_4 . La adición de nanopartículas de espínela condujo a la mejora apreciable de la resistencia al corte de los refractarios, así como al logro de una mayor densidad de matriz. Teniendo en cuenta lo anterior, el presente trabajo de investigación es un complemento al trabajo de investigación anterior [63], cuyo objetivo es investigar el efecto del contenido de nano- Al_2O_3 (η - Al_2O_3) sobre las propiedades termo mecánicas y la evolución microestructural de un refractario de MgO libre de carbono sinterizado a 1300°C , 1500°C y 1600°C .

2. Materiales y métodos

2.1 Materiales

En esta investigación se utilizó magnesia (MgO) de grado industrial con óxido de nano alúmina de alta pureza y alto grado (η - Al_2O_3) en α fase polimórfica. La composición química del MgO, con un tamaño medio de partícula <45 μm , se determinó mediante un espectrómetro de fluorescencia de rayos X (XRF) de Philips (modelo X Pert) y se especifica en la Tabla 1. La Figura 1 muestra los patrones de difracción de rayos X (XRD) de polvos verdes de MgO donde los picos principales corresponden a MgO, mientras que los picos débiles corresponden a $\text{Mg}(\text{OH})_2$ o fase brucita (PDF #84-2163). La formación de $\text{Mg}(\text{OH})_2$ puede atribuirse a la reacción del MgO activo con la humedad en el ambiente.

Tabla 1. Composición química (% en peso) de magnesia.

MgO	CaO	MnO	Fe_2O_3	SiO_2	Otros	LOI
90.73	0.871	0.020	0.064	0.630	0.230	7.455

Tabla 2. Características del óxido de nano alúmina de alto grado (α -alúmina).

Purity (wt. %)	Size (nm)	SSA (m^2/g)	Color
99.9	50	18	White

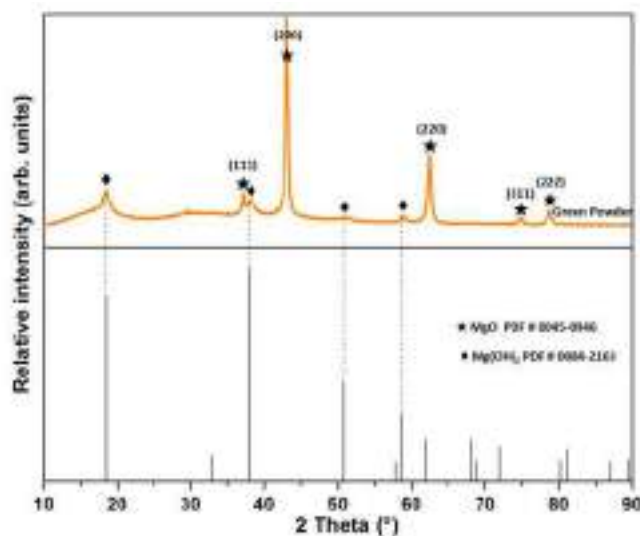


Figura 1. Patrones de difracción de rayos X (XRD) de MgO como materia prima (polvo verde).

2.2 Preparación de la muestra

Como es bien sabido, una de las cuestiones más críticas relacionadas con el uso de nanopartículas es su dispersión. Así, para obtener una suspensión dispersa de $\eta\text{-Al}_2\text{O}_3$, se añadió a la acetona Zephrym PD3315, un copolímero acrílico utilizado como vehículo dispersante. La suspensión ($\eta\text{-Al}_2\text{O}_3$, Zephrym y acetona) se agitó durante 1 h en un Aquasonic TM 75T para obtener una suspensión estable. La suspensión se vertió en el polvo de magnesia y se homogeneizó durante 10 minutos utilizando un mezclador mecánico. Las mezclas refractarias se realizaron de acuerdo con las composiciones de lotes dadas en la Tabla 3. Luego, las mezclas se prensaron en forma uniaxial por debajo de 100 MPa para dar forma a muestras cilíndricas (25.4 mm de diámetro y aproximadamente 25.4 mm de altura).

Tabla 3. Códigos de muestras y composiciones de lotes (% en peso) sinterizados a 1300°C, 1500°C y 1600 °C y muestras utilizadas en el análisis DSC.

Temperatura	Código de muestra	% en peso	
		MgO	Al ₂ O ₃
1000°C (DSC)	A0	100	0
	A1	99	1
	A3	97	3
	A5	95	5
1300°C (Temperatura de sinterización)	A0 ₁₃	100	0
	A1 ₁₃	99	1
	A3 ₁₃	97	3
	A5 ₁₃	95	5
1500°C (Temperatura de sinterización)	A0 ₁₅	100	0
	A1 ₁₅	99	1
	A3 ₁₅	97	3
	A5 ₁₅	95	5
1600°C (Temperatura de sinterización)	A0 ₁₆	100	0
	A1 ₁₆	99	1
	A3 ₁₆	97	3
	A5 ₁₆	95	5

Las muestras verdes se secaron a 120°C durante 24 h. Después del proceso de secado, las muestras se sinterizaron en un horno eléctrico Lindbergh/Blue M (modelo BF51524C) a 1300°C, 1500°C y 1600°C con una velocidad de calentamiento de 5°C/min y se remojaron durante 4 h a la temperatura designada.

2.3. Métodos

2.3.1. Análisis microestructural

La composición de la fase se analizó utilizando un difractómetro de rayos X (XRD; Bruker D8 Advance model) con radiación Cu K α ($\lambda = 1,5406 \text{ \AA}$) operada a 40 kV y 30 mA. Los escaneos se realizaron en el rango de 2θ de 10 a 90° con un paso de escaneo de 0.05° y 1.5 s por paso en modo continuo. La densidad aparente (BD) y la porosidad aparente (AP) de las muestras sinterizadas se evaluaron mediante el principio de Arquímedes (ASTM-C20).

2.3.2. Análisis Morfológico

La microestructura de las muestras refractarias se estudió utilizando un microscopio electrónico de barrido (SEM) FEI Nova NanoSEM 200 equipado con un detector de rayos X dispersivos de electrones (EDX) (EDAX, modelo Apollo XP 2930).

2.3.3. Propiedades mecánicas

La resistencia mecánica se determinó mediante el método de resistencia a la trituración en frío (CCS). Además, la micro dureza se evaluó mediante la técnica Vickers (HV). Especímenes 25. En ambas evaluaciones se utilizaron 4 mm de diámetro y 25.4 mm de altura y los valores reportados son el promedio de 15 mediciones para cada composición diseñada.

2.3.4. Análisis térmico

Las composiciones refractarias (A0, A1, A3 y A5) se sometieron a análisis simultáneos de calorimetría diferencial de barrido (DSC)/termogravimétrica (TGA) utilizando un instrumento TGA-DSC modelo Q600 simultáneo para evaluar los eventos térmicos relacionados con la adición de $\eta\text{-Al}_2\text{O}_3$ durante el proceso de sinterización hasta 1000 °C.

3. Resultados y discusión

La figura 2(a) muestra una imagen TEM correspondiente a los restos de $\eta\text{-Al}_2\text{O}_3$ en la matriz de MgO de la muestra sinterizada A5₁₆. Las partículas casi esféricas con un tamaño promedio de 50 nm se pueden observar una encima de la otra. La Figura 2(b) muestra los patrones de difracción electrónica del área seleccionada (SAED) de $\eta\text{-Al}_2\text{O}_3$ en la muestra A5₁₆. Este patrón coincide con el patrón estándar de $\alpha\text{-alúmina}$ ($\alpha\text{-Al}_2\text{O}_3$) (PDF#88-0826). Los datos SEM-EDX de la figura 2(c) confirman una dispersión adecuada de $\eta\text{-Al}_2\text{O}_3$ en la matriz de MgO en la muestra verde A5₁₆, es decir, antes del proceso de sinterización.

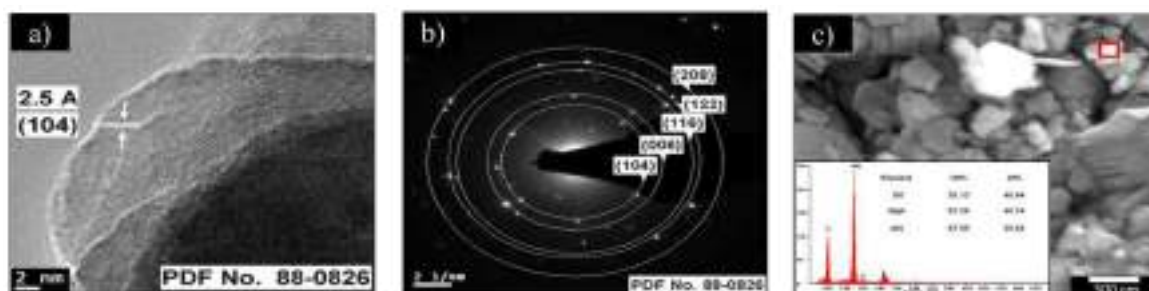


Figura 2. (a) imagen TEM de una nanopartícula de Al_2O_3 , (b) patrón de difracción de electrones de Al_2O_3 , (c) imagen SEM de nanopartículas de $\alpha\text{-Al}_2\text{O}_3$ dispersas en matriz de MgO en una muestra verde.

Las figuras 3(a) y (b) muestran los resultados de la densidad y la porosidad aparentes de muestras sinterizadas a 1300°C , 1500°C y 1600°C (según la relación de muestras mostrada en la Tabla 3). En la figura 3(a), se puede observar un aumento en la densidad aparente en todas las composiciones refractarias a medida que aumenta la temperatura de sinterización. Sin embargo, la densidad aparente disminuye a medida que aumenta el contenido de $\eta\text{-Al}_2\text{O}_3$ en todas las composiciones refractarias. Este último efecto fue más evidente a una temperatura de sinterización de 1300°C . Este fenómeno puede atribuirse a la formación in situ de espinelas de MgAl_2O_4 ya que la menor expansión de la espinela frente a la magnesia (MgO) conduce a la formación de microfisuras que afectan a la densidad aparente, pero estas microfisuras actúan como supresores de grietas mejorando la resistencia mecánica de los cuerpos refractarios. El valor máximo de la densidad aparente fue de 3.31 g/cm^3 , que correspondió a la muestra A0_{16} sinterizada a 1600°C . En la figura 3(b), se puede observar una disminución de la porosidad aparente a medida que aumenta la temperatura de sinterización en todas las composiciones refractarias; sin embargo, la porosidad aparente aumentó a medida que aumentaba el contenido de $\eta\text{-Al}_2\text{O}_3$.

Este fenómeno se explica por la observación de que la formación in situ de espinela en la matriz de MgO (generalmente lograda a temperaturas entre 1000 y 1200°C) hace que se formen microfisuras y resulta en un aumento de la porosidad aparente. El valor mínimo de porosidad aparente fue del 3% para A1_{16} muestras sinterizadas a 1600°C . Es evidente que tanto la densidad aparente como la porosidad aparente dependen en gran medida de la temperatura; a medida que aumenta la temperatura, se produce la difusión de especies, lo que aumenta el tamaño de los granos y elimina la porosidad en la muestra para dar como resultado muestras densas.

Las figuras 4 (a) a (c) muestran los resultados de XRD de muestras sinterizadas a 1300°C , 1500°C y 1600°C (según las muestras que se muestran en la Tabla 3). Como referencia, también se trazó magnesia pura. Para todas las composiciones refractarias (incluida la composición de referencia) a todas las temperaturas de sinterización, podemos observar reflexiones de los planos (111), (200), (220), (311) y (222) que coinciden con el patrón estándar para MgO (PDF # 0045-0946). El silicato tricálcico (C_3S) y el silicato dicálcico (C_2S) no se producen desde que se utilizó magnesia de pureza de alto grado; estas son fases de unión que generalmente se pueden detectar.

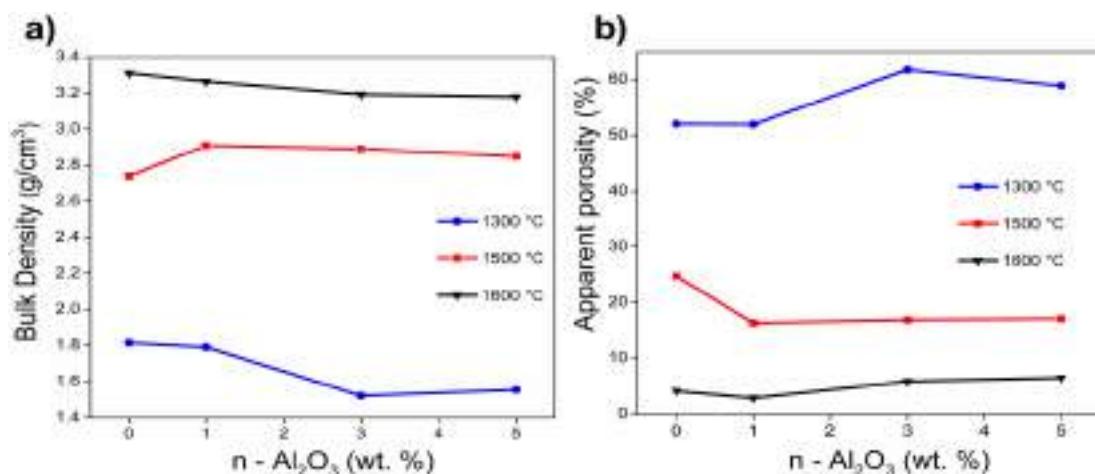


Figura 3. a) Variación de la densidad aparente y b) variación de la porosidad aparente de la magnesia refractaria en función del contenido de nanopartículas de Al_2O_3 .

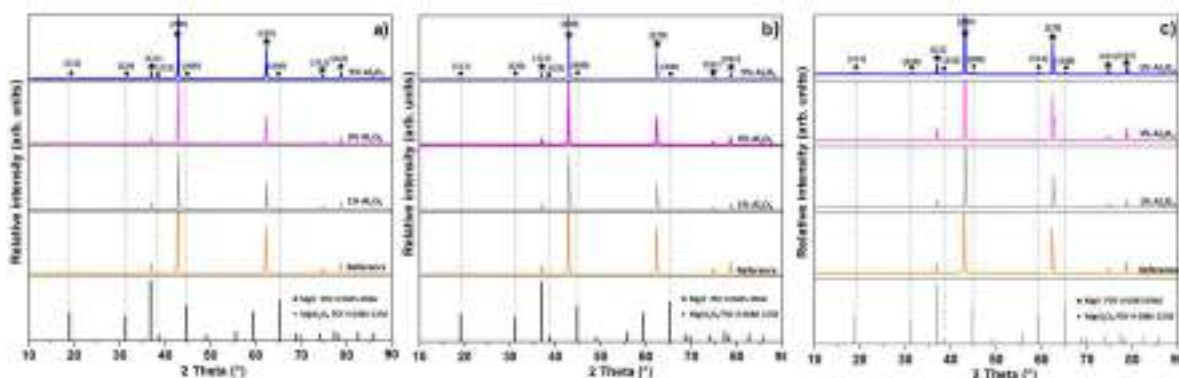


Figura 4. Diagramas XRD de las muestras que contienen diferentes niveles de nano- Al_2O_3 a diferentes temperaturas: (a) 1300, (b) 1500 y (c) 1600°C.

Para muestras A1₁₃, A1₁₅ y A1₁₆ (1300°C, 1500°C y 1600°C, respectivamente) y A3₁₅, A3₁₃ (1300°C y 1500°C, respectivamente), podemos observar reflexiones que corresponden a la fase MgO (PDF# 0045-0946). Sin embargo, en estas condiciones específicas, no fue posible detectar η - Al_2O_3 o cualquier nueva formación de fase. Este fenómeno puede asociarse a dos hipótesis: la primera está asociada a una restricción del equipo en la que la concentración mínima de compuesto detectada por el equipo XRD debe ser superior al 3% en peso, ya que las concentraciones inferiores a este valor parecen difíciles de detectar; la segunda hipótesis puede asociarse con la temperatura de reacción requerida para formar un nuevo compuesto, que podría ser in situ MgAl_2O_4 espinela junto con el porcentaje de adición de η - Al_2O_3 . En el caso de la muestra A3₁₆ sinterizada a 1600°C, podemos observar reflexiones que corresponden a la fase MgO y las reflexiones de los planos (111), (220), (222), (400) y (440) que coinciden con el patrón estándar de MgAl_2O_4 (PDF#0086-2258). Como era de esperar, la cantidad de fase de espinela aumentó con temperaturas más altas.

Para las muestras A5₁₃, A5₁₅ y A5₁₆, podemos observar fuertes reflexiones de los planos (111), (200), (220), (311) y (222) que corresponden a la fase MgO (PDF#0045-0946). Además, hay reflexiones débiles, pero fácilmente detectables en (111), (220), (222), (400) y (440) que coinciden con el patrón estándar de MgAl_2O_4 (PDF # 0086-2258). Comparando

las intensidades de los picos para MgO y $MgAl_2O_4$, podemos ver que la fase mayor corresponde a MgO, y el $MgAl_2O_4$ está presente como una segunda fase.

Las composiciones de fase del silicato están determinadas por la relación de CaO/SiO₂ ya que la relación CaO/SiO₂ era de 1,5 en este sistema refractario, por lo que las fases esperadas eran silicato dicálcico (Ca₂SiO₄) y Merwinita (Ca₃MgSi₂O₈) [2]. Sin embargo, solo MgO y $MgAl_2O_4$ fueron detectados por la evaluación XRD. Estas dos fases fueron corroboradas por el análisis SEM y EDX.

La figura 5 muestra las muestras superficiales (A0₁₃, A0₁₅ y A0₁₆) sinterizadas a (a) 1300°C, (b) 1500°C y (c) 1600°C de 100 % en peso de MgO, que se utilizaron como referencia. La figura 5 (a) muestra una microestructura correspondiente a una segunda etapa de sinterización (generación de puntos de contacto entre partículas adyacentes con formación de cuello) porque la temperatura utilizada no fue suficiente para obtener una microestructura densa. En la muestra sinterizada a 1500°C (A0₁₅), se detectó cal libre en la matriz de MgO, como se indica en la figura 5(b). La figura 5 (c) mostró una microestructura más densa correspondiente a la muestra A0₁₆, con porosidad cerrada, mediante análisis puntual EDX, también se detectaron fases CaO (impureza de materia prima) y MgO.

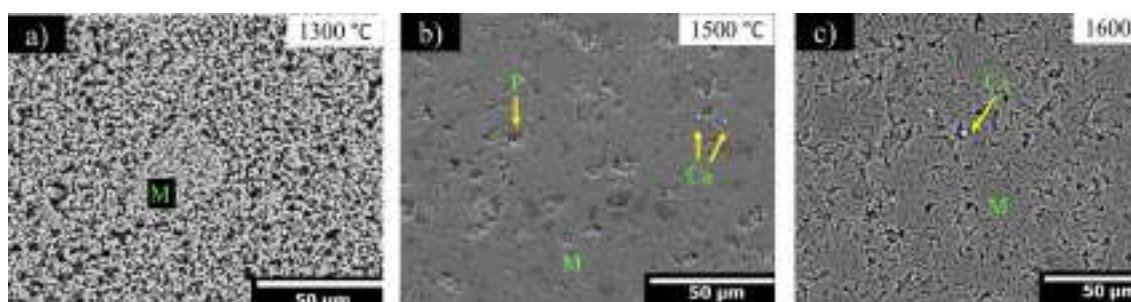


Figura 5. Micrografía SEM en modo de imagen electrónica retro dispersada correspondiente a una microestructura típica de magnesia, sinterizada a a)1300°C, b)1500°C y c) 1600°C. Donde, M= Magnesia, Ca= CaO, P= Porosidad.

Por lo general, una microestructura típica de magnesia sinterizada corresponde a fases aisladas de silicato que se encuentran en los límites del grano de magnesia y fases de calcio que se encuentran en los granos de magnesia, como se encontró en las muestras de referencia A0₁₅ y A0₁₆. Las figuras 6-8 muestran la evolución microestructural de las muestras de magnesia con la adición creciente de η -Al₂O₃ (1, 3 y 5 % en peso) sinterizados a 1300°C [Figuras 6(a)–(c)], 1500°C [Figuras 7(a)–(c)] y 1600°C [Figuras 8(a)–(c)].

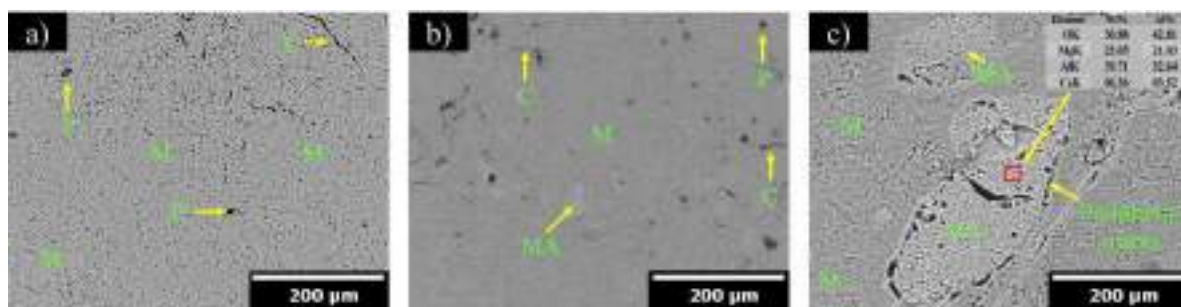


Figura 6. Micrografía SEM de la evolución microestructural de muestras de magnesia con adición creciente de η -Al₂O₃ sinterizado a 1300°C. a)1% en peso, b) 3% en peso y c) 5% en peso. M= Magnesia, C= micro fisuras, P= poros y MA= $MgAl_2O_4$ espinela.

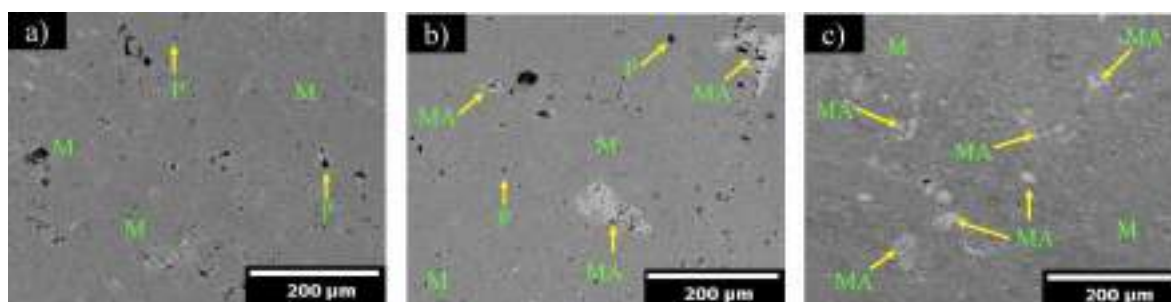


Figura 7. Micrografía SEM de la evolución microestructural de muestras de magnesita con adición creciente de η - Al_2O_3 sinterizados a 1500°C . a) 1% en peso, b) 3% en peso y c) 5% en peso. M= Magnesita, C= microfisuras, P= poros y MA= MgAl_2O_4 espinela.

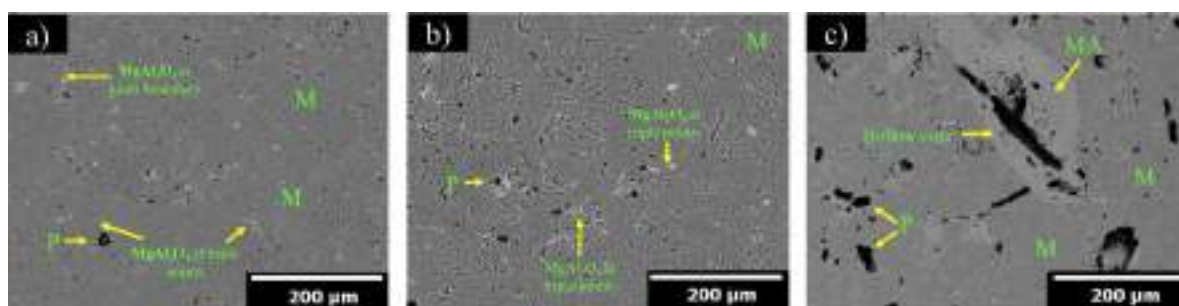


Figura 8. Micrografía SEM de la evolución microestructural de muestras de magnesita con adición creciente de η - Al_2O_3 sinterizado a 1600°C . a) 1% en peso, b) 3% en peso y c) 5% en peso. M= Magnesita, P= poros y MA= MgAl_2O_4 espinela.

La figura 6(a) muestra la microestructura correspondiente a la muestra con un 1% en peso de adición de η - Al_2O_3 , donde se observaron poros casi esferoidales, pequeños y homogéneos, así como una fase gris claro correspondiente a la magnesita. A medida que aumenta la adición de η - Al_2O_3 , se generan microfisuras, como se muestra en las Figuras 6 (b) y (c). Es bien sabido que la formación de espinela de MgAl_2O_4 se acompaña de una expansión de volumen del 5-7%, lo que contribuye a la generación de microfisuras. Además, la gran diferencia en el coeficiente de expansión térmica entre MgO ($13.6 \times 10^{-6} \text{ }^\circ\text{C}^{-1}$ desde 25°C a 1000°C) y MgAl_2O_4 espinela ($8.4 \times 10^{-6} \text{ }^\circ\text{C}^{-1}$ desde 25°C a 1000°C) genera tensiones de tracción de aro muy grandes alrededor de las partículas de espinela, que producen microfisuras extensas. Estas redes de microfisuras desarrolladas alrededor de partículas de espinela también pueden ser barreras para la propagación posterior de grietas en servicio o permitir el alivio de la tensión durante el calentamiento. Por lo tanto, la propagación de grietas es un proceso de consumo de energía mucho mayor que la iniciación de grietas en la matriz de magnesita-espinela. En la Figura 6(c), la formación de la fase MgAl_2O_4 de la espinela fue corroborada por el análisis EDX. Aquí, se puede observar que la formación inicial de espinela ocurrió alrededor de la periferia de las partículas de alúmina y procedió hacia el centro de partículas.

En las figuras 7(a) y (b), se puede observar la fase de MgO con límites de grano bien definidos (partículas de color gris oscuro). Además, se puede observar una reducción de la porosidad en comparación con las muestras refractarias sinterizadas a 1300°C ; Esto significa que las temperaturas de sinterización más altas aumentan la velocidad de

difusión, lo que redujo la porosidad y creó un proceso de densificación efectivo. En la figura 7(c), se observa claramente la fase de espinela $MgAl_2O_4$ (partículas de color gris claro).

En las figuras 8 (a) y (b), la formación de espinela se observa cerca del límite del grano y los puntos triples, ya que estos lugares específicos pueden actuar como fuentes de núcleos. A mayor aumento, se puede ver una espinela periférica fuertemente unida y un núcleo hueco, como se indica en la Figura 8 (c). Se afirma que esta característica microestructural proporciona una mejor tenacidad a la fractura [64].

El mecanismo de densificación de la matriz se promovió evidentemente a la temperatura de $1500^{\circ}C$ y $1600^{\circ}C$. El uso del polvo de $\eta-Al_2O_3$ jugó un papel importante en el control preciso de la formación de espinela in situ y en la generación efectiva del desarrollo de redes de micro fisuras alrededor de las partículas de espinela. El análisis microestructural muestra una fuerte correlación con las propiedades físicas estudiadas previamente.

La Figura 9 muestra los resultados de la resistencia de trituración en frío para diferentes contenidos de $\eta-Al_2O_3$. Se encontró que, a $1300^{\circ}C$, el CCS se mantuvo casi sin cambios con el aumento de $\eta-Al_2O_3$. Sin embargo, después de la sinterización a $1500^{\circ}C$, hubo una mejora significativa en la resistencia mecánica; el valor máximo registrado fue de 156 MPa y correspondió al 5% en peso $\eta-Al_2O_3$ de adición (A5₁₅). Esta resistencia reportada representa una mejora de alrededor del 245%, considerando que la resistencia registrada para A0₁₅ a $1500^{\circ}C$ (muestra de referencia) fue de 64 MPa. A $1600^{\circ}C$, cuando el contenido de $\eta-Al_2O_3$ aumentó de 1 a 5% en peso, la CCS disminuyó. Este comportamiento puede atribuirse a la formación de $MgAl_2O_4$, que resultó en la formación de redes de micro fisuras alrededor de esta fase, debido a la gran diferencia en los coeficientes de expansión térmica entre MgO y $MgAl_2O_4$. Estas micro fisuras son beneficiosas (hasta cierto límite) para las propiedades mecánicas, ayudando a disipar la energía almacenada en la carga de compresión, como se muestra en las muestras probadas a $1500^{\circ}C$. Sin embargo, cuando la temperatura de sinterización aumentó a $1600^{\circ}C$, el tamaño y el número de micro fisuras también aumentaron, lo que tuvo un efecto perjudicial al reducir la resistencia general y la rigidez de las muestras refractarias.

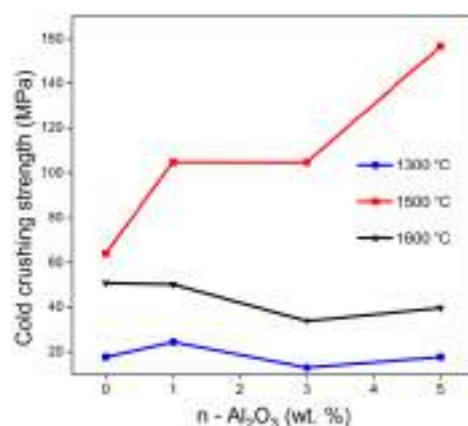


Figure 9. Resistencia a la trituración en frío a diferentes contenidos de nanopartículas de Al_2O_3 .

Por otro lado, la dureza ayuda a caracterizar la resistencia a la deformación, densificación y fractura [65]. La dureza de la cerámica depende de su composición química y de las siguientes características de microestructura: porosidad, tamaño de grano y fases límite de grano. La Figura 10 muestra la relación entre la micro dureza y el contenido de $\eta-Al_2O_3$ a $1300^{\circ}C$, $1500^{\circ}C$ y $1600^{\circ}C$, respectivamente. El análisis de los

resultados muestra claramente que un aumento en la temperatura de sinterización condujo a un aumento de la dureza. Estos resultados están bien correlacionados con la microestructura de la muestra; principalmente debido a la densificación, ya que la matriz más densa es la muestra más dura. A 1300°C, se puede observar una reducción en la micro dureza cuando se agregó η -Al₂O₃. Este fenómeno puede estar relacionado con la porosidad originada durante la formación de la espinela. A 1500°C, los especímenes alcanzaron valores de HV casi tres veces mayores que los especímenes sinterizados a 1300 °C.

Según esta observación, cuanto mayor es la temperatura de sinterización, mayores son los valores de dureza alcanzados. Sin embargo, a 1500°C, se puede observar una reducción en la dureza HV cuando se agregó η -Al₂O₃. Esta tendencia es similar a la registrada en los ejemplares sinterizados a 1300°C. Este fenómeno también se atribuye a la formación de espinelas. El valor máximo de dureza fue de 430 HV correspondiente a la muestra A0₁₆ sinterizada a 1600°C; a esta temperatura de sinterización, se observó una fuerte disminución de la dureza HV después de que se añadiera η -Al₂O₃ seguido de un cambio insignificante en la dureza HV a medida que aumentaba el η -Al₂O₃.

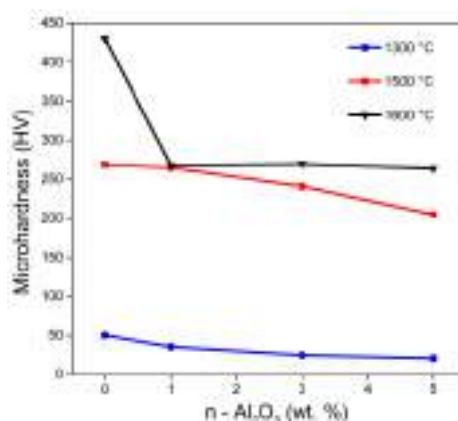


Figura 10. Variación de la micro dureza con adiciones de nanopartículas de α -alúmina.

Las figuras 11(a) a (d) muestran los termogramas DSC-TGA de muestras refractarias A0, A1, A3 y A5, respectivamente. Se identifican varios eventos térmicos en el análisis de hasta 1000 °C, que involucraron la evaporación de H₂O, descomposición de brucita y formación de espinelas.

En todos los termogramas, un evento térmico identificado como pico A se presenta a aproximadamente 100°C, que está relacionado con la evaporación de H₂O. La pérdida de peso intensa (~ 17% en peso ocurrió en todas las muestras probadas entre 300 y 425°C (una etiqueta de evento térmico como pico B), que se asocia con la deshidratación del MgO; es decir, la descomposición de brucita. MgO aparentemente absorbió algo de humedad ambiental debido a su naturaleza higroscópica. Un pequeño pico exotérmico a 550°C [66] que no aparece en el termograma de referencia (A0) se asigna a la nucleación y formación de espinela por la reacción entre alúmina y magnesia (pico C). Según la literatura, algunos autores afirmaron una formación de espinela a una temperatura inferior (alrededor de 550°C) que la presentada en esta investigación [62, 67-70]

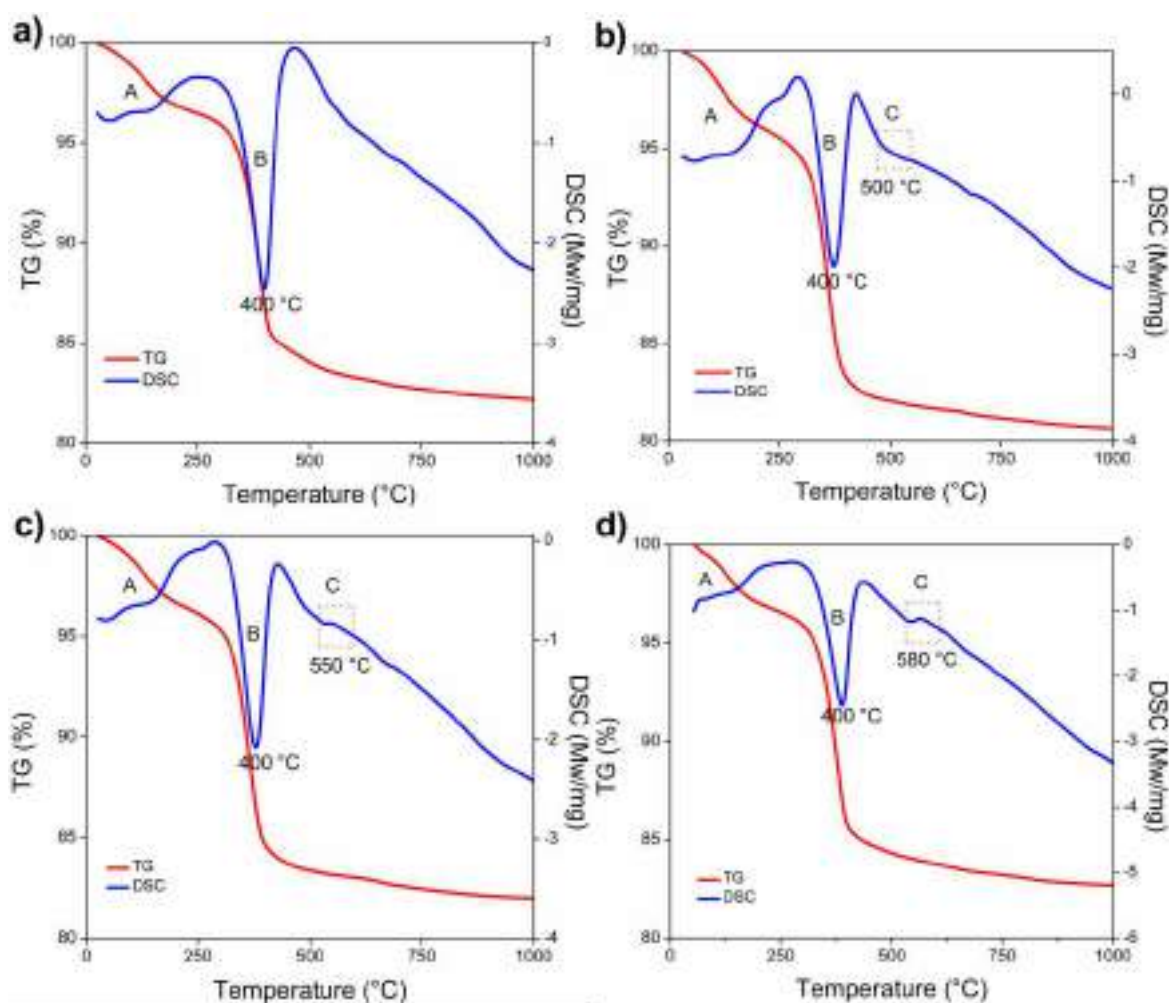


Figura 11. Resultados DSC-TG de las muestras: (a) MgO, (b) 1% en peso de Al_2O_3 , (c) 3% en peso de Al_2O_3 , y (d) 5% en peso de Al_2O_3 .

4. Conclusiones

La densificación de la matriz de magnesita se promovió evidentemente a temperaturas de 1500°C y 1600°C. El uso de polvo de $\eta\text{-Al}_2\text{O}_3$ desempeñó un papel importante para controlar con precisión la formación de espinela in situ y para desarrollar eficazmente redes de microfisuras alrededor de las partículas de espinela.

El valor máximo de CAC registrado fue de 156 MPa, lo que correspondió a la adición del 5% en peso $\eta\text{-Al}_2\text{O}_3$ a 1500°C. La mejora fue casi 2,5 veces superior a la resistencia registrada para A0₁₅ a 1500°C (muestra de referencia) que fue de 64 MPa. La formación de MgAl_2O_4 dio lugar a la formación de redes de microfisuras alrededor de esta fase debido a la gran diferencia en el coeficiente de expansión térmica entre MgO y MgAl_2O_4 . Estas microfisuras son beneficiosas (hasta cierto límite) para las propiedades mecánicas, ayudando a disipar la energía almacenada en cargas de compresión, como se muestra en las muestras probadas a 1500°C. Sin embargo, cuando la temperatura de sinterización aumentó a 1600°C, el tamaño y el número de microfisuras también aumentaron, lo que tuvo un efecto perjudicial, reduciendo la resistencia general y la rigidez de las muestras refractarias.

Se demostró claramente que el aumento de la temperatura de sinterización condujo al aumento de la dureza, porque las temperaturas de sinterización más altas favorecieron la creación de enlaces más fuertes entre los granos de MgO.

Se encontró un pequeño pico exotérmico a 550°C, y se correlacionó con la nucleación y formación de una espinela, gracias a la reacción entre η -Al₂O₃ y magnesia.

Financiamiento: El autor Cristian Gómez Rodríguez quiere expresar su agradecimiento al Consejo Nacional de Tecnología de México (CONACYT-Proyecto No. 2018-000022-01EXTV-00052) por la ayuda económica en estancia postdoctoral en la Universidad de Oviedo (Oviedo/Uviéu, Asturias, España).

Conflictos de intereses: Los autores declaran no tener conflicto de intereses

Referencias

- Sadik, C.; Moudden, O.; El Bouari, A.; El Amrani, I. Review on the elaboration and characterization of ceramics refractories based on magnesite and dolomite. *J. Asian Ceram. Soc.* 2016, 4, 219–233. DOI: <https://dx.doi.org/10.1016/j.jascer.2016.06.006>
- Schacht, C. A. (Ed.). *Refractories Handbook*, first ed.; Marcel Dekker, Inc.: New York, USA, 2004.
- Routschka, G. (Ed.). *Refractory Materials-Pocket Manual*, second ed.; Vulkan Verlag, Essen, Germany, 2004.
- Szczerba, J. Modified magnesia refractory materials. *Ceramics*. 2007, 99, 1-2.4, in Polish.
- Lee, K. S.; Jo, G.; Jung, Y.; Byeun, Y. Effect of carbon content on the mechanical behavior of MgO-C refractories characterized by Hertzian indentation. *Ceram. Int.* 2016, 42, 9955–9962. DOI: <https://doi.org/10.1016/j.ceramint.2016.03.097>
- Benavidez, E.; Brandaleze, E.; Musante, L.; Galliano, P. Corrosion Study of MgO-C Bricks in Contact with a Steelmaking Slag. *Proc. Mat. Sci.* 2015, 8, 228–235. DOI: <https://doi.org/10.1016/j.mspro.2015.04.068>
- Baudson, H.; Debucquoy, F.; Huger, M.; Gault, C.; Rigaud, M. Ultrasonic measurement of Young's modulus MgO/C refractories at high temperature. *J. Eur. Ceram. Soc.* 1999, 19, 1895–1901. DOI: [https://doi.org/10.1016/S0955-2219\(98\)00268-4](https://doi.org/10.1016/S0955-2219(98)00268-4)
- Hashemi, B.; Nemati, Z. A.; Faghihi-Sani, M. A. Effect of resin and graphite content on density and oxidation behavior of MgO-C refractory brick. *Ceram. Int.* 2006, 32, 313–319. DOI: <https://doi.org/10.1016/j.ceramint.2005.03.008>
- Musante, L.; Martorello, L. F.; Galliano, P. G.; Cavalieri, A. I.; Tomba Martinez, A. G. Mechanical behavior of MgO-C refractory bricks evaluated by stress-strain curves. *Ceram. Int.* 2012, 38, 4035–4047. DOI: <https://doi.org/10.1016/j.ceramint.2012.01.062>
- Mohamed, E.; Ewais, M. Carbon based refractories. *J. Ceram. Soc. Jpn.* 2004, 112, 517–532. DOI: <https://doi.org/10.2109/jcersj.112.517>
- Qeintela, M. A.; Santos, F.D.; Pessoa, C.A.; Rodrigues, J.A.; Pandolfelli, V. C. MgO-C refractories for steel ladles slag line. *Refract. Appl. News*. 2006, 11, 15–19.
- Aneziris, C.G.; Borzov, D.; Ulbricht, J. Magnesia carbon bricks a high duty refractory material. *Inter. Refract. Man.* 2003, 22–27.
- Han, B.; Ke, C.; Wei, Y.; Yan, W.; Wang, C.; Chen, F.; Li, N. Degradation of MgO-C refractories corroded by SiO₂-Fe₂O₃-V₂O₅-TiO₂-MnO-MgO slag. *Ceram. Int.* 2015, 41, 10966–10973. DOI: <https://doi.org/10.1016/j.ceramint.2015.05.040>
- Ghasemi-Kahrizsangi, S.; Dehsheikh, H. G.; Karamian, E. Impact of Titania nanoparticles addition on the microstructure and properties of MgO-C refractories. *Ceram. Int.* 2017, 43, 15472–15477. DOI: <https://doi.org/10.1016/j.ceramint.2017.08.094>
- Yua, C.; Dingb, J.; Denga, C.; Zhua, H.; Peng, N. The effects of sintering temperature on the morphology and physical properties of in situ Si₃N₄ bonded MgO-C refractory. *Ceram. Int.* 2018, 44, 1104–1109. DOI: <https://doi.org/10.1016/j.ceramint.2017.10.058>
- Mahato, S.; Pratihari, S. K.; Behera, S. K. Fabrication and Properties of MgO-C refractories improved with expanded graphite. *Ceram. Int.* 2014, 40, 16535–16542. DOI: <https://doi.org/10.1016/j.ceramint.2014.08.007>
- Bag, M.; Adak, S.; Sarkar, R. Study on low carbon containing MgO-C refractory: use of nanocarbon. *Ceram. Int.* 2012, 38, 2339–2346. DOI: <https://doi.org/10.1016/j.ceramint.2011.10.086>
- Behera, S.; Sarkar, R. Effect of different metal powder anti-oxidants on N220 nano carbon containing low carbon MgO-C refractory: An in -depth investigation. *Ceram. Int.* 2016, 42, 18484–18494. DOI: <https://doi.org/10.1016/j.ceramint.2016.08.185>
- Uchida, S.; Ichikawa, K.; Niihara, K. High-temperature properties of unburned MgO-C bricks containing Al and Si powders. *J. Am. Ceram. Soc.* 1998, 81, 2910–2916. DOI: <https://doi.org/10.1111/j.1151-2916.1998.tb02713.x>
- Gokce, A. S.; Gurcan, C.; Ozgen, S.; Aydin, S. The effect of antioxidants on the oxidation behavior of magnesia-carbon refractory bricks. *Ceram. Int.* 2008, 34, 323–330. DOI: <https://doi.org/10.1016/j.ceramint.2006.10.004>
- Ghosh, N. K.; Jagannathan, K. P.; Ghosh, D. N. Oxidation of magnesia-carbon refractories with addition of aluminum and silicon in air. *Interceram.* 2001, 50, 196–202.

22. Ghasemi-Kahrizangi, S.; Gheisari Dehsheikh, H.; Boroujerdnia, M. Effect of micro and nano-Al₂O₃ addition on the microstructure and properties of MgO-C refractory ceramic composite. *Mater. Chem. Phys.* 2017, 189, 230–236. DOI: <https://doi.org/10.1016/j.matchemphys.2016.12.068>
23. Bavand-Vandchali, M.; Sarpoolaky, H.; Golestani-Fard, F.; Rezaie, H. R. Atmosphere and carbon effects on microstructure and phase analysis of in situ spinel formation in MgO-C refractories matrix. *Ceram. Int.* 2009, 35, 861–868. DOI: <https://doi.org/10.1016/j.ceramint.2008.03.001>
24. Liua, H.; Meng, F.; Lib, Q.; Huanga, Zh.; Fanga, M.; Liua, Y.; Wu, X. Phase behavior analysis of MgO-C refractory at high temperature: influence of Si powder additives. *Ceram. Int.* 2015, 41, 5186–5190. DOI: <https://doi.org/10.1016/j.ceramint.2014.12.029>
25. Yamakuchi, A. Behaviors of SiC and Al added to carbon-containing refractories. *Taikabutsu Overseas* 1984, 4, 14–18.
26. Aneziris, C. G.; Hubalkov, J.; Barabas, R. Microstructure evaluation of MgO-C refractories with TiO₂- and Al-additions. *J. Eur. Ceram. Soc.* 2007, 27, 73–78. DOI: <https://doi.org/10.1016/j.jeurceramsoc.2006.03.001>
27. Bitencourta, C. S.; Luzan, A. P.; Pagliosab, C.; Pandolfelli, V. C. Phase and microstructural evolution based on Al, Si and TiO₂ reactions with a MgO-C resin-bonded refractory. *Ceram. Int.* 2016, 42, 16480–16490. DOI: <https://doi.org/10.1016/j.ceramint.2016.06.180>
28. Nemati, Z. A.; Poya-Mehr, M. R. Effects of aluminum, silicon and ferro-silicon antioxidants in MgO-C refractories. *IJE Trans. B: Appl.* 2003, 16, 361–372.
29. Suruga, T. Effect of Mg-B material addition to MgO-C bricks. *Taikabutsu Overseas* 1995, 15, 25–31.
30. Wang, T.; Yamaguchi, A. Oxidation protection of MgO-C refractories by means of Al₈B₄C₇. *J. Am. Ceram. Soc.* 2001, 84, 577–58. DOI: <https://doi.org/10.1111/j.1151-2916.2001.tb00701.x>
31. Sunwoo, S.; Kim, J. H.; Lee, K. G.; Kim, H. Preparation of ZrO₂ coated graphite powders. *J. Mater. Sci.* 2000, 35, 3677–3680. DOI: <https://doi.org/10.1023/A:1004894404376>
32. Shaowei, Zh.; Akira, Y. Effects of CaO and Al₂O₃ added to MgO-C refractories on MgO-C reaction. *J. Ceram. Soc. Jpn.* 1996, 104, 84–88. DOI: <https://doi.org/10.2109/jcersj.104.84>
33. Ichikawa, K.; Nishio, H.; Nomura, O.; Hoshiyama, Y. Suppression effects of aluminum on oxidation of MgO-C bricks. *Taikabutsu Overseas* 1995, 15, 21–24.
34. Rekha Das, R. Effect of micron and nano MgAl₂O₄ spinel addition on the properties of magnesia-carbon refractories. Thesis for the Degree of Master of Technology (Research) in Ceramic Engineering, National Institute of Technology Rourkela, Rourkela (India), October 25, 2010.
35. Saber, A.; Golestani-Fard, F.; Sarpoolaky, H.; Willert-Porada, M.; Gerdes, T.; Simon, R.; Liebscher, Ch. Development of MgAl₂O₄ spinel coating on graphite surface to improve its water-wettability and oxidation resistance. *Ceram. Int.* 2009, 35, 457–461. DOI: <https://doi.org/10.1016/j.ceramint.2007.12.007>
36. Ganesh, I.; Bhattacharjee, S.; Saha, B. P.; Johnson, R.; Rajeshwari, K.; Sengupta, R.; Ramana, M. V.; Mahajan, Y. R. An efficient MgAl₂O₄ spinel additive for improved slag erosion and penetration resistance of high-Al₂O₃ and MgO-C refractories. *Ceram. Int.* 2002, 28, 254–253. DOI: [https://doi.org/10.1016/S0272-8842\(01\)00086-4](https://doi.org/10.1016/S0272-8842(01)00086-4)
37. Zhu, T.; Li, Y.; Sang, S.; Xie, Z. Fracture behavior of low carbon MgO-C refractories using the wedge splitting test. *J. Eur. Ceram. Soc.* 2017, 37, 1789–1797. DOI: <https://doi.org/10.1016/j.jeurceramsoc.2016.11.013>
38. Wang, Q.; Li, Y.; Li, S.; Xu, N.; Xiang, R.; Yang, O.; Ni, Y. Effects of nano-alumina content on the formation of interconnected pores in porous purging plug materials. *Ceram. Int.* 2017, 43, 16722–16726. DOI: <https://doi.org/10.1016/j.ceramint.2017.09.064>
39. Shahraki, A.; Ghasemi-Kahrizangi, S.; Nemati, A. Performance improvement of MgO-CaO refractories by the addition of nano-sized Al₂O₃. *Mater. Chem. Phys.* 2017, 198, 354–359. DOI: <https://doi.org/10.1016/j.matchemphys.2017.06.026>
40. Ghasemi-Kahrizangi, S.; Sedeh, M. B.; Dehsheikh, H. G.; Shahraki, A.; Farooghi, M. Densification and properties of ZrO₂ nanoparticles added magnesia-dolomite refractories. *Ceram. Int.* 2016, 42, 15658–15663. DOI: <https://doi.org/10.1016/j.ceramint.2016.07.021>
41. Dehsheikh, H. G.; Ghasemi-Kahrizangi, S. The influence of silica nanoparticles addition on the physical, mechanical, thermo-mechanical as well as microstructure of Mag-Dol refractory composites. *Ceram. Int.* 2017, 43, 6780–16786. DOI: <https://doi.org/10.1016/j.ceramint.2017.09.073>
42. Ghasemi-Kahrizangi, S.; Dehsheikh, H. G.; Karamian, E.; Nemati, A. A comparative evaluation of the additional impact of nanometer-sized tetravalent oxides on the performance of Dolomite-Magnesia ceramic refractories. *Ceram. Int.* 2018, 44, 2058–2064. DOI: <https://doi.org/10.1016/j.ceramint.2017.10.151>
43. Yuan, W.; Tang, H.; Zhou, Y.; Zhang, D. Effects of fine reactive alumina powders on properties of alumina-magnesia castables with TiO₂ addition. *Ceram. Int.* 2018, 44, 5032–5036. DOI: <https://doi.org/10.1016/j.ceramint.2017.12.100>
44. Bag, M.; Adak, S.; Sarkar, R. Nano carbon containing MgO-C refractory: effect of graphite content. *Ceram. Int.* 2012, 38, 4909–4914. DOI: <https://doi.org/10.1016/j.ceramint.2012.02.082>
45. Tamura, S.; Ochiai, S.; Takanaga, S.; Kanai, T.; Nakamura, H. Nano-tech. refractories-1: the development of the nano structural matrix. In *Proceedings of UNITECR '03 Congress, Osaka, Japan, October 19–22, 2003*, pp. 515–520.

46. Takanaga, S.; Ochiai, T.; Tamura, T.; Kanai, T.; Nakamura, H. Nano-tech. refractories-2: the application of the nano structural matrix to MgO-C bricks. In Proceedings of UNITECR'03 Congress, Osaka, Japan, October 19-22, 2003, pp. 521-524.
47. Zhu, T. B.; Li, Y. W.; Sang, S. B.; Jin, S. L.; Li, Y. B.; Zhao, L.; Liang, X. Effect of nanocarbon sources on microstructure and mechanical properties of MgO-C refractories. *Ceram. Int.*, 2014, 40, 4333–4340. DOI: <https://doi.org/10.1016/j.ceramint.2013.08.101>
48. Zhu, T. B.; Li, Y. W.; Luo, M.; Sang, S. B.; Wang, Q. H.; Zhao, L.; Li, Y. B.; Li, S. J. Microstructure and mechanical properties of MgO-C refractories containing graphite oxide nanosheets (GONs). *Ceram. Int.* 2013, 39, 3017–3025. DOI: <https://doi.org/10.1016/j.ceramint.2012.09.080>
49. Zhu, T. B.; Li, Y. W.; Jin, S. L.; Sang, S. B.; Wang, Q. H.; Zhao, L.; Li, Y. B.; Li, S. J. Microstructure and mechanical properties of MgO-C refractories containing expanded graphite. *Ceram. Int.* 2013, 39, 4529–4537. DOI: <https://doi.org/10.1016/j.ceramint.2012.11.049>
50. Mahato, S.; Behera, S. K. Oxidation resistance and microstructural evolution in MgO-C refractories with expanded graphite. *Ceram. Int.* 2016, 42, 7611–7619. DOI: <https://doi.org/10.1016/j.ceramint.2016.01.169>
51. Luo, M.; Li, Y. W.; Jin, S. L.; Sang, S. B.; Zhao, L.; Li, Y. B. Microstructures and mechanical properties of Al₂O₃-C refractories with addition of multi-walled carbon nanotubes. *Mater. Sci. Eng.: A.* 2012, 548, 134–141. DOI: <https://doi.org/10.1016/j.msea.2012.04.001>
52. Wei, G.P.; Zhu, B. Q.; Li, X. C.; Ma, Z. Microstructure and mechanical properties of low carbon MgO-C refractories bonded by an Fe nanosheet-modified phenolic resin. *Ceram. Int.* 2015, 41, 1553–1566. DOI: <https://doi.org/10.1016/j.ceramint.2014.09.091>
53. Matsuo, Y.; Tanaka, M.; Yoshitomi, S.; Yoon, S.; Miyawaki, J. Effect of the carbon nanofiber addition on the mechanical properties of MgO-C brick. In Proceedings of UNITECR'11 Congress, Kyoto, Japan, October 30-November 2, 2011, pp. 959-962.
54. Ghasemi-Kahrizsangi, S.; Karamian, E.; Dehsheikh, H. G. The impact of ZrSiO₄ nanoparticles addition on the microstructure and properties of dolomite based refractories. *Ceram. Int.* 2017, 43, 13932–13937. DOI: <https://doi.org/10.1016/j.ceramint.2017.07.122>
55. Zargar, H. R.; Oprea, C.; Oprea, G.; Troczynski, T. The effect of nano-Cr₂O₃ on solid-solution assisted sintering of MgO refractories. *Ceram. Int.* 2012, 38, 6235–6241. DOI: <https://doi.org/10.1016/j.ceramint.2012.04.077>
56. Azhari, A.; Golestani-Fard, F.; Sarpoolaky, H. Effect of nano iron oxide as an additive on phase and microstructural evolution of Mag-Chrome refractory matrix. *J. Eur. Ceram. Soc.* 2009, 29, 2679–2684. DOI: <https://doi.org/10.1016/j.jeurceram-soc.2009.03.032>
57. Huizhong, L. H.; Jianxiu, W. Influence of nano-Fe₂O₃ on sintering and mechanical property of magnesia-chrome refractories. *Refractories* 2003, 5, 002.
58. Chen, M.; Lu, C.; Yu, J. Improvement in performance of MgO-CaO refractories by addition of nano-sized ZrO₂. *J. Eur. Ceram. Soc.* 2007, 27, 4633–4638. DOI: <https://doi.org/10.1016/j.jeurceramsoc.2007.04.001>
59. Ghasemi-Kahrizsangi, S.; Dehsheikh, H. G.; Karamian, E.; Boroujerdnia, M.; Payandeh, K. Effect of MgAl₂O₄ nanoparticles addition on the densification and properties of MgO-CaO refractories. *Ceram. Int.* 2017, 43, 5014–5019. DOI: <https://doi.org/10.1016/j.ceramint.2017.01.011>
60. Ghasemi-Kahrizsangi, S.; Dehsheikh, H. G.; Boroujerdnia, M. MgO-CaO-Cr₂O₃ composition as a novel refractory brick: Use of Cr₂O₃ nanoparticles. *Bol. Soc. Española Cerámica Vidr.* 2017, 56, 83–89. DOI: <https://doi.org/10.1016/j.bsecv.2016.11.002>
61. Rodríguez, E.; Moreno, F. H.; Aguilar-Martínez, J. A.; Montes-Mejía, A. E.; Ruiz-Valdés, J. J.; Puente-Ornelas, R.; Contreras, J. E. Effect of nano-titania (η-TiO₂) content on the mechano-physical properties of a magnesia refractory composite. *Ceram. Int.* 2016, 42, 844–8452. DOI: <https://doi.org/10.1016/j.ceramint.2016.02.064>
62. Saberi, A.; Golestani-Fard, F.; Willert-Porada, M.; Negahdari, Z.; Liebscher, C.; Gossler, B. A novel approach to synthesis of nanosized MgAl₂O₄ spinel powder through sol-gel citrate technique and subsequent heat treatment. *Ceram. Int.* 2009, 35, 933–937. DOI: <https://doi.org/10.1016/j.ceramint.2008.03.011>
63. Gómez Rodríguez, C.; Das Roy, T. K.; Shaji, S.; Castillo Rodríguez, G. A.; García Quiñonez, L.; Rodríguez, E.; González, J. O.; Aguilar-Martínez, J. A. Effect of addition of Al₂O₃ and Fe₂O₃ nanoparticles on the microstructural and physic-chemical evolution of dense magnesia composite. *Ceram. Int.* 2015, 41, 7751–7758. DOI: <https://doi.org/10.1016/j.ceramint.2015.02.107>
64. Soady, J. S.; Plint, S. A quantitative thermal shock approach to the development of magnesia-spinel refractories for the cement kiln. In Proceedings of UNITECR'91 Congress, Aachen Germany, 1991, pp. 443–449.
65. Hardness Testing of Ceramics. Available online: http://www.spectru.com.br/hardness_testing_ceramics.pdf (accessed on 19 November 2019).
66. Sainz, M. A.; Mazzoni, A. D.; Aglietti, E. F.; Caballero, A. Thermochemical stability of spinel (MgO-Al₂O₃) under strong reducing condition. *Mater. Chem. and Phys.* 2004, 86, 399–408. DOI: <https://doi.org/10.1016/j.matchemphys.2004.04.007>
67. Liu, C.-M.; Chen, J.; Chen, C.-J. The growth of an epitaxial Mg-Al spinel layer on sapphire by solid-state reactions. *J. Cryst. Growth.* 2005, 285, 275–283. DOI: <https://doi.org/10.1016/j.jcrysgro.2005.08.023>

68. Saberi, A.; Golestani-Fard, F.; Sarpoolaky, H.; Willert-Porada, M.; Gerdes, T.; Simon, R. Chemical synthesis of nanocrystalline magnesium aluminate spinel via nitrate-citrate combustion route. *J. Alloy. Comp.* 2008, 462, 142–146. DOI: <https://doi.org/10.1016/j.jallcom.2007.07.101>
69. Alinejad, B.; Sarpoolaky, H.; Beitollahi, A.; Saberi, A.; Afshar, S. Synthesis and characterization of nanocrystalline MgAl₂O₄ spinel via sucrose process. *Mater. Res. Bull.* 2008, 43, 1188–1194. DOI: <https://doi.org/10.1016/j.materresbull.2007.05.031>
70. Su, X.; Du, X.; Li, S.; Li, J. Synthesis of MgAl₂O₄ spinel nanoparticles using a mixture of bayerite and magnesium sulfate. *J. Nanopart. Res.* 2010, 12, 1813–1819. DOI: <https://doi.org/10.1007/s11051-009-9739-2>
71. © 2019 by the authors. Submitted for possible open access publication under the terms and conditions of the Creative Commons Attribution (CC BY) license (<http://creativecommons.org/licenses/by/4.0/>).

7. Conclusiones

A continuación, se presentan las conclusiones relacionadas con las dos líneas descritas en el presente trabajo:

1. *Línea de síntesis de materiales cerámicos.*
2. *Línea de sinterización de materiales compuestos de matriz cerámica.*

Conclusiones de línea de síntesis de materiales cerámicos.

En este caso, lo que se buscaba era el empleo de la energía solar concentrada para la síntesis de dos materiales cerámicos de uso relativamente común, como son la zirconia y la espinela de aluminato de magnesio. En ambos casos se puede concluir que se logró la formación de los compuestos ZrO_2 y $MgAl_2O_4$ empleando energía solar. Así, se puede concluir que cuando se encuentra adecuadamente concentrada la energía solar permite suministrar la energía térmica suficiente para lograr la síntesis de materiales cerámicos, pudiendo contribuir de modo decisivo a reducir las emisiones de gases de efecto invernadero.

A continuación, se exponen las conclusiones derivadas de los artículos de esta línea:

+ Obtención de ZrO_2 por descomposición térmica de arena de silicato de zirconio (*Solar dissociation of zirconium silicate sand: A clean alternative to obtain zirconium dioxide*):

- Se obtiene por primera vez ZrO_2 por descomposición térmica del silicato de zirconio empleando energía solar, empleando un proceso que combina la pirometalurgia y la hidrometalurgia.
- La descomposición del $ZrSiO_4$ empleando energía solar se logra en todas las rutas estudiadas: 100 % $ZrSiO_4$, 90 % en peso de $ZrSiO_4$ + 10 % en peso de Na_2CO_3 , y

$ZrSiO_4$ + 10, 25 o 50 % en peso de CaO, aunque solamente en la primera se logra ZrO_2 en una forma fácilmente separable por vía hidrometalúrgica.

- La mejor ruta para la obtención del ZrO_2 puro es el tratamiento en reactor presurizado en medio acuoso con NaOH durante 6 horas a 200 °C sobre muestras obtenidas por aplicación directa de la energía solar sobre 100% de arena de silicato de zirconio.
- Se obtiene tras el tratamiento hidrometalúrgico ZrO_2 insoluble y silicato soluble de sodio que, tras filtrado, permite lograr una zirconia monoclinica de pureza superior al 95%.

Se puede concluir que se obtiene ZrO_2 con una pureza superior al 95% por descomposición térmica empleando energía solar concentrada y posterior tratamiento hidrometalúrgico con sosa partiendo únicamente de arena de silicato de zirconio sin aditivos.

+ Obtención de $MgAl_2O_4$ a partir de residuos de la industria del aluminio empleando energía solar concentrada (Solar Assisted Production of $MgAl_2O_4$ from Bayer Process Electrofilter

Fines as Source of Al_2O_3):

- Se logra por primera vez la síntesis de $MgAl_2O_4$ a partir de finos de electrofiltro generados en la industria del aluminio empleando energía solar concentrada.
- Se obtiene una fase cristalina de $MgAl_2O_4$ independientemente de los finos de electrofiltro del proceso Bayer empleados.
- Se logra la síntesis de la espinela en tiempos muy cortos (<5 minutos) de aplicación del haz de energía solar concentrada.

- Las reducciones en emisiones de dióxido de carbono podrían exceder las 12000 toneladas al año para plantas de un tamaño de 25000 toneladas de $MgAl_2O_4$ producidas al año.

Conclusiones de línea de sinterización de materiales compuestos de matriz cerámica.

Se propuso el estudio de sinterización en horno convencional de cerámicas refractarias agregando diferentes óxidos metálicos como segunda fase, para mejorar propiedades físicas, químicas, mecánicas, morfológicas y microestructurales de los composites cerámicos.

- La incorporación de nanopartículas de óxidos metálicos ZrO_2 , TiO_2 , SiO_2 , Al_2O_3 , Fe_2O_3 y $Fe_2Al_2O_4$ en diferentes contenidos a un cerámico de matriz MgO produce una mejora en la densificación del material compuesto obtenido. Igualmente, se produce una mejora de las propiedades mecánicas, que, en el caso de la resistencia a la compresión en frío, para el composite MgO -5% en peso de ZrO_2 permite prácticamente triplicar la del MgO sinterizado en las mismas condiciones (prensado uniaxial + prensado isostático (ambos en frío y 100 MPa) y sinterización a 1650 °C durante 4 horas).
- Precisamente en los composites MgO - ZrO_2 , el de un 5% en peso de segunda fase prensado en uniaxial y en isostático (ambos en frío y 100 MPa) para obtener el compacto en verde y sinterizado a 1650 °C durante 4 horas permite obtener los menores valores de porosidad (14.485%), los mayores valores de densidad (3.0599 g/cm^3) y un valor de resistencia a la compresión en frío un 80.87% mayor que la del MgO sin aditivos.
- En el caso de los composites de MgO - TiO_2 se pueden obtener estos nanocomposites por diferentes rutas, ya sea partiendo del MgO directamente o empleando $Mg(OH)_2$

como precursor del MgO. La adición de las nanopartículas de TiO_2 sobre el $\text{Mg}(\text{OH})_2$ y la posterior calcinación a $960\text{ }^\circ\text{C}$ durante 2 horas, permite que, tras la obtención del compacto en verde (prensado uniaxial a 150 MPa) y sinterización ($1600\text{ }^\circ\text{C}$ durante 4 horas), se obtenga un material compuesto con una mayor densidad para todas las composiciones estudiadas (1, 3 y 5% en peso), que se cuantifica en el rango 2.5-3% con relación a la adición de las nanopartículas de TiO_2 sobre el MgO directamente. Por otra parte, la mejora en la ruta novedosa en términos de resistencia a la compresión en frío se sitúa en el rango 16-23%. Los mejores resultados se obtienen en la muestra con un 5% en peso de nanopartículas de TiO_2 donde la resistencia a la compresión en frío llega a 236 MPa .

- En el caso de los composites MgO- $\eta\text{-Al}_2\text{O}_3$ se logra una mejora de casi 2.5 veces de la resistencia a la compresión en frío en la muestra con un 5% de nanopartículas con relación a la muestra de referencia cuando la sinterización se lleva a cabo a $1500\text{ }^\circ\text{C}$ sin nanopartículas. Un incremento de la temperatura de sinterización ($1600\text{ }^\circ\text{C}$) no se tradujo en una mejora en términos de la resistencia a la compresión en frío.
- La incorporación de nanopartículas de Fe_2O_3 y SiO_2 contribuyó a la formación de magnesio ferrita y silicatos de calcio y magnesio que alteraron la sinterización de la muestra, en muestras compactadas uniaxialmente en frío a 100 MPa y sinterizadas durante 4 horas a $1600\text{ }^\circ\text{C}$. En el caso de las nanopartículas de SiO_2 resultó ser negativo para la muestra sinterizada debido a la formación de porosidad abierta. Por el contrario, en el caso de emplear un 5% en peso de nanopartículas de Fe_2O_3 , se logró una mejora en la densidad y una baja porosidad (1.8%).
- La incorporación de nanopartículas de hercinita ($\text{Fe}_2\text{Al}_2\text{O}_4$) en refractarios de magnesia condujo a una mejora de la dureza del composite, especialmente con un

20% en peso de esta segunda fase. Asimismo, se apreció una mejora en la densificación del composite.

Se propuso estudiar el empleo de novedosas tecnologías de sinterización (utilizando sinterización por spark plasma sintering y láser de CO₂) para procesamiento de polvos en la obtención de cuerpos densos de un cerámico común, como es la Al₂O₃, con una segunda fase de molibdeno añadida para mejorar las propiedades mecánicas derivadas de una inhibición en el crecimiento del tamaño de grano del constituyente matriz.

Sinterización de composites de alúmina y molibdeno empleando láser de CO₂ (*Selective laser sintering of alumina-molybdenum nanocomposites*):

- Se obtuvieron por primera vez compuestos de alúmina y molibdeno empleando la tecnología de sinterización de láser de CO₂ para obtener cuerpos densos, variando el contenido en molibdeno (1, 2.5, 5, 10 y 20 % en peso).
- Incrementar el contenido en molibdeno conducía a menor porosidad en el composite, aunque los mejores resultados se obtuvieron con un 10% en peso de molibdeno. Igualmente, es para este material para el que se observan los menores tamaños de grano de Al₂O₃ motivados por el efecto *pinning* que produce este metal.
- Contenidos superiores al 10% en peso de molibdeno conducen a la formación significativa de óxido de molibdeno (VI) que aparece en la muestra, aunque también se pierde por volatilización.

Síntesis por ruta coloidal y sinterización de composites de alúmina y molibdeno por Spark Plasma Sintering (*Alumina/molybdenum nanocomposites obtained by colloidal synthesis and spark plasma sintering*):

- Se obtuvieron por primera vez nanocomposites de alúmina y molibdeno densos mediante la ruta coloidal, empleando cloruro de molibdeno como precursor del molibdeno, y sinterización por *spark plasma sintering* en tiempos muy cortos (3 minutos a la temperatura de sinterización de 1400 °C).
- La dureza y la tenacidad se incrementan al menos un 25% con relación a la muestra de alúmina sin nanopartículas. En este sentido, el composite con un 1% en peso de molibdeno presenta una dureza un 28% superior, mientras que la tenacidad es un 50% mayor para el composite con un 5% en peso de molibdeno. Por el contrario, la resistencia a la flexión en tres puntos es al menos un 18% inferior al emplear molibdeno.
- Las nanopartículas de molibdeno inhiben el crecimiento del tamaño de grano de la alúmina. Así, el grano de Al_2O_3 en el composite es $<1.6 \mu\text{m}$, mientras que en la alúmina monolítica $> 70\%$ de los granos de alúmina tiene un tamaño de grano $>2 \mu\text{m}$.
- El empleo del SPS y la ruta coloidal permiten un control efectivo del crecimiento del tamaño de grano que se traduce a una mejora de alguna de las propiedades mecánicas.

8. Conclusions

We are going to present the conclusions related to the two lines described in this research:

1. *Line of synthesis of ceramic materials.*
2. *Line of sintering of ceramic matrix composites.*

Conclusions of the line of synthesis of ceramic materials.

In this case, we proposed the utilization of concentrated solar energy to synthesize two ceramic materials of common use, the zirconia and the magnesium aluminate spinel. In both cases, it is possible to conclude that the formation of the compounds ZrO_2 and $MgAl_2O_4$ was achieved with the competition of solar energy. Therefore, it is possible to conclude that when solar energy is adequately concentrated allows sufficient thermal energy to attain the synthesis of ceramic materials, contributing decisively to reduce the emissions of greenhouse gases.

Now, we present the conclusions deduced from the articles presented in this line:

+ Obtaining of ZrO_2 by thermal decomposition of the zirconium silicate sand (*Solar dissociation of zirconium silicate sand: A clean alternative to obtain zirconium dioxide*):

- We obtain for the first time ZrO_2 by thermal decomposition of the zirconium silicate sand using solar energy, employing a process that combines the pyrometallurgy and the hydrometallurgy.
- The decomposition of the $ZrSiO_4$ using solar energy is achieved in all the studied routes: 100 wt. % $ZrSiO_4$, 90 wt. % $ZrSiO_4$ + 10 wt. % Na_2CO_3 , and $ZrSiO_4$ + 10, 25 or 50 wt. % CaO , although only the first route provided ZrO_2 in a form that allows separating it in an easy manner using the hydrometallurgical route.

- The best route for obtaining pure ZrO_2 is the treatment in a pressurized reactor using an aqueous medium with NaOH for 6 hours at 200 °C on samples obtained by direct application of the solar energy over 100% zirconium silicate sand samples.
- We obtain after the hydrometallurgical treatment: insoluble ZrO_2 and soluble sodium silicate that, after filtering allows obtaining a monoclinic zirconia with a purity above the 95%.

It is possible to conclude that ZrO_2 is obtained with a purity above 95% by thermal decomposition using concentrated solar energy and posterior hydrometallurgical treatment with caustic soda starting from only zirconium silicate sand (without additives).

+ Obtaining of $MgAl_2O_4$ using residues of the aluminium industry using concentrated solar energy (Solar Assisted Production of $MgAl_2O_4$ from Bayer Process Electrofilter Fines as Source of Al_2O_3):

- It is achieved for the first time the synthesis of $MgAl_2O_4$ using electrofilter fines generated in the aluminium industry using concentrated solar energy.
- A crystalline $MgAl_2O_4$ is obtained independently on the electrofilter fines generated in the Bayer process that was used in the process.
- The synthesis of the spinel is achieved in very short times (<5 minutes) of application of the beam of concentrated solar energy.
- The reductions in the emissions of carbon dioxide might exceed 12000 tons per year for factories with a size of 25000 tons of $MgAl_2O_4$ produced per year.

Conclusions of the line of sintering of ceramic matrix composites.

We proposed the study of the sintering in a conventional furnace of refractory ceramics adding different metallic oxides as the second phase to improve the physical, chemical, mechanical, morphological, and microstructural properties of the ceramic composites.

- The incorporation of nanoparticles of metallic oxides ZrO_2 , TiO_2 , SiO_2 , Al_2O_3 , Fe_2O_3 , and $Fe_2Al_2O_4$ in different contents to a ceramic of MgO matrix produces an improvement in the densification of the obtained composite. Moreover, an improvement in the mechanical properties is produced which, in the case of the cold crushing strength, for the composite MgO-5 wt. % of ZrO_2 allows practically to triplicate that of the MgO sintered in the same conditions (uniaxial pressing + isostatic pressing (both in cold and 100 MPa) and sintering at 1650 °C for 4 hours).
- It is precisely in the composites of MgO- ZrO_2 , that with 5 wt. % of the second phase and uniaxially and isostatically pressed (both in cold and 100 MPa) to obtain the green compact and sintered at 1650 °C for 4 hours allows obtaining the lowest values of porosity (14.485%), the greatest values of density (3.0599 g/cm³) and a value of cold crushing strength an 80.87% bigger than that of the MgO without additives.
- In the case of the MgO- TiO_2 composites, it is possible to obtain them by different routes, either starting directly from the MgO or using $Mg(OH)_2$ as the precursor of the MgO. The addition of TiO_2 nanoparticles to the $Mg(OH)_2$ and, the subsequent calcination at 960 °C for 2 hours, allows that, after the obtaining of the green compact (uniaxial pressing at 150 MPa) and sintering (1600 °C for 4 hours), obtaining a composite with a greater density for all the studied compositions (1, 3 and 5 wt. %), which is quantified in the range 2.5-3% with relation to the addition of TiO_2

nanoparticles directly to the MgO. On the other hand, the improvement achieved in the novel route in terms of cold crushing strength is in the range of 16-23%. The best results are obtained in the sample with 5 wt. % of TiO₂ nanoparticles, where the cold crushing strength reaches 236 MPa.

- In the case of the MgO- η-Al₂O₃ composites, an improvement of almost 2.5 times was achieved in the cold crushing strength in the sample with 5% of nanoparticles in relation to the reference sample when the sintering was conducted at 1500 °C without nanoparticles. An increase in the sintering temperature (1600 °C) was not translated into an improvement in terms of cold crushing strength.
- The incorporation of Fe₂O₃ and SiO₂ nanoparticles contributed to the formation of magnesium ferrite and silicates of calcium and magnesium that altered the sintering of the samples, in those uniaxially cold pressed at 100 MPa and sintered for 4 hours at 1600 °C. In the case of SiO₂ nanoparticles, its presence was negative for the sample due to the formation of open porosity. On the contrary, in the case of using a 5 wt. % of Fe₂O₃ nanoparticles, an improvement of the density was achieved, and a low porosity was attained (1.8%).
- The incorporation of hercynite nanoparticles (Fe₂Al₂O₄) into refractories of magnesia led to an improvement in the hardness of the composite, specifically with a 20 wt. % of molybdenum. Additionally, an increase in the relative density of the composite was achieved.

We proposed to study the utilization of novel technologies of sintering (spark plasma sintering and CO₂ laser) to process powders in the obtaining of dense bodies of a common ceramic, as it is the Al₂O₃, with a second phase of molybdenum added to improve the

mechanical properties resulted from the inhibition of the grain growth of the matrix constituent.

Sintering of alumina and molybdenum composites using CO₂ laser (*Selective laser sintering of alumina-molybdenum nanocomposites*):

- We obtained for the first-time composites of alumina and molybdenum using the sintering technology with CO₂ laser to obtain dense bodies, varying the molybdenum content (1, 2.5, 5, 10, and 20 wt. % Mo).
- Increasing the molybdenum content led to less porosity in the composite, although the best results were obtained with a 10 wt. % of molybdenum. Additionally, for this material, the smallest grain sizes of Al₂O₃ are observed, which are produced by the *pinning* effect produced by this metal.
- Molybdenum contents above 10 wt. % lead to the formation of significant quantities of molybdenum (VI) oxide that appears in the sample, although it is also lost by volatilization.

Synthesis of alumina-molybdenum composites by colloidal processing route and sintering of the composites by Spark Plasma Sintering (*Alumina/molybdenum nanocomposites obtained by colloidal synthesis and spark plasma sintering*):

- We obtained for the first time dense nanocomposites of alumina and molybdenum by the colloidal processing route, using molybdenum chloride as the precursor of the molybdenum, and sintering using *spark plasma sintering* in very short times (3 minutes at a sintering temperature of 1400 °C).

- The hardness and toughness increase by at least 25% concerning the alumina without nanoparticles. This way, the composite with a 1 wt. % of molybdenum has a hardness of 28% greater, while the toughness is 50% greater for the composite with a 5 wt. % of molybdenum. On the contrary, the flexural strength in the three-point bending test is at least 18% lower than in the case of using molybdenum.
- The nanoparticles of molybdenum inhibit the grain growth of the alumina. Therefore, the grain of Al_2O_3 in the composite is $<1.6 \mu\text{m}$, while in the monolithic alumina, more than 70% of the alumina grains have a size $>2 \mu\text{m}$.
- The utilization of the SPS and the colloidal processing route allows effective control of the grain size growth that is translated into improving the mechanical properties.